Agota Mockutė

Suitability of Wave Loading Models for Offshore Wind Turbine Monopiles in Rough Seas

SHAKER VERLAG

Heft 8

SUITABILITY OF WAVE LOADING MODELS FOR OFFSHORE WIND TURBINE MONOPILES IN ROUGH SEAS

Dissertation

submitted to and approved by the

Faculty of Architecture, Civil Engineering and Environmental Sciences
Technische Universität Braunschweig

and the

Department of Civil and Environmental Engineering
University of Florence

in candidacy for the degree of a
Doktor-Ingenieurin (Dr.-Ing.) /
Dottore di Ricerca in Civil and Environmental Engineering[*)]

by

Agota Mockutė
born 11 December 1992
from Vilnius, Lithuania

Submitted on	20 August 2019
Oral examination on	06 November 2019
Professorial advisors	Prof. Claudio Borri Prof. Klaus Thiele

2020

*) Either the German or the Italian form of the title may be used. (Please leave this remark on the cover page.)

Schriftenreihe des Instituts für Stahlbau

Heft 8

Agota Mockutė

Suitability of Wave Loading Models for Offshore Wind Turbine Monopiles in Rough Seas

Shaker Verlag
Düren 2020

Bibliographic information published by the Deutsche Nationalbibliothek
The Deutsche Nationalbibliothek lists this publication in the Deutsche Nationalbibliografie; detailed bibliographic data are available in the Internet at http://dnb.d-nb.de.

Zugl.: Braunschweig, Techn. Univ., Diss., 2019

Printed in Germany.

ISBN 978-3-8440-7438-3
ISSN 2198-8722

Shaker Verlag GmbH • Am Langen Graben 15a • 52353 Düren
Phone: 0049/2421/99011-0 • Telefax: 0049/2421/99011-9
Internet: www.shaker.de • e-mail: info@shaker.de

Acknowledgments

I would like to express my gratitude to the people and institutions without who and which this thesis would not have been possible.

To my supervisors, Prof. Claudio Borri (University of Florence, Italy) and Prof. Klaus Thiele (TU Braunschweig, Germany). For believing in me and granting me this opportunity, for your continuous support, guidance, advice and encouragement. You lead by example and have shaped me as a young researcher.

To my advisors, Dr Enzo Marino (University of Florence, Italy) and Prof. Claudio Lugni (CNR-INSEAN, Italy). For all those hours beyond count you have dedicated to me despite my silly questions and poor connection on Skype. Without your expertise, patience and willingness to help this thesis would not exist.

To the Marie Skłodowska-Curie Innovative Training Network (ITN) "AEOLUS4FUTURE – Efficient harvesting of the wind energy" (H2020-MSCA-ITN-2014: Grant agreement no. 643167), funded by the European Commission's Framework Program "Horizon 2020". For enabling me to spend three wonderful years on this exciting research and all the associated training.

To Dr Rob Dorrell (University of Hull, UK), as well the Aura team and Energy and Environment Institute. For believing in me and this research, and creating conditions for continuation.

To the COST TU1304 action WINERCOST. For the training schools and Short Term Scientific Missions which enabled me to establish a professional network in the field of wind energy.

To my family and friends. For everything. It would take another book to describe all your support.

Abstract

Motivated by the ever-growing need for secure and cost-efficient renewable energy, this thesis discusses the suitability of current numerical wave loading models for monopile-supported offshore wind turbines in highly nonlinear rough seas. To discuss the distinct influences of nonlinearities in wave loading models, combinations of six increasingly nonlinear regular wave theories, three irregular wave solvers, and three hydrodynamic loading models were modelled. Wave loading was discussed on increasingly complex slender structures: fixed rigid cylinder, bottom-hinged rigid cylinder and a fully flexible monopile-supported offshore wind turbine.

It was found that in deep water the hydrodynamic loading models tend to dominate, therefore solvers can be optimised by compromising on the wave kinematics. However, in intermediate water depth, where monopile-supported offshore wind turbines are commonly placed, the nonlinearities in wave kinematics become more significant. To fully capture the nonlinear phenomena in rough seas and intermediate water depth fully nonlinear wave kinematics were found to be required. Nonetheless, if unavailable or unfeasible, less computationally intensive second order wave kinematics were found to show a significant improvement from the linear wave kinematics, which continuously resulted in underestimation of wave loading. However, attention should be paid when applying the second order wave kinematics in steeper waves where it tends towards overestimation.

Attention was also drawn to several fundamental issues. Wave loading across all numerical models shows monotonic growth with increasing wave steepness in every harmonic. Such behaviour is not seen in the higher harmonics of the reported experimental values, leading to an increasing overprediction at the higher wave steepness. Moreover, nonlinear fluid-structure interaction was noted to have an effect on the natural frequency of the offshore structure. If unaccounted for, this may lead to design frequencies which fall in the resonant range of wave frequencies, causing unexpected oscillations from the nonlinear phenomena.

To conclude, the findings of this thesis are expected to contribute to more efficient and accurate modelling of wave loading to aid safer and more economical next generation monopile supports for offshore wind turbines, helping the world transform towards becoming carbon-emissions neutral.

Contents

List of Figures

List of Tables

Chapter 1

Introduction

This chapter details the motivation behind the work displayed in this thesis – the global need to shift towards renewable energy and the advantages of wind energy, focusing on offshore wind power. The need for numerical modelling of offshore wind turbines and its current status are discussed, identifying the gap in knowledge which this thesis aims to fill. Finally, the scope and structure of this work are summarised.

1.1 Need for renewable energy

Energy sector in the post-industrial world is facing three main requirements, also known as the energy trilemma: energy security, energy equity and environmental sustainability (World Energy Council, 2017). There is no unique solution to such problem to this date, but renewable energy sources provide a step forward in all three aspects. Firstly and most straightforwardly, the renewable technologies offer clean energy and an opportunity towards decarbonisation. Moreover, the fact that these technologies are easily scalable, adaptable, and widely distributed helps reaching equally available energy across the globe, even in remote areas (World Energy Council, 2017). Examples at household or small community level include urban or small wind turbines, solar panels, and pico hydro power plants; whereas industrial or country level covers examples such as hydroelectric power, concentrated solar energy, or offshore wind farms. Finally, the weakest aspect of renewable energy due to its intermittency, the energy security, can be addressed by additional consideration of well interconnected energy markets and storage systems (World Energy Council, 2017). All of these factors determine renewable energy sources as strong contributors towards the solution for a more sustainable future.

Nearing 2020, a major worldwide milestone for tackling climate change, it is undeniable that the main trend in the energy sector is indeed the shift towards green and renewable energy. For example, such energy giant as China, which heavily impacts the world energy statistics, is confidently shifting towards renewables with its New Policies Scenario: already generating 35% of its capacity from renewables in 2016, and aiming to expand to nearly 60% by 2040 (IEA, 2017). In the European Union (EU) the 2020 strategy set the so-called 20-20-20 goals: 20% reduction of the greenhouse gas emissions when compared to the levels in 1990, 20% of consumed energy from renewables and 20% improvement in energy efficiency by 2020. As seen from Figure 1.1, which shows the progress towards meeting the goal of 20% energy from renewable sources, nearly 40% of EU member states had already met their national 2020 targets by year 2017. The EU as a whole was also rapidly nearing its aim with 17.5% in 2017, a major improvement from 8.5% in 2004 (Eurostat, 2017). Sadly even mid-2019 the most updated official European Union renewable energy statistics remain from

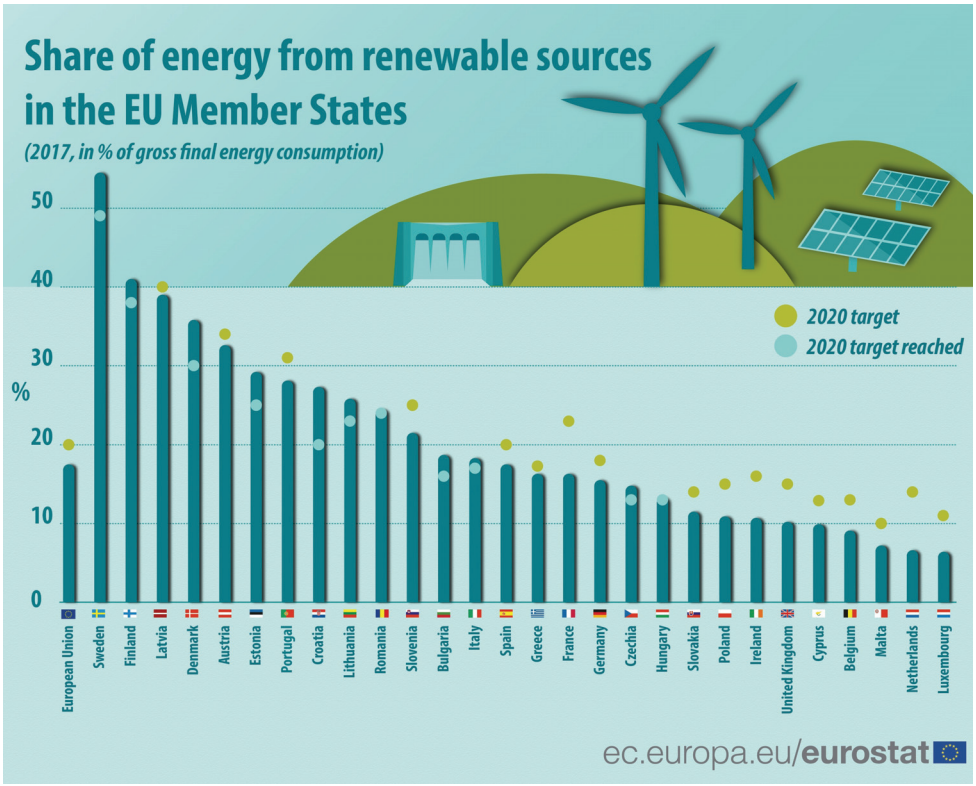

Figure 1.1: Share of energy from renewable sources in the EU member states as of 2017, with regards to their 2020 targets. Source: Eurostat (2017).

year 2017 (Eurostat, 2017), therefore a comment on the situation closer to the 2020 deadline cannot be given at this stage.

More importantly, such trend is continuous with further milestones already set for the upcoming decades. Most universally these include the global Paris agreement, aiming to keep the global average temperature increase well below 2 degrees Celsius compared to the pre-industrial levels, and as of October 2018 specified for below 1.5 degrees Celsius (United Nations, 2019). In the EU the 2020 targets are already extended to year 2030, with targets of at least 40% cuts in greenhouse gas emissions, at least 27% share for renewable energy, and at least 27% improvement in energy efficiency (European Commission, 2014). A 2050 roadmap for low-carbon economy (European Commission, 2018) is also published with ambitious goals of 80% cut in greenhouse gas emissions (with milestones of 40% by 2030 and 60% by 2040). It is expected that all sectors would contribute, including transport, buildings, industry and agriculture, while the strongest carbon cut is foreseen for the power sector – a reduction to nearly 0% by 2050 (European Commission, 2018). To achieve such goals, naturally, clean and renewable energy is required, and wind is one of the most promising sources.

1.2 Wind as a prevailing energy resource

Wind energy is already accepted as an important contributor to the energy market, both worldwide and in Europe. According to the yearly review by the Global Wind Energy Council (GWEC, 2018b), in most of the developed world wind energy has reached the first tipping point – it is the cheapest new technology to be installed. Moreover, in some parts of the world wind energy has already reached the second tipping point – it is cheaper to install wind energy converters than run existing energy alternatives. To illustrate, out of all newly installed power capacity in year 2016, 11.4% world-wide and 51% in Europe was wind power (GWEC, 2017b).

To follow on the examples given in Section 1.1, in China, one of the key energy consumers, a significant part of the energy strategy is dedicated to wind. By 2016 wind already accounted for 9% of their total energy capacity (while renewables in total for 35%), and this share from wind energy was expected to nearly double by 2040 (18% for wind while total from renewables is foreseen at 60%) (IEA, 2017). In the European Union the contribution from wind is even higher: wind energy accounts for 10.4% of total electricity consumption on an average year (GWEC, 2017b), whereas the total share from renewables was 17.5% by 2017, as seen in Figure 1.1. Nonetheless, single countries have shown that these number can be significantly exceeded. For example, Denmark is a world-leading example in wind energy and repeatedly breaks records of the percentage of annual electricity consumption delivered from wind – rising from 17% in 2005 to astonishing 43.6% in 2017 (Gottlieb and Milepael, 2018).

The main benefits of wind energy are no greenhouse emissions after manufacturing, renewable and free source of energy, and adjustability – it can be implemented in any scale from small urban turbines or a single household to massive offshore wind farms. However, the size of the turbine, and its placement, are significant for its power output, defined in Equation 1.1.

$$P = 0.5 C_p \rho_{air} (\pi D_{rotor}^2 / 4) V_{wind}^3 , \tag{1.1}$$

where C_p is the power coefficient, ρ_{air} – density of air, $\pi D_{rotor}^2/4$ is rotor swept area with D_{rotor} being the diameter of the rotor, and V_{wind} – the wind velocity.

It can be seen that the power generated from a wind turbine is mostly dependent on wind velocity (cubed), and the turbine size (rotor diameter squared). Therefore ideally the wind turbine should be as large as possible, and placed in the highest possible wind speeds. The average wind speed map shown in Figure 1.2 highlights the significant difference between the range of wind speeds over water and over land, as well as pin-points the locations with higher wind speeds, such as mountainous locations, vast flatlands, coastal lines and most offshore locations.

However, the differences are not limited to the undisturbed wind speeds measured on a horizontal plane. Figure 1.3 illustrates the key differences between the onshore and offshore wind environments in more detail. Firstly, the onshore environment is subjected to significant surface roughness due to vegetation and settlements, therefore its atmospheric boundary layer is disrupted. This firstly leads to much higher turbulence than offshore. Secondly, the

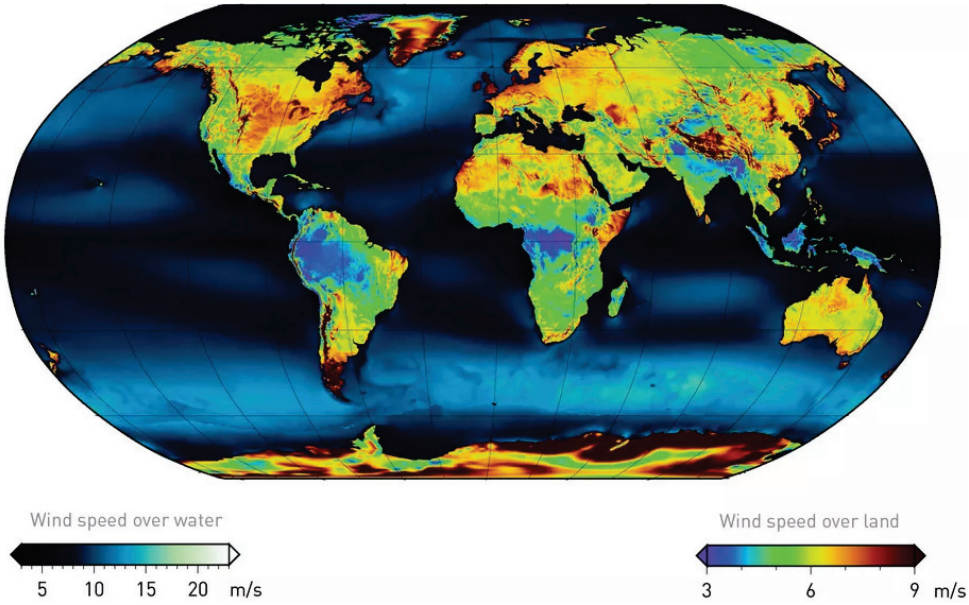

Figure 1.2: Global mean wind speed map for year 2005 at 80 m above sea level. Copyright: 2008 3TIER, Inc.

undisturbed wind velocity v_0 is only reached at inconvenient heights ($z_0 \approx 400\ m$), for which the supporting structure becomes unfeasible. And finally, the mean wind profile $\overline{u}(z)$ near ground is strongly distorted, therefore wind speeds in the range of 70% of undisturbed wind velocity v_0 are reached only in the range of $\approx 100\ m$ above the ground. Higher altitudes for the rotor and nacelle require taller towers, and since wind turbines behave similarly as cantilever structures with bulk mass at the top, this places very large bending forces close to the ground. Taking the most common tubular steel tower as illustration, this results in the need of thicker and wider bottom rings of the tower. This increases the price of manufacturing, as well as causes problems with transportation: road width and weight limitations, and the general difficulty to reach some of the windy onshore locations, such as mountain ranges.

On the contrary, the offshore environment is subjected to a very low surface roughness, leading to lower turbulent fluctuations and less disrupted mean wave profile. Even though the undisturbed wind velocity v_0 is reached at unfeasible heights of $z_0 \approx 250\ m$, the mean wind profile $\overline{u}(z)$ is less deviated from the undisturbed profile. It allows wind speeds in the range 70% of the undisturbed wind speed v_0 to be reached reasonably close to the water surface (see Fig. 1.3), therefore the blade length becomes the limiting factor for the tower height to prevent the blade sweeping the water. Consequently, going offshore allows for much higher growth in size, which, in combination to higher wind speeds than over land, leads to more power per turbine. Another factor allowing larger wind turbines offshore is the remoteness from habitats, which minimises the noise and visual constraints. To summarise, offshore wind energy provides an opportunity for very large scale renewable energy generation, which is needed for the ever-growing energy demand.

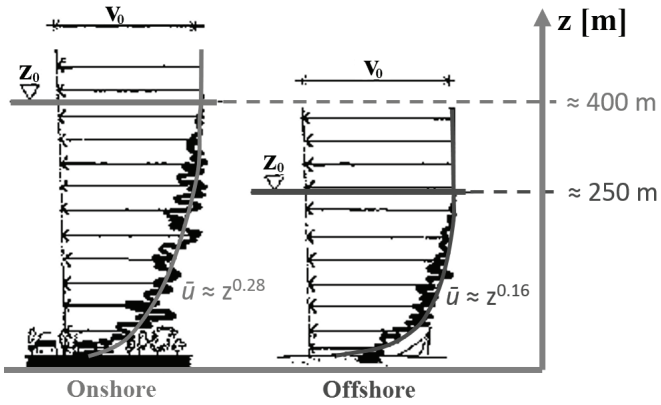

Figure 1.3: Comparison between wind conditions in onshore and offshore environment. v_o stands for the undisturbed wind velocity, z_o is the height above ground at which the undisturbed wind velocity is reached, and $\overline{u}$ is the mean wind speed. Adapted from Plate (1971).

1.3 Offshore wind market and structures

As discussed in Section 1.2, offshore conditions allow for the largest wind turbines. To illustrate the magnitude of the turbines at such scale, the largest installed turbine to the date of the thesis, MHI Vestas V164-8.0 MW is discussed. It has 8 *MW* rated power, therefore with just one rotation at the rated speed it is said to generate enough energy to power an average European household for 29 hours. It's blades are 80 *m* long, which is equivalent of nine double decker London buses, resulting in 21, 124 m^2 swept area, significantly larger than the London Eye (MHI Vestas Offshore Wind, 2017). This turbine has broken the world record of a single wind turbine production in 24-hour period by generating 216 *MWh* in December 2016 (MHI Vestas Offshore Wind, 2017). On top of that, in September 2018 MHI Vestas have launched the first double-digit (10 *MW*) offshore wind turbine in history, available for commercial installation from 2021, and allowing to generate even more power from a single turbine – sufficient to power six thousand German homes (MHI Vestas Offshore Wind, 2018). To put it in comparison, the capacity of the largest current onshore wind turbines falls around 5 *MW* (Wind Power Monthly, 2018; GE Renewable Energy, 2017).

The main reason for lack of investment in offshore wind turbines was the cost of this relatively new technology. Nonetheless, 2016 was the unique year when, after the record breaking investment in offshore wind turbines (OWTs) in 2015, the price of offshore energy fell below the cost of onshore wind (GWEC, 2017a). Instead of the predicted gradual decrease of the offshore energy cost until 2020, already in 2016 the price of MWh fell well below 100 euros (GWEC, 2017a) and the trend was continued in 2017 (GWEC, 2018a). A halt in the decrease of prices was predicted until around 2020 because the governmental subsidies are being retreated, requiring the markets to rearrange (GWEC, 2018a). This, however, is not stopping the developments – continuous growth in offshore wind is predicted out to 2030 as can be seen in Figure 1.4, reinforcing the viability of it.

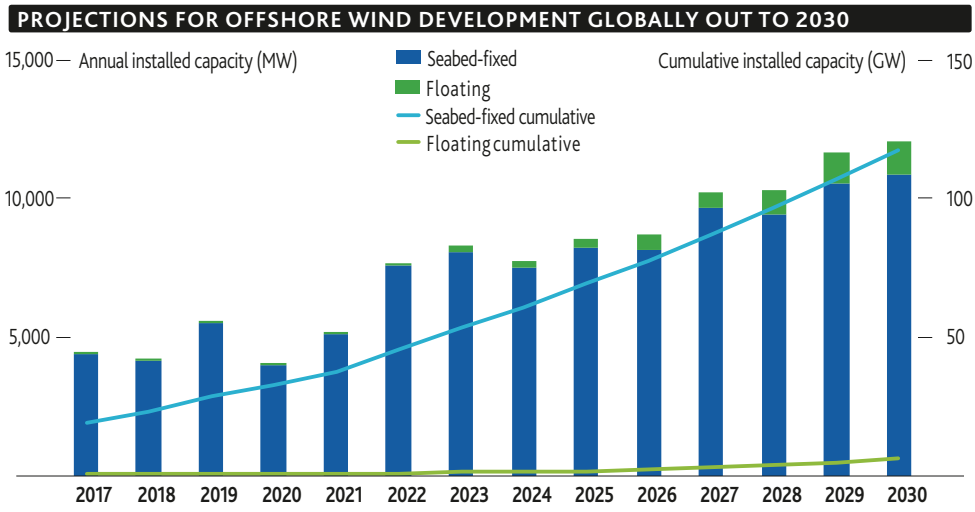

Figure 1.4: Predictions for the offshore wind energy capacity. Source: BVG Associates.

Offshore locations have their challenges, including difficult and costly maintenance, high cost of installation, energy losses during the transmission to the coast, but most of all – harsh and unpredictable environmental loading. Offshore structures are subjected to wind, waves, current, snow, ice and rain, interactions of the aforementioned, as well as constantly changing support from the ground due to bedform migration and scour. All the loading on the turbine is transmitted through the tower to the submerged support structure (substructure). Since it has to withstand all these complex loads, sturdy structure is required, which becomes one of the costliest parts of the offshore wind turbine (Stehly et al., 2017).

As illustrated in Figure 1.5, there are various types of substructures, each fitting better than others depending on the site conditions. First of all, the choice between the two main categories – fixed and floating – is mostly dependent on the water depth. Fixed substructures, especially the monopiles, are cheaper and easier to design, manufacture and install, therefore they are by far more commonly installed than floating (refer back to Figure 1.4). However, they are only viable in shallow to intermediate depths, while in deep water floating structures are required (Jonkman, 2007). Additionally, specific soil conditions need to be taken into account; for example, due to the rocky terrain of the Northern part of the Baltic sea monopile substructures are much harder to install than in sand or silt common in the Northern Sea, therefore gravity base platforms are preferred (4C Offshore, 2018b; 4C Offshore, 2018a).

To conclude, the substructure is a key component ensuring stability of the offshore wind turbine, as well as one of the most expensive parts of it. Therefore more accurate prediction of environmental loads on it would help to design safer, more cost efficient and longer lasting structures, as well as promoting offshore wind turbines and increasing their competitiveness. Therefore Section 1.4 discusses the methods of loading prediction on substructures and the ways to improve it.

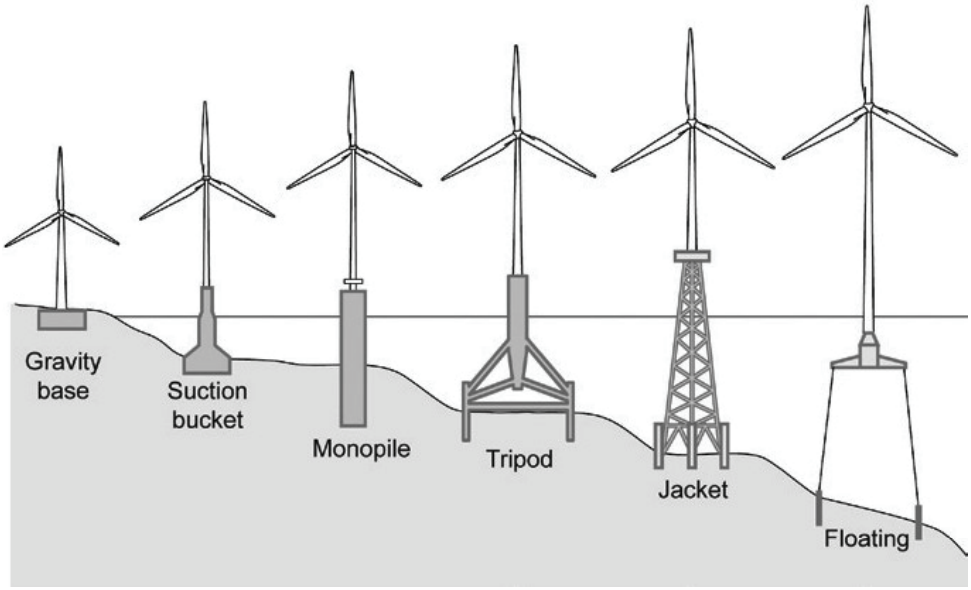

Figure 1.5: Illustration of a selection of offshore wind turbine substructures. Courtesy: World Steel Association.

1.4 Numerical modelling of wave loads and the need to advance it

Three main ways to test the loading on structures are: full scale tests, model experimental tests, and numerical modelling. Bearing in mind the size of these offshore structures, testing in full scale becomes cumbersome and could potentially be afforded only in the final stage of a new design, if at all. Model tests in wave tanks, on the other hand, allow to observe all physical phenomena, even if on a scaled version, but are also too expensive and time-consuming to be carried out on every new design. Therefore validated numerical simulations are the cheapest and fastest tools to design the offshore structures.

Nonetheless, the actual sea and its interaction with offshore structures is very complex, leaving two main options for its numerical representation: a) linearising the problem and omitting the complex nonlinear phenomena, compensating for it by safety factors and over-designing; or b) conducting much lengthier and costlier simulations with more nonlinear methods to try to account for the nonlinear phenomena. It leads to the ongoing struggle to improve the numerical methods in both accuracy and efficiency.

A major catalyst for improving the numerical modelling of offshore wind turbines is the Offshore Code Comparison Collaboration (OC3, Jonkman and Musial, 2010), at the end of its second extension (OC5, (Robertson et al., 2016; Robertson et al., 2017)) at the date of the thesis. These collaborations compare various numerical codes for environmental loading on offshore wind turbines from numerous international participants, paving the way to improved numerical modelling. In the first two projects, OC3 and OC4, the comparison

was conducted just between numerical models (Jonkman and Musial, 2010; Vorpahl, 2011), whilst during OC5 experimental results were added to the comparison (Robertson et al., 2016; Robertson et al., 2017). Moreover, largest discrepancies during OC4 project (Jonkman et al., 2012) were found in the modelling of hydrodynamic loading, therefore in OC5 it became the focus (Robertson et al., 2016).

The main relevant finding of the collaboration to the date of the thesis is that while linear sea and its loading are modelled well enough by most of the currently available solvers in both academia and industry, the more complex and nonlinear cases are not yet thoroughly understood or modelled efficiently (Robertson et al., 2017). These complex nonlinear phenomena include ringing – dangerous very high and nonlinear resonant amplifications of the response triggered by the steepest waves of the sea state, illustrated in Figure 1.6 and discussed in detail in Chapter 2. Since monopiles are the most common support for OWTs and are susceptible to such nonlinear phenomenon, this work focuses on the strongly nonlinear wave loading on fixed-bottom surface-piercing monopiles, with application to offshore wind turbines, and excludes the floating structures and complex geometries found in other substructures.

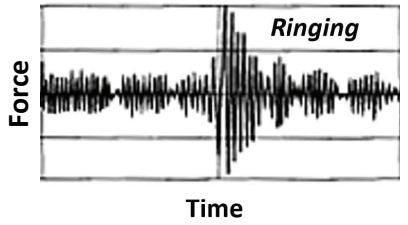

Figure 1.6: Illustration of ringing response over time. Adapted from Norwegian Petroleum Directorate (1992).

Numerical modelling of wave loads requires two phases: simulating the sea itself to attain wave kinematics, and simulating the wave-structure interaction. Wave kinematics are the velocities and accelerations of water particles in the area of interest, where the structure is placed. These wave kinematics, together with structural qualities such as diameter, are then used as input in the hydrodynamic loading models to estimate the resulting forces and moments. Both the wave kinematics and the fluid-structure interaction are nonlinear by nature. However, modelling the full extent of nonlinearity is very complex and time consuming, therefore increasingly nonlinear methods have been derived over the years.

For example, linear wave solvers consider only the first order of wave kinematics and neglect the higher order components, leading to sinusoidal portrayal of wave profile. They are therefore more straightforward to implement and faster to compute leading to their popularity, especially in industry. However, they have been shown to omit nonlinear effects, such as the resonant ringing response (Marino et al., 2013b; Marino et al., 2014b; Schløer et al., 2016). Same has been shown true for the more complex second order wave kinematics (Marino et al., 2014b), which account for the first two orders and neglect the higher order components. Only the fully nonlinear wave kinematics were seen to capture ringing numeri-

cally (Marino et al., 2013b; Marino et al., 2014b; Schløer et al., 2016). However, even though fully nonlinear wave kinematics are now common in academic research, they are not often considered in industry as the simulations are lengthy and costly, therefore become infeasible.

The hydrodynamic loading models, used to account for the fluid-structure interaction, also vary in their complexity. The most common and straightforward of these is the Morison equation (Morison et al., 1950), which in fact was used in the aforementioned studies (Marino et al., 2013b; Marino et al., 2014b; Schløer et al., 2016). Nonetheless, more sophisticated hydrodynamic loading models which may lead to better wave load estimation have been derived in the last three decades.

These two components tend to be treated as separate issues: investigating the importance of nonlinearities in wave kinematics, or the suitability of hydrodynamic loading models separately. This leaves a lack of understanding of the interconnection between various degrees of nonlinearities in both. For example, whether the nonlinearities in hydrodynamic loading models could substitute the nonlinearities in wave kinematics allowing to optimise the numerical wave loading methods without omitting important nonlinear phenomena. For this a better understanding in which wave and structure conditions which type of nonlinearities dominates would be beneficial. Moreover, each wave theory and each hydrodynamic loading model have assumptions they are based on, leading to limitations especially in the more severe cases. Therefore it is of interest to test their performance in the off-design values. This is especially applicable to the hydrodynamic loading models since none of them are by definition designed for the steepest waves.

Thus, the aim of this thesis is to check how wave loading could be modelled more efficiently by using the right combination of wave kinematics and hydrodynamic loading models for the right wave and monopile conditions, especially in the severe seas where ringing would be expected. To accomplish this, the importance of nonlinearities stemming from wave kinematics and from hydrodynamic loading models is investigated in various wave and cylinder conditions, and then applied to a monopile-supported offshore wind turbine.

1.5 Scope and structure of the thesis

This thesis investigates the question of what is the most efficient combination of wave kinematics and hydrodynamic loading model based on the specific wave and monopile conditions, especially in steep waves where monopile-supported offshore wind turbines are prone to ringing phenomenon and the commonly used wave loading models tend to lose validity. To achieve it the following objectives are outlined:

- to summarise the current knowledge on the ringing phenomenon in a comprehensive review (Chapter 2).
- to summarise the different methods of wave load modelling, to discuss the limitations associated with their derivation, to identify any missing links, and to implement them (Chapter 3 for wave kinematics, Chapter 4 for fluid-structure interaction).
- to systematically investigate the performance of different wave loading model combinations, comparing to experimental campaigns (Chapter 5):

  - the influences of the nonlinearities in both wave kinematics and hydrodynamic loading models (Section 5.4);
  - the behaviour in the off-design values (Sections 5.6-5.7);
  - and the best suited loading models for the wave and cylinder conditions (Section 5.8).
- to investigate how the wave loading combinations impact the dynamic structural response (Chapter 6) in increasingly complex modelling of wave and structure:
  - one-degree-of-freedom cylinder in regular waves (Section 6.1) to investigate the performance of the wave loading models with a simplified yet representative structural motion;
  - offshore wind turbine in regular waves (Section 6.2) to investigate the influence of the complex geometry on the response;
  - an offshore wind turbine in irregular waves (Section 6.3) to investigate the coupled influences of a complex multi-degree-of-freedom system, aerodynamic damping, and increasingly nonlinear wave loading models on the dynamic response and its amplifications.
- to summarise the findings and their impact, and to suggest areas for future work (Chapter 7).

Chapter 2

Review of nonlinear wave loading phenomena

This chapter gives an extensive summary of related work on the nonlinear phenomena observed experimentally and numerically on slender structures in very steep waves. Firstly, an overview of the dynamic ringing phenomenon is given, including its history and the known analysis to date. Then the secondary load cycle, observed on fixed structures in the similar to ringing wave conditions, is introduced. Finally, the applicability of the ringing phenomenon to monopile-supported offshore wind turbines is discussed, as well as the effect of the aerodynamic damping on the oscillations.

2.1 Introduction to nonlinear resonant phenomena

The first time when significant amplifications in the response of a large-scale offshore structure were observed was in the 1992 Heidrun platform model tests, where much larger vibrations than those predicted occurred (Norwegian Petroleum Directorate, 1992). The phenomena were named twin effects – 'ringing' and 'springing', and both are illustrated in Figure 2.1.

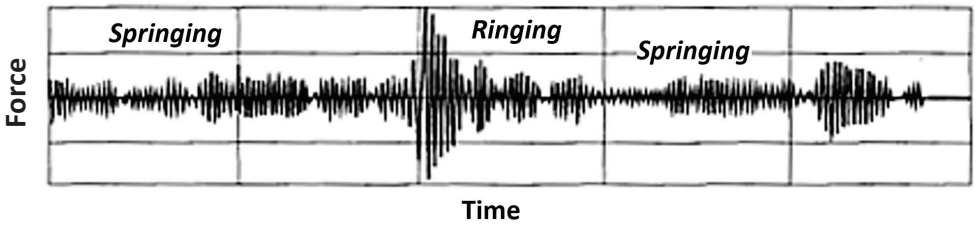

Figure 2.1: Illustration of ringing and springing responses over time (time period of 500 *s* reported in the figure). Adapted from Norwegian Petroleum Directorate (1992).

Both ringing and springing are resonant phenomena causing strong amplifications in the structural response, occurring after a passage of sufficiently steep wave. However, as seen from Figure 2.1, springing is a more continuous strain, while ringing is more sporadic, non-Gaussian, burst-like, building up to the maximum value within the order of one wave period and then slowly dissipating (Norwegian Petroleum Directorate, 1992; Grue et al., 1993; Chaplin et al., 1997; Huseby and Grue, 2000; Grue and Huseby, 2002).

A major difference between the 'twin effects' was that springing, associated with second order loading components (i.e. loading around two times the predominant frequency of waves), had already been successfully numerically modelled at the time of discovery. On the contrary ringing was not captured by any numerical models at that time, therefore associated with higher order components (Norwegian Petroleum Directorate, 1992). After Grue et al. (1993) experimentally confirmed that second order wave theory is not sufficient for ringing, a

scientific consensus seemed to have been reached with most researchers agreeing that ringing is a third-order phenomenon, therefore associated with loading at around three times the frequency of waves (Grue et al., 1994; Chaplin et al., 1997; Huseby and Grue, 2000; Grue and Huseby, 2002).

2.2 Higher harmonics and ringing

Ringing being a third-order phenomenon (Grue et al., 1993) meant that for it to be captured numerically, third order loading has to be modelled. However, the main wave loading combination used at the time was linear wave kinematics with Morison equation (Morison et al., 1950). Morison equation was derived in 1950 and consists of linear inertia and quadratic drag terms, therefore combined with linear wave kinematics can in theory lead to the maximum of second order loading. This triggered developments in third-order hydrodynamic loading models.

Two main paths were taken. On one hand, corrections to third order were suggested to the linear inertia term from Morison equation. Most well-known of these are by Rainey (Rainey, 1989; Rainey, 1995), known as slender-body or Rainey theory. On the other hand, perturbation theories were derived directly to third-order, most well-known of which are 'FNV', named after Faltinsen, Newman and Vinje (Faltinsen et al., 1995) and 'M&M', after Malenica and Molin (1995). The hydrodynamic loading models are discussed extensively in Chapter 4.

More recently it was also argued that ringing may be associated with fourth or even higher order harmonics, not only third. Huseby and Grue (2000) noticed that the measured fourth harmonic force was of comparable magnitude with the third and second order loads, while fifth and higher were notably smaller. Grue and Huseby (2002) experimentally observed resonant responses when the cylinder's natural frequency was equal to four times the frequency of waves, while Rainey (2007) expanded these findings to even higher multiples of wave frequency. Rainey (2007) therefore denounced that ringing is strictly a third order phenomenon and stated that in the cases where ringing is associated with higher frequencies it is a strongly nonlinear phenomenon, therefore the weakly nonlinear third-order perturbation theories (FNV and M&M) may be insufficient to capture it.

Nonetheless, nonlinearities are stemming from wave kinematics as well. In fact, even though Morison equation (Morison et al., 1950) has been shown to omit ringing with linear (Marino et al., 2013a; Marino et al., 2014b; Schløer et al., 2016) and second order (Marino et al., 2014b) wave kinematics, with fully nonlinear wave kinematics ringing is observed (Marino et al., 2013a; Marino et al., 2014b; Schløer et al., 2016). However, as introduced in Section 1.4, fully nonlinear wave kinematics are normally too computationally heavy for industrial use. Therefore it is of interest to see whether second order waves with a more nonlinear hydrodynamic loading model could capture the nonlinear resonant amplifications. It would in turn reduce the need for costly and lengthy fully nonlinear wave simulations and improve the loading predictions in industry.

However, the interconnections between the nonlinearities in wave kinematics and in the hydrodynamic loading models, and the effect of their combined nonlinearity on ringing have not been investigated in depth, therefore this thesis is aiming to bridge this gap. The closest research has been conducted by Swan et al. (2002), who compared Morison equation (Morison et al., 1950) and Rainey corrections (Rainey, 1989; Rainey, 1995) with both linear (Airy, 1845) and fully nonlinear (Rienecker and Fenton, 1981) wave kinematics in very nonlinear wave conditions. They stated that fully nonlinear wave kinematics are much more significant for recreating ringing numerically than hydrodynamic loading models. The transient response was stated as arising from the nonlinearities in wave motion (wave particle acceleration) rather than the hydrodynamic model. Therefore when wave kinematics are fully nonlinear, the additional corrections become less relevant for both maximum potential loads and high-frequency forcing. Nonetheless, the influence of weakly nonlinear (second order) wave kinematics and the third-order perturbation theories on ringing have not been investigated in Swan et al. (2002).

Various loading models with at least fully nonlinear wave kinematics have also been implemented in Paulsen et al. (2014) and Schløer et al. (2016) among others; however, the focus of the studies was not on the distinct influences of the nonlinearities but rather on the investigation of the nonlinear phenomena themselves.

2.3 Secondary load cycle

From the first experiments ringing has been associated with secondary loading cycle (Grue et al., 1993; Chaplin et al., 1997; Grue and Huseby, 2002). Secondary loading cycle (also called "secondary force oscillation", "secondary force cycle", "secondary load cycle", and abbreviated as SLC within this thesis) appears as a second smaller peak in loading, taking place around one quarter of period after the main peak, as illustrated in Figure 2.2 at time $t \approx [0.65 - 0.85]\, s$. However, what this phenomenon is caused or governed by has been a topic of interest in the recent decades.

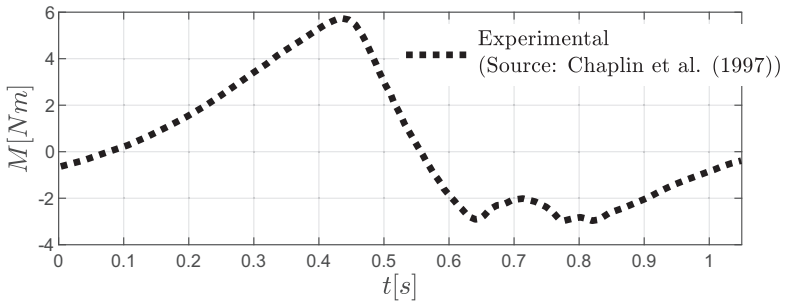

Figure 2.2: Experimentally observed secondary load cycle as base bending moment time series on a fixed cylinder in the study by Chaplin et al. (1997).

Grue et al. (1993) described secondary loading cycle as additional loading due to a suction force caused by free surface effects, taking place below free water surface. They did not ob-

serve flow separation and suggested that this may have induced the secondary loading. They concluded that it was closely related to Froude number ($Fr = \omega\eta_m/\sqrt{2gR}$, where ω is the wave frequency; η_m - maximum wave elevation, g - the acceleration of gravity; R - cylinder radius) – appearing when Fr exceeds 0.35 and becoming pronounced from $Fr = 0.4$.

Stansberg et al. (1995) conducted two sets of physical experiments on rigid cylinders: on a single cylinder and on an array of cylinders, in both regular and irregular waves. Numerical predictions of Morison inertia term with second-order wave kinematics were compared with the measured forces. It revealed the inappropriateness of Morison equation in capturing second-order effects, as well as the strong influence of the third-order components on the measurements.

The experimental study of Stansberg et al. (1995) was extended in Stansberg (1997) with a wider selection of monopile diameters and water depths, where in the steeper waves SLC became more pronounced. It was shown that the sensitivity to increasing wave steepness kA (where k is the wave number, A – wave amplitude) is much stronger for higher harmonics rather than the main loading at the wave frequency. Comparison was conducted with linear wave kinematics and FNV perturbation theory for infinite water depth (Faltinsen et al., 1995) as hydrodynamic loading model. It was found that the first harmonic was captured well while the second and third harmonics tended towards overprediction (Stansberg, 1997). Effect of the nondimensional wave number kR (R being cylinder radius) was also investigated, decreasing the second harmonic and increasing the third harmonic (Stansberg, 1997). Part of this experimental campaign is investigated within the results of this thesis in Chapter 5.

Chaplin et al. (1997) investigated the secondary load cycle and ringing in focussed waves both experimentally and numerically. Their findings were mostly in agreement with Grue et al. (1993), including the secondary load cycle being a suction force. Nonetheless, Chaplin et al. (1997) concluded that wave steepness kA is a more definitive factor on SLC rather than Froude number, since SLC was only found to become prominent from $Fr > 0.6$ rather than $0.35 - 0.4$ in Grue et al. (1993). Morison equation (Morison et al., 1950) and slender-body corrections (Rainey, 1989; Rainey, 1995) with nonlinear 16^{th} order stream function wave kinematics were compared with experimental values. Initial experiments in regular waves could not be used since the incoming regular waves were interfering with the ongoing ringing response, therefore experiments were conducted with focused waves. Best agreement with these experimental values was found with second-order slender body corrections (Rainey, 1989), but only when focused wave kinematics were numerically simulated, rather than equivalent regular wave kinematics since these are less severe. Moreover, the results led to doubts on the suitability of Morison equation (Morison et al., 1950) and Rainey's third-order slender-body term (Rainey, 1995). Finally, all of the investigated numerical loading models omitted the experimentally observed SLC.

Chaplin et al. (1997) placed their and other related experiments (Grue et al., 1993; Stansberg et al., 1995) on the (kA, kR)-plane (refer to the adapted Figure 2.3). To briefly explain the figure, the majority of the experimental conditions being in the Keulegan-Carpenter (KC) number range $\pi - 10$ implies that the tested cylinders are in the inertia-dominated regime instead of drag or diffraction. This is also confirmed by the Stokes first-order diffraction ef-

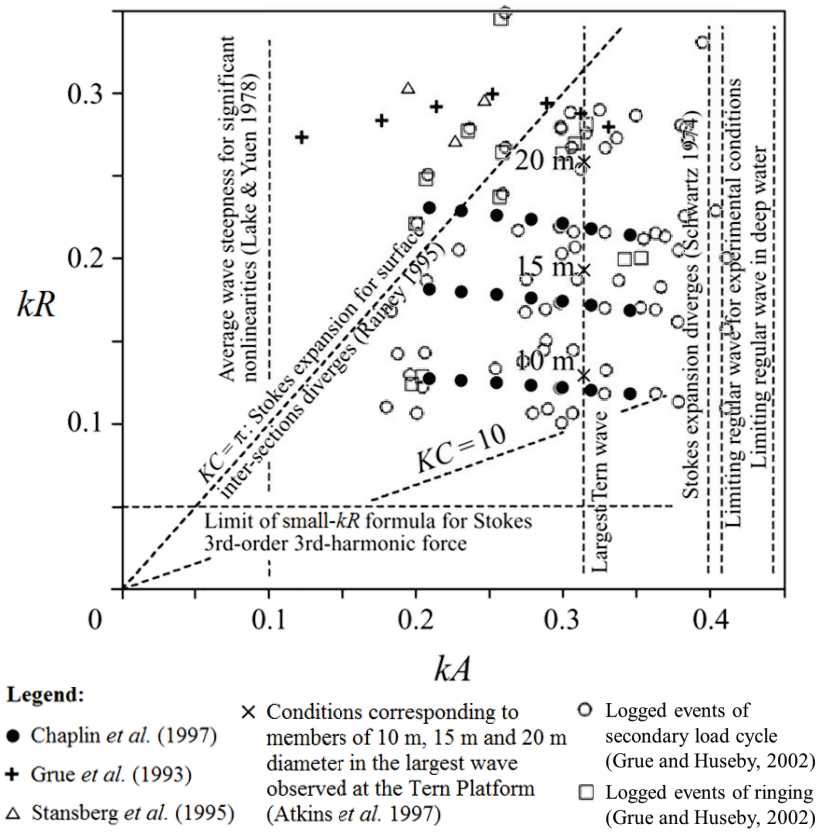

Figure 2.3: Related experiments and wave theory limits on (kA, kR)-graph from Chaplin et al. (1997), combined with the observed SLC and ringing events from Grue and Huseby (2002).

fects starting at $kR \approx 0.5$, and all experimental values falling below such threshold. On the other hand, the threshold of Stokes third-order diffraction effects, determined as $kR = 0.05$ by Malenica and Molin (1995), would be applicable to the region where secondary loading cycle occurs, but is dismissed by the authors due to the local breaking of the free water surface around the cylinder, which cancels the validity of all perturbation schemes and the asymptotic forms derived from them. The data points falling to the right of $kA = 0.1$ denote that substantial phase speed nonlinearities are probable. The significance and relevance of ringing to the full-scale offshore structures is shown by the authors by augmenting the figure with the conditions corresponding to 10 m, 15 m and 20 m diameter cylinders being placed in the North Sea (at the location of Tern Platform) during the highest extreme wave recorded during the 1990-92 (crosses on the vertical dashed line at $kA = 0.314$). The (kA, kR)-graph will remain critical throughout the thesis to discuss wave and cylinder conditions in regular waves.

Later SLC was also described as 'hydraulic jump', or local wave breaking and filling the cavity at the back of the cylinder. This was deducted by both Krokstad and Solaas (2000) and Rainey (2007). The main difference, however, is that from their findings Krokstad and Solaas (2000) denounced the direct link between SLC and ringing based on the time of occurrence of the two phenomena, while Rainey (2007) confirmed the correlation. Other findings worth mentioning are that Krokstad and Solaas (2000) observed increasing amplitudes of the 'hydraulic jump' as both wave steepness and wavelength increase, while their observed ringing oscillations were amplified with the wave steepness increasing but wavelength decreasing.

Meanwhile Huseby and Grue (2000) found that the higher harmonics became larger as the wave amplitude increased to be of the same order as the cylinder radius. Even though the fifth to seventh harmonics remained negligible, second to fourth harmonics became significant, together accounting for as much as 10% of the first harmonic. Moreover, as the steepness kA increased, the analytical predictions by perturbation theories started deviating. The relevance of these findings lies in the association of the higher harmonics with ringing. In addition, wave amplitude being of the order of cylinder radius is a common occurrence for the offshore wind turbine monopiles, as well as is it an underlying assumption for the long-wave perturbation theory FNV (Faltinsen et al., 1995), which is one of the investigated hydrodynamic loading models.

Grue and Huseby (2002) experimentally confirmed the findings of Grue et al. (1993), namely that the past occurrences of ringing and secondary load cycle overlap on the (kA, kR)-graph, and can be expected when Froude number exceeds 0.4. They also observed the dependence of the kA range on the scale of the experiments with the SLC occurring from larger kA values in smaller scale experiments ($kA > 0.3$ for small scale and $kA > 0.2$ for moderate scale). A potential reason for the earlier occurrence of SLC in the moderate scale was suggested as the decreased flow separation in comparison to small scale experiments, which would imply that flow separation has a pejorative effect on the secondary loading cycle. For a broader context, no flow separation was observed by Huseby and Grue (2000), while the importance of flow separation was stressed by Grue (2002), who suggested that SLC may be initiated by the resonance between the structure and the resulting local flow around it.

The main finding of a CFD study by Paulsen et al. (2014) is that the secondary load cycle can be explained by wave diffraction – the passing wave crest creates a vortex at the back of the cylinder and the interaction between the opposing flows (wave continuing to pass in the direction of main wave propagation and the opposing flow within the vortex) create a temporary reduction in pressure at the downstream side of the cylinder, which is observed as SLC. Moreover, a harmonic analysis has shown that not even the first six harmonics recreate SLC. This leads to both deductions: that therefore it cannot be captured by weakly nonlinear hydrodynamic loading models with linear wave kinematics as input; and that SLC cannot be directly related to ringing since ringing is normally associated with third order.

Interestingly, the finding that wave diffraction is causing secondary load cycle (Paulsen et al., 2014) contradicts (or broadens) the assumptions and findings of previous researchers, e.g. Chaplin et al. (1997), Krokstad and Solaas (2000), and Grue and Huseby (2002), who neglected diffraction and observed SLC in the range before diffraction effects were theo-

retically expected. On the other hand, the importance of diffraction justifies the fact that neither Morison equation (Morison et al., 1950) nor its corrections (Rainey, 1989; Rainey, 1995) have captured secondary load cycle in Chaplin et al. (1997), since these hydrodynamic loading models are inertia-based and neglect diffraction. Third-order perturbation theories take diffraction into account (Faltinsen et al., 1995; Malenica and Molin, 1995). FNV theory (Faltinsen et al., 1995) models three-dimensional wave scattering and it has been recently generalised to finite water depth (Kristiansen and Faltinsen, 2017), but this formulation has not yet been tested to recreate SLC.

Suja-Thauvin et al. (2017) have conducted physical experiments on two cylinders in parallel: fixed and moving cylinders subjected to the exact same incoming wave events. The key finding was that not all of the events where SLC was observed on the fixed cylinder ringing was occurring on the moving one, and vice versa – not all wave events which triggered ringing were causing SLC. Thus the findings of Paulsen et al. (2014) and Krokstad and Solaas (2000) were confirmed that the two phenomena are not directly linked.

Two parallel studies were conducted on both the secondary load cycle (Riise et al., 2018a) and ringing phenomenon (Riise et al., 2018b) in deep water. SLC was found to occur from Froude number $Fr \approx 0.3$-0.4 (Riise et al., 2018a) and the extreme dynamic responses from $Fr > 0.4$ (Riise et al., 2018b), therefore local wave effects at the scale of cylinder diameter are expected to matter. The correlation of SLC with Fr reiterates the findings of Grue et al. (1993) and Grue and Huseby (2002). Similarly, since these regions correspond to SLC starting from $KC \approx 4$-5 and dynamic amplifications from $KC > 5$ (Riise et al., 2018b), flow separation can be expected to influence the phenomena. The importance of flow separation agrees with the recent findings of Paulsen et al. (2014) and Kristiansen and Faltinsen (2017).

Liu et al. (2019) added the distinction between breaking and non-breaking cases to the findings of previous investigations. In a CFD study with a sloping wave tank bottom it was found that SLC was pronounced from $Fr > 0.4$ for non-breaking cases, but in the cases where wave was breaking the SLC was prominent already from $Fr = 0.35$, yet of significantly lower magnitude due to the additional slamming force. It was also noted that the duration of the secondary load cycle was never observed to be longer than a quarter of the incoming wave period, and that for cylinders with larger radius, such as the wind turbine monopiles growing in size, SLC was occurring at higher wave steepness.

To summarise, secondary load cycle (SLC) has been found to occur due to wave diffraction and has only been successfully modelled by three-dimensional CFD studies to the date of this thesis. Nonetheless, finite-depth FNV theory (Kristiansen and Faltinsen, 2017) – a perturbation theory which considers diffraction – has been recently developed but not yet tested to recreate SLC. This study was therefore conducted within the framework of this thesis and is described in Section 5.3. Moreover, most recent literature negates the direct link between SLC and ringing, therefore SLC remains of more interest to fundamental rather than applied studies.

2.4 Applicability to monopile-supported OWTs

Ringing has been shown to be a high frequency response resonating with a $3 - 5$ s period when the typical wave period is 15 s, therefore the offshore structures of natural frequency less than 15 s are susceptible to it (Norwegian Petroleum Directorate, 1992; Grue et al., 1994). With a typical natural frequency around 0.28 Hz (Jonkman and Musial, 2010), which is approximately 3.6 s, monopile-supported offshore wind turbines fall in this category.

The first generation monopiles were designed to hold smaller capacity turbines, therefore their typical diameters were in the range of $3 - 4$ m, placing them closer to the drag-dominated regime (Langen et al., 1998). However, with the constantly growing offshore wind turbines (refer back to Section 1.3), the monopiles are growing wider as well, placing them in inertia-dominated regime, where the resonant phenomena are observed (see Section 2.3).

To illustrate this on the (kA, kR)-graph (Figure 2.3), a monopile with a standard diameter of 6 m (Jonkman et al., 2009) is placed in a typical depth for monopile-supported offshore wind turbines of 20 m. Then an example stormy sea with peak period of 15 s and significant wave height of 10 m (which has 39/100,000 joint probability in the northern North Sea (Faltinsen, 1990)) would lead to (kA, kR) values of $(0.22, 0.13)$. Such values place the scenario within the range of past observations of both secondary load cycle and ringing.

Numerically offshore wind turbines have been repeatedly shown to be prone to ringing phenomenon (Marino et al., 2013b; Marino et al., 2014b; Schløer et al., 2016; Marino et al., 2017). It has been shown that the accumulated fatigue from such nonlinear oscillations, omitted with linear wave kinematics, can account to as much as 15% higher extreme loads and 17% higher accumulated fatigue loads (Marino et al., 2017). Experimentally cylinders and monopiles representing a scaled offshore wind turbine monopile have been tested (Suja-Thauvin et al., 2017; Suja-Thauvin et al., 2018; Bachynski et al., 2019), mostly to validate numerical models. Significant nonlinear excitations were observed on such cylinders in steep waves. Nonetheless, there is a general lack of real-life data on monopile-supported offshore wind turbines and their response, therefore the actual impact of ringing on offshore wind turbines has not been assessed yet.

2.5 Effect of aerodynamic damping

A major difference from the structures in the oil and gas field is the fact that offshore wind turbines are dynamic structures. When the turbine is operating, the bottom-fixed structure undergoes oscillations with notable tower top displacements due to operational loads. Nonetheless, the offshore wind turbine may be non-operational on numerous occasions as well: when the wind is below the cut-in speed (around 3 m/s (Jonkman and Musial, 2010)), when the wind is too strong and the turbine is parked to avoid damage (around 25 m/s (Jonkman and Musial, 2010)), or when there is a failure preventing the turbine from operating.

The response of an operating turbine has been seen to significantly differ from a non-operational wind turbine. It has been shown that in the non-operational state a monopile-

supported offshore wind turbine behaves as a static structure and is very sensitive to the dynamic amplifications, such as ringing (Marino et al., 2013a; Marino et al., 2015; Schløer et al., 2016; Marino et al., 2017). However, when the turbine is operating, no pronounced ringing events are seen, presumably because they are damped out by the aerodynamic damping (Marino et al., 2013b; Schløer et al., 2016; Marino et al., 2017).

Nonetheless, since the majority of the offshore wind turbines are equipped with rotating nacelles to face the incoming wind, the aerodynamic damping in the direction of incoming waves might be reduced due to wind-wave misalignment. As pointed out by Marino et al. (2017), the studies stating that operating offshore wind turbines are not as sensitive to resonant responses as parked, tend to simulate co-aligned wind and waves.

However, a fatigue assessment study by Van Der Meulen et al. (2012) has shown that in the case of misaligned wind and waves the fatigue accumulation was the highest, presumably due to the reduced aerodynamic damping in the direction of the waves. The study could not have investigated ringing phenomenon because linear wave kinematics were used (Van Der Meulen et al., 2012); nonetheless, the same principle may apply. Due to wind-wave misalignment in very rough seas the aerodynamic damping in the direction of incoming waves may be reduced enough for the nonlinear amplifications to still be triggered.

Since the co-directional wind and waves cause the largest loading, the misaligned wind and waves in operational case are neither a recommended case by the IEC 61400-3 design standards for offshore wind turbines (International Electrotechnical Commission, 2009), nor have been investigated in depth. Therefore the influence of wind-wave misalignment on the sensitivity to wave nonlinearities is investigated in this thesis, described in Section 6.3.2.

2.6 Summary of the Chapter

This chapter discussed the literature on nonlinear wave loading phenomena and their applicability to monopile-supported offshore wind turbines. Key points are summarised below:

- Ringing:
  - Ringing has been shown to be a dangerous phenomenon which causes large amplifications in the structural response and affects both extreme and fatigue loads.
  - Ringing was found to be associated with 3^{rd} or higher order wave loading components and occurring mostly in inertia region.
  - Numerically ringing has been shown to be captured with fully nonlinear waves and Morison equation, but omitted with linear wave kinematics regardless of the hydrodynamic loading model. Second order wave kinematics have been shown to omit ringing when used as input to Morison equation. Nonetheless, the capability of second order waves has not been investigated in combination with more nonlinear hydrodynamic loading models. Hence such study will be carried out in this thesis.
- Secondary load cycle:
  - Secondary load cycle (SLC) has been observed on fixed cylinders in the same wave conditions where ringing has been observed on a moving cylinder, therefore it was believed to be the cause of ringing.

  - Nonetheless, recently it has been shown that SLC occurs due to wave diffraction and is not directly linked with ringing.
  - To date SLC has only been numerically captured by three-dimensional CFD studies. However, the recently derived finite-depth FNV theory (hydrodynamic loading model which considers diffraction) has not yet been applied for a study on such steep waves where SLC occurs, therefore is tested in this thesis.
  - Finally, the fact that secondary load cycle is not the direct cause of ringing signifies that omitting SLC does not indicate that ringing would be omitted as well with the same combination of wave kinematics and hydrodynamic loading models.
- Applicability to offshore wind turbines:
  - Ringing has been shown to affect the monopile-supported offshore wind turbines, especially since their continuous growth is placing them more directly in the inertia region.
  - Offshore wind turbines in non-operational state have been seen to be extremely sensitive to the resonant amplifications, and significant damage in terms of increased extreme and fatigue loads has been numerically estimated.
  - When the turbine is operating the oscillations are dampened, presumably due to the aerodynamic damping.
  - However, the aerodynamic damping in the direction of incoming waves may be reduced on an operating turbine in the case of wind-wave misalignment, but such scenario has not been investigated in literature, therefore is conducted within this thesis.

Chapter 3

Wave kinematics

This chapter introduces the modelling of wave kinematics used in this thesis. The first part presents the analytical models of increasing nonlinearity which are used for regular waves in this study: Airy, Stokes and Rienecker-Fenton theories. Then the methods for simulating linear and second order irregular waves are presented. Finally, the need for a numerical model is discussed and the implemented Higher-Order Boundary Element Method model is introduced, including the overcome compatibility issue between periodic boundary conditions and corner continuity.

3.1 Regular wave theories

Regular wave theories simulate a wave train consisting of identical waves. Even though they are not representative of the real random sea, they allow an easier analysis of the loading harmonics. They also provide a more contained and predictable study environment, both experimentally and numerically, enabling more direct and meaningful comparisons.

A number of regular wave theories have been derived, increasing in nonlinearity. The simplest linear Airy theory (Airy, 1845) neglects all higher order terms, therefore is the most straightforward to implement. However, it quickly becomes unsuitable when the nonlinearities in waves start to matter. Since the nonlinearities in waves increase both as the wave height increases and as the water depth decreases, the limits of wave theory validity are commonly displayed on the normalised water depth h to wave height H graph. This thesis follows the wave theory limits recommended by the IEC 61400-3 design requirements for offshore wind turbines (International Electrotechnical Commission, 2009), shown in Figure 3.1. As seen from the Figure 3.1, the upper limit for analytical wave theories, regardless of their nonlinearity, is $0.9H_b$ where H_b is the wave breaking limit. It is defined as wave height over water depth ratio $H/h = 0.78$ for shallow to intermediate water and as wave height to wavelength ratio $H/\lambda = 0.14$ for deep water. Above this limit numerical models are necessary.

As illustrated in Figure 3.2a, the additional considerations of nonlinearities change the regular wave profile. When computed with linear Airy theory (Airy, 1845) which neglects all higher order terms, the wave profile corresponding to only the first order is completely sinusoidal (black line). As the increasing order of nonlinearities is taken into account, the crests become increasingly sharp, and the troughs – increasingly shallow. This is evident when comparing the 2^{nd} (blue), 3^{rd} (green) and 5^{th} (cyan) order Stokes theories (Stokes, 1847; Stokes, 1880). The sharper crests lead to more extreme wave kinematics. The fully nonlinear Rienecker-Fenton (Rienecker and Fenton, 1981) wave profile (red line) shows the sharpest peak, which, for such a steep wave (wave steepness $kA \approx 0.30$, where k is the wave number, and A – wave amplitude) would in reality tend towards overturning and breaking. This constraint to symmetry along vertical axis is a limitation of analytical wave theories.

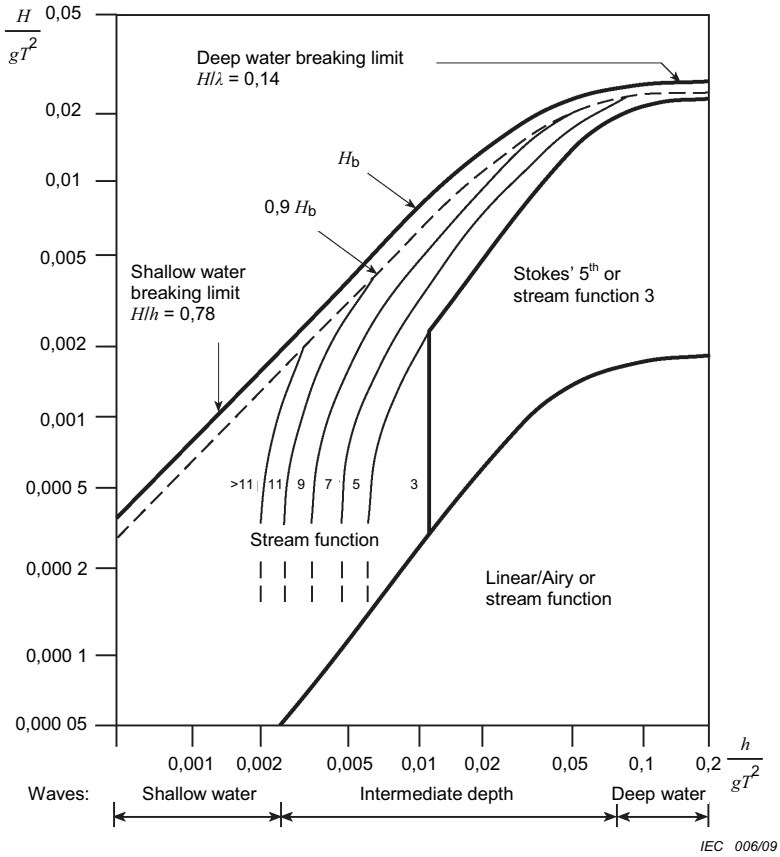

Figure 3.1: Regular wave theory limits as recommended by the IEC 61400-3 design standard for offshore wind turbines (International Electrotechnical Commission, 2009). H stands for wave height, g – gravitational acceleration, T – wave period, λ – wavelength, h – water depth, H_b – wave height corresponding to the wave breaking limit.

Another limitation of the linear (Airy, 1845) and weakly nonlinear (Stokes, 1847; Stokes, 1880) analytic theories is that by definition they are only valid up to the mean water level (i.e. $z = 0$ in Figure 3.2b). For the kinematic values above the mean water level, where the theories do not apply, kinematic stretching needs to be applied. The choice of kinematic stretching is crucial especially in the steepest waves, since the wave elevation is significantly higher than the mean water level and the kinematics are most severe. The commonly used methods are vertical stretching (also known as constant extension or constant stretching), extrapolation, Taylor expansion, or Wheeler stretching. All four methods are illustrated in Figure 3.2b for the horizontal velocity of an extremely steep wave of steepness $kA \approx 0.31$ in water depth $h = 0.6\ m$.

The first three methods (constant extension, extrapolation and Taylor expansion) are identical below $z = 0$, but deal with the values above the mean water surface differently. First of

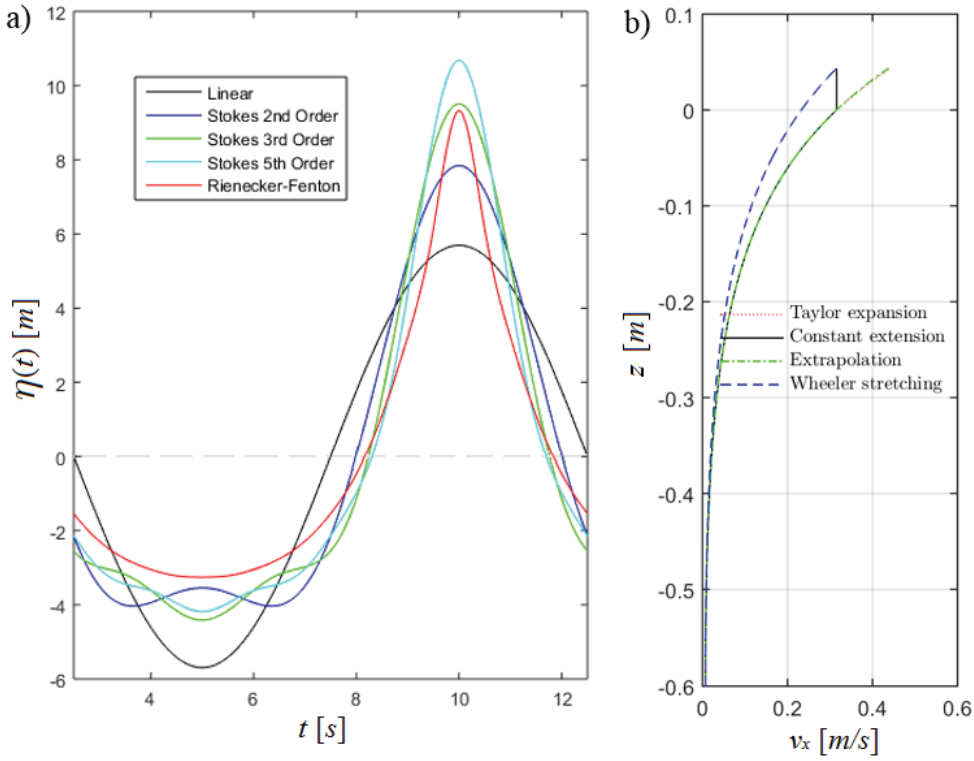

Figure 3.2: a) One period of elevation profiles computed with linear, Stokes 2^{nd}, 3^{rd} and 5^{th} order, and Rienecker-Fenton regular wave theories for an extremely steep wave of steepness $kA \approx 0.30$; b) Horizontal wave velocity profile with constant, Taylor, Wheeler and extrapolation methods for kinematic stretching above the mean sea level, for an extremely steep wave of steepness $kA \approx 0.31$.

all, vertical stretching (black solid line) assigns the value of the kinematic at $z = 0$ for all the values above it, keeping a constant value up to the instantaneous free surface. Extrapolation method (green dash-dot line), on the other hand, extends the kinematic values above mean water level at the same rate as they were increasing below the mean water level, tending towards the largest predictions. Taylor expansion (red dotted line, behind green dashed line) in this thesis follows the formulation implemented by Kristiansen and Faltinsen (2017), formulated in accordance with the Stokes 5^{th} order theory. It is reported in Equation 3.1 and applied for points $0 <= z <= \eta$, where η is the instantaneous free surface. In the studies with regular waves (Chapter 5 and Sections 6.1-6.2) this kinematic stretching was applied in order to allow more appropriate comparison with the loading studies conducted in Kristiansen and Faltinsen (2017). Finally, in contrast to the other kinematic stretching methods, Wheeler stretching (blue dashed line) is applied throughout the depth. It replaces the actual coordinate in vertical direction z with $z' = h(h + z)/(h + \eta) - h$ in the equations for kinematics, leading to a completely different kinematic profile. Wheeler stretching provides

the least conservative kinematics which, together with constant extension, are considered to represent steeper wave kinematics better.

$$f(z) = (f_1 + f_2 + f_3 + f_4 + f_5) + z\frac{\partial(f_1 + f_2 + f_3 + f_4)}{\partial z} + \\ + \frac{z^2}{2}\frac{\partial^2(f_1 + f_2 + f_3)}{\partial z^2} + \frac{z^3}{6}\frac{\partial^3(f_1 + f_2)}{\partial z^3} + \frac{z^4}{24}\frac{\partial^4 f_1}{\partial z^3} \tag{3.1}$$

The following subsections introduce the main regular wave theories in more detail, including the formulations for wave elevation and velocity potential for the theories implemented in the thesis. Nevertheless, for a deeper insight including derivations please refer to the numerous excellent textbooks, e.g. Sarpkaya and Isaacson (1981), Chakrabarti (1987), Dean and Dalrymple (1984), and Kim (2008).

3.1.1 Linear wave theory

Airy theory (Airy, 1845) is the simplest and most commonly implemented wave theory. It is based on linearisation of the boundary conditions neglecting all second and higher order terms, therefore follows a sinusoidal wave of a certain amplitude, period and phase. Its formulation for wave elevation and potential is described in Equations 3.2 and 3.3 consequently and illustrated as the black sinusoidal curve in Figure 3.2a.

$$\eta_{Airy}(x,t) = A\cos(kx - \omega t), \tag{3.2}$$

$$\varphi_{Airy}(x,z,t) = A\frac{\omega}{k}\frac{\cosh(k(z+h))}{\sinh(kh)}sin(kx - \omega t), \tag{3.3}$$

where $A = H/2$ is the linear wave amplitude equal to half the wave height H, k is the wave number $k = 2\pi/\lambda$ with λ being the wavelength, $\omega = 2\pi/T$, where T is the wave period, and h – still water depth. x is the position on the horizontal axis, z – on vertical, and t is the time instance.

Also known as the small amplitude theory it is only appropriate for relatively smooth seas in deep to intermediate water before the nonlinearities become pronounced, as shown in Figure 3.1. From there weakly nonlinear wave theories are normally employed.

3.1.2 Weakly nonlinear wave theories

Weakly nonlinear wave theories are commonly utilised outside the range of the linear wave theory's validity, such as waves with higher amplitudes or in shallower waters. As was seen in Figure 3.2a, the nonlinearities cause the wave crests to sharpen and the troughs to shallow, thus the wave profiles from weakly nonlinear wave theories lose the symmetry along horizontal axis, although the symmetry along vertical axis is maintained.

As seen in wave theory limit graph (Figure 3.1), limitations apply for each weakly nonlinear wave theory depending on its derivation. Three most commonly implemented weakly nonlinear theories are cnoidal wave theory, stream function, and Stokes theory, each briefly introduced in the following subsections. Since the conditions of interest are in the deep to

intermediate water, in the rest of the thesis for weakly nonlinear wave kinematics Stokes theories are chosen. Moreover, as discussed in Section 2.2, the interest of this thesis lies primarily within the first three to five harmonics, therefore Stokes formulations of 2^{nd}, 3^{rd} and 5^{th} order are implemented to better investigate the influence of wave nonlinearities.

3.1.2.1 Cnoidal wave theory

Cnoidal wave theory (Korteweg and de Vries, 1895) is the most common choice for very shallow water depths because it provides a proper description for finite amplitude long waves in shallow waters. It was originally based on the expansion about the term $\varepsilon = H/h$, where H is the wave height and h is the water depth (Fenton, 1979), but later reformulated around the shalowness parameter $\delta = h^2/\lambda^2$, where λ is the wavelength. Its limits in wave steepness are between Airy theory and solitary wave (limiting wave profile with wave period tending to infinity). This theory is not implemented within the thesis therefore equations are not provided.

3.1.2.2 Stream function

The stream function (Dean, 1965), as seen from wave theory limits graph (Figure 3.1), is the most versatile of the weakly nonlinear theories: it is valid both in shallow and intermediate waters (increasing in the needed order of nonlinearity as the water depth decreases), as well as in the deep water for larger wave heights than Stokes 5^{th} order theory. It satisfies the Laplace equation, but is derived from the stream function ψ instead of potential φ as in Stokes theory ($\nabla^2\psi = \nabla^2\varphi = 0$). Moreover, it utilises the simplification of the coordinate system attached to the wave profile rather than the bottom of the domain, thus removing the dependency on time. Weakly nonlinear truncations of the stream function theory are not implemented in the thesis since Stokes theory was deemed more appropriate for the investigated wave conditions. Nonetheless, the fully nonlinear formulation by Rienecker and Fenton (1981) is a key part of the thesis and is discussed in more detail in Section 3.1.3.

3.1.2.3 Stokes theory

Stokes theory (Stokes, 1847; Stokes, 1880) is a perturbation theory, also known as finite amplitude wave theory. It is derived from the potential flow theory therefore subjected to all of its limitations, later discussed in Section 3.3.3.1. Referring to the wave theory limits (Figure 3.1), the different orders of Stokes theory are normally employed in similar water depth range as Airy theory, but for higher wave heights, where higher order effects are apparent.

Expansion takes place around the term $\varepsilon = kA$, where k is the wave number $k = 2\pi/\lambda$, and A – wave amplitude. The two key equations are $\eta = \sum_{n=1}^{\infty} \varepsilon^n \eta_n$ and $\varphi = \sum_{n=1}^{\infty} \varepsilon^n \varphi_n$ for elevation and potential consequently. For implementation they were expanded to Equations 3.4 and 3.5 using the predefined non-dimensional coefficients $A_{(n,m)}$ and $B_{(n,m)}$, given by Skjelbreia and Hendrickson (1961) and reported in Appendix A, Section A.2. The truncation can be to any wanted order, first order leading to Airy theory, and higher orders (normally 2^{nd}, 3^{rd}, 5^{th} or rarely 9^{th}) permitting to describe increasingly steep waves.

$$\eta_{Stokes^N}(x,t) = \frac{1}{k}\sum_{n=1}^{N}\varepsilon^n\sum_{m=1}^{N}B_{(n,m)}\cos(m\Theta), \tag{3.4}$$

$$\varphi_{Stokes^N}(x,z,t) = \frac{c}{k}\sum_{n=1}^{N}\varepsilon^n\sum_{m=1}^{N}A_{(n,m)}\cosh(mk(z+h))\sin(m\Theta), \tag{3.5}$$

where N is the order of truncation ($N = [2,3,5]$ in this study), $A_{(n,m)}$ and $B_{(n,m)}$ are predefined non-dimensional coefficients, c is the nonlinear wave celerity given in Equation 3.6, k is the wave number, and $\Theta = kx - \omega t$, where $\omega = 2\pi/T$ with T being the wave period. h is the still water depth, x is the position on the horizontal axis, z – on vertical, and t is the time instance.

It should be noted, however, that the wave celerity and wave height become nonlinear as well. Firstly, the nonlinear celerity c is given by Equation 3.6. Note that for second and third orders the celerity is corrected to include the square term (middle term in the brackets) while the fourth order term is only applied for the fifth order formulation.

$$c^2 = c_0^2(1+\varepsilon^2 C_1 + \varepsilon^4 C_2), \tag{3.6}$$

where $c_0^2 = (g/k)\tanh kh$ is the celerity from the linear wave theory with g standing for the gravitational constant, k – wave number and h – water depth. C_1 and C_2 are non-dimensional coefficients, which can be found in Appendix, Section A.2.

The wave height becomes nonlinear as well, as described by Equation 3.7. Bearing in mind that $\varepsilon = kA$, note that for the second order wave height stays equal to $H = 2A$ since only the first term in the square brackets stays after the truncation. For third order wave height the third order correction term (middle term in the square brackets) is added, and for the fifth order the full formulation is used. The nonlinear wave height is therefore higher than linear and it is evident in the wave profiles, as shown earlier in Figure 3.2a.

$$H = \frac{2}{k}[\varepsilon + B_{33}\varepsilon^3 + (B_{35}+B_{55})\varepsilon^5], \tag{3.7}$$

where B_{33}, B_{35} and B_{55} are same non-dimensional coefficients used in Equation 3.4, listed in Appendix .

3.1.3 Fully nonlinear wave theory

Fully nonlinear wave kinematics are modelled with Rienecker-Fenton wave theory (Rienecker and Fenton, 1981). The theory is based on perturbation of stream function $\nabla^2\psi = 0$ with no approximation except for the truncation of Fourier series. Therefore it is valid for any water depth and any wave steepness.

The main three boundary conditions describing the theory are: i) no flow at the bottom boundary ($\psi(x,-h) = 0$); ii) constant total volume flow rate within a steady wave ($\psi(x,\eta(x)) = -Q$); and iii) Bernoulli's equation for the constant pressure on the free surface $\left(\frac{1}{2}\left[\left(\frac{\partial\psi}{\partial x}\right)^2 + \left(\frac{\partial\psi}{\partial y}\right)^2\right] + \eta = R\right)$, where Q is a positive constant for the total volume flow rate, and R is a constant, both unknown.

Skipping the derivation which can be found in the original paper (Rienecker and Fenton, 1981), the system of equations becomes as described in Equations 3.8-3.9. Note should be taken that all variables have to be non-dimensionalised with mean water level h and gravitational constant g.

$$B_0\eta + \sum_{j=1}^{N} B_j \frac{\sinh(jkz)}{\cosh jkD} \cos jkx = -Q, \tag{3.8}$$

$$\frac{1}{2}\left[B_0 + k\sum_{j=1}^{N} jB_j \frac{\cosh(jk\eta)}{\cosh jkD}\cos jkx\right]^2 + \frac{1}{2}\left[k\sum_{j=1}^{N} jB_j \frac{\sinh(jk\eta)}{\cosh jkD}\sin jkx\right]^2 + \eta = R, \tag{3.9}$$

for all x, where x is the horizontal coordinate. B_0 to B_N are constants for particular wave, k is the wave number as usual, η is the free surface elevation, which, together with constants Q and R, are all unknown. Finally, D is an arbitrary reference level taken as $D = h/h = 1$ because of normalisation.

With the normalised wave height H and the normalised wave period T specified, the system of nonlinear equations closes to solve for η, B coefficients, c, k, Q and R. Newton's method to solve this system of equations is suggested in the original paper (Rienecker and Fenton, 1981). Iterations are required, therefore this theory is not strictly analytical; nonetheless, the convergence was fast already in the time of the original paper (1981), and even more so with current computational facilities.

Even though this theory is the most nonlinear, it still follows the wave symmetry around its crest (see red line in Figure 3.2a). Full nonlinearity of the wave profile would allow for the asymmetry along both axes with sharper, nearly-vertical forward-facing crests and much shallower troughs, which lead to more extreme wave kinematics. However, for this a numerical method is required. In this thesis Boundary Element Method (BEM) model is used, introduced in Section 3.3, with formulation for period regular waves in Section 3.3.4.

3.2 Irregular wave theories

Irregular waves in this study are modelled in three different levels of nonlinearity: linear, second order and fully nonlinear. The overview of the methodology for simulating the irregular waves is shown in Figure 3.3.

The irregular wave generation starts with the description of the random sea: predefined peak wave period T_p, significant wave height H_s and water depth h, from which the wave spectrum $S(\omega)$ is formulated. Two most commonly used spectra are JONSWAP and Pierson-Moskowitz, explained in detail in numerous textbooks, e.g. Sarpkaya and Isaacson (1981), Chakrabarti (1987), and Faltinsen (1990). JONSWAP spectrum is derived from the sea states in the North Sea, where monopile-supported offshore wind turbines are commonly placed, therefore is used in this thesis.

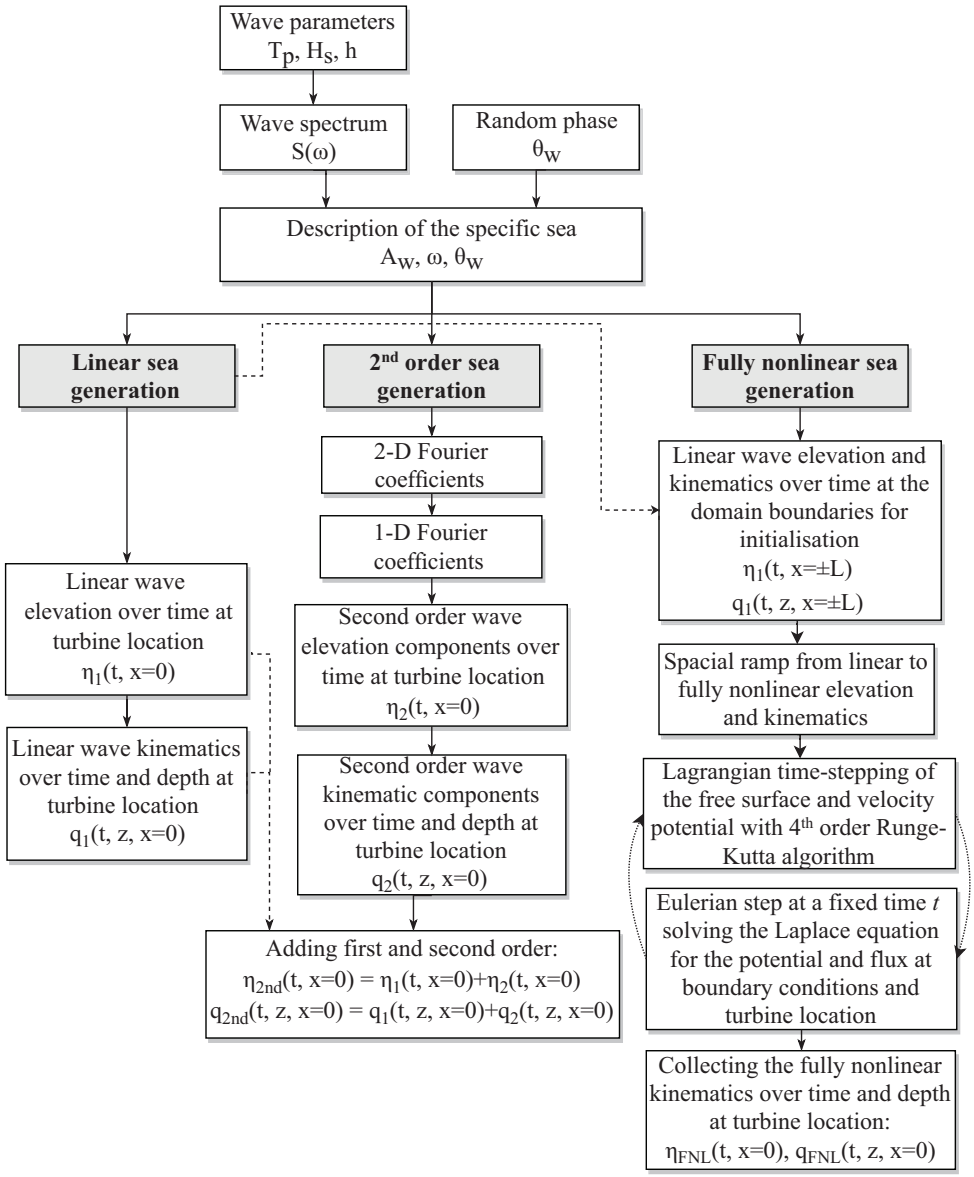

Figure 3.3: Flowchart of the methodology for linear, 2^{nd} order and fully nonlinear irregular waves, where T_p is the peak wave period, H_s - significant wave height, h - water depth, $S(\omega)$ - wave spectra as a function of angular wave frequency ω, θ_w - random wave phase, A_w - wave amplitude, η and q - wave elevation and kinematic values of the order of the subscript, L - length of the domain from location of the turbine at $x = 0$.

A number of different time series of sea surface may be modelled from the same spectrum, the difference in time domain coming from a randomly generated phase θ_w. In order to allow a direct comparison of the influence of nonlinearities in wave kinematics, the same specific sea is applied for all three irregular wave solvers by assigning identical wave amplitude A_w, angular wave frequency ω and random phase θ_w.

The generation of wave elevation and the wave kinematics differs depending on the method. Linear and second order random wave solvers are discussed in Sections 3.2.1-3.2.2, while the computation of fully nonlinear irregular waves is discussed in Section 3.3.5 after introducing the numerical solver throughout Section 3.3.

3.2.1 Linear random wave solver

Linear irregular waves are modelled as simple superimposition of regular linear waves. The Airy theory (see Section 3.1.1) is simply summed for every time instant t with all amplitude A, angular frequency ω and phase θ values. The main equations, for the free surface profile and velocity potential, are listed in Equations 3.10-3.11 correspondingly. Nonetheless, the linear irregular sea is extensively explained in numerous textbooks, e.g. Sarpkaya and Isaacson (1981), Chakrabarti (1987), and Faltinsen (1990), to which the reader is referred to for more details.

$$\eta_1(x,t) = \sum_{n=1}^{N} A_n \cos(k_n x - \omega_n t + \theta_n), \tag{3.10}$$

$$\varphi_1(x,z,t) = \sum_{n=1}^{N} A_n \frac{\omega_n}{k_n} \frac{\cosh(k_n(z+h))}{\sinh(k_n h)} sin(k_n x - \omega_n t + \theta_n), \tag{3.11}$$

where A_n is the wave amplitude, k_n – wave number, ω_n – angular wave frequency, and θ_n – phase selected at random, to be summed for the superimposition. h is the water depth at still water, x – the position on the horizontal axis, z – on vertical, and t is the time instance.

The largest limitation of the linear irregular sea is the same as the linear regular waves, discussed in Section 3.1.1 – the applicability to relatively low steepness and deeper waters only. Moreover, as pointed out in the literature review (Section 1.4), linear wave kinematics lead to the omission of the highly nonlinear phenomena. Its limitations and performance in the off-design values are assessed in Section 6.3, where it is compared with more nonlinear wave kinematics solvers, introduced in Sections 3.2.2 and 3.3.5.

3.2.2 Second order random wave solver

Second order irregular sea is the natural next step from linear. Sharma and Dean (1981) is the first and most widely implemented formulation of second order irregular waves for finite water depth. It is a perturbation-based method to solve the Laplace equation with velocity potential φ. The wave elevation, velocity potential and wave kinematics are modelled by adding a second order term to the first order term from linear irregular waves, described in Section 3.2.1, Equations 3.10-3.11. The second order term is calculated as the summation of sum-frequency interactions and difference-frequency interactions, as shown

in Equations 3.12 and 3.13 for wave elevation and potential. The time vector is defined by $t_p = p\Delta t$, where $\Delta t = T_{sim}/(N-1)$ is the time step, T_{sim} – total simulation time, N – number of samples, and $p = 0, 1, 2, ..., N-1$.

$$\eta_2(x,t) = \sum_{m=1}^{N}\sum_{n=1}^{N}\left[A_m A_n\{B_{mn}^{-}\cos(\psi_m - \psi_n) + B_{mn}^{+}\cos(\psi_m + \psi_n)\}\right], \tag{3.12}$$

$$\varphi_2(x,z,t) = \frac{1}{4}\sum_{m=1}^{N}\sum_{n=1}^{N}\left[b_m b_n \frac{\cosh(k_{mn}^{\pm}(h+z))}{\cosh(k_{mn}^{\pm}h)}\frac{D_{mn}^{\pm}}{(\omega_m \pm \omega_n)}\sin(\psi_m \pm \psi_n)\right], \tag{3.13}$$

where $m, n = 1, 2, ..., N$ and A_m is the wave amplitude. For brevity $b_m = A_m g/\omega_m$, $k_{mn}^{\pm} = |k_m \pm k_n|$, and $\psi_m = k_m x - \omega_m t + \theta_m$. $B_{mn}^{\pm}$ and $D_{mn}^{\pm}$ are transfer functions derived by Sharma and Dean (1981) and reported in Appendix A, Section A.3.

This double summation $\left(\sum_{m=1}^{N}\sum_{n=1}^{N}\right)$ can become very time consuming for longer simulations. The efficiency can be signifantly enhanced if double summation can be avoided, and this can be achieved by re-writing the Fourier coefficients from 2D to 1D, and solving in frequency domain. Such solution is described in Agarwal and Manuel (2011), which this thesis follows and to which the reader is referred to for full details.

This second order irregular wave formulation is said to be valid to wave steepness $s = H_s/\lambda_z = 0.08$, where H_s is significant wave height and λ_z is the wavelength derived from the mean zero-crossing period with linear dispersion relation (Hu and Zhao, 1993; Agarwal and Manuel, 2011). Nonetheless, in this thesis it is applied for waves with much higher steepness in order to assess its limits and behaviour in the off-design values when compared with the fully nonlinear irregular wave solver, introduced in Section 3.3.5.

3.3 BEM code for fully nonlinear wave kinematics

As mentioned in Section 3.1.3, the most severe wave kinematics are associated with breaking or nearly breaking waves, when the wave profile becomes nearly vertical before it starts overturning. The wave kinematics especially intensify close to the free surface where the nonlinearities gather (Marino, 2010). Not accounting for the increased velocities and accelerations could lead to underprediction of wave loading, in particular the base bending moment as the high crest of the steep wave leads to very high bending arm.

Numerical wave modelling can allow for full development of wave profile, leading to more accurate wave kinematics. Moreover, as seen in Section 3.2, irregular wave theories are limited to linear and second order accuracy, which have been discussed to omit nonlinear resonant phenomena (see Section 1.4). Therefore a fully nonlinear computational model is needed for comprehensive discussion of the suitability of wave loading models. In this thesis a two-dimensional potential flow-based Higher-Order Boundary Element Method (HOBEM, or BEM) model for fully nonlinear wave kinematics is implemented.

The BEM model implements a Mixed Eulerian Lagrangian approach. Firstly, the steady state solution at every time step is solved in the Eulerian step, described in Section 3.3.1.

Then the steady state solution is stepped in time in the Lagrangian step, described in Section 3.3.2. The main limitations, associated with the potential flow description of waves, two-dimensional implementation, and modelling of extremely steep waves, are discussed in Section 3.3.3. Finally, the implementation of regular periodic waves is discussed in Section 3.3.4, while the adaptation to irregular waves is discussed in Section 3.3.5.

3.3.1 Fundamental BEM principles

The Boundary Element Method (BEM) model is based on the potential flow description of waves. The BEM model for gravity water waves solves the Laplace equation $\nabla^2\varphi = 0$ within a rectangular domain Ω, bounded by boundary Γ, consisting of Γ_b – impermeable bottom boundary, Γ_i – time-dependent inlet vertical wall, Γ_o – time-dependent outlet vertical wall, and Γ_f – a moving free surface, as illustrated in Figure 3.4.

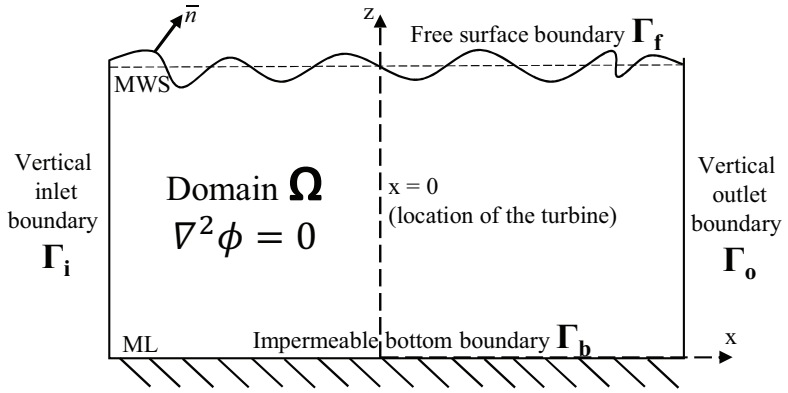

Figure 3.4: Domain of the BEM solver for fully nonlinear waves and the associated coordinate system. MWS stands for mean water surface, ML - mudline.

The greatest advantage of the Boundary Element Method model is that the Laplace equation is solved not within the whole domain, but only on the boundary. It saves computational time and allows to concentrate on the free surface, which is the key unknown in the system. Nonetheless, additional nodes may be placed within the domain as well, but only at the points of interest. In this thesis internal points are placed along the vertical axis at $x = 0$ representing the location of the turbine monopile (refer to Figure 3.4).

The methodology implemented in this thesis for the steady BEM solution within the domain closely follows the routines provided by Brebbia and Dominguez (1998), where the reader is referred to for full details.

First of all, the domain boundary is discretised into elements, which contain nodes, in order to write Boundary Integral Equations for the φ (velocity potential) and q (flux, normal velocity, derivative of φ in the normal to the surface ($q = v_n = \nabla\varphi \cdot \bar{n}$)). The choice of BEM elements is illustrated in Figure 3.5.

Constant elements (Fig. 3.5a) only contain one node in each element, therefore allow for a single constant value of potential or flux across the element. Linear elements (Fig. 3.5b)

have nodes on each end of the element, therefore allow for linear distribution of the potential or flux values from the node on one end of the element to the other. Nonetheless, the closest fit to the nonlinear geometry, such as the nonlinear free water surface, is provided by quadratic elements which contain three nodes (Fig. 3.5c). The higher order elements come at a cost of a longer simulation time because every node introduces an additional equation to be solved. Nonetheless, quadratic elements are more precise in nonlinear problems than linear or constant elements (Brebbia and Dominguez, 1998), therefore are implemented in the BEM model used in this thesis.

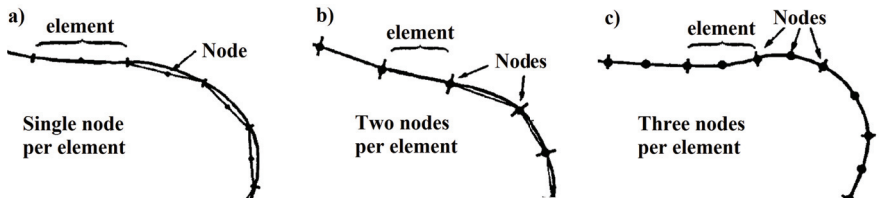

Figure 3.5: Illustration of BEM elements: a) constant, b) linear, c) quadratic. Adapted from Brebbia and Dominguez (1998).

After the discretisation into elements and nodes, the system of Boundary Integral Equations can be formed. Firstly, the known values of either velocity potential φ or flux q are assigned to each node. The impermeable bottom is always assigned a Neumann condition of flux $q = 0$. For the vertical inlet and outlet boundaries the assigned condition depends on which type of sea is modelled. For regular waves periodic conditions are assigned, discussed in Section 3.3.4. For irregular waves Neumann boundary is assigned (q is given at every time step), as described in detail in Section 3.3.5.

Finally, the most complex boundary is the free surface, which is in itself unknown. Nonetheless, it is modelled with the Dirichlet condition, where the potential φ is assigned and the flux q is computed. The unknown potential φ at the first time step ($t = 0\,s$) is assigned from an analytical wave theory. The initial free surface conditions are described separately for regular and irregular waves in Sections 3.3.4-3.3.5. In the subsequent time steps ($t \neq 0$) the potential φ is derived from the time-stepping procedure, described in Section 3.3.2, allowing fully nonlinear development of free surface.

To solve the Boundary Integral Equations for the unknown values, influence matrices are also needed. Influence matrices represent the interconnection between the nodes based on their coordinates, separately for the potential φ and for flux q (H and G matrices correspondingly). To calculate the influences between the nodes, a fundamental solution is applied the first node, denoted as node i (see Figure 3.6). While the fundamental solution is applied on node i, every element is taken out in turn, such as the element on outlet boundary Γ_o in Figure 3.6. From the coordinates of every node on the selected element, such as node j, the influence factors H_{ij} and G_{ij} for potential φ and flux q consequently are computed. Different algorithms are applied if the node j is within the same element as the node i where the fundamental solution was applied in order to avoid singularity, but all details are provided

in Brebbia and Dominguez (1998). Therefore by the end of this process for each node j an Equation 3.14 is written:

$$H_{ij}\varphi_j = G_{ij}q_j \tag{3.14}$$

Each element being selected separately for node j results in the end nodes of each element accounted for twice. Therefore the H_{ij} and G_{ij} matrices are initially not square, but rather of the size of number of nodes (where node i was applied) by three times the number of elements (where node j was applied). In the example illustrated in Figure 3.6 this would lead to matrices of size 24x36. The influence factors for the same nodes then need to be collated, leading to a square matrix (of size 24x24 in the example). The algorithms are provided in Brebbia and Dominguez (1998), or Marino (2010), namely Appendix B.

It should also be noted that corners of the rectangular domain in combination with quadratic elements cause an additional issue. In each corner there is a single equation 3.14, single potential φ value, but two values for flux q due to two directions for normal vectors (illustrated in top left corner of Figure 3.6). A number of solutions are available for this problem, but in this thesis the double node technique was implemented. It places two identical nodes in the corners for each flux value, and replaces the duplicate Equations 3.14 with the potential continuity in corners (potentials of both nodes in the same corner have to be equal). This therefore increases the number of nodes by four additional corner nodes, and the example influence matrices become of size 28x28. For more details refer to Section B.1 in Appendix B, or to Grilli et al. (1989) where the double node technique was introduced.

The equation system is later solved by redistributing the known values (i.e. imposed by the Neumann or Dirichlet boundary conditions) and unknown values to different sides of the equation: collecting all unknown φ and q values to vector X, the calculated influence

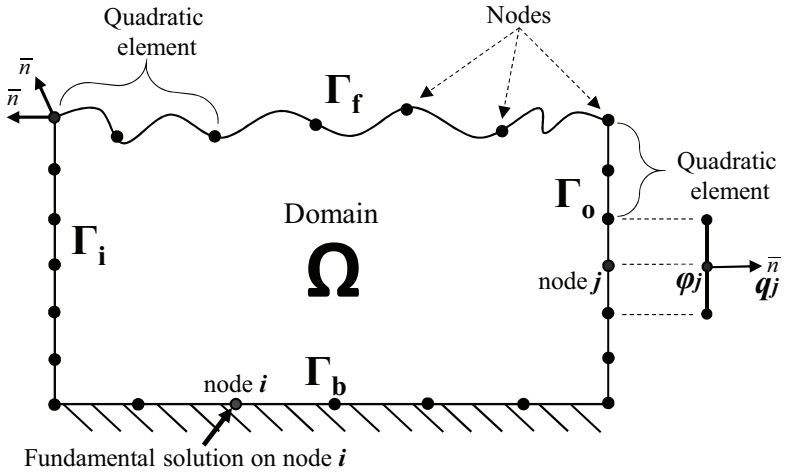

Figure 3.6: Illustration of the boundary element method on a rectangular domain with 3 quadratic elements per side (12 elements, 24 nodes).

coefficients H and G which corresponding to unknown values to matrix A, and all the known values φ and q (already multiplied by their corresponding influence coefficients H and G) to vector F. Then Equation 3.15 is solved to find the values for vector X. The calculated values from vector X can then be assigned back to the nodes – potential φ where Neumann boundary was imposed, and flux q where Dirichlet boundary was assigned.

$$X = A^{-1}F \tag{3.15}$$

Final step within the steady solution is to compute the wave kinematics on the vertical axis which represents the monopile (taken at $x = 0$ in this thesis). The horizontal and vertical velocities at the intersection of the instantaneous free surface with the monopile are taken directly from the core solution of the free surface boundary Γ_f, while the rest of the nodes down the z-axis are computed as internal nodes. Care should be taken to place the internal nodes with enough distance from both the free surface and the bottom boundaries to avoid singularity, but not too far as well, to avoid approximations of the solutions between the internal nodes and the boundary solutions. Appropriate distance has been found to be in the order of the distance between the nodes on the free surface boundary. The internal nodes are solved similarly to the boundary nodes, with the use of H and G matrices, using the boundary solution of the same time step. Full details for the algorithms may be found in Brebbia and Dominguez (1998).

This completes the steady Eulerian step of the solution, for a given time step t. Stepping in time is then conducted in the Lagrangian step, described in Section 3.3.2.

3.3.2 Time stepping

The Eulerian solution, calculated at every time step as discussed in Section 3.3.1, is then stepped in time with 4^{th} order Runge-Kutta time-stepping algorithm in the Lagrangian phase. Lagrangian time-stepping allows for the complete non-symmetry of the wave profile because the nodes on free surface are permitted to move both vertically and horizontally. This way the strong nonlinearities such as breaking waves may be modelled.

The variables that need to be stepped in time are the wave elevation, to get the updated location of the free surface nodes at the next time step ($t + dt$), and the potential φ at the updated nodes in order to be assigned as the known values at the next Eulerian step, described in Section 3.3.1. Stepping the wave elevation in time in Lagrangian manner requires to step each node both horizontally and vertically. For this the first order Lagrangian derivatives of the position vector (x_f, z_f) are computed in both directions, as given in Equations 3.16-3.17. This gives the horizontal and vertical velocities, v_f^x and v_f^z correspondingly, of each node on the free surface.

$$\frac{Dx_f}{Dt} = v_f^x = v_f^n n^x + v_f^t t^x, \tag{3.16}$$

$$\frac{Dz_f}{Dt} = v_f^z = v_f^n n^z + v_f^t t^z, \tag{3.17}$$

where v_f^n is the normal velocity of every node, direct output of the Eulerian step (Section 3.3.1), the v_f^t is the tangential velocity, derived from the differentiated shape functions, while the n^x, n^z, t^x, and t^z are the Cartesian components of the normal and tangential vectors.

Projecting the velocity potential φ in time requires its first order Lagrangian derivative as well, which is derived from the dynamic boundary condition and given in Equation 3.18:

$$\frac{D\varphi}{Dt} = -gz_f + \frac{1}{2}\left((v_f^x)^2 + (v_f^z)^2\right), \tag{3.18}$$

where g is the gravitational constant, and z_f is the vertical coordinate of the free surface. It should be noted that the expressions for the first order Lagrangian derivatives, as well as the mentioned Jacobian shape functions, closely follow Marino (2010), namely Section 4.2 and Appendix B, to which the reader is directed if more detailed information is sought after.

To get a more accurate projection in time, 4^{th} order Runge-Kutta time stepping is used, meaning that each time step dt is divided into four smaller intermediate time steps. Runge-Kutta method itself is well known and the equations are widely available, therefore it is not detailed here. However, it should be noted that the intermediate Runge-Kutta time steps must solve for the updated wave elevation and for the updated velocity potential to be assigned to the updated nodes. The internal nodes, nonetheless, can for efficiency be solved only at the full time steps, since they do not influence the development of the free surface.

3.3.3 Limitations associated with BEM

3.3.3.1 Potential flow description of waves

A major advantage of the BEM solver is that it is suitable for regular and irregular waves as well as numerical wave tanks without limitations on water depth, wavelength or steepness. However, the most fundamental limitations of the BEM model are stemming from the potential flow description of the fluid, namely the assumption of irrotational flow, valid only up to the re-entry of the plunging breaking wave (Newman, 1977).

Plunging wave breaker, modelled in higher-order BEM solver (Marino, 2010), is illustrated in Figure 3.7a, whereas Figure 3.7b shows the crashed simulation due to the re-entry of this plunging breaker. Nonetheless, modelling the wave up to its re-entry is considered sufficient because, as discussed by Marino (2010) and Bredmose et al. (2013), the accelerations from an overturning wave are the largest before it re-enters, leading to the highest impact on the structure before the re-entry anyway.

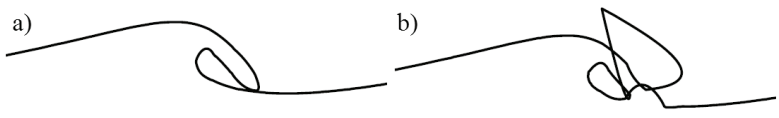

Figure 3.7: Illustration of: a) plunging wave breaker; and b) simulation crash due to re-entry of the plunging wave breaker. Courtesy of Marino (2010).

The impact of breaking or near-breaking wave could be modelled with the available impact models, such as Wienke and Oumeraci (2005), Marino (2010), Marino et al. (2011a), and Marino et al. (2011b); but slamming impact is of different nature from the resonant phenomena investigated in this thesis, therefore is outside of the scope of this study.

In addition, the present model is based on the assumption of inviscid fluid. It results in no drag contribution from the wave kinematics, leading to reduced loading. Although it should be mentioned that the contribution of drag on the loading may be included via the fluid-structure interaction; for example, Morison equation (Morison et al., 1950) provides the quadratic drag term, as discussed in Section 4.1.1. This limitation would be especially applicable in the wave and cylinder conditions where drag contribution is significant. On the (kA, kR)-graph (Figure 2.3) this corresponds to large wave steepness and extremely slender cylinders resulting in Keulegan-Carpenter number $KC > 10$, where $KC = uD_{cyl}/T$ (with u being the horizontal velocity, D_{cyl} – cylinder diameter, and T – wave period).

Nonetheless, as discussed in Section 2.4, monopiles for offshore wind applications are growing in diameter, leading to inertia or even diffraction dominated regimes. Moreover, as shown in Figure 2.3, both secondary load cycle and ringing are normally associated with inertia regime rather than drag. Finally, the experimental campaigns to which the numerical loading models are compared to in this thesis are also placed over diffraction and inertia regimes, avoiding drag regime (see Figure 5.1). Therefore contribution from drag in the cases discussed in this thesis can be assumed negligible and this limitation is not considered crucial.

3.3.3.2 A note on two-dimensional assumption

The main advantage of a two-dimensional model is significantly reduced complexity which saves both time and computational resource. It is considered appropriate to reduce the problem to two dimensions since ringing is an amplification of the response occurring on the same plane as the propagation of waves, without significant motion in the perpendicular direction (Chaplin et al., 1997). Moreover, most of the typical wave conditions where OWT monopiles are placed lead to long-crested waves, which further justify the use of two-dimensional solver.

The main limitation of modelling two-dimensional flow is the neglection of any occurring three-dimensional effects. These arise both within the flow itself and due to the presence of the cylinder. While the former is omitted due to the two-dimensional domain for wave kinematics, the presence of the cylinder is accounted for by the hydrodynamic loading models, discussed in Section 4.1.

3.3.3.3 Avoiding numerical instabilities

There are two most well-known numerical instabilities in steep wave modelling, illustrated in Figure 3.8 (Dold, 1992). The first type is the strong instability which occurs due to a too large time step. It appears as sharpened wave surface in a concentrated area, usually localised behind the crest of the wave (Dold, 1992), as illistrated in Fig. 3.8a. It is easy to avoid it by keeping the Courant number ($Co = c\ dt/dz$, where c is wave celerity, dt is the time step,

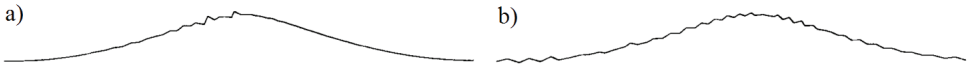

Figure 3.8: Examples of wave profiles affected by a) strong and b) saw-tooth numerical instability. Courtesy of Dold (1992).

and dz is the distance between the nodes on the boundary) below one (Dold, 1992), or even around 0.5 as recommended by Grilli and Svendsen (1990).

The second type is the steep wave, or "saw-tooth", instability (Dold, 1992). It occurs in steep waves and causes the free surface elevation to develop a zig-zag-like instability which resembles saw-tooth and spreads across the wave profile (Fig. 3.8b). Smoothing and regridding techniques are commonly employed to avoid such instability. Regridding is a technique which re-spaces the nodes on the free surface with equal spacing to avoid the nodes overstepping each other in the Lagrangian motion (described in Section 3.3.2). Smoothing, on the other hand, takes a number of points (at least 5) on the free surface, and by the use of a specially adapted filtering, diminishes the zig-zag oscillations. The x- and z-coordinates of free surface, as well as velocity potential values on the free surface, are rearranged. In this thesis the 7-point smoothing technique for non-equally spaced nodes was applied (Dold, 1992). However, care should be taken with applying smoothing and regridding as both these techniques dissipate energy (Dold, 1992; Marino, 2010).

It should be noted that in this thesis wave overturning and resulting re-entry which causes the simulation to crash, previously illustrated in Figure 3.7, could not be allowed. In the studies on breaking wave impact this issue is surpassed by restarting the simulation after the impact since the largest impact is exerted before the re-entry anyway (Marino, 2010; Bredmose et al., 2013). However, in the study on ringing the oscillations after the main impact of the wave are the focus, therefore restarting the simulation was not considered fitting. Therefore additional smoothing was applied to avoid the overturning of the steepest waves at the cost of dissipated energy. The impact of smoothing on the final loading from fully nonlinear waves is assessed in Section 6.3.3.

3.3.4 Implementation of regular waves

Regular waves provide a controlled environment which allows for easier analysis of wave loads and harmonics. A common way to numerically model regular waves is by the use of a numerical wave tank, e.g. Grilli and Subramanya (1996), Guyenne et al. (2000), Wang and Wu (2010), and Marino (2010). However, when a paddle or a piston generates waves at one end of the numerical wave tank, an absorbing beach is required at the other end. If the absorbing beach dampens the solution excessively, the reduction in energy may affect the incoming wave kinematics. Consequently, if the beach is not absorbing enough energy, wave reflection and interference might be expected. Tuning the absorbing beach perfectly is an intricate task, and remains as another potential source of inaccuracy.

Therefore in this thesis a completely periodic domain was implemented. The domain Ω (back in Figure 3.4) became of exactly one wavelength λ length in x-direction with periodic vertical wall conditions. This way it was ensured that the wave which was going out of the

outlet boundary Γ_o was coming in the inlet boundary Γ_i. No values are assigned to neither the wave potential φ nor the normal velocity q on both boundaries, i.e. neither Neumann, nor Dirichlet condition is assigned on the vertical walls. Instead, periodic boundary conditions are imposed: the values for wave potential φ have to be identical on both boundaries, and the values for normal velocity q have to be of the same magnitude but opposite direction (sign).

Imposing such periodic boundary condition together with the corner continuity (due to quadratic boundary elements on a rectangular domain, Section 3.3.1) resulted in an over-imposed system. Such compatibility issue has not been found to be previously studied in literature. Nonetheless, it was successfully overcome within this thesis and is therefore described in great detail in Appendix B as original contribution.

Lastly, as was described in Section 3.3.1, the bottom boundary Γ_b is assigned Neumann condition with normal velocity $q = 0$ (impermeable bottom) at every time step, while the free surface boundary Γ_f has to be initalised. The wave profile η and the values of the potential on free surface φ_f have to be assigned at the very first time step ($t = 0\ s$) before allowing it to freely develop in time as described in Section 3.3.2. For the fully nonlinear regular waves the solver is therefore initialised with the most nonlinear regular wave theory (Rienecker and Fenton, 1981), imposing no limitations in terms of water depth or wave steepness as discussed in Section 3.1.3.

3.3.5 Adaptation to irregular waves

The simulation of fully nonlinear irregular waves is a crucial step in this thesis. Irregular waves in their random nature closely represent the real sea to which the offshore wind turbines are exposed, and fully nonlinear irregular waves are expected to recreate such conditions the closest.

As discussed in Section 3.3.1, in order to solve the boundary equations, some variables have to be imposed on the boundary. The bottom boundary Γ_b is the most straightforward one with Neumann condition of $q = 0$ at every time step. Assigning values for the other boundaries (vertical boundaries Γ_i and Γ_o at every time step and the free surface Γ_f at the first time step) is more complicated, since in irregular waves there is no fully nonlinear irregular wave theory which could be applied as Rienecker-Fenton is used for initialisation in regular waves (Section 3.3.4).

The two main solutions are either modelling a numerical wave tank, e.g. Grilli and Subramanya (1996), Guyenne et al. (2000), Wang and Wu (2010), and Marino (2010), or initialisation with the lower order wave theories described in Section 3.2. For the latter method adjustment schemes are required to allow fully nonlinear development of the waves, such as a ramp from linear to nonlinear sea (Marino et al., 2013a). A very computationally efficient solution was implemented by Marino et al. (2013a), following the work of Dommermuth (2000). In Marino et al. (2013a) a spacial and time ramp was implemented to transit from linear sea to fully nonlinear sea on part of the domain, only at the time instants when a nonlinear event is foreseen. This was said to decrease the simulation time by 88% compared to using fully nonlinear potential flow solver for the whole duration and across the whole domain (Marino et al., 2013a).

In this thesis capturing all nonlinear events was prioritised over computational efficiency, therefore only the spacial ramp was implemented. It is described by Equation 3.19 and allows the transition from linear to fully nonlinear waves at the inlet boundary, and back to linear at the outlet boundary (Marino et al., 2013a). A quadratic damping function (Equation 3.20) in employed in parallel to dampen out the nonlinearities on both boundaries as per Marino et al. (2013a).

$$R_s(x) = \begin{cases} \frac{1}{2}\left[\sin\left(\frac{x-x_1}{l_1}\pi - \frac{\pi}{2}\right) + 1\right] & \text{for } x \in [x_1, x_1 + l_1] \\ 1 & \text{for } x \in (x_1 + l_1, x_2 - l_2)\ , \\ \frac{1}{2}\left[\sin\left(\frac{x_2-x}{l_2}\pi - \frac{\pi}{2}\right) + 1\right] & \text{for } x \in [x_2 - l_2, x_2] \end{cases} \tag{3.19}$$

where x_1 and x_2 are the coordinates on x-axis where the first ramp starts and the second ramp ends, while l_1 and l_2 are the corresponding length of both ramps.

$$v(x) = \begin{cases} \alpha\left(\frac{-x + x_1 + l_1}{l_1}\right)^2 & \text{for } x \in [x_1, x_1 + l_1] \\ 0 & \text{for } x \in (x_1 + l_1, x_2 - l_2)\ , \\ \alpha\left(\frac{x - x_2 + l_2}{l_2}\right)^2 & \text{for } x \in [x_2 - l_2, x_2] \end{cases} \tag{3.20}$$

where α is the damping coefficient, taken as $\alpha = 4$ in this thesis, following Marino et al. (2013a).

This ramp formulation allows for fully nonlinear development of waves in the inner domain between the ramps where the turbine is located. Meanwhile the wave conditions are kept linear at both ends, allowing to assign the fluxes on the vertical walls as horizontal velocities from linear irregular wave theory, discussed in Section 3.2.1. The ramp method has been proven to be accurate and efficient by Marino et al. (2013a) and used in a number of subsequent peer-reviewed studies (Marino et al., 2014a; Marino et al., 2015; Marino et al., 2017). Therefore it is implemented in this thesis with confidence.

It was deemed worthy of mentioning that in the search of the most efficient method to initialise the irregular fully nonlinear waves various other methods have been tested. It was attempted to initialise the fully nonlinear sea with second order wave kinematics – firstly directly without a ramp, and secondly with second order input and an absorbing beach at the outlet. However, it was found that second order waves without a spacial ramp are insufficient to initialise the fully nonlinear solver. Since horizontal velocities at the vertical boundaries Γ_i and Γ_o, as well as the wave elevation and velocity potential at the free surface Γ_f, have to be assigned at every time step, the use of second order wave kinematics increases the computational time significantly when compared to initialisation with linear wave kinematics. Since the spacial ramp was inevitable within the framework of this thesis, and the suitability of linear wave kinematics with ramp was already established, this thesis employs the described method of simulating fully nonlinear irregular waves by initialising with linear wave kinematics and transitioning with nonlinear ramp.

3.4 Summary of the Chapter

This chapter described the methodology used in this thesis to simulate the regular and irregular wave environments of increasing nonlinearity, to which offshore structures are subjected.

- Regular waves:
  - Linear wave kinematics are simulated with the simplest sinusoidal Airy wave theory;
  - Weakly nonlinear wave kinematics are simulated with the 2^{nd}, 3^{rd} and 5^{th} order Stokes perturbation theories;
  - Fully nonlinear wave kinematics are simulated with Rienecker-Fenton theory as well as two-dimensional higher-order Boundary Element Method model, for which:
    * the vertical domain boundaries (inlet and outlet) are assigned periodic conditions,
    * a compatibility issue between corner continuity and periodic vertical walls was overcome and presented as original work,
    * the initial boundary conditions for free surface elevation and velocity potential are assigned from Rienecker-Fenton theory,
    * free surface is allowed to develop in the Mixed Eulerian-Lagrangian scheme to achieve fully nonlinear wave conditions.
- Irregular waves:
  - Linear irregular waves are simulated with the random linear Airy superimposition;
  - Weakly nonlinear irregular waves are simulated with the second order Sharma-Dean wave solver in frequency domain;
  - Fully nonlinear wave kinematics are simulated with the two-dimensional higher-order Boundary Element Method, enabled for irregular waves:
    * initialised with linear wave kinematics with spacial ramps to transit from linear to fully nonlinear wave kinematics and back,
    * free surface is allowed to develop in the Mixed Eulerian-Lagrangian scheme to achieve fully nonlinear wave conditions.

Chapter 4

Fluid-structure interaction

This chapter discusses the fluid-structure interaction modelling implemented in this thesis. First of all, the hydrodynamic loading models for slender offshore structures are discussed in great detail, highlighting the differences between them. Three models are compared throughout this thesis: the most common and straightforward Morison equation; Rainey's potential flow corrections to Morison inertia term; and Faltinsen-Newman-Vinje (FNV) third-order perturbation theory which considers wave diffraction. Then the investigated dynamic structures are introduced: moving cylinder, as well as the dynamic 5-MW baseline offshore wind turbine, including the implementation of the discussed hydrodynamic loading models in the open-source hydro-aero-servo-elastic solver.

4.1 Hydrodynamic loading models

Hydrodynamic loading models are the second critical part of wave loading computation. They translate the kinematics of the simulated waves (Chapter 3) into forcing on a specific offshore structure by taking into account its characteristics, such as monopile diameter.

Fully nonlinear wave kinematics have been shown to be needed in order to model highly nonlinear waves and capture the potential dynamic amplifications of the structural response (see Sections 1.4 and 2.2). On the other hand, the hydrodynamic loading model normally used for monopiles due to their slenderness relative to wavelength is Morison's equation (Morison et al., 1950). This widely applied semi-empirical equation has proven to be working well in linear and weakly nonlinear waves. However, in extreme conditions and strong nonlinearities the original Morison's model is considered insufficient. Additional third order models have been derived in the last three decades, and the main ones are discussed in the following subsections.

4.1.1 Morison equation

Morison equation (Morison et al., 1950), listed in Eq. 4.1, is the most commonly used method to account for hydrodynamic loading. It is a semi-empirical formula consisting of linear inertia component M and quadratic drag d, which are integrated along the length of the pile as shown in Figure 4.1.

$$F_{Morison} = \underbrace{\int_{-h}^{\eta} C_m \rho \pi R^2 \frac{\partial u_w}{\partial t} dz - \int_{-h}^{\eta} C_a \rho \pi R^2 \frac{\partial u_b}{\partial t} dz}_{M} + \underbrace{+ \int_{-h}^{\eta} C_d \rho R \left|(u_w - u_b)\right| (u_w - u_b) dz}_{d} \tag{4.1}$$

where η is the instantaneous free surface, h – water depth, ρ – water density, R – cylinder radius. C_m is inertia coefficient, C_a – added mass coefficient ($C_a = C_m - 1$), and C_d – drag coefficient. u_w is the horizontal wave velocity, while u_b – horizontal velocity of the body (cylinder or monopile).

Eq. 4.1 is the full formulation for a moving cylinder. The formulation for a fixed cylinder simply neglects the terms associated with the motion of the body u_b. The inertia term M remains as only the first term, and for the drag term d the relative velocity $(u_w - u_b)$ remains simply the velocity of waves u_w.

Depending on the regime in which the slender structure is placed, i.e. inertia or drag dominated, one of these components are commonly neglected. Since diffraction and inertia regimes dominate in the conditions investigated throughout this thesis, unless otherwise specified the drag term of the full Morison equation is neglected and only Morison inertia term is applied, as given in Eq. 4.2.

$$F_{Mor} = \int_{-h}^{\eta} C_m \rho \pi R^2 \frac{\partial u_w}{\partial t} dz - \int_{-h}^{\eta} C_a \rho \pi R^2 \frac{\partial u_b}{\partial t} dz \tag{4.2}$$

The inertia and drag coefficients C_m and C_d must be estimated by the help of experiments and/or theoretical best practice guidelines. Where not specified, in this thesis the hydrodynamic coefficient C_m is kept equal to 2 for consistency across hydrodynamic loading models, and C_d is equal to 1.

The main limitations of Morison equation can be summarised as not accounting for the free surface and wave diffraction, and semi-empirical nature. Despite these drawbacks Morison equation is still the most used method due to its simplicity and fast implementation. It has been deemed suitable for most situations; however, when it comes to more complex cases such as higher order effects of steep waves or shallow waters, the suitability of Morison equation has been extensively doubted (Grue et al., 1994; Malenica and Molin, 1995; Chaplin et

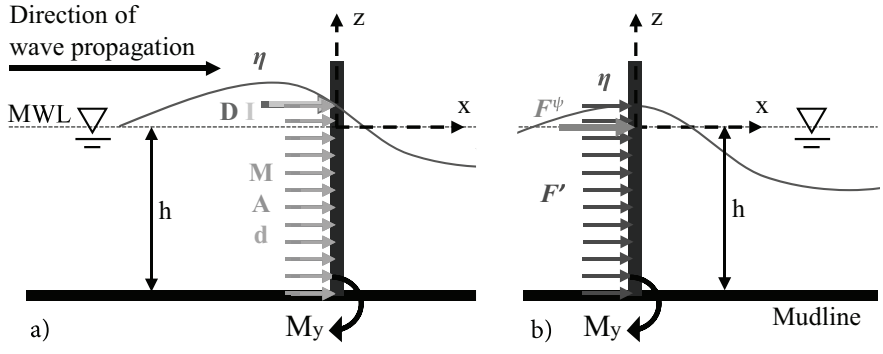

Figure 4.1: Coordinate system and implemented hydrodynamic loading model components of: a) Morison equation (M, d) and slender-body theory (A, D, I); b) FNV theory (F', F^{ψ}). MWL – mean water level, η – instantaneous free surface, and M_y – base bending moment.

al., 1997; Huseby and Grue, 2000; Ma et al., 2009; Paulsen et al., 2014). Therefore corrections and alternatives have been developed, discussed in Sections 4.1.2 and 4.1.3.

4.1.2 Slender-body theory

Corrections to Morison equation started with Lighthill (1979), who postulated that there are more nonlinear potential flow loads which should be considered together with Morison inertia term. The most widely implemented correction method is the slender-body theory, also known as Rainey theory, proposed by Rainey (1989) and extended in Rainey (1995). It separates the inertia term from Morison equation and corrects it by adding potential flow terms which, following the formulation of Chaplin et al. (1997), are: axial divergence term A (formulation for force F_A is given in Eq. 4.3), the surface intersection term I (force F_I in Eq. 4.4) and surface distortion term D (force F_D in Eq. 4.5). The axial divergence A is an integrated term along the cylinder length to the instantaneous free surface, while forces resulting from surface intersection term I and surface distortion term D are applied as point loads applied at the instantaneous free surface, as illustrated in Figure 4.1. Axial torque for the members that are not circular and the loads at joints are also described by the theory (Rainey, 1995), but are out of the scope of this research project therefore are not detailed here.

$$F_A = \int_{-h}^{\eta} \rho\pi R^2 \frac{\partial w}{\partial z} u dz \tag{4.3}$$

$$F_I = -\frac{\rho\pi R^2}{2} u^2 \frac{\partial \eta}{\partial x}, \text{ at } z = \eta \tag{4.4}$$

$$F_D = \frac{7\rho\pi R^2}{2g} u^2 \frac{\partial u}{\partial t}, \text{ at } z = \eta \tag{4.5}$$

In the Equations 4.3-4.5 the horizontal velocity u is defined as $u = u_w$ for the fixed case and as $u = u_r$ for the moving cylinder. Since the slender-body corrections are based on Morison equation, the relative velocity u_r is defined as $u_r = u_w - u_b$. The vertical velocity of the moving body is assumed negligible, therefore w is vertical wave velocity. Other quantities are as defined in Subsection 4.1.1.

The original slender-body theory with only the terms A and I correcting the Morison inertia term M (MAI) is based on the expansion of the slenderness parameter, which is the cylinder diameter over a defining characteristic such as wavelength or cylinder length (Rainey, 1989). This gives a definite advantage over the Stokes expansion – since the nondimensional wave number kR (k - wave number, R - cylinder radius) is tending to zero instead of wave steepness kA, the theory is suitable to any wave steepness, including breaking waves, where Stokes expansion would lose validity. However, even with the addition of both A and I terms a third-order error remains. It was corrected by the surface distortion term D in Rainey (1995). Nonetheless, the derivation of term D rests on the Stokes small amplitude assumption – it assumes small wave height in order to be a point load, therefore its suitability in higher wave steepness is limited (Chaplin et al., 1997). This limitation has refrained some researchers from using the full MAID formulation, using the MAI formulation instead. For

example, Chaplin et al. (1997) have assessed that the surface distortion term D was causing major deviation at steepness $kA \approx 0.299$, and were recommending the MAI formulation instead, while Schløer et al. (2016) simply used MAI formulation in their study. Therefore both variations of this slender-body theory are analysed in this study: MAI, correct to second order and without limitations in wave steepness; and MAID – third-order theory but with limitation in steepness.

The main approximation worth noting is that the body has to be in fact slender: the slenderness ratio kR has to be much less than 1, and the free surface shape has to be assumed not affected by the presence of the cylinder in order for the derivation on the energy conservation to be valid (Rainey, 1989; Chaplin et al., 1997).

4.1.3 FNV theory

Perturbation theories can be expanded to take any order of hydrodynamic loading components into account, at the cost of increasing complexity and computational effort. Both of the most established theories, M&M and FNV, have been derived with interest to study ringing phenomenon, therefore include third order loading components.

M&M, named after the originators Malenica and Molin (1995), is a perturbation theory formulated in diffraction regime for finite depth, following a classical Stokes perturbation technique to the third order. The main difference between M&M and FNV is that FNV assumes the radius of the structure to be of the same order as the wave amplitude (Malenica and Molin, 1995).

FNV theory, named after its originators Faltinsen, Newman and Vinje, was derived during the peak of interest in ringing phenomenon. Therefore it considers the local disturbance of the wave field due to the presence of the cylinder and immediately takes into account third order hydrodynamic loading components (Faltinsen et al., 1995). It was formulated in the long-wave regime, originally for deep water regular waves (Faltinsen et al., 1995) but was quickly extended to irregular waves by Newman (1996) and generalised for structural members of non-circular cross-sections by Faltinsen (1999). Very recently the theory has been generalised to finite depth by Kristiansen and Faltinsen (2017) and is suitable for regular waves, irregular long-crested waves and numerical wave tanks.

In this study the finite depth formulation (Kristiansen and Faltinsen, 2017) is implemented, where the horizontal force F_{FNV} (Eq. 4.6) consists of an integrated term to the instantaneous free surface F' (Eq. 4.7) and a point load at the still water level F^{Ψ} (Eq. 4.8), as also illustrated in Figure 4.1b. It should be noted that since this study considers only cylinders with circular cross-section, in the formulation of F' in Eq. 4.7 the two-dimensional added mass coefficient a_{11} is replaced by $\rho\pi R^2$. The theory has only been derived for a fixed cylinder in Kristiansen and Faltinsen (2017); nonetheless, the derivation including the effect of body motion was acquired via private communication with prof. Faltinsen (2018).

$$F_{FNV} = \int_{-h}^{\eta} F'(z,t)dz + F^{\Psi}\,, \tag{4.6}$$

where

$$F' = \rho\pi R^2 \left(2\frac{\partial u}{\partial t} + u\frac{\partial u_w}{\partial x} + 2w\frac{\partial u}{\partial z} \right), \tag{4.7}$$

and

$$F^{\Psi} = \frac{4\rho\pi R^2}{g} u^2 \frac{\partial u}{\partial t}, \text{ at } z = 0. \tag{4.8}$$

For a fixed cylinder $u = u_w$, while for a moving cylinder $u = u_{rel}$. The relative horizontal velocity u_{rel} for the integrated force F' (Eq. 4.7) follows the formulation of $u_{rel} = u_w - \frac{1}{2}\left(\frac{\partial \zeta}{\partial t} + w\frac{\partial \zeta}{\partial z}\right)$, while for the point load F^{Ψ} (Eq. 4.8) $u_{rel} = u_w - \frac{\partial \zeta}{\partial t} - w\frac{\partial \zeta}{\partial z}$. ζ stands for the lateral deflection of the cylinder, which with small angle assumption can be approximated to $\zeta = z\theta$. Lastly, w is vertical wave velocity.

The finite-depth FNV formulation is the only model in this study to consider diffraction. The integrated term F' satisfies the two-dimensional Laplace equation in each horizontal plane up to and including the instantaneous free surface, although the second order wave scattering is excluded (Kristiansen and Faltinsen, 2017). The integrated term differs from Morison equation since it takes the flow nonlinearities into account; i.e. the F' term without the nonlinear terms ($2\rho\pi R^2 \frac{\partial u}{\partial t}$) would be equal to Morison inertia term with inertia coefficient $C_m = 2$.

The F^{Ψ} term, on the other hand, satisfies the approximate free-surface condition and three-dimensional Laplace equation, and accounts for the third-order incident wave potential (Faltinsen et al., 1995). It considers the local disturbance of wave field due to the presence of the cylinder. F^{Ψ} follows the formulation of the original theory (Faltinsen et al., 1995), therefore it is applied at $z = 0$ (Kristiansen and Faltinsen, 2017).

This third-order term F^{Ψ} is another major difference from Morison equation (Morison et al., 1950), and from the original Rainey theory (Rainey, 1989), which is limited to MAI. Nonetheless, the third-order surface distortion term D (Eq. 4.5) was introduced by Rainey (1995). The three main differences between these third-order point loads are their point of action, the coefficient in the equation, and formulation of relative accelerations. The point of action for F_D is at the instantaneous free surface ($z = \eta$), while for F^{Ψ} – mean water surface ($z = 0$). As the waves steepen and the wetted length above the still water level increases, both of these point loads tend towards an error in the opposite directions – an overestimation for distortion term D and an underestimation for F^{Ψ}. On the other hand, the different coefficients, 4 for FNV (Eq. 4.8) and 3.5 for slender-body theory (Eq. 4.5), potentially cover for the different points of action. Lastly, the relative acceleration in the case of a moving cylinder are different due to different derivations: $u_r = u_w - \frac{1}{2}\left(\frac{\partial \zeta}{\partial t} + w\frac{\partial \zeta}{\partial z}\right)$ for FNV (Eq. 4.8) and $u_r = u_w - u_b$ for D (Eq. 4.5) .

The main limitations of the FNV theory include neglection of viscosity and the exclusion of breaking waves. This is because in the original FNV (Faltinsen et al., 1995) the effects of viscous drag were considered negligible in the cases where wave amplitude is of the same magnitude as the cylinder radius, which is a basic assumption of this model. This also applies for very steep waves which are associated with the nonlinear effects, justifying the neglection of viscosity. The limit at the wave breaking, where additional slamming impact would need

to be considered, could be fixed by inclusion of models which include slamming loads, e.g. Marino (2010), but it is outside the scope of this thesis. Finally, the conditions in which this theory is valid are evident from the definition of the long-wave theory: the wavelength has to be much larger than the wave amplitude or cylinder radius ($A_w/\lambda << 1$ and $R/\lambda << 1$), as well as the radius of the monopile to be of the same order as the wave amplitude ($R/A_w \approx 1$). Nevertheless, the suitability of the FNV theory will be tested against the experimental values in its off-design range as well (Chapter 5).

4.2 Modelling of dynamic structural response

4.2.1 One-degree-of-freedom cylinder

The one-degree-of-freedom (1DOF) system is modelled as a rigid cylinder on a spring, the stiffness of which can be adjusted, as illustrated in Figure 4.2. The equation of motion (Eq. 4.9) is solved with the ordinary differential equation solver ODE45 in MATLAB by MathWorks, Inc. Main limitations include the neglection of vertical cylinder motion (relative vertical velocity stays as only the velocity of waves) and the fact that 1DOF system only recreates the first structural mode of a flexible cylinder, not the higher modes. Even though the higher modes are more important for body motion, especially acceleration, loading is primarily associated with the first mode, therefore such simplification is considered acceptable.

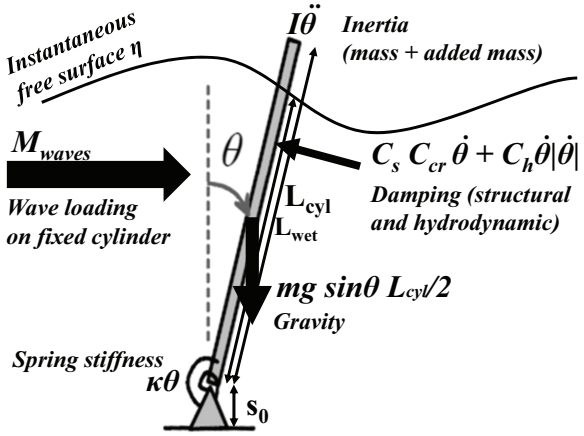

Figure 4.2: Coordinates and the acting components in the one-degree-of-freedom system.

$$I_b\ddot{\theta} = m_{cyl}g\frac{L_{cyl}}{2}\sin\theta - C_s\dot{\theta} - C_h\dot{\theta} \mid \dot{\theta} \mid -\kappa\theta + M_{waves}\,, \tag{4.9}$$

where θ is the deflection angle with $\dot{\theta}$ and $\ddot{\theta}$ being its first and second derivatives in time, I_b is the second moment of inertia of the system, m_{cyl} – mass of the cylinder, g – gravitational constant, L_{cyl} – total length of the cylinder, C_s – structural coefficient, C_h – hydrodynamic damping coefficient based on Morison drag term, κ is the spring stiffness, and M_{waves} is the

overturning moment of the waves, calculated from the chosen combination of wave kinematics and hydrodynamic loading model.

The inertia of the body $I_b = I_{cyl} + I_{added}$, where I_{cyl} is the second moment of inertia of a hollow cylinder fixed at one end, and $I_{added} = \rho\pi R^2 L_{wet}^3/3$ is the added mass due to the motion of the cylinder. It is the 2D added mass for circular cylinders at very high frequencies ($a_{11} = \rho\pi R^2$) integrated from the bottom to the instantaneous free surface, and L_{wet} is the length of the wetted cylinder. It should be noted that in the presence of waves the added mass contribution I_{added} is modelled by every hydrodynamic loading model individually, by the inclusion of additional relative acceleration terms, as given in Sections 4.1.1-4.1.3. Therefore the added mass contributions become loading model-dependent.

The structural damping coefficient C_s is typically defined as the percentage of the critical damping of the system $C_{crit} = 2\sqrt{I_b\left(\kappa - m_{cyl}g\frac{L_{cyl}}{2}\right)}$, therefore unless otherwise specified, this thesis implements the percentage formulation as well. The hydrodynamic damping arises from viscous forces due to cylinder motion in the water. Therefore quadratic hydrodynamic damping is considered in this thesis, dependent on $\dot{\theta} \mid \dot{\theta} \mid$. The hydrodynamic damping coefficient is defined as $C_h = \rho R L_{wet}^3/3$. This corresponds to the formulation of the quadratic Morison drag term already integrated from the bottom to the instantaneous free surface with the drag coefficient $C_d = 1$. Finally, the spring on which the rigid cylinder is mounted, represents the soil-structure interaction. Its stiffness κ represents the stiffness of the soil on which the natural frequency of the system depends. Therefore it is adjusted in each study depending on either pre-described experimental stiffness or natural frequency of the system, or to set the natural frequency of the system in the range of interest.

4.2.2 Offshore wind turbine

4.2.2.1 Hydro-aero-servo-elastic solver FAST

In order to investigate the structural response of a parked or operating offshore wind turbine subjected to the combined action of wind and waves, a coupled solver is required. In this study the open-source hydro-aero-servo-elastic solver FAST (Jonkman and Buhl Jr., 2005), developed by the National Renewable Energy Laboratory (NREL) in Colorado, USA, and available from Jonkman (2018), is coupled with the wave loading models developed in this thesis.

The FAST hydro-aero-servo-elastic solver, as the name suggests, consists of four main modules: aero, hydro, servo and elastic. The aero module deals with the wind input, such as steady or turbulent wind, mean wind speed and turbulence category, wind direction and so on. The servo module allows to control the turbine, such as pitch and yaw angles, and allows to model the turbine as parked or operational. The elastic solver contains the geometric and material properties of the turbine. In this study the NREL 5MW baseline offshore wind turbine is modelled on a monopile support, as described in Section 4.2.2.4.

Finally, the hydro model is computing the hydrostatic and hydrodynamic input, including the action of waves and current. It is modelled by the HydroDyn module (Jonkman et al., 2014), with which the main aero-servo-elastic FAST model is coupled. However, the cur-

rently implemented selection of wave kinematic and hydrodynamic loading model options are limited, therefore the wave kinematics and hydrodynamic loading models discussed in this thesis are implemented in FAST as described in Sections 4.2.2.2-4.2.2.3.

4.2.2.2 Coupling with external wave kinematics

The incident wave kinematics available in FAST are only linear: plane progressive (regular) or JONSWAP/Pierson-Moskowitz spectrum (irregular). Two additional options are implemented: to use user-defined spectrum in order to compute linear irregular waves or, most importantly for this thesis, to read in user-generated wave data (known as *GH Bladed wave data*). Therefore wave kinematics of all orders of nonlinearity, modelled externally as described in Chapter 3, are imported to the solver to allow easy comparison of the response of the turbine to different wave loading models.

The capability already implemented in FAST is to read in three text files:

1. `[kin]_FAST.txt` which contains the number of nodes that contain the wave kinematics and then their vertical coordinates. `[kin]` stands for the string assigned for different order of wave kinematics, e.g. `FNL_FAST.txt` for fully nonlinear wave kinematics. The same string has to be defined in the platform data input file under `GHWvFile` (the root name of GH Bladed files containing wave data).
2. `[kin]_surface.txt` with two columns, including a text heading *Time [s] Sea surface elevation [m]* and then listing the time and the free surface elevation values. To ensure that the simulation is running, the time step defined in this file must match the one stated as `WaveDT` in the platform file. Recommended by FAST as 0.1 <=WaveDT<= 1.0.
3. `[kin]_kinematics.txt` which contain seven columns listing the wave velocity in (*x,y,z*) directions, wave acceleration in (*x,y,z*) directions, and pressure, which is not used in FAST by default, therefore kept as zero within this study. Moreover, since this study is in two dimensions only, the wave kinematics in *y* direction are written as zeros as well.

Nonetheless, the Rainey and FNV loading models need additional wave kinematic values. In order to interfere with the existing functionality the least, two additional text files were generated and compiled in FAST. These were named `_extrakinsurf.txt` and `_extrakinturb.txt`, for extra kinematics on free surface and along the depth consequently.

4. `[kin]_extrakinsurf.txt` contains five columns: the $\partial\eta/\partial x$, wave velocity and acceleration on the mean water surface for FNV and wave velocity and acceleration on the free surface elevation for Rainey; at every time step.
5. `[kin]_extrakinturb.txt` contains three columns: the $\partial v_x/\partial x$, $\partial v_x/\partial z$, and $\partial v_z/\partial z$; at every node along the depth at every time step.

These values are read in the FAST source file `HydroCalc.f90`, module `Waves`. It is necessary to ensure that all the new variables are initialised and allocated appropriately in the module and in the subroutine `InitWaves`. Note should also be taken that the FAST integration time step ($\approx$ 0.0125) is much smaller than the wave time step, therefore additional interpolation functions have to be added within the module to be later called in the hydrodynamic loading model computations, described in Section 4.2.2.3.

4.2.2.3 Implementing hydrodynamic loading models

The default choice of hydrodynamic loading models in FAST is none, Morison's equation or user-defined loading model from routine `UserTwrLoad`. Dummy placeholder for `UserTwrLoad` is implemented in the source file `HydroCalc.f90`, module `FixedBottomSupportStructure`, therefore the integration of additional loading models is made easier. Nonetheless, at least basic Fortran coding knowledge had to be acquired in order to successfully integrate the loading models: ensuring that the right variables are read in the modules and routines, deriving additional variables, as well as recompiling the whole programme. FAST was recompiled following the guidelines listed in FAST User's Guide (Jonkman and Buhl Jr., 2005) and Instructions for Compiling FAST (Jonkman, 2012) with Intel Visual Fortran 64 Compiler, Version 19.0.2.190, available for free with student license.

The subroutines `UserTwrLoad` for all three additional loading models are given in Appendix C. Master thesis of Asgeir Hovdelien Midthaug (NTNU, Norway; Midthaug (2014)) is acknowledged, where the older infinite-depth FNV (Faltinsen et al., 1995) and the original Rainey theory with only MAI model (Rainey, 1989) were implemented and the subroutines were provided. This reference aided and accelerated the process of implementing the finite-depth FNV (Kristiansen and Faltinsen, 2017) and MAID (Rainey, 1995) models in this thesis.

However, additional steps beyond writing the subroutines had to be implemented. The most notable change was due to the relative velocity defined by the finite depth FNV theory. It requires second order derivatives of tower displacement in both space (over the vertical coordinate) and time. To compute the derivatives in space, the tower motion across all vertical nodes is needed. The FAST programme, however, loops over each node calculating the tower motion and the hydrodynamic loading for one node before computing it for the next one. Therefore the code had to be adapted, requiring to split the calculation into two separate loops: for the tower motion across all nodes and then for the hydrodynamic loading for all nodes in the `RtHS` subroutine without interfering with the functionality of the rest of the programme. After trial and error, rigorous debugging and extensive checks, the additional loading models were implemented.

Finally, the limitations need to be discussed. It should be noted that since the wave kinematics are computed in two dimensions, the tower motion in the third dimension was omitted for the derived values for the ease of implementation. It is considered acceptable since ringing is a predominantly two-dimensional phenomenon, as discussed in Section 3.3.3.2. It is also acknowledged that the code could be written in a smoother manner with better knowledge of Fortran coding, especially for the derivatives of tower motion in FNV (Section C.3), but this is not expected to have affected quality of the results.

4.2.2.4 Details of the turbine model

Due to strong confidentiality from wind turbine manufacturers it is extremely difficult to acquire enough details on a real offshore wind turbine to model it numerically. Nonetheless, NREL have derived a 5-MW baseline wind turbine for research purposes (Jonkman et al., 2009). It is a representative multimegawatt turbine, combining properties of two actual offshore wind turbines – 6-MW Pre-Design of the *Dutch Offshore Wind Energy Converter (DOWEC)* and 5-MW *REpower 5M*. The properties of the NREL 5-MW baseline wind tur-

bine are freely available, including a range of realistic support structures for both fixed and floating offshore wind turbines, making it ideal for conceptual studies in offshore wind field. The detailed description of this baseline model can be found in Jonkman et al. (2009) with the key aspects are summarised in Table 4.1 and illustrated in Figure 4.3.

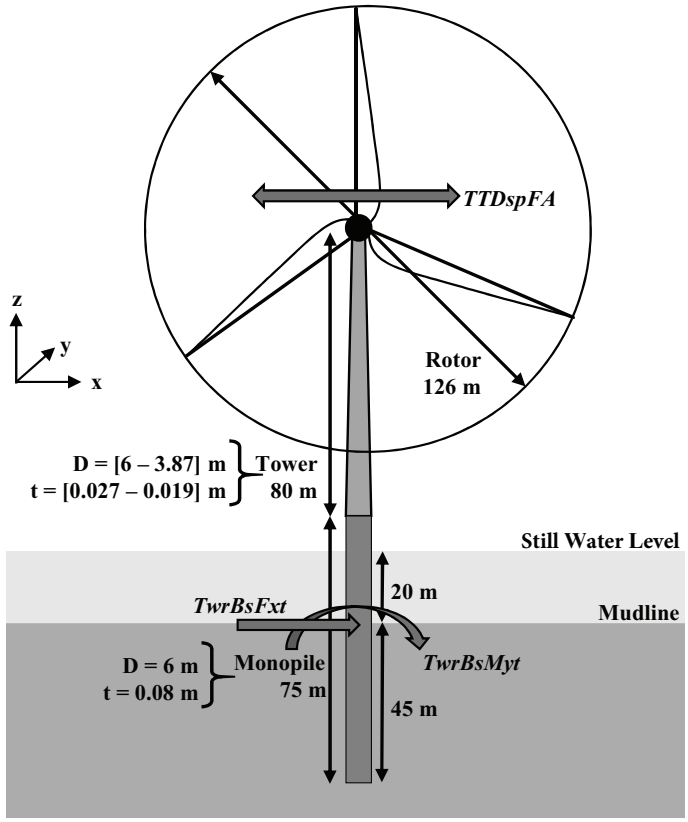

Figure 4.3: Dimensions of the reference monopile-supported 5-MW offshore wind turbine, associated coordinate system, and the investigated responses.

Rating	5 MW
Rotor Orientation, Configuration	Upwind, 3 Blades
Control	Variable Speed, Collective Pitch
Rotor, Hub Diameter	126 m, 3 m
Hub Height	90 m
Cut-In, Rated, Cut-Out Wind Speed	3 m/s, 11.4 m/s, 25 m/s
Rotor, Nacelle, Tower Mass	110 t, 240 t, 347.46 t
Tower Base Diameter and Thickness	6 m, 0.027 m

Table 4.1: NREL offshore 5-MW baseline wind turbine specifications. For full details refer to Jonkman et al. (2009).

The support structure used in this study is a 6 m diameter monopile support in 20 m water depth. The first eigenfrequency (the natural frequency f_n) of the whole system varies depending on the foundation: for a stiff support it is estimated at around 0.28 Hz while for flexible foundation around 0.25 Hz (Jonkman and Musial, 2010). In the case of misaligned wind and waves the natural frequency of the stiff system can increase up to 0.295 Hz due to the different distribution of the tower top mass (the rotor not being aligned with the direction of the wind and waves), as seen in Mockute et al. (2017a).

Finally, the multiple degree of freedom turbine in the FAST solver allows to analyse a wide variety of variables, such as power generation, rotor torque, blade deflection, bending moments at a number of nodes, and many more. Nonetheless, three critical and most representative variables in this study on the dynamic amplifications due to wave nonlinearities are the tower base shear force (TwrBsFxt), tower base bending moment at the seabed (TwrBsMyt), and the fore-aft tower top displacement (TTDspFA). Tower base shear force allows more direct comparison to the fundamental studies on cylinders, while the importance of the mudline bending moment (TwrBsMyt) comes from the fact that the monopile-supported OWT is a cantilevered structure: bending moments are significantly more affected by the nonlinear waves than shear force due to the high arm, leading to the weakest structural point of offshore wind turbine at the seabed or just below (Rezaei et al., 2018). The importance of the tower top displacement might be slightly less structural, but rather human – the most repaired part of the offshore wind turbine tends to be the electrical parts in the nacelle (around 60% of failures according to Hyers et al. (2006)), requiring the maintenance engineers to spend time at the tower top. The sensitivity of the turbine to strong oscillations might cause inconvenience if not danger to the maintenance workers.

4.3 Summary of the Chapter

This chapter described the methodology for fluid-structure interaction modelling in this study.

- This study investigates three hydrodynamic loading models:
  - Morison equation, consisting of linear inertia and quadratic drag (latter mostly neglected due to inertia-dominance in the investigated conditions);
  - Rainey theory (with and without the surface distortion term D, the suitability of which at steep waves has been doubted);
  - diffraction-based third-order finite-depth perturbation theory FNV.
- The study is conducted on:
  - A fixed cylinder, to study solely the influence of the wave loading;
  - One-degree-of-freedom moving cylinder, to add the aspect of motion without the complexity of the geometry and multiple degrees of freedom;
  - A representative baseline 5-MW monopile-supported offshore wind turbine.
- Open-source aero-hydro-servo-elastic solver FAST is used to study the response of the offshore wind turbine, with the following considerations:
  - Externally simulated wave kinematics are coupled into the solver;

- The solver was advanced by directly implemented hydrodynamic loading models (finite-depth FNV and full formulation of the Rainey's model as original contribution);
- Mudline shear force, mudline bending moment and tower top displacement are selected as the key representative variables for the offshore wind turbine response.

Chapter 5

Regular wave loads on a fixed cylinder

This chapter investigates a bottom-fixed rigid cylinder in regular waves. Such setting allows for the most controlled testing environment and clearest analysis. Comparison with past experimental data is conducted throughout the Chapter, therefore first of all the experimental campaigns are overviewed. The capability to numerically capture the experimentally observed secondary load cycle is tested. Then the fundamental distinction of the influences of nonlinearities in wave kinematics and in the hydrodynamic loading models are discussed. The discussion on the influences is extended over increasing wave steepness and over increasing slenderness ratio, where the behaviour of the wave loading models in their off-design values is discussed. Finally, the best performing wave loading models for the wave and cylinder condition in each harmonic are discussed.

5.1 Introduction

Modelling a fixed cylinder in regular waves is a crucial step of this research since it allows to assess wave forcing only, without any influence of the cylinder response, in the most predefined and predictable environment. Numerous experiments and past comparisons with numerical loading models also allow to validate the implementations of the loading models utilised in this study. On top of that, fixed cylinder is where the secondary load cycle is experimentally observed in very steep waves.

The wave and cylinder conditions in which the numerically recreated experiments are set, along with past observations of secondary load cycle and ringing (as collected by Grue and Huseby, 2002), are shown on the (kA, kR)-graph (Figure 5.1). As already introduced in Chapter 2, the dashed lines represent Keulegan-Carpenter number ($KC = u_w D_{cyl}/T$, where u_w is the horizontal wave velocity, D_{cyl} – cylinder diameter, and T – wave period) equal to π and 10, to give indications of the diffraction, inertia and drag regimes.

To assess the numerical hydrodynamic loading models in a range of conditions, the experiments from literature were selected to fill a wide range of wave and cylinder conditions in Figure 5.1. The experiments of Grue and Huseby (2002) are right in the center of the conditions where the two nonlinear phenomena of interest occur, while Kristiansen and Faltinsen (2017) cover both inertia and diffraction regimes systematically over increasing wave steepness kA (k being the wave number, A – wave amplitude) and nondimensional wave number kR (R being the cylinder radius). It should be noted that the identical markers in Kristiansen and Faltinsen (2017) cases refer to all cases across increasing wave steepness H_1/λ of the same period T and depth h. Finally, the experimental campaign of Stansberg (1997) bridges the gap in wave steepness between the former two, as well as provides an opportunity to investigate the influence of the cylinder diameter in identical wave conditions.

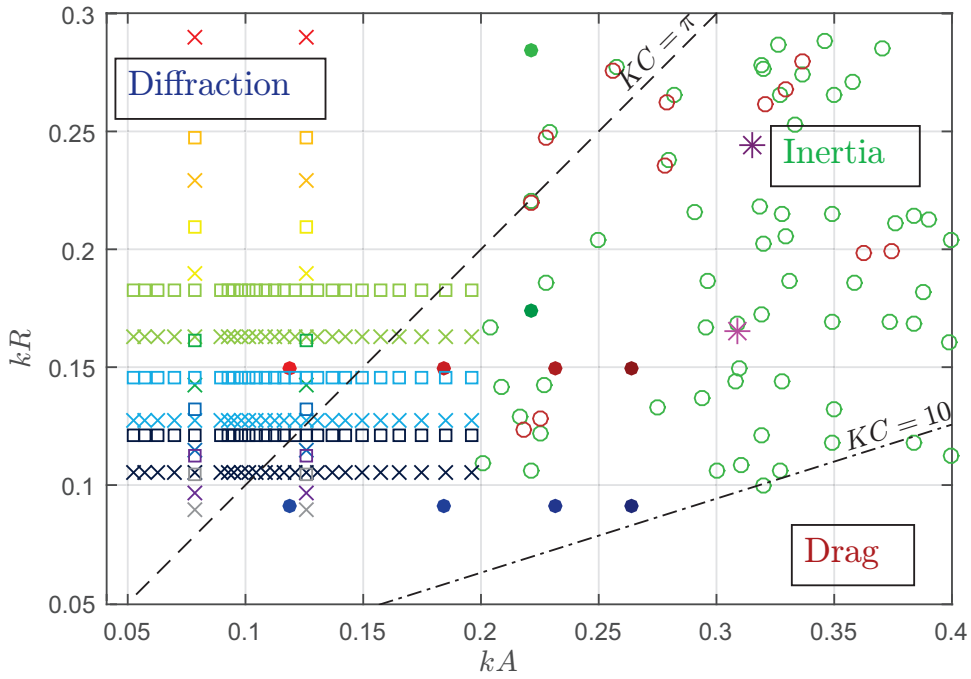

Logged events of: ○ secondary load cycle, ○ ringing (Grue and Huseby, 2002)
Grue and Huseby (2002): ✳ T = 0.856 s, H = 0.112 m ✳ T = 0.703 s, H = 0.077 m

Stansberg (1997)	T = 2.10 s, A = 0.130 m:	● R = 0.10 m	● R = 0.16 m
Stansberg (1997)	T = 2.10 s, A = 0.202 m:	● R = 0.10 m	● R = 0.16 m
Stansberg (1997)	T = 2.10 s, A = 0.254 m:	● R = 0.10 m	● R = 0.16 m
Stansberg (1997)	T = 2.10 s, A = 0.289 m:	● R = 0.10 m	● R = 0.16 m
Stansberg (1997)	T = 1.52 s, A = 0.127 m:	● R = 0.10 m	● R = 0.16 m
Kristiansen and Faltinsen (2017)	T = 1.010 s:	× h = 0.563 m	
Kristiansen and Faltinsen (2017)	T = 1.155 s:	× h = 0.563 m	□ h = 0.396 m
Kristiansen and Faltinsen (2017)	T = 1.299 s:	× h = 0.563 m	□ h = 0.396 m
Kristiansen and Faltinsen (2017)	T = 1.443 s:	× h = 0.563 m	□ h = 0.396 m
Kristiansen and Faltinsen (2017)	T = 1.588 s:	× h = 0.563 m	□ h = 0.396 m
Kristiansen and Faltinsen (2017)	T = 1.732 s:	× h = 0.563 m	□ h = 0.396 m
Kristiansen and Faltinsen (2017)	T = 1.876 s:	× h = 0.563 m	□ h = 0.396 m
Kristiansen and Faltinsen (2017)	T = 2.021 s:	× h = 0.563 m	□ h = 0.396 m
Kristiansen and Faltinsen (2017)	T = 2.165 s:	× h = 0.563 m	□ h = 0.396 m
Kristiansen and Faltinsen (2017)	T = 2.309 s:	× h = 0.563 m	□ h = 0.396 m

Figure 5.1: Experimental studies in regular waves analysed in this thesis on the (kA, kR)-grid (k – wave number, A – wave amplitude, R – cylinder radius) with reference to historically observed secondary load cycle and ringing occurrences (Grue and Huseby, 2002). The diffraction, inertia and drag regimes are separated by the KC number equal to π and 10.

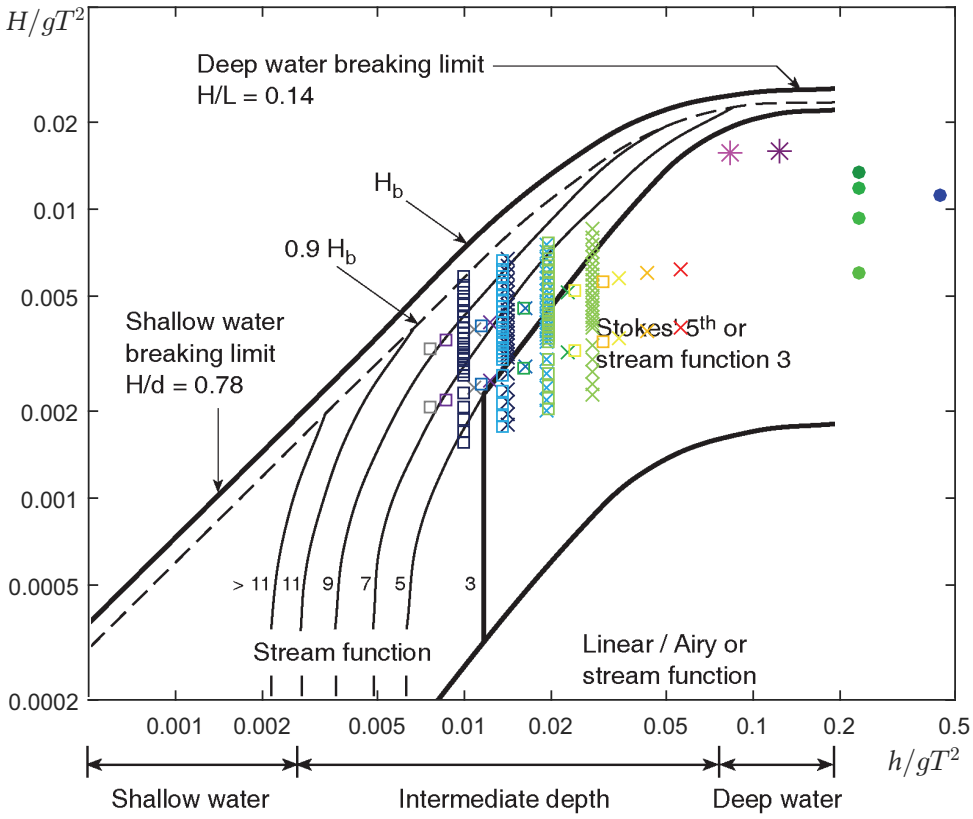

Grue and Huseby (2002): ✳ T = 0.856 s, H = 0.112 m ✳ T = 0.703 s, H = 0.077 m

Stansberg (1997)	T = 2.10 s, A = 0.130 m:	● R = 0.10 m	
Stansberg (1997)	T = 2.10 s, A = 0.202 m:	● R = 0.10 m	
Stansberg (1997)	T = 2.10 s, A = 0.254 m:	● R = 0.10 m	
Stansberg (1997)	T = 2.10 s, A = 0.289 m:	● R = 0.10 m	
Stansberg (1997)	T = 1.52 s, A = 0.127 m:	● R = 0.10 m	
Kristiansen and Faltinsen (2017)	T = 1.010 s:	× h = 0.563 m	
Kristiansen and Faltinsen (2017)	T = 1.155 s:	× h = 0.563 m	□ h = 0.396 m
Kristiansen and Faltinsen (2017)	T = 1.299 s:	× h = 0.563 m	□ h = 0.396 m
Kristiansen and Faltinsen (2017)	T = 1.443 s:	× h = 0.563 m	□ h = 0.396 m
Kristiansen and Faltinsen (2017)	T = 1.588 s:	× h = 0.563 m	□ h = 0.396 m
Kristiansen and Faltinsen (2017)	T = 1.732 s:	× h = 0.563 m	□ h = 0.396 m
Kristiansen and Faltinsen (2017)	T = 1.876 s:	× h = 0.563 m	□ h = 0.396 m
Kristiansen and Faltinsen (2017)	T = 2.021 s:	× h = 0.563 m	□ h = 0.396 m
Kristiansen and Faltinsen (2017)	T = 2.165 s:	× h = 0.563 m	□ h = 0.396 m
Kristiansen and Faltinsen (2017)	T = 2.309 s:	× h = 0.563 m	□ h = 0.396 m

Figure 5.2: Experimental studies in reference to the regular wave theory limits as defined in IEC 61400-3 design standards for offshore wind turbines (International Electrotechnical Commission, 2009). H_b – wave breaking limit, H – wave height, h – water depth, both nondimensionalised with g – gravitational constant and T – wave period.

The (kA, kR)-graph allows to discuss the expected performance of the hydrodynamic loading models. Firstly, it can be seen that none of the analysed experimental cases fall in the drag regime, therefore the drag term in the Morison equation (Eq. 4.1) is neglected and Morison equation represents inertia only, as per Eq. 4.2. Moreover, since only the FNV theory (Eq. 4.6) considers diffraction, it could be expected to perform better than the inertia-based models for the experimental cases in the diffraction regime.

The same experiments are shown on the wave theory limit graph in Figure 5.2, already seen in Chapter 3. First of all, it can be seen that water depth in these experiments ranges from intermediate to deep, therefore shallow water and associated limitations are certainly avoided. This distribution also enables the discussion on influence of water depth on the behaviour of wave loading model combinations. Moreover, all the cases fall above the limit of the linear (Airy) wave kinematics, therefore nonlinearities in wave kinematics may be expected to be significant. It can also be observed, that the cases in intermediate water depth, despite the smaller wave height, fall closer to the wave breaking limit into the range where more nonlinear wave theories are recommended. Therefore it can be expected that for the steepest cases in the intermediate water depth more nonlinear wave kinematics would predict the experimental loading better than linear or weakly nonlinear wave theories.

5.2 Overview of past experimental data

The experimental results reported in literature help to assess the appropriateness of the numerical results, but there are associated limitations, such as errors in the digitisation of the previously plotted graphs or the post-processing of the digitised data. Therefore this section overviews the past experimental set-ups, and discusses the methods used and the limitations associated with digitisation of the printed experimental data.

In Kristiansen and Faltinsen (2017) the generalised FNV theory for finite depth was validated by experimental data on a detailed grid of conditions up to steepness of nearly $kA \approx 0.2$. The cylinder radius was $R = 0.072\ m$ in two water depth settings: $h/R = 7.83$ and $h/R = 5.51$. A number of periods from $T = 0.866\ s$ to $T = 2.309\ s$ and steepnesses from $H_1/\lambda = 1/140$ to $H_1/\lambda = 1/16$ were investigated. To avoid errors stemming from post-processing of the digitised data from Kristiansen and Faltinsen (2017), the comparison of the numerical wave loading models with the experimental results from Kristiansen and Faltinsen (2017) is displayed in the same format as given in the original paper (Sections 5.6-5.7). Post-processing was only required for determining the best-suited numerical wave loading models, presented in Section 5.8. A single value of experimental loading was required for each modelled case (determined by water depth, wave period and wave steepness) in order to determine which numerical loading model captures the experimental results best. However, the graphs in Kristiansen and Faltinsen (2017) provided more than one value per experimental case. Therefore the average of the distribution of reported experimental data in the vicinity of the case was used. The experimental values were redimensionalised by water density, gravitational constant and the cube of cylinder radius to return to absolute values for comparison. The resulting error of this post-processing is expected to be negligible in the cases over increasing steepness H_1/λ (Fig. 5.8) since the graphs mostly had a single value,

and slightly higher over the increasing kR (Fig. 5.11) due to the larger scatter. Nonetheless, when commenting on the best-fitting loading models in Section 5.8 it was referred back to the original data to compensate for the potential discrepancies due to post-processing.

Ten cases from Stansberg (1997) were numerically recreated in this thesis: two wave periods ($T = 1.52\ s$ and $T = 2.10\ s$) with a selection of wave amplitudes ($A = [0.130, 0.202, 0.254, 0.289]\ m$ for $T = 2.10\ s$ and only $A = 0.127\ m$ for $T = 1.52\ s$, which was determined by Stansberg (1997) to act as the scaled version for the $T = 2.1\ s$ with $A = 0.254\ m$ case in terms of the steepness kA), all on single cylinders of radii $R = 0.1\ m$ and $R = 0.1635\ m$. More cases were discussed in Stansberg (1997), both in time and frequency domains, but only the cases reported in the frequency domain are recreated in this study to avoid inconsistencies due to FFT analysis of only a short part of time series of the loading. The original normalisation is followed for the comparison with the results of Stansberg (1997), therefore they are presented without any post-processing (Figs. 5.9 and 5.10). For the best-suited wave loading models, presented in Section 5.8, however, the digitised values had to be redimensionalised with the radius squared and the linear amplitude to the power of the harmonic. This could lead to an error since the waves produced experimentally do not always match the pre-described wave amplitude. Nonetheless, since these values are reported in Stansberg (1997), the error is expected to be minimised. Lastly, the experimental waves were generated in the water depth of $h = 10\ m$, but the fixed cylinder in the experimental study is only immersed to the length of $L_{cyl} = 1.44\ m$. Therefore wave kinematics computed numerically as described in Chapter 3 are those of 10 m depth, but for the fluid-structure interaction the cylinder length used in the hydrodynamic loading model equations listed in Chapter 4 is $L_{cyl} = 1.44\ m$.

The experiments reported in Grue and Huseby (2002) were conducted in water depth of $h = 0.6\ m$ on a cylinder of radius $R = 0.03\ m$. Both the wave elevation and horizontal loading time series were digitised, and, since both of the experimental cases were strongly nonlinear and therefore very unsteady, the experimental time series were superimposed. The time series of both the experimental elevation and loading were cut at zero-upcrossings, and the mean of those six-seven periods is shown as the main loading while the standard deviation is shown as the error bars. The superimposed mean wave elevation was then used to tune the numerical wave height and wave period for each wave theory by the least-square method on the elevation – the wave height H and period T were adjusted for each wave kinematics so that they would lead to the lowest root-mean-square-error between the experimental superimposed elevation and the numerical one. This led to wave period $T = 0.70\ s$ and wave steepness $kA \approx 0.32$ for the first case and $T = 0.85\ s$ and $kA \approx 0.31$ for the second case. No frequency domain data was available for these two cases in Grue and Huseby (2002), therefore the FFT analysis was conducted with the digitised data. The error bars in the frequency domain represent the FFT analysis of the top and bottom boundaries of the standard deviation in time domain.

5.3 Capability to capture secondary load cycle

As discussed in Section 2.3, secondary load cycle (SLC) has only been successfully numerically captured by 3D CFD to date (Paulsen et al., 2014; Kristiansen and Faltinsen, 2017). To discuss the capability of all combinations of wave loading models analysed in this study to capture the secondary load cycle, they are compared with the experiments of Grue and Huseby (2002), where SLC has been clearly experimentally observed in both cases, as shown in Figure 5.3. The SLC is observed as the reduced loading or secondary peak at the minima of the loading, around $t = [0.4 - 0.65]\ s$ in Figure 5.3a and around $t = [0.5 - 0.75]\ s$ in Figure 5.3b.

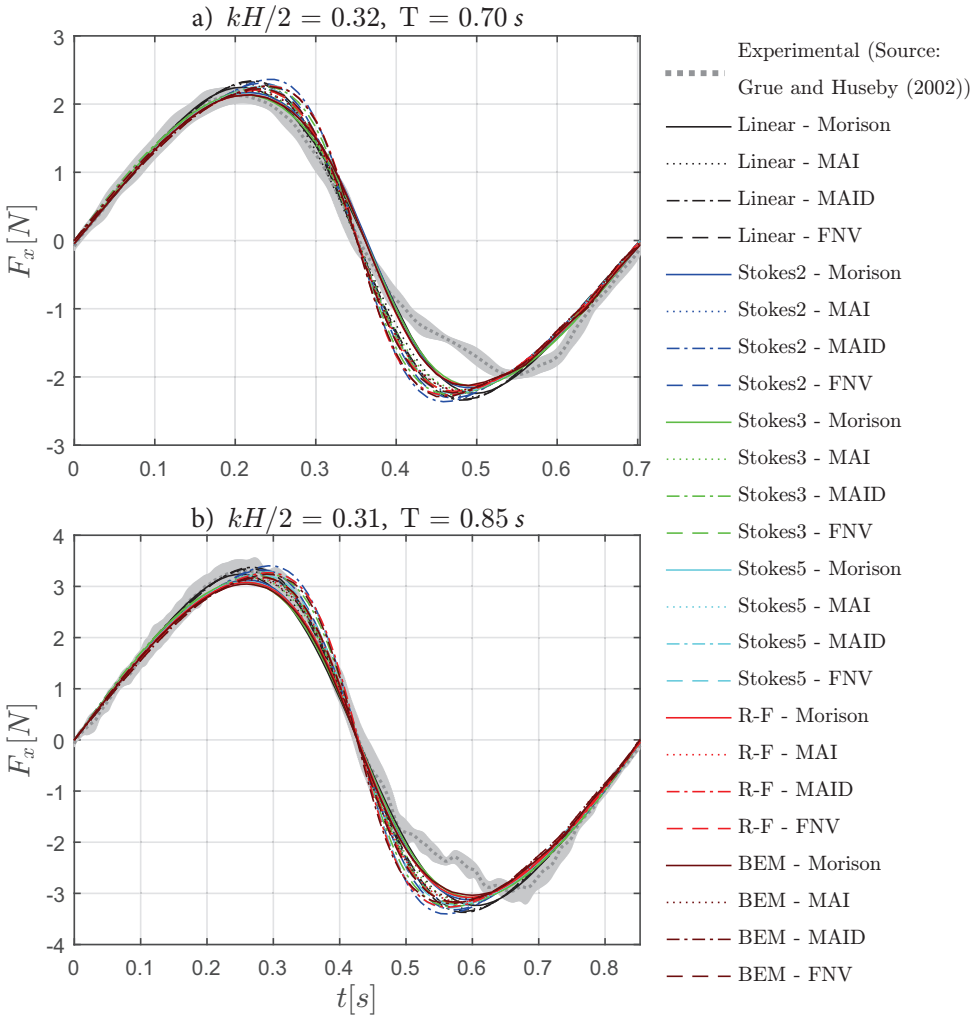

Figure 5.3: Comparison of all computed wave loading combinations with the superimposed horizontal force measurements for two cases reported in Grue and Huseby (2002), where error bars are the standard deviation from the superimposition at zero-upcrossings.

Morison inertia term (Eq. 4.2) is linear, making it a first-order loading model. Meanwhile, in the slender-body theory terms A (Eq. 4.3) and I (Eq. 4.4) correct Morison inertia term to second order and do not imply limitations on wave steepness. Even though there would be nonlinearities stemming from nonlinear kinematics, second order hydrodynamic loading model MAI is considered insufficient to capture SLC. The surface distortion term D (Eq. 4.5) corrects the remaining third order error in Stokes expansion making MAID a third-order hydrodynamic loading model. However, as discussed in Section 4.1.2, it is based on small amplitude assumption, therefore could be considered invalid in high wave steepness such as here, leaving the theory correct to second order in MAI formulation. The finite-depth FNV theory is derived to third order with which ringing is associated, and considers diffraction, by which secondary load cycle has been explained (Paulsen et al., 2014), therefore could be expected to have a strong potential to recreate the secondary load cycle. In the recent paper by Kristiansen and Faltinsen (2017) where the finite depth formulation for FNV was derived no SLC has been observed due to steepness kA only up to ≈ 0.2, leaving no studies to the date of this phase of the thesis assessing its suitability to capture the SLC.

However, the fact that the finite-depth FNV (dashed lines in Figure 5.3) omits the secondary load cycle, even with fully nonlinear BEM wave kinematics, drives the conclusion that secondary load cycle is caused by effects neglected by the theory in this two-dimensional study: either three-dimensional effects or loading higher than third order to which the theory is derived. However, it was recently suggested from the numerical study by Paulsen et al. (2014) and later confirmed experimentally by Suja-Thauvin et al. (2017) that even though the secondary load cycle occurs in the same wave conditions as ringing, the two phenomena are not directly linked.

Therefore the fact that SLC is not captured by any of the analysed combinations of wave models does not imply that ringing would be omitted too. In fact, as it was previously mentioned in Section 2.2, with fully nonlinear wave kinematics Morison equation is already sufficient to capture ringing numerically (Marino et al., 2013a; Marino et al., 2014b; Schløer et al., 2016). Nevertheless, the simulations for fully nonlinear wave kinematics are time consuming and are cumbersome for the design phase where numerous simulations are needed. Therefore the aim is to see whether ringing could be captured without the computationally heavy fully nonlinear wave kinematics but with a more sophisticated hydrodynamic loading model to compensate for the nonlinearities. For this a good understanding of where the predominant nonlinearities in loading are stemming from is crucial. Thus in Section 5.4 the distinction between the nonlinearities in wave kinematics and in hydrodynamic loading models is discussed.

5.4 Distinction of nonlinearities in wave kinematics and in hydrodynamic loading models

To discuss the influences of nonlinearities in wave kinematics and in the hydrodynamic loading models separately, Figure 5.4 shows the frequency domain analysis of the loading corresponding to Grue and Huseby (2002) case shown in Figure 5.3b. The first five harmonics (left to right) are shown for four selected cases, representing each case of nonlinearities.

Firstly, the most linear wave loading model combination consists of linear wave kinematics (Eqs. 3.2-3.3) with the linear Morison inertia term (Eq. 4.2), noted by black circle, and plotted as the reference case. The influence of nonlinearities in hydrodynamic loading models is revealed by plotting the loading computed with linear wave kinematics and FNV loading model (Eq. 4.6), marked as black star. On the contrary, the most nonlinear kinematics simulated with fully nonlinear BEM model (refer to Section 3.3) with the linear (Morison) loading model (dark red circle) represents the influence of nonlinearities in wave kinematics,

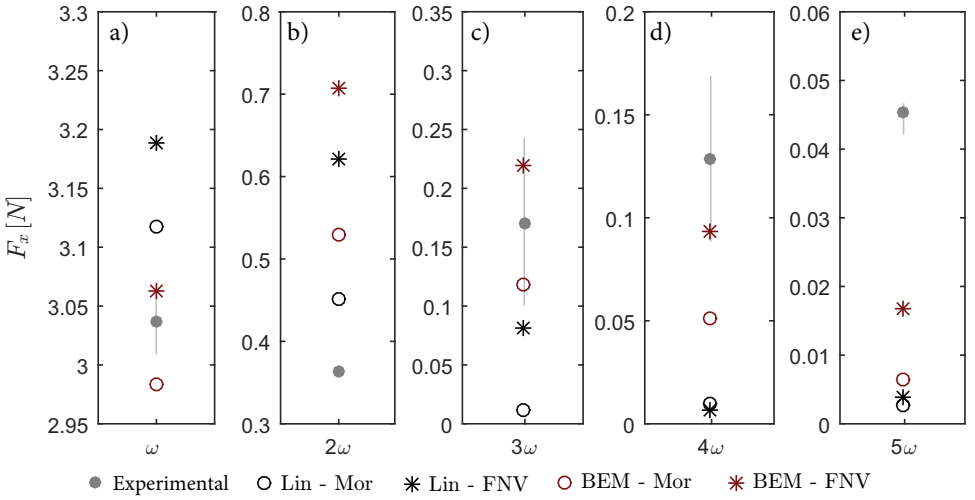

Figure 5.4: First five harmonics (ω-5ω) of the FFT analysis of the mean superimposed horizontal force F_x measurements (Grue and Huseby, 2002) and the computed loading with linear and BEM kinematics with Morison and FNV loading models. Error bars correspond to the standard deviation of the superimposed loading.

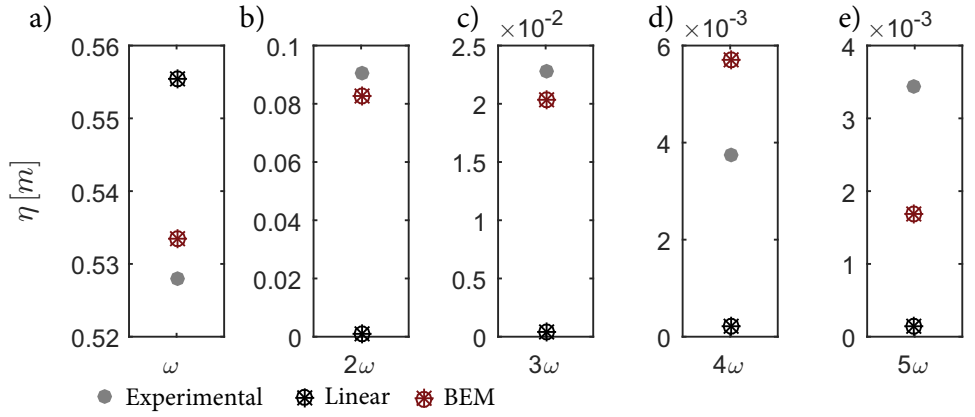

Figure 5.5: First five harmonics (ω-5ω) of the FFT analysis of experimental wave elevation η (Grue and Huseby, 2002) and the computed wave elevation with linear and BEM kinematics.

and the fully nonlinear wave kinematics with FNV theory (dark red star) lead to combined nonlinearities.

The first evident finding is that the nonlinearities in wave kinematics (compare dark red circle to black circle) reduce the first harmonic (Fig. 5.4a), but increases all the higher harmonics (Fig. 5.4b-e). Such behavior corresponds with the influence of nonlinearities in wave kinematics on wave elevation η, shown in Figure 5.5. It can be seen that linear wave kinematics (black markers) result in very high first harmonic (Fig. 5.5a), while all the higher harmonics are negligible (Fig. 5.5b-e). On the other hand, the fully nonlinear wave kinematics (dark red markers) redistribute the energy by reducing the first harmonic (Fig. 5.5a) but increasing the higher harmonics (Fig. 5.5b-e), and therefore following the behaviour of the experimental (grey markers) wave elevation significantly closer. This behaviour of the kinematics translates in the forcing as well (Figure 5.4).

The influence of the nonlinearities in the hydrodynamic loading model on the final loading (Figure 5.4) is represented by the FNV theory with linear wave kinematics as input (black star). Comparing it with the most linear case (black circle) it can be seen that the nonlinearities in the hydrodynamic loading model increase all harmonics. In particular the second harmonic (Figure 5.4b) is a significant increased by the nonlinearities in the hydrodynamic loading model. However, this strong increase is enlarging the overprediction of the experimental loading. It might be explained by the fact that the finite-depth FNV theory does not consider the second order scattering and has been seen to overpredict loading in cases where kR (k – wave number, R – cylinder radius) value is above 0.12 (Kristiansen and Faltinsen, 2017), while this case has $kR = 0.17$.

Nonetheless, in the higher harmonics (Fig. 5.4c-e) the importance of wave kinematics overtakes the importance of hydrodynamic loading model by predicting higher loading (compare red circle to black star). In the fourth and fifth harmonics (Fig. 5.4d-e) it is expected – since FNV is a third-order theory, it should have no contribution in the harmonics above. In fact, it can be seen that with linear wave kinematics as input (black star), the FNV model does not predict higher loading than linear Morison inertia (black circle). Nonetheless, the effect of combined nonlinearities is evident (dark red star): even in the highest harmonics (Fig. 5.4d-e) the FNV hydrodynamic loading model shows an increase from the fully nonlinear kinematics with Morison equation (dark red circle). These nonlinearities in the FNV hydrodynamic loading model are stemming purely from the incident wave potential. The effect of combined nonlinearities (dark red star) therefore causes the largest increase in all the higher harmonics (Fig. 5.4b-e).

5.5 Suitability of the surface distortion term

The rest of the hydrodynamic loading models and their suitability in predicting the two Grue and Huseby (2002) cases, reported in time domain in Figure 5.3, are shown in Figure 5.6.

As seen from Figure 5.6, the second harmonic (2ω) is captured most poorly with a very strong overprediction. Rather surprisingly the third harmonic is captured very well in both cases. The closest match is by MAI loading model (diamonds) regardless of the kinematics

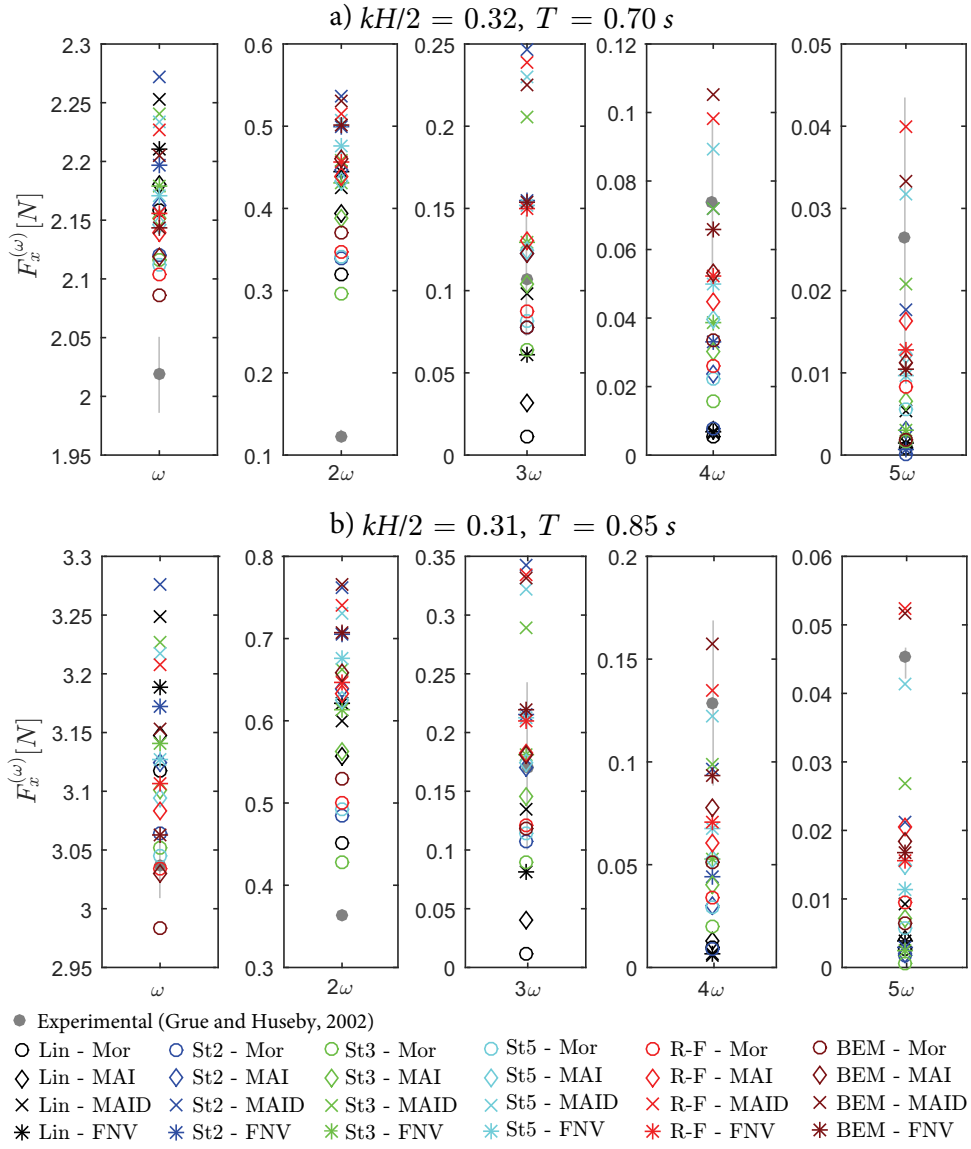

Figure 5.6: First five harmonics (ω-5ω) of the computed wave loading models compared with the FFT of the mean superimposed horizontal force F_x measurements for two cases reported in Grue and Huseby (2002). The experimental error bars are the higher and lower bands of the standard deviation from the superimposition (see Section 5.2).

as long as they were nonlinear, while linear MAI (black diamond) underpredicted significantly. Nonetheless, the large experimental error bar encloses most of the models. The only exceptions on both extremes are: models with linear wave kinematics (black markers) which underestimate the third harmonic significantly; and MAID hydrodynamic loading model

which regardless of the kinematics used above linear (all crosses except black) overestimates the third harmonic by nearly double. Such strong overprediction, as well as such great difference from the other nonlinear hydrodynamic loading models, raises the question of the suitability of the surface distortion term D, especially in combination with nonlinear wave kinematics.

As already discussed in Section 4.1.2, the surface distortion term D (Eq. 4.5) is based on the Stokes small amplitude assumption and therefore its suitability has been repeatedly doubted. As noted by Swan et al. (2002), Rainey (1995) where the surface distortion term D was introduced suggested that the surface distortion term D is likely to be more suited for the third-order load prediction in small waves rather than exciting ringing response. Additionally, as discussed in the methodology, Section 4.1.3, a critical difference between the D term in Rainey theory and F^{ψ} term (Eq. 4.8) is that the surface distortion term is applied at the instantaneous free surface rather than mean water surface as in the case with F^{ψ}, leading to very large arm for the bending moment at steepest waves. In fact as already seen in the preliminary stages of this research (Mockute et al., 2017b), the D term was causing a strong deviation in the comparison with Chaplin et al. (1997) at steepness of $kA = 0.299$, therefore the findings of this study too support the claim that the surface distortion term D have reached its limit at steepness $kA \approx 0.3$.

In particular, the interaction of the MAID hydrodynamic loading model with nonlinear wave kinematics should be discussed. In fact, with sufficiently nonlinear kinematics the MAID models (cyan, red and dark red crosses) are the only loading combinations that even remotely capture the highest – fourth and fifth – harmonics ($4\omega - 5\omega$), as seen in Figure 5.6. Even though both MAID (Eq. 4.5) and FNV (Eq. 4.6) are considered third-order hydrodynamic loading models, FNV, marked by star symbols, is a perturbation theory truncated at third order, therefore the scattering potential is only correct to third order and the nonlinearities above the third order are stemming only from the incoming wave potential (Kristiansen and Faltinsen, 2017). In contrary, the D term brings MAID third order, but the theory is not limited to third order, as clearly seen from the fourth and fifth harmonics in Figure 5.6. However, the strong overprediction of the third harmonic highlights that the strong increase in loading predictions from the D term is likely to have detrimental effects in steeper waves, especially when in conjunction with the effect of nonlinearities in wave kinematics to increase all the higher harmonics as seen in Section 5.4.

5.6 Non-monotonic experimental increase with increasing wave steepness

Figure 5.7 shows the first three harmonics of horizontal loading modelled with the discussed wave loading models over increasing steepness H_1/λ, where H_1 is the linear wave height, λ is the wavelength, and it relates to the steepness kA by the magnitude of π ($k = 2\pi/\lambda$, $A = H/2$). A representative case of Kristiansen and Faltinsen (2017) is shown ignoring experimental values since the behaviour of the numerical models is similar across the different wave periods and water depths. The wave loading is normalised by the steepness H_1/λ to the power of the harmonic in order to observe the behaviour of the loading models and the relation between them over increasing steepness better. It should be noted that the y-axis

in Fig. 5.7a for the first harmonic ω spans over a small range of values. It can then be seen that the progression of all the normalised wave loading models over increasing steepness is nearly constant. Such behaviour denotes that the numerical loading models are in direct proportionality with the increasing steepness: they increase linearly with steepness in the first harmonic ω (Fig. 5.7a), quadratically in the second harmonic 2ω (Fig. 5.7b), and cubically in the third harmonic 3ω (Fig. 5.7c). Nonetheless, as was denoted by Kristiansen and Faltinsen (2017), the behaviour of the experimental results does not follow the same trend of monotonic increase with increasing steepness.

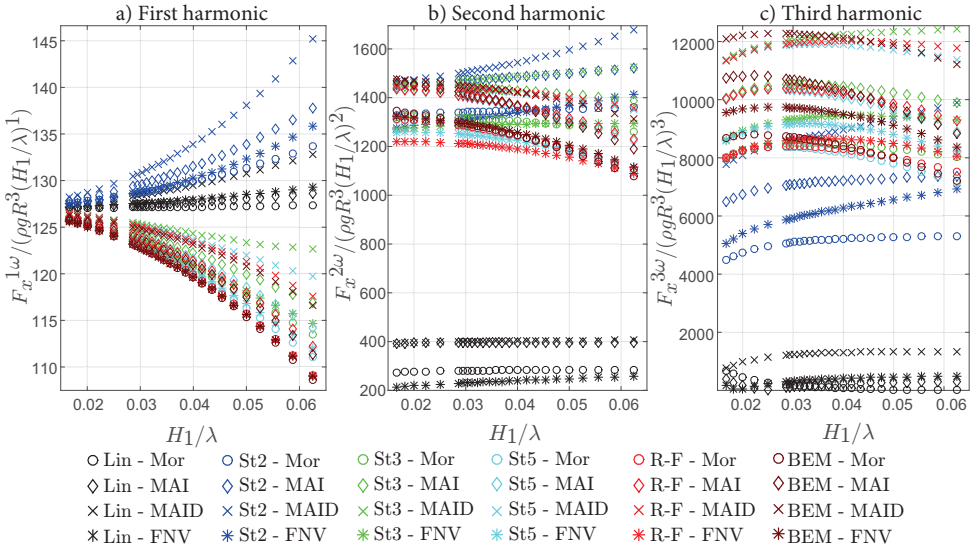

Figure 5.7: The first three harmonics (from left to right) of the normalised horizontal force over the increasing wave steepness H_1/λ. The wave and cylinder settings correspond to the experimental cases by Kristiansen and Faltinsen (2017) with $T = 2.021\ s$ in depth $h = 0.564\ m$.

Figure 5.8 shows the FFT analysis of the first three harmonics (from top to bottom) of the normalised horizontal force ($F_x/(\rho g R^3)$) over increasing steepness H_1/λ for three periods of $T = 1.443\ s$ (left), $T = 1.732\ s$ (middle) and $T = 2.021\ s$ (right), in depth $h = 0.397\ m$. Same was conducted for the depth $h = 0.564\ m$, but since similar behaviour was observed it was omitted from the thesis for brevity. The y-axis is fixed for each harmonic for the ease of comparison. For the steepest four cases with wave period $T = 2.021\ s$, wave breaking was reported (Figure 5.8c,f,i). They nearly coincide with the theoretical upper limit of Stokes fifth order theory, defined as Ursell number $Ur = 40$ ($Ur = H_1\lambda^2/h^3$) and indicated by the vertical dotted line in Figure 5.8.

Except for the breaking wave cases, the first harmonic is captured well by all kinematics and loading models. Nonetheless, the experimental values at the higher steepnesses are better captured by the nonlinear wave kinematics regardless of the hydrodynamic loading model, while the linear and second order kinematics tend towards overestimation. However, the second harmonic already shows an extremely non-monotonic behaviour. The cases

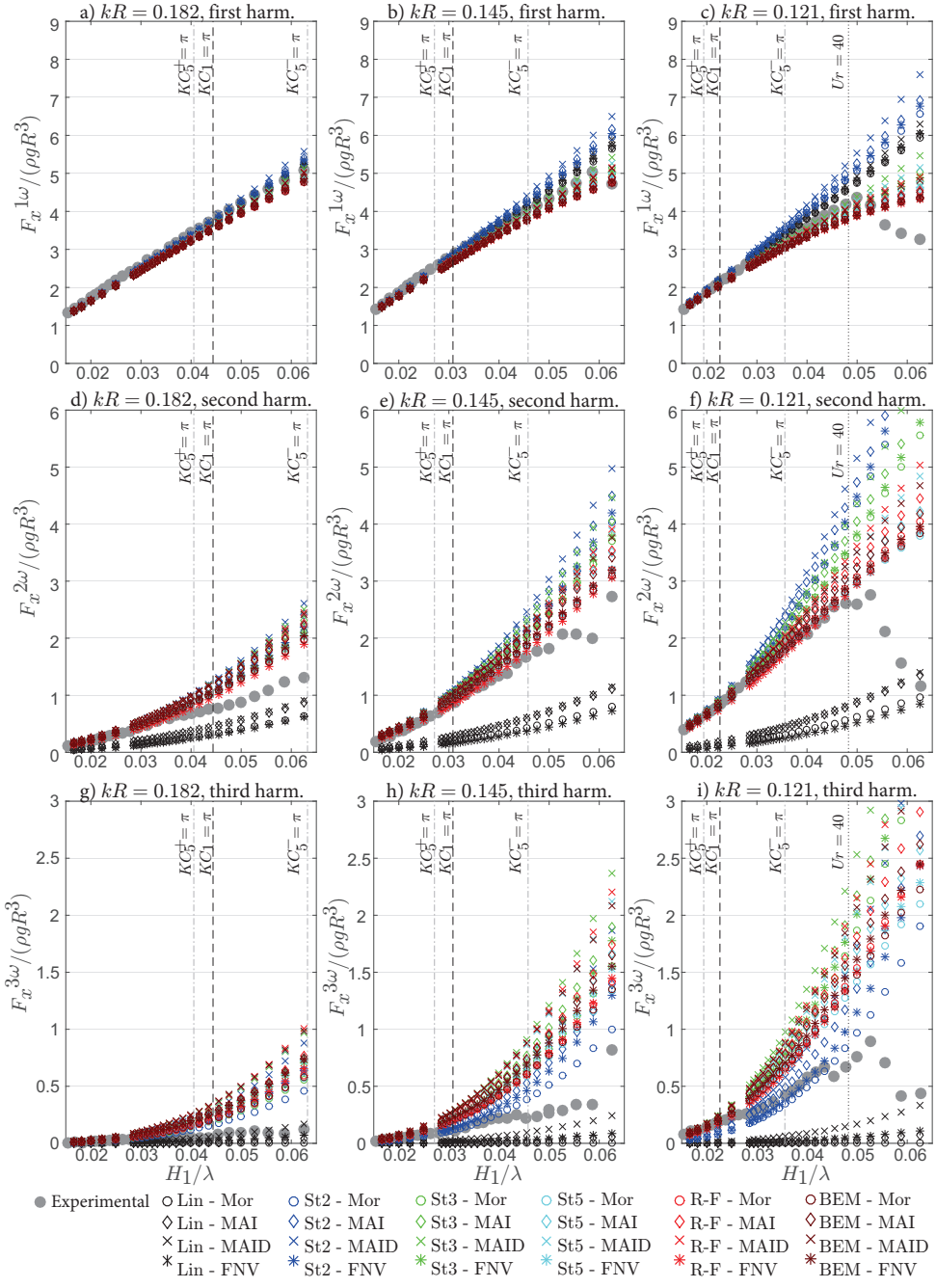

Figure 5.8: The first three harmonics (from top to bottom) of the nondimensionalised horizontal force $F_x/(\rho g R^3)$ over the increasing wave steepness H_1/λ for $T = 1.443\ s$ (left column), $T = 1.732\ s$ (middle column) and $T = 2.021\ s$ (right column) for water depth $h = 0.397\ m$, compared with experiments (grey dots, Kristiansen and Faltinsen (2017)).

of breaking waves aside, after a certain wave steepness the experimental loading hardly grows with the increasing steepness. Some of the cases are showing such small increment in the loading over increasing steepness, that the monotonically increasing linear wave kinematics with nonlinear loading models, e.g. MAID (black cross) or MAI (black diamond) are becoming the closest predicting models. In the third harmonic such effect is amplified even more, especially in the cases with the largest kR number, where even the linear kinematics with the MAID model (black cross) are overestimating the loading (see Figure 5.8g). In Kristiansen and Faltinsen (2017) the discrepancies are explained by flow separation, although the addition of drag and reduction of mass coefficient corresponding to the local KC numbers did not offer a correcting solution to the FNV theory regardless of whether third or fifth-order wave theory was used. The main contribution of this thesis on this discussion is that all of the considered wave theories and loading models are also increasing monotonically with wave steepness and therefore overpredicting the higher harmonics because of the non-monotonic growth of the experimental results with increasing steepness.

To better understand the limiting wave steepness at which the agreement between the loading models and the experimental values ceases, vertical lines representing $KC = \pi$ were added to Figure 5.8. The sub- and superscripts represent which maximum horizontal velocity was used for its calculation: linear (KC_1), fifth order taken at the crest of the wave (KC_5^+), or fifth-order taken at the trough of the wave (KC_5^-). In fact the change in behaviour falls within that range, although the exact KC number depends on the specific case. The general trend is that the change in the experimental behaviour starts earlier for lower kR numbers. This again is represented well in the wave limits graph (Figure 5.2) – lower kR numbers indicate shallower waters and proximity to the wave breaking limit, where even the lower wave steepness makes the wave loading models become inappropriate. The worrying finding is, however, that since more nonlinear wave theories are suggested in such wave conditions by the IEC 61400-3 design requirements for offshore wind turbines (International Electrotechnical Commission, 2009), and, as discussed in Section 5.4, the nonlinearities in wave kinematics increase the higher harmonics, the overprediction would be increased even more.

As discussed in Kristiansen and Faltinsen (2017), such discrepancy between the numerical and experimental loading, increasing monotonically with increasing steepness, was also observed in deep water in third harmonic by Huseby and Grue (2000). The deep-water cases in this study by Stansberg (1997) are shown in Figure 5.9. The comparison is conducted with the experimental results from Stansberg (1997) for the wave period $T = 2.10\ s$ over the increasing wave steepness for both radii ($R = 0.1\ m$ and $R = 0.1635\ m$), normalised by the cylinder radius squared and the linear amplitude A to the power of the harmonic. The first three harmonics are shown from left to right, and the y-axis is fixed to the same value across the harmonics.

The first harmonic (Figure 5.9a) is captured well in all steepnesses for both cylinders, therefore a zoom is provided. Only the highest steepness starts to get overestimated by the MAID model (crosses) and underestimated by Morison equation (circles). The second harmonic (Figure 5.9b) displays a distinct non-monotonic behaviour, but also strongly differs for the different cylinder radius even at the lowest steepness with nonlinear loading models fitting

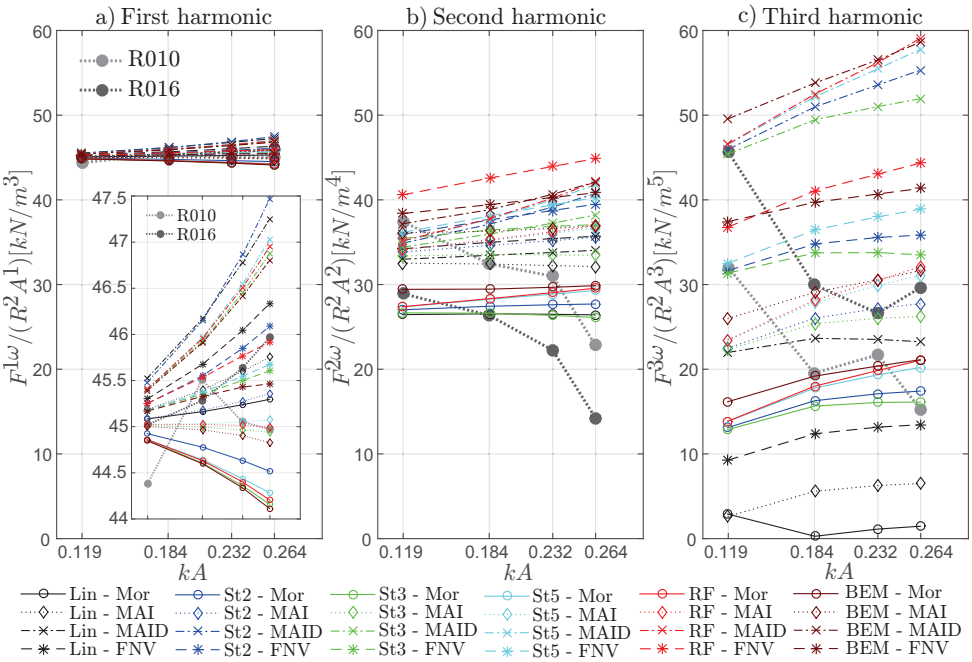

Figure 5.9: First three harmonics (from left to right) of the normalised horizontal force over increasing steepness kA with period $T = 2.10\ s$. Comparison between the experimental results from Stansberg (1997) and numerical loading models. The y-axis is fixed to the same values for easier comparison, therefore a zoom of the first harmonic is provided in panel a.

the smaller radius (light grey dot) better, and Morison equation (circles) fitting best for the larger radius (dark grey dot). As the steepness increases the second harmonic starts to get strongly overestimated by all models, a behaviour already seen in the comparison with Grue and Huseby (2002) in Figure 5.6 with an even higher steepness ($kA \approx 0.31 - 0.32$), hence even closer to the wave breaking limit. It is worth noting that in contrary to Kristiansen and Faltinsen (2017) linear wave kinematics are still suitable in capturing the second harmonic, potentially due to the larger distance from the wave breaking limit despite the larger steepness due to deeper water depth (refer to Figure 5.2). Third harmonic (Figure 5.9c) is surprisingly well captured, in contrary to the intermediate depth cases (Figure 5.8g-i). Nonetheless, the non-monotonic behaviour is seen here as well. Therefore as the steepness increases the loading is captured better by wave loading models of lower order. On the contrary to the second harmonic, in the third harmonic the larger cylinder shows higher loading than the smaller cylinder, therefore more nonlinear loading models are suiting it better, decreasing in nonlinearity as the steepness increases.

A notable difference of these deep-water cases from the cases in intermediate water depth by Kristiansen and Faltinsen (2017) (Figures 5.7-5.8) is that the hydrodynamic loading models have a much stronger influence than wave kinematics, especially in the first harmonic. For example, in deep water (Figure 5.9a) regardless of which order of wave kinematics were

used, the final loading is similar for all wave kinematics with the same hydrodynamic loading model, while in intermediate water depth (Figure 5.7a) the models are grouped by the kinematics. This could be explained by looking at the graph of wave theory limits in Figure 5.2, where the cases from Figure 5.7 refer to the dark blue crosses while the cases shown in Figure 5.9 refer to the green circles. It can be seen that the Stansberg (1997) cases are in deeper water while the Kristiansen and Faltinsen (2017) cases are in intermediate water depth and therefore, regardless of the lower steepness, are closer to the wave breaking limit, crossing over to the range where more nonlinear wave kinematics are recommended, namely the 5^{th} and 7^{th} order stream functions. It could be deducted that wave kinematics have stronger influence in shallower water while hydrodynamic loading models – in deeper. This explains the different focus of offshore industries: oil and gas field, mostly in deep water, investigating the hydrodynamic loading models with linear wave kinematics (e.g. Grue et al., 1993; Stansberg, 1997; Grue and Huseby, 2002); and offshore wind, with monopiles in shallow to intermediate water depth, focusing on fully nonlinear wave kinematics regardless of hydrodynamic loading model (e.g. Marino et al., 2013b; Marino et al., 2014b; Schløer et al., 2016; Marino et al., 2017).

5.7 Influence of kR number

The nondimensional wave number kR is an important factor for slender body modelling, since it determines the slenderness ratio. The slender body hydrodynamic loading models have limitations relating to this term: FNV (Eq. 4.6) is a long-wave theory, therefore one of its fundamental requirements for validity is $kR << 1$, while the Rainey theory terms A (Eq. 4.3) and I (Eq. 4.4) are both derived expanding around the kR term, requiring it to tend towards zero as well. Thus, comparing the numerical loading models over a range of kR numbers is expected to give an insight into the limitations of the hydrodynamic loading models and their behaviour in the off-design values.

Figure 5.10 shows all models compared with experimental data from Stansberg (1997) with two different wave periods $T = 2.10\ s$ and $T = 1.52\ s$ on two cylinders of radii $R = 0.1\ m$ and $R = 0.1635\ m$. Normalisation of the Figure 5.10 follows the original paper (Stansberg, 1997), using the radius squared and the linear amplitude to the power of the harmonic. Since all considered hydrodynamic loading models are inertia-based, they are proportional to the cylinder radius squared. Therefore with the normalisation by R^2, as done in Figure 5.10, the numerical results for both cylinders in the same wave conditions are identical. The multiplication by the R^2 term would only increase the absolute values but not the distribution among the models. The same reasoning is applied for plotting Figure 5.10 over wave number k rather than kR. Meanwhile, Figure 5.11 considers intermediate water depth, showing the behaviour of all models compared with the experimental data over the increasing nondimensional wave number kR for two wave steepnesses – $H_1/\lambda = 1/40$ (left column) and $H_1/\lambda = 1/25$ (right column). Water depth is $h = 0.397\ m$ and the first three harmonics are shown in panels from top to bottom.

The main observation is that the importance of nonlinearities in the wave loading models increases as the kR number decreases, i.e. the differences between the loading models be-

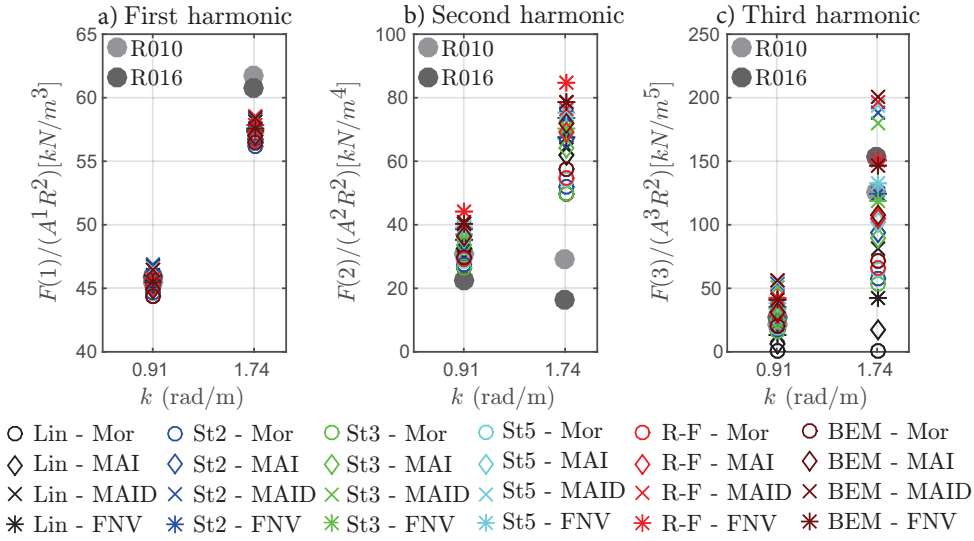

Figure 5.10: First three harmonics (from left to right) of the normalised horizontal force over the increasing wave number k for the two cylinders with steepness $kA \approx 0.232$, compared with experiments from Stansberg (1997) (grey dots – lighter grey with smaller radius $R = 0.1\ m$, darker grey with larger radius $R = 0.1635\ m$).

come more significant, whereas at larger kR numbers there is no notable difference between the different wave kinematics or hydrodynamic loading models. As it was seen from the reference to wave theory limits (Figure 5.2), the experiments of Kristiansen and Faltinsen (2017) are in intermediate water depth, therefore even at smaller wave heights than Stansberg (1997) much more nonlinear wave kinematics are required. This holds especially true with increasing wave period T, which leads to decreasing kR. In the cases of smallest kR and largest kA the wave breaking limit is approached, and even 9^{th} order steam function is recommended by the IEC design standard for offshore wind turbines (International Electrotechnical Commission, 2009). The importance of wave nonlinearities in intermediate water depth is clearly seen when comparing how quickly and strongly the linear theory differentiates itself in Kristiansen and Faltinsen experiments (Fig. 5.11), while in Stansberg experiments in deep water (Fig. 5.10) linear theory is performing rather well up to the third harmonic despite much higher wave steepness kA. Similar effect is seen with second order wave theory as well.

As seen in Figure 5.11, the experimental wave loading from Kristiansen and Faltinsen (2017) increases with decreasing kR but stops growing monotonically from $kR < 0.15$ or so, from where the trend is best captured by nonlinear wave kinematics. The only exception is the third harmonic (Fig. 5.11e-f) where while in the lower steepness ($H_1/\lambda = 1/40$, Fig. 5.11e) the higher order wave kinematics are still predicting well, in the higher wave steepness ($H_1/\lambda = 1/25$, Fig. 5.11f) the nonlinear wave kinematics tend towards overprediction whereas the second order wave kinematics match the loading well. The lowest kR numbers, especially at lower wave steepness, may coincide with re-entering the diffraction regime from inertia (refer to Figure 5.1). It should also be noted that even though in the higher kR num-

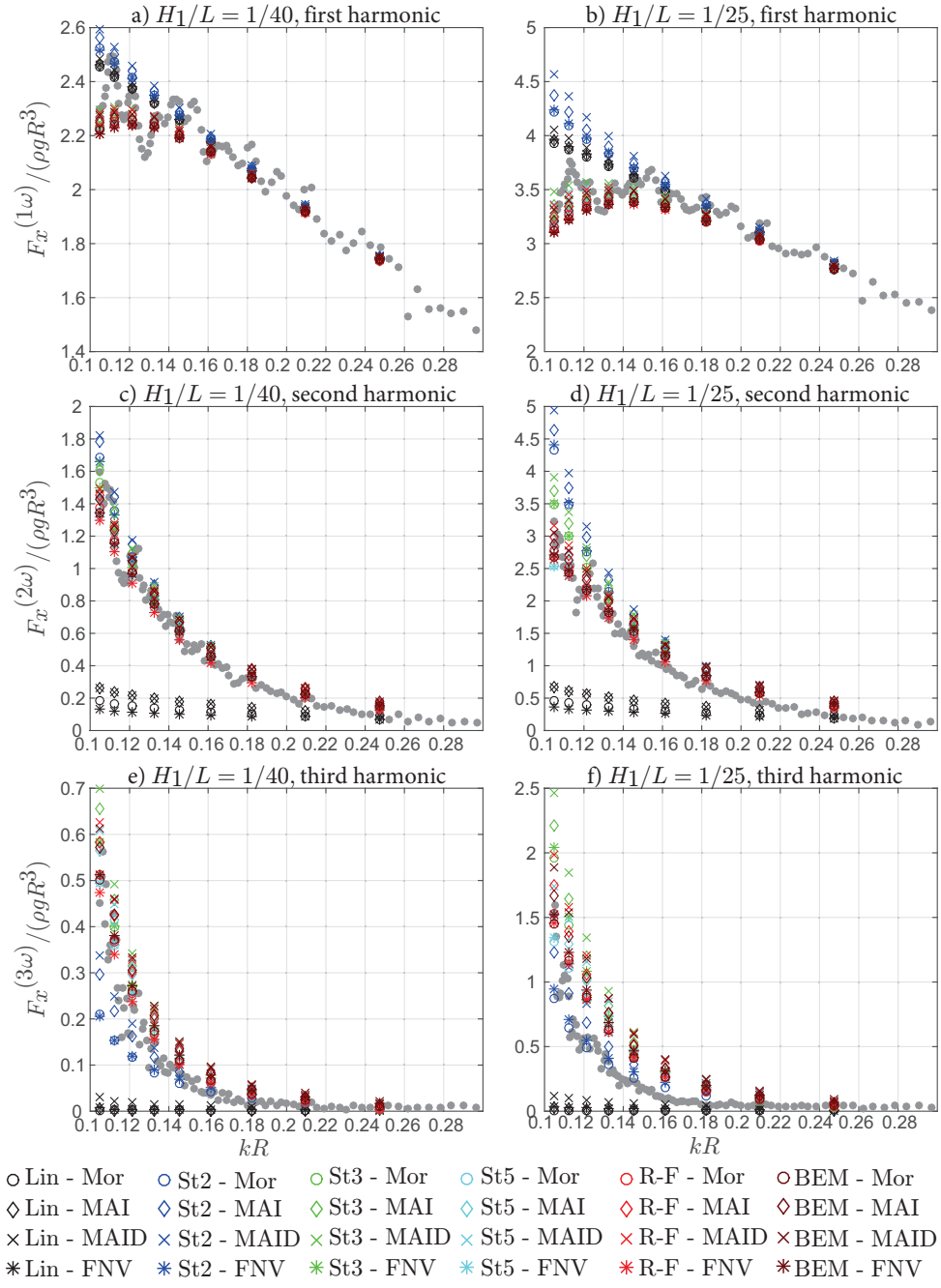

Figure 5.11: First three harmonics (from top to bottom) of the normalised horizontal force over the increasing wave number kR for two steepnesses of $H_1/\lambda = 1/40$ (left column) and $H_1/\lambda = 1/25$ (right column) for the depth $h = 0.397$ m, compared with experiments from Kristiansen and Faltinsen (2017) (grey dots).

bers the difference between various loading models is reduced, all models are increasingly overpredicting the experimental loading in the second harmonic (Fig. 5.11c-d) as the kR number increases.

There are two main additions to the findings of Stansberg (1997), who compared the experimental results with linear infinite-depth FNV. Firstly, even though in the third harmonic for the larger k number the infinite-depth FNV with linear wave kinematics was overestimating (Stansberg, 1997), it was found that with nonlinear wave kinematics finite-depth FNV captures the loading much better than the other models (Figure 5.10c). Secondly, despite the doubts on its suitability, Morison equation was found to capture the second harmonic (Figure 5.10b) for the lower k number best. Otherwise, the other models with a range of kinematics show very similar results – underpredicting the loading for the higher k number in the first harmonic (Figure 5.10a) and strongly overpredicting the same in the second harmonic (Figure 5.10b). This strong overprediction of the second harmonic in Stansberg (1997) cases bridges the gap between the findings in the other experiments in Fig. 5.1. In the comparison with Kristiansen and Faltinsen (2017) it was seen that as both steepness and kR increased the overestimation of the second harmonic increased as well. In Stansberg (1997) the second harmonic is overpredicted significantly more as the kR number increases. And finally on the highest end of both the kR number and wave steepness kA in comparison with the Grue and Huseby (2002) the second harmonic was overestimated the most (see Figure 5.6). A discussion on the overestimation of the second harmonic is further given in Section 5.8.2.

5.8 Best performing wave loading models for specific wave and cylinder conditions

The three previously discussed experimental campaigns (Kristiansen and Faltinsen (2017), Grue and Huseby (2002) and Stansberg (1997)) fill a large part of the (kA, kR)-graph (Fig. 5.1) and a range of wave conditions (Fig. 5.2). Therefore some general trends for the best-fitting numerical wave loading models for certain wave and cylinder conditions can be investigated.

For each of the first three harmonics (Sections 5.8.1-5.8.3) three best-fitting numerical wave loading models are discussed in reference to both the (kA, kR)-graph (Figures 5.12-5.20a) and to the wave theory limits on $(h/gT^2, H/gT^2)$-graphs (Figures 5.12-5.20b). Relative error $err_{num/exp}$ between the modelled and experimental loading is calculated by Equation 5.1, which is then plotted as background intensity behind each marker, where darker background signifies larger error.

$$err_{num/exp} = \frac{\mid F_{num} - F_{exp} \mid}{F_{exp}} * 100\%, \tag{5.1}$$

where F_{num} is the loading modelled with the numerical wave loading models introduced in Sections 3.1, 3.3.4, and 4.1, while F_{exp} is the experimentally measured loading from the experimental campaigns overviewed in Section 5.2.

In overview, the first harmonic (Section 5.8.1) is captured the best with maximum error (Eq. 5.1) for the three best-fitting models of 33%, while second harmonic (Section 5.8.2) is

captured the worst with the error bar scale of 250%. Third harmonic (Section 5.8.3) falls in-between with the worst error (Eq. 5.1) of 90%. The largest errors also fall in different regions for different harmonics, as discussed in Sections 5.8.1-5.8.3. Moreover, different trends are observed in different parts of the graphs, therefore an inner range $(kA, kR)<(0.2, 0.2)$ and outer range $(kA, kR)>(0.2, 0.2)$ are defined. In terms of the wave theory limits they corresponds to the intermediate depth (inner range) and the deep water cases (outer range).

It should be noted that in some cases similar wave conditions overlap on the wave theory $(h/gT^2, H/gT^2)$-graphs (Figures 5.12-5.20b). For this reason Stansberg (1997) cases with radius $R = 0.1635\ m$ were plotted slightly to the right of the cases with $R = 0.1\ m$ to observe the differences between the cylinder radius. Moreover, Kristiansen and Faltinsen (2017) case of $T = 1.443\ s, h = 0.396\ m$ overlaps the $T = 1.732\ s, h = 0.563\ m$ case, therefore the former was moved slightly to the right in order to see the difference in the suitability of the loading models for the same h/gT^2 value but different ratio between the water depth and the wave period.

5.8.1 First harmonic

The first harmonic, shown in Figures 5.12-5.14, is captured relatively well across all wave and cylinder conditions. The only exception are the three steepest wave cases of the shallowest water depth from Kristiansen and Faltinsen (2017) experimental campaign, where local wave breaking was reported by the authors. The breaking cases aside, the largest error falls to the cases of largest kA and kR, as could be expected, since in such conditions wave theories and hydrodynamic loading models tend to lose validity.

A clear trend for the best-fitting wave loading model of the first harmonic stands out at the diffraction regime (on the left side of the black dashed line which stands for $KC = \pi$) in Figures 5.12-5.14a, which coincides with the range of validity for the Stokes theories in Figures 5.12-5.14b. In these conditions second order wave kinematics (interchanged with linear) with more nonlinear hydrodynamic loading models (both versions of slender-body theory – diamonds and crosses) are performing best. It is counter-intuitive if only nonlinearities in wave kinematics would have been considered, since, as seen in Figure 5.12b, all of these experiments fall significantly above linear wave theory limits and in the range where Stokes 5^{th} order theory or a stream function of at least third order would be suggested. This finding emphasises the importance of considering the nonlinearities in the hydrodynamic loading model as well, since they may substitute the nonlinearities in the wave kinematics.

Meanwhile, in the inertia regime much more nonlinear kinematics (5^{th} order or higher) seem to be needed (Figures 5.12-5.13a), which is in accordance with the wave theory limits seen in Figures 5.12-5.14b. For example, as in Grue and Huseby (2002) cases, the recommended Stokes 5^{th} order wave theory with Morison equation (cyan circle) is capturing wave loading fine – it is the third best model to capture the first harmonic (Figure 5.14b). Nonetheless, more nonlinear wave kinematics (R-F and BEM) capture the first harmonic even better (Figures 5.12-5.13b). With regards to the hydrodynamic loading models, the full formulation of slender-body theory, including the widely discussed (see Section 5.5) surface distortion force D (crosses) dominates the first harmonic until $kA \approx 0.23$, from where MAI

(diamonds) and FNV (stars) are taking over until $kA \approx 0.3$, above which Morison (circles) with highly nonlinear wave kinematics fits the best.

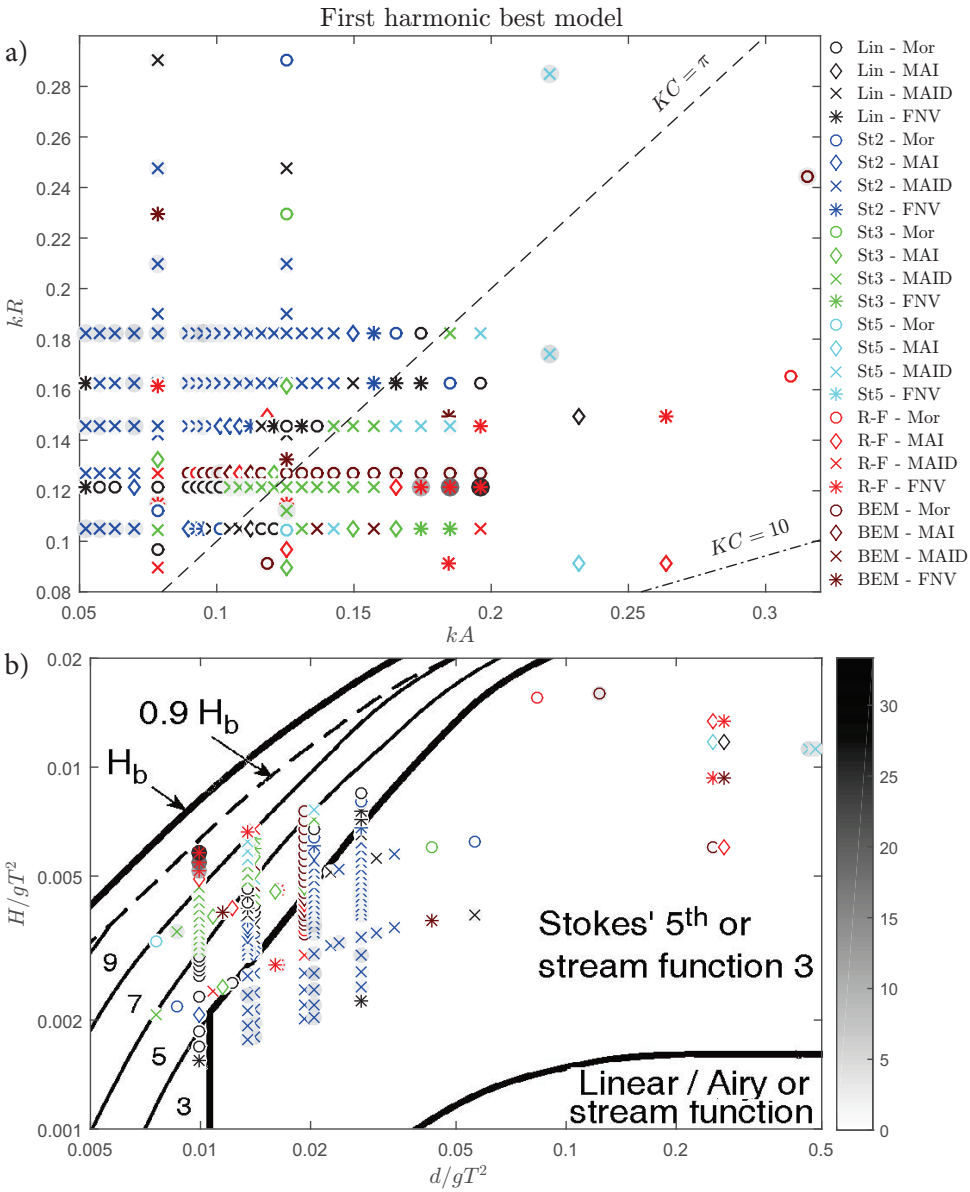

Figure 5.12: The best-fitting numerical models for first harmonic with its relative error: a) on (kA, kR)-grid and b) in reference to wave theory limits.

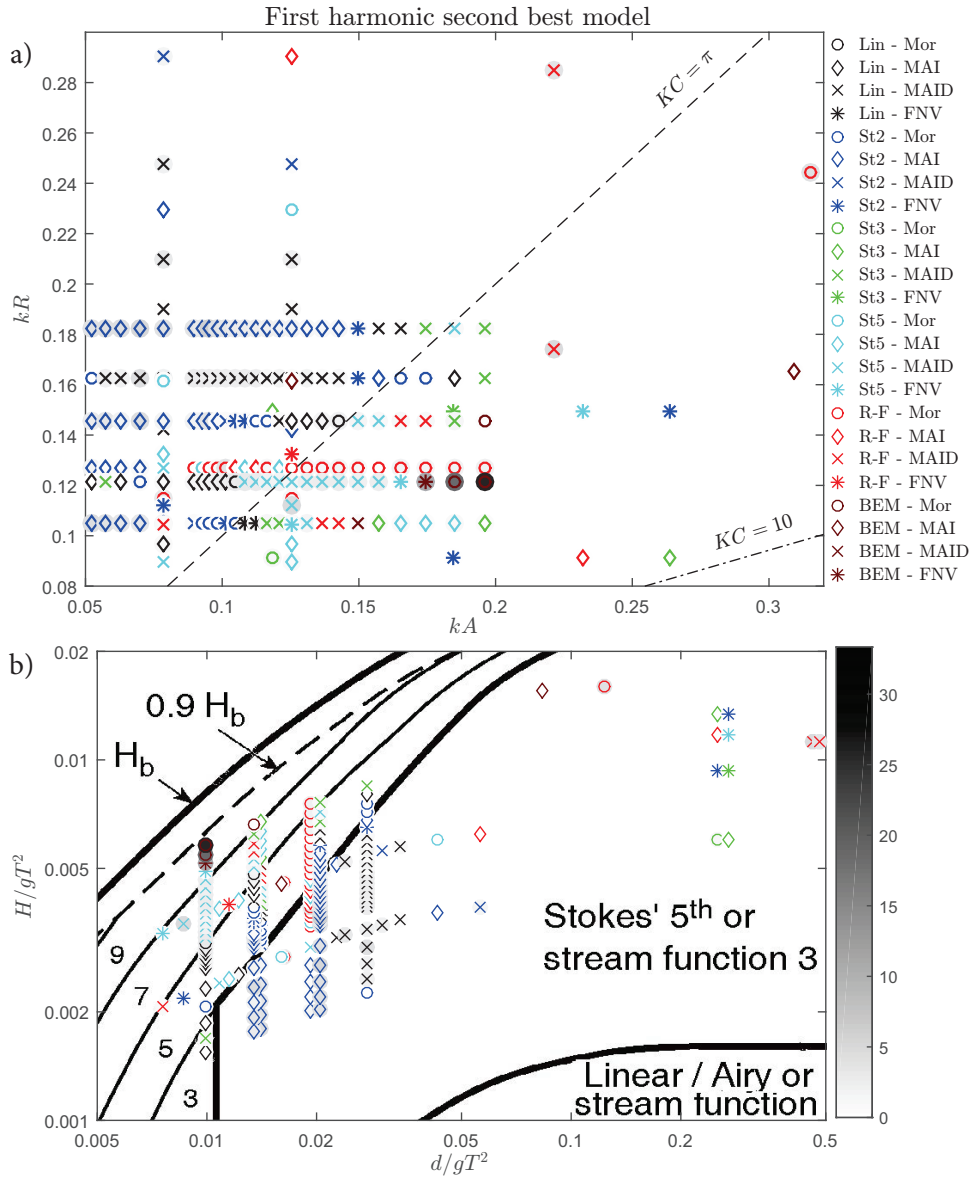

Figure 5.13: Second best-fitting numerical models for first harmonic with its relative error: a) on (kA, kR)-grid and b) in reference to wave theory limits.

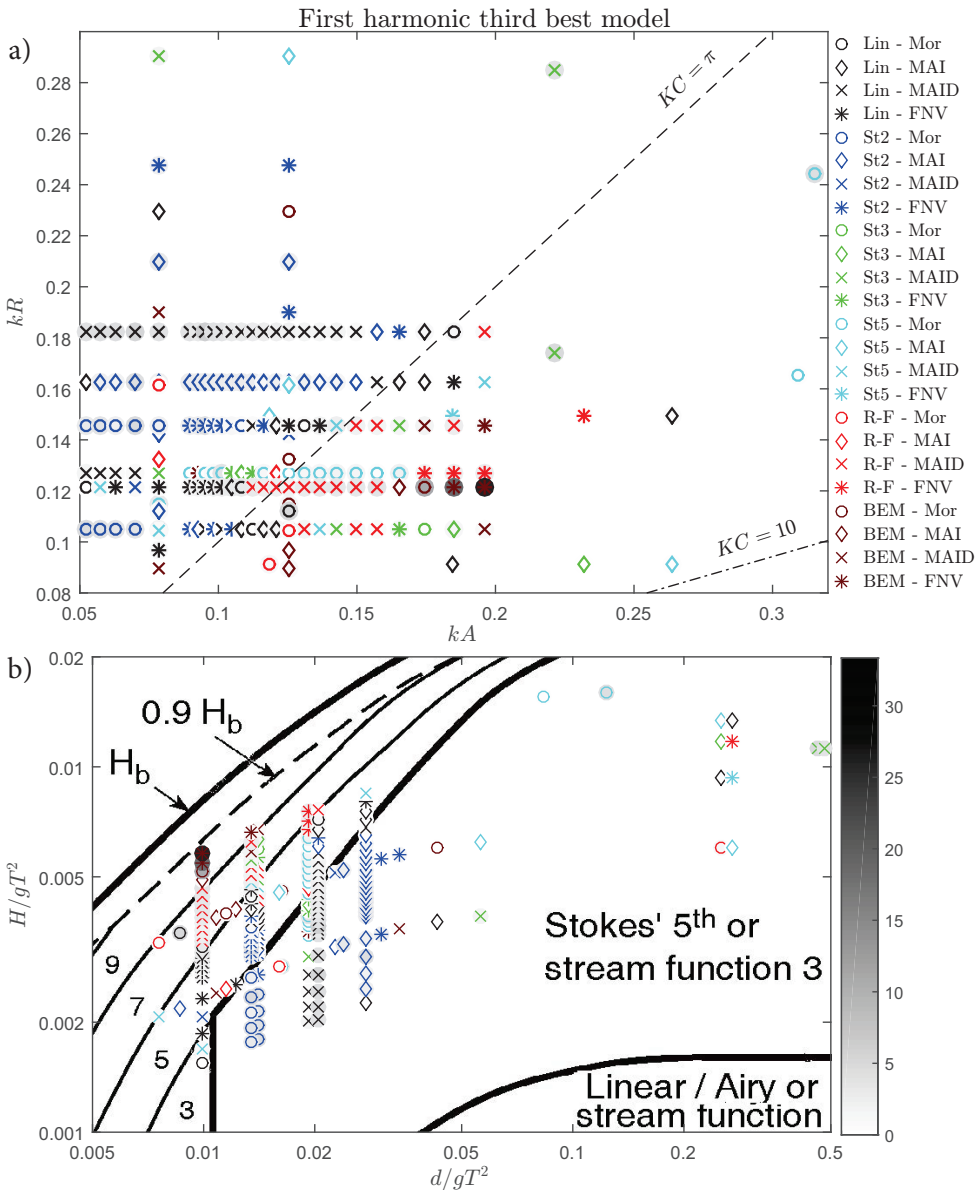

Figure 5.14: Third best-fitting numerical models for first harmonic with its relative error: a) on (kA, kR)-grid and b) in reference to wave theory limits.

5.8.2 Second harmonic

The trends for the error in the second harmonic are very clear – increasing error with increasing both kA and kR (Figure 5.15a). Regarding the best-fitting wave loading models, the inner range (up to (kA, kR)=(0.2, 0.2)) is dominated by nonlinear wave kinematics and more sophisticated loading models, especially FNV (star markers). Interestingly, the Rienecker-

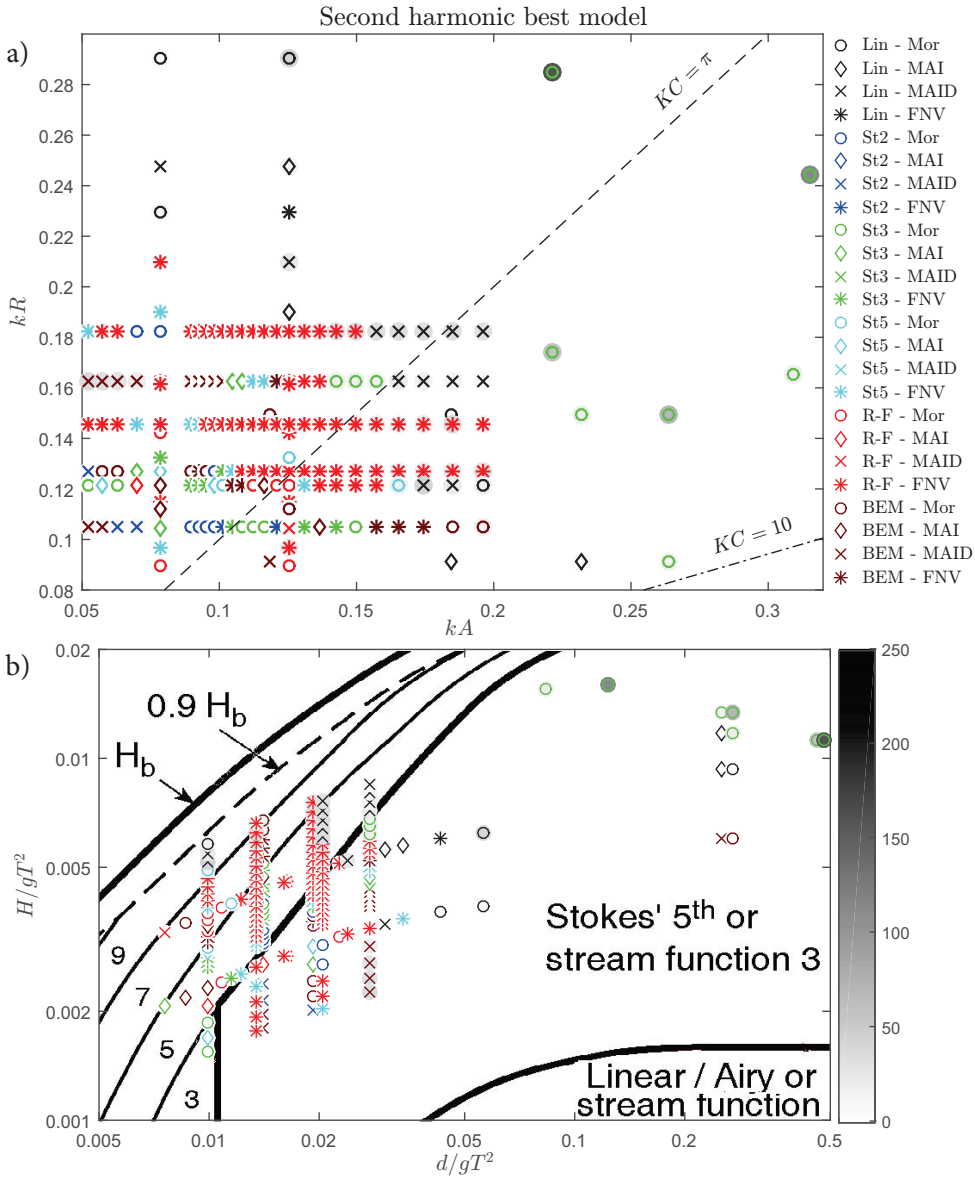

Figure 5.15: The best-fitting numerical models for second harmonic with its relative error: a) on (kA, kR)-grid and b) in reference to wave theory limits.

Fenton wave kinematics (red markers) is the best choice across all the different ranges of the wave theory limits, as seen in Figure 5.15b. It can be interchanged with Stokes 5^{th} order wave kinematics (cyan markers (Figure 5.16b), but the nonlinearities in the most sophisticated BEM solver (dark red markers) are not offering the right corrections.

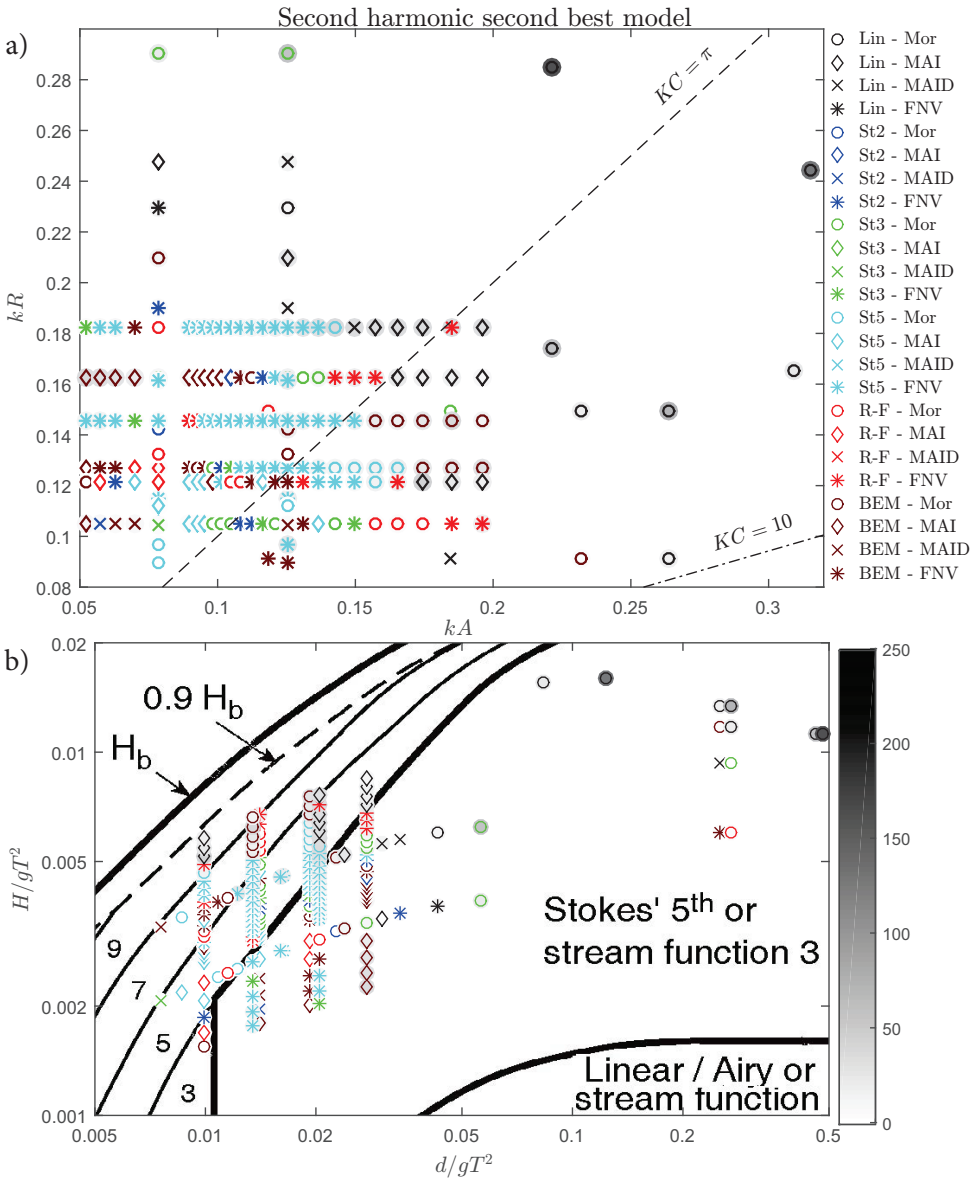

Figure 5.16: Second best-fitting numerical models for second harmonic with its relative error: a) on (kA, kR)-grid and b) in reference to wave theory limits.

At the higher kR values (shorter waves) the long-wave FNV theory (star markers) is not expected to perform better than other models since FNV theory does not consider the second order scattering (Kristiansen and Faltinsen, 2017). Kristiansen and Faltinsen (2017) have observed the FNV to overpredict from $kR > 0.12-0.15$, but it is apparent from Figures 5.15-

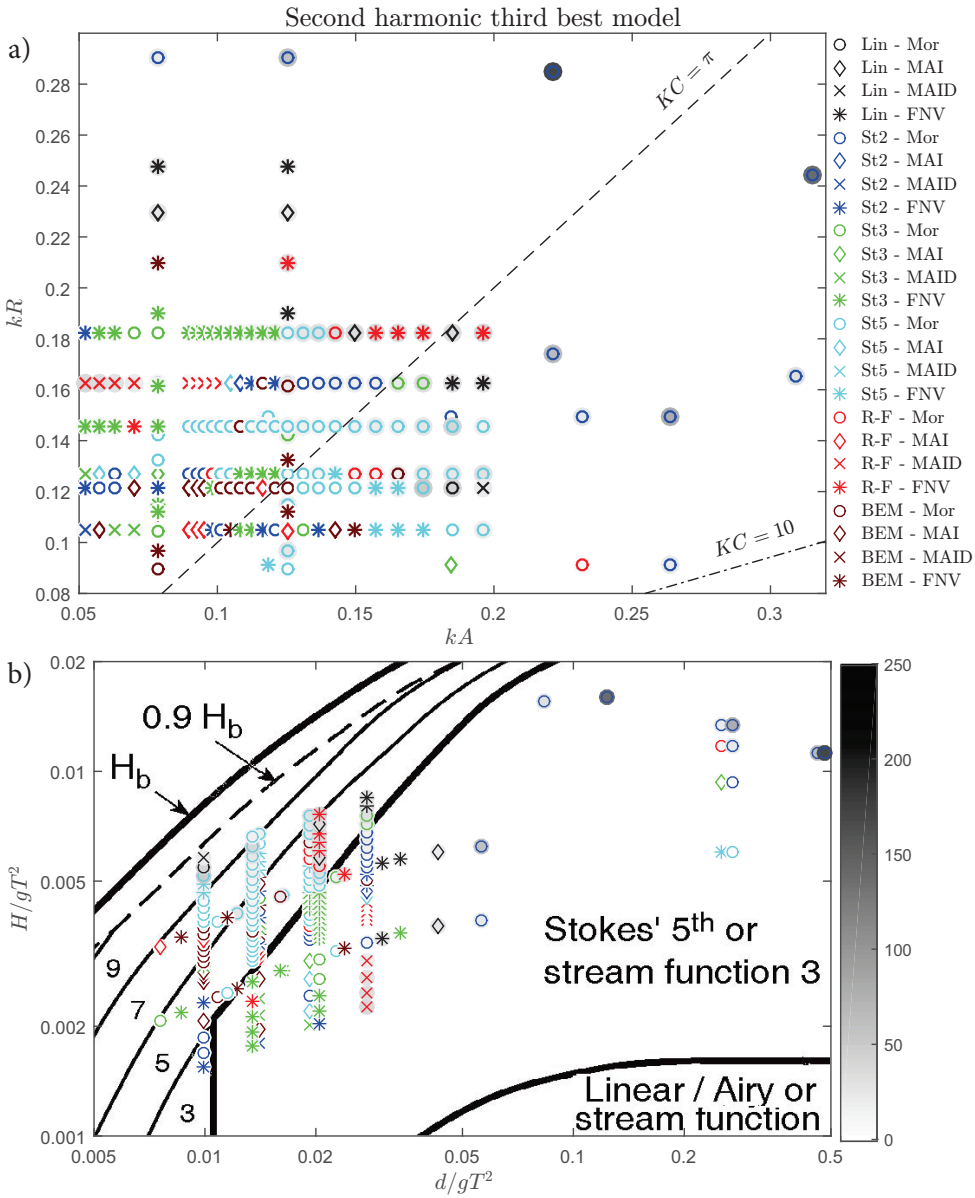

Figure 5.17: Third best-fitting numerical models for second harmonic with its relative error: a) on (kA, kR)-grid and b) in reference to wave theory limits.

5.17a that none of the other models are performing significantly better up to $kR \approx 0.2$ in the second harmonic.

The cases in the inner range up to $(kA, kR)=(0.2, 0.2)$, where linear wave kinematics (black markers) are the best-fitting model with large errors, are the same cases where the non-monotonic experimental behaviour was seen (refer to Section 5.6, Figure 5.8). The non-monotonic increase of experimental loading with increasing wave steepness carries on as both the kA and kR increase to the outer range (Figure 5.15a). It was confirmed in Section 5.4 that the second harmonic is increased by the nonlinearities in both wave kinematics and hydrodynamic loading models, therefore all models have highly overestimated the loading, leaving Morison equation (circles) with wave kinematics up to third order dominating, despite the increasingly high errors. The finding that in deep water settings the influence of the hydrodynamic loading model has been observed to be stronger than the influence of wave kinematics (refer to Section 5.6) explains why Morison equation – the most linear hydrodynamic loading model – with a range of most linear wave kinematics is the closest match rather than linear wave kinematics with a range of hydrodynamic loading models.

5.8.3 Third harmonic

In the third harmonic, surprisingly, the outer range with the highest kA and kR values is predicted relatively well. The worst-captured cases are within the inner range in Figure 5.18a, or in the intermediate water in Figure 5.18b. This can be associated with the previously observed non-monotonic behaviour – more cases do not grow as the wave steepness grows and therefore are best captured by the linear wave kinematics (black markers).

The danger of this non-monotonic behaviour can be seen clearly whilst comparing with the wave theory limits (Figures 5.18-5.20b), because these are the conditions when the wave breaking limit is being approached. Therefore the wave kinematics recommended by the IEC 61400-3 design standard (International Electrotechnical Commission, 2009) are even higher, and, as found in Section 5.4, increase the predicted loading leading to an even stronger overestimation. If this effect could be taken into account, the strong overestimation, as well as the overestimation in the second harmonic, could potentially be avoided. It is interesting to note that the third harmonic is affected much stronger in the intermediate water depth than in deep water, while in the second harmonic the phenomenon was observed as the wave steepness increased regardless of water depth settings. However, further investigation remains outside the scope of this thesis.

It is interesting to see that the third order loading in the highest kA (comparison with the two Grue and Huseby (2002) cases) the second-order MAI loading model (diamonds) dominates over the other loading models (see Figure 5.18a) and over the influence of wave kinematics (it remains the most fitting model in Figures 5.19-5.20a as well). This could potentially be explained by the fact that since the derivation of the slender-body terms A and I rests on the expansion of kR term rather than kA, it remains valid in all ranges of wave steepness (Rainey, 1989). Nonetheless, referring to Figure 5.6 it should be noted that the third harmonic was captured well by all loading models as long as the wave kinematics were of higher order than first. The only exception is the MAID model which strongly overestimated the third harmonic with all the kinematics above linear, potentially due to the fact that

the derivation of the surface distortion term D rests on Stokes small amplitude theory (refer to Section 5.5).

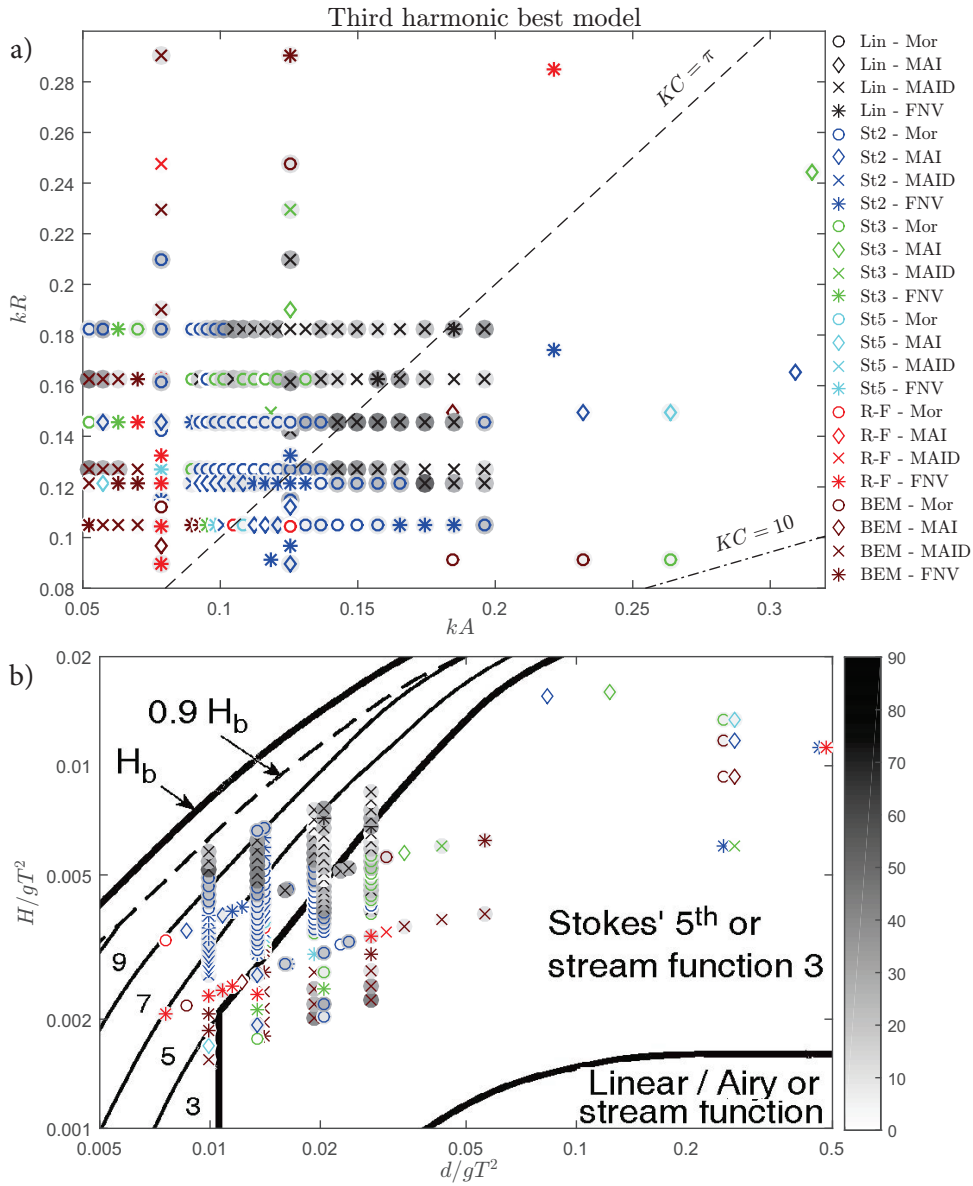

Figure 5.18: The best-fitting numerical models for third harmonic with its relative error: a) on (kA, kR)-grid and b) in reference to wave theory limits.

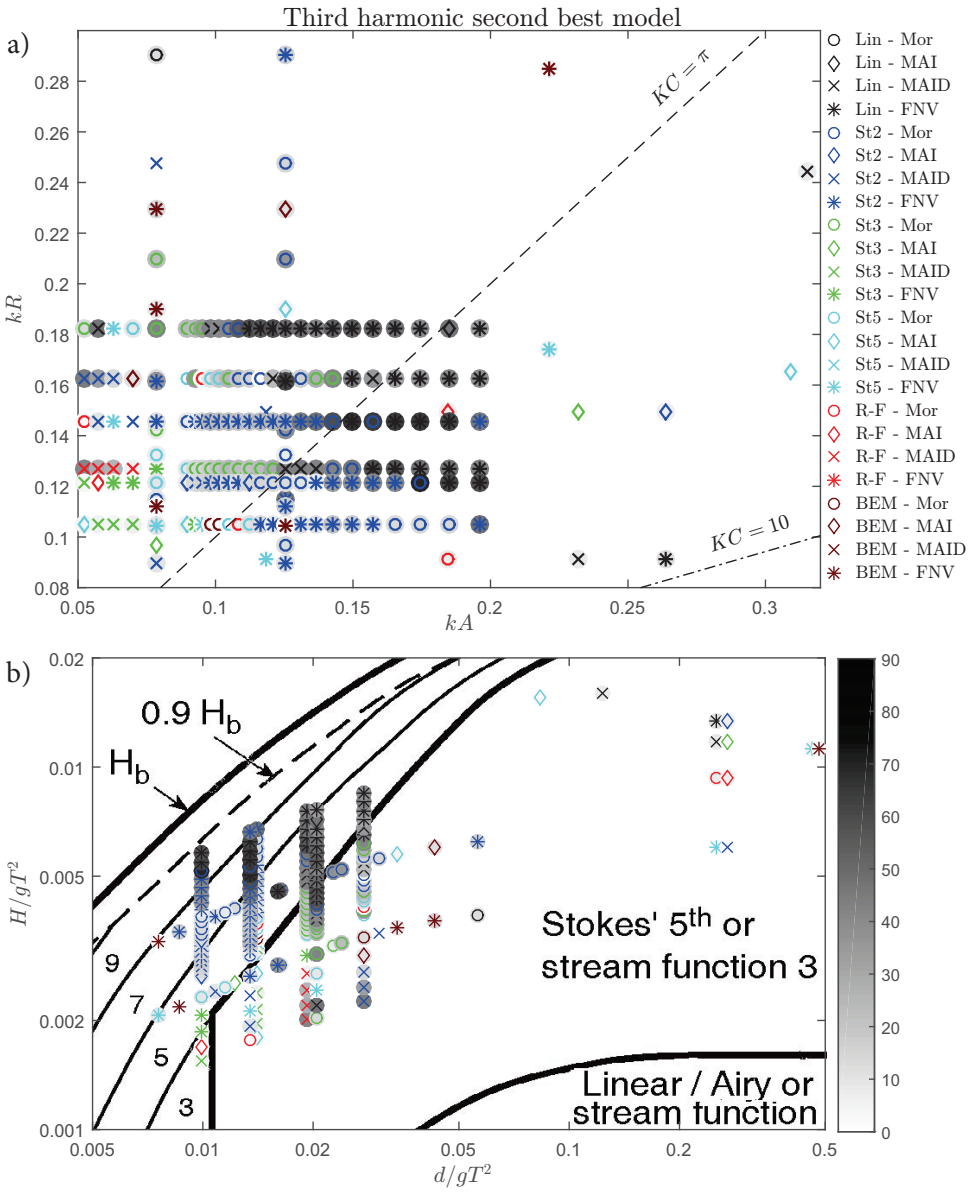

Figure 5.19: Second best-fitting numerical models for third harmonic with its relative error: a) on (kA, kR)-grid and b) in reference to wave theory limits.

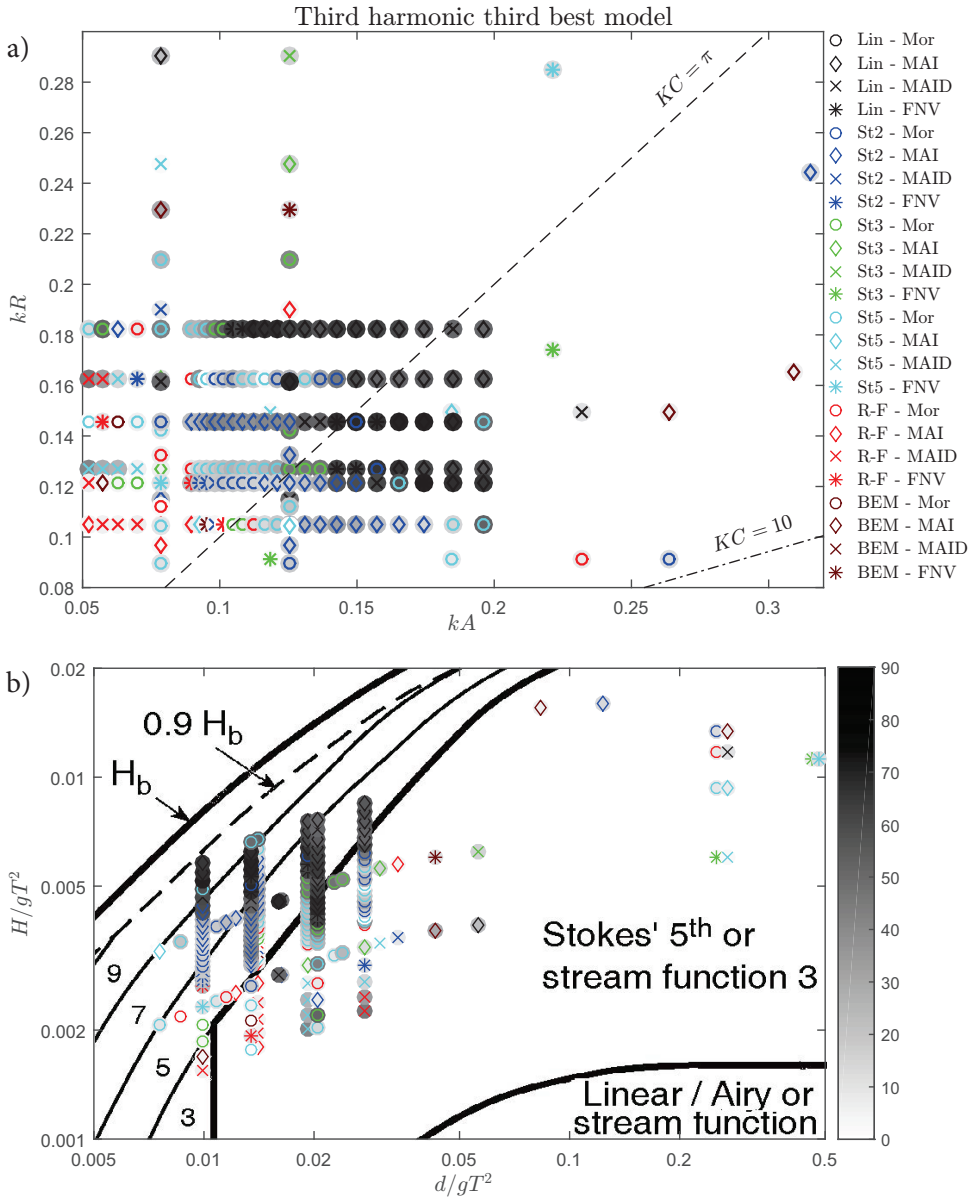

Figure 5.20: Third best-fitting numerical models for third harmonic with its relative error: a) on (kA, kR)-grid and b) in reference to wave theory limits.

5.9 Conclusions of the Chapter

In this section six methods of increasing nonlinearity for wave kinematics and four hydrodynamic loading models were compared against experiments in increasingly nonlinear conditions. The following conclusions have been drawn:

- None of the loading models managed to recreate the experimentally observed secondary load cycle, including the newly derived diffraction-based finite-depth FNV theory, implying that the SLC is related to three-dimensional, or higher than third order effects.
- The suitability of surface distortion term D in Rainey's theory in steeper waves was concurred to be limited:
  - Tending towards overprediction, especially in combination with nonlinear wave kinematics.
  - Unsuitable from wave steepness $kA \approx 0.3$, but already not the best-fitting hydrodynamic loading model from $kA \approx 0.2$.
- The distinction between the nonlinearities in wave kinematics and hydrodynamic loading models was investigated, and it was found that:
  - The nonlinearities in wave kinematics decreased the first harmonic and increased the higher harmonics.
  - The nonlinearities in hydrodynamic loading models caused an increase in the loading predictions in all harmonics.
  - The interaction between the two nonlinearities becomes crucial in much higher harmonics, such as fourth and fifth.
  - Increasing steepness kA and decreasing kR number were found to amplify these effects. They correspond to approaching the breaking wave limit, and nearing the drag regime rather than diffraction or inertia.
  - The distinct regions of influences were identified: in deep water the influence of the hydrodynamic loading model prevails, while in the intermediate water depth the influence of wave kinematics is much stronger.
- Attention was drawn to the issue of non-monotonic growth over increasing steepness:
  - Experimental loading increases non-monotonically with increasing wave steepness, while all numerical models were increasing rather proportionally to the wave steepness, causing overpredictions.
  - This non-monotonic behaviour coincides with the most nonlinear wave conditions, where highly nonlinear wave kinematics are theoretically recommended, leading to an even stronger overestimation.
  - If this effect could be quantified and accounted for, large overestimations could potentially be avoided.
- The suitability of the models in comparison with experimental values was assessed. It was found that:
  - The zones of the poorest prediction coincide with the zones where nonlinearities matter the most: vicinity to the wave breaking limit (more applicable to intermediate water depth) and the high kA and kR values (more influencial for deep water conditions).

- Overall the first harmonic was seen to be captured with good accuracy in all cases except for the wave conditions in the vicinity of the wave breaking limit.
- The second harmonic was captured most poorly, tending towards strong overestimation as both the wave steepness kA and nondimensional wave number kR increase.
- Third harmonic was captured better than second, relatively well even in very high steepness. The worst predictions were in intermediate water: at the limit of the Stokes theories, coinciding with the non-monotonic experimental growth.

Chapter 6

Response of offshore wind turbine monopiles to wave loading

This chapter analyses the dynamic structural response of offshore wind turbine monopiles to nonlinear wave loading. Three stages of increasingly complex conditions are analysed. Firstly a one-degree-of-freedom monopile is subjected to regular waves, allowing comparison with past experiments and analysis of the influence of nonlinear free surface terms. Then a fully flexible parked offshore wind turbine is modelled in regular waves in order to assess the appropriateness of extending the trends observed on a cylinder to a more complex offshore structure. Lastly, the offshore wind turbine is subjected to increasingly nonlinear irregular seas. The influence of wind-wave misalignment on the sensitivity of an operating offshore wind turbine to nonlinear resonant responses is presented as original work. Limitations of irregular wave theories are assessed. Finally, encompassing all the findings, a realistic case study of an offshore wind turbine in a rough sea is conducted to determine the impact of nonlinearities in wave loading and the limitations of numerical wave loading modelling. This also answers the question whether the second order irregular waves with more sophisticated hydrodynamic loading models are able to capture ringing.

6.1 Moving cylinder in regular waves

The study on the dynamic response of offshore wind turbines starts with the most simplified system: the monopile support structure is considered as a cylinder limited to one-degree-of-freedom (1DOF), and is subjected to regular waves. It allows to extend the studies on fixed cylinder (Chapter 5) with a single additional factor of motion. The formulation used in this study is described by the Equation 4.9 in Section 4.2.1.

Initially the wave loading model combinations on the 1DOF moving cylinder are compared with experimental results in small wave steepness in Section 6.1.1. It discusses the influence of structural damping (Section 6.1.1.1) and the suitability of the investigated wave loading models in recreating these experiments in relatively low wave steepness (Section 6.1.1.2).

The study on a moving 1DOF cylinder is then numerically extended to very steep regular waves in Section 6.1.2. It is conducted in order to study the response of the simplified structure to higher-order loading close to its natural frequency, as well as to discuss the additional differences between the hydrodynamic loading models and their impact on loading once the motion of the cylinder is allowed.

6.1.1 Numerical model comparison with experiments in small wave steepness

Since ringing normally lasts for longer than the period of the wave that triggered it (Chaplin et al., 1997), experiments in steep regular waves are not informative due to incoming regular

waves interfering with the response. Therefore experiments on a moving cylinder in very steep regular waves are limited, and tend to be instead conducted in smaller wave steepness where no resonant response is triggered.

In this study the experiment of de Ridder et al. (2011) is recreated, with the wave steepness $kA \approx 0.08$. Experimental (scaled) and numerical (full scale) study was conducted on a bottom-hinged cylinder representing an offshore wind turbine de Ridder et al. (2011). In the thesis the full scale study was recreated, and compared to both experimental and numerical (FEM) findings of de Ridder et al. (2011).

Wave settings included wave period $T = 15\ s$ and wave height $H = 5.98\ m$ (de Ridder et al., 2011), while the water depth, cylinder length and pivot height were taken as $h = 30\ m$, $L_{cyl} = 109.943\ m$, and $s_0 = (115.347 - L_{cyl})$ consequently. Monopile diameter $D_{cyl} = 6\ m$ was used for the hydrodynamic loading models. For the sake of repeatability it should be noted that rather than regarding the monopile and tower (with diameter of $5.4\ m$) as separate parts, the moment of inertia of the dry cylinder was calculated using averaged mass and diameter of both. These values led to the intermediate water depth on the wave theory limits graph (Figure 5.2) and on the verge between the diffraction and inertia regimes on the (kA, kR)-graph (Figure 5.1).

If the trends of the numerical wave loading models observed on a fixed cylinder (Chapter 5) can be extended to the moving cylinder, the following behaviour can be expected in these wave and cylinder conditions. The influence of wave kinematics would dominate over the influence of hydrodynamic loading models, resulting in linear wave kinematics (and potentially second order wave kinematics as well) becoming inappropriate. The vicinity to diffraction regime would suggest that FNV theory could be expected to exceed; nonetheless MAID model was also seen to perform well in this (kA, kR)-range.

The kinematics used by de Ridder et al. (2011) in their numerical study are 7^{th} order stream function, exceeding the recommendation by the IEC 61400-3 design standard (International Electrotechnical Commission, 2009) previously displayed in Figure 5.2. Full Morison equation was used by de Ridder et al. (2011), where the drag and inertia coefficients were defined as $C_d = 0.7$ and $C_m = 1.8$. Therefore the drag and inertia coefficients are implemented as such values in this study as well, for all Morison inertia based hydrodynamic loading models (Mor (Eq. 4.2), MAI (Eq. 4.2-4.4) and MAID (Eq. 4.2-4.5)). Consequently, resulting from the fact that the inertia coefficient $C_m \neq 2$, FNV theory (Eq. 4.6) is not equivalent to Morison inertia based loading models as was seen throughout the study on the fixed cylinder in Chapter 5.

Lastly, in de Ridder et al. (2011) a significant asymmetry in the experimental values of the tower top displacement was reported, which, for the ease of comparison, was removed in this study for the first two wave periods shown in Figures 6.1 and 6.2.

6.1.1.1 Influence of structural damping on the structural response to wave loading

In experimental setups the presence of structural damping is inevitable. However, structural damping has not been discussed in de Ridder et al. (2011), therefore this study starts with assessing its influence on the structural response. This is undertaken by comparing the

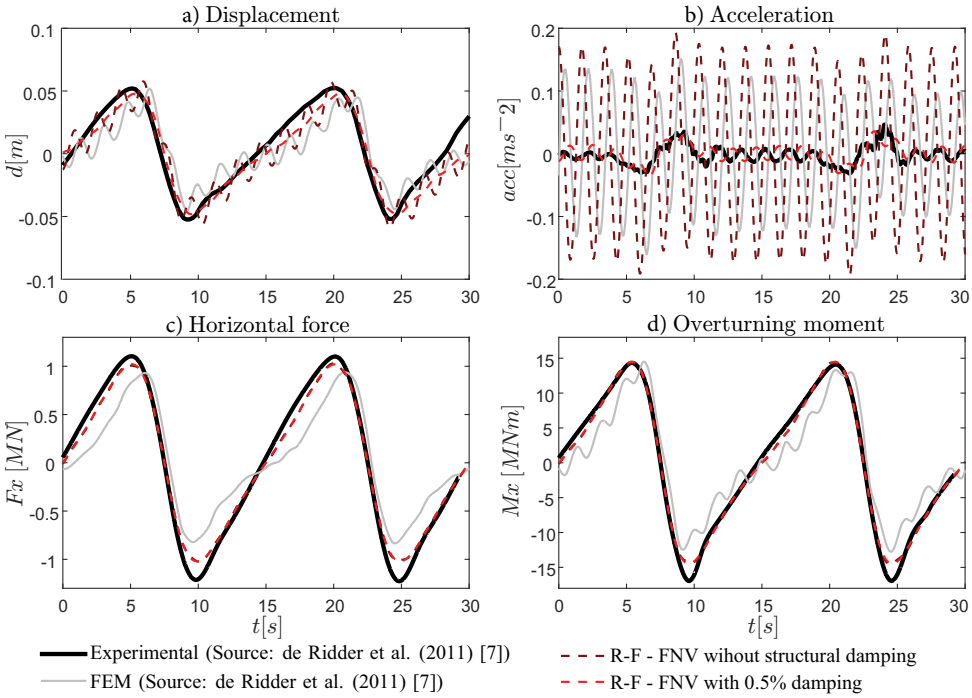

Figure 6.1: Influence of structural damping comparing the experiments (thick black solid line) and numerical results (solid grey line) of de Ridder et al. (2011) with Rienecker-Fenton wave theory and FNV hydrodynamic loading model both without structural damping (darker dashed line) and with structural damping of 0.5% of critical damping (lighter dashed line) in terms of: a) tower top displacement, b) tower top acceleration, c) horizontal force, d) base bending moment.

numerical predictions without structural damping, and with a standard value of 0.5% of critical damping (as in, e.g. Chaplin et al., 1997), with experimental and numerical results of de Ridder et al. (2011). Results for both motion (tower top displacement and tower top acceleration) and forcing (horizontal force and overturning moment) are shown in Figure 6.1 consequently.

It can be seen that the forcing on the structure (Fig. 6.1c,d) is barely influenced by accounting for the structural damping, while its effect on the motion (Fig. 6.1a,b) is clear. The consideration of structural damping reduces the tower top motion to the level of experimental values, whereas the motion without the structural damping follows the trend of the numerical values of de Ridder et al. (2011) more closely. This is in accordance with the fact that structural damping has much stronger influence on the higher structural modes rather than first. Therefore to analyse the suitability of wave loading models in recreating the experimental values of de Ridder et al. (2011) in the following section structural damping of 0.5% was applied.

6.1.1.2 *Suitability of wave loading models*

The suitability of the compared wave loading models is overviewed in Figure 6.2, where each panel shows the experimental (thick black solid line) and numerical results (solid grey line) of de Ridder et al. (2011) in comparison with a selection of wave loading model combinations from this study. From top to bottom tower top displacement (Fig. 6.2a,b), tower top acceleration (Fig. 6.2c,d), horizontal force (Fig. 6.2e,f) and base bending moment (Fig. 6.2g,h) are shown. To discuss the influence of nonlinearities in wave kinematics, the left column shows all wave theories with the nonlinear FNV hydrodynamic loading model (Eq. 4.6)).

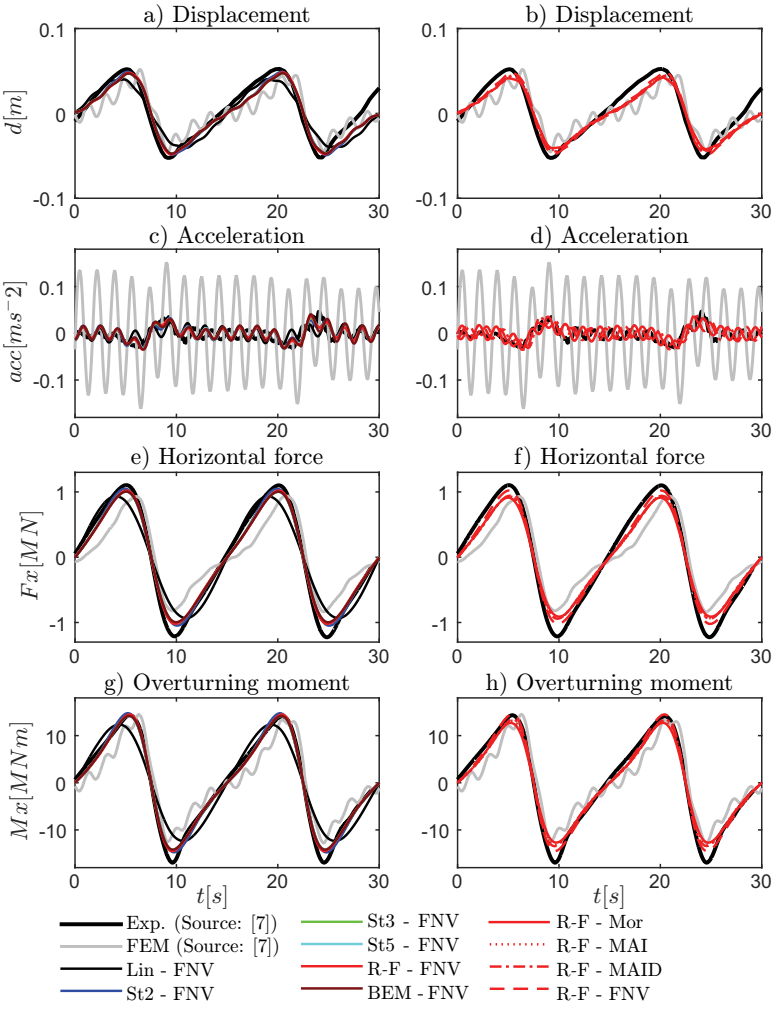

Figure 6.2: Influence of the nonlinearities in wave kinematics (left column) and in hydrodynamic loading models (right column), compared with experiments (thick black solid line) and numerical results (solid grey line) of de Ridder et al. (2011) in terms of: a-b) tower top displacement, c-d) tower top acceleration, e-f) horizontal force, g-h) base bending moment.

On the other hand, the right column shows all hydrodynamic loading models with the nonlinear Rienecker-Fenton wave kinematics (R-F; Section 3.1.3) for easier comparison of the influence of nonlinearities in hydrodynamic loading models.

Firstly, very good overall capturing of the cylinder motion and the loading on it can be seen. However, as expected from intermediate water depth conditions, the choice of wave kinematics has a stronger influence than the choice of hydrodynamic loading model. It is most evident from the underestimation of wave loading when linear wave kinematics (thin black line) are used. The nonlinear trends in sharper maxima and minima are missed, and the loading remains more sinusoidal than other more nonlinear wave kinematics (Fig. 6.2e,g). Similar behaviour to a lesser extent is seen in cylinder's motion as well (Fig. 6.2a,c). The second order wave kinematics (blue line) also differentiate themselves from the more nonlinear wave kinematics, but rather tending towards overestimation, as already seen in the fixed cylinder case (Chapter 5). Lastly, all higher order kinematics behave very similarly due to relatively low wave steepness ($kA \approx 0.08$).

In terms of the suitability of hydrodynamic loading models, FNV theory results in noticeably larger wave loading on the cylinder than other Morison inertia based models. The main reason for such difference is presumed due to the inertia coefficient reported as $C_m = 1.8$ in de Ridder et al. (2011), while $C_m = 2$ would make the hydrodynamic loading models comparable. Since there is a tendency for underestimation of the wave loading on the moving cylinder in this case, FNV is seen to perform the best. Therefore it may be suggested that if the inertia coefficient C_m was set to a larger value the Morison and Rainey theories could have captured the loading better, emphasising the importance and difficulty of choosing the most appropriate coefficients for the semi-empirical hydrodynamic loading models.

6.1.2 Influence of nonlinear free surface terms on the natural frequency of offshore structures

Offshore wind turbines are commonly designed so that their natural frequency falls at much higher frequencies than the dominant wave frequency. Nonetheless, as the offshore wind turbines grow larger their natural frequency reduces. The one-number value for the natural frequency of an offshore system is often determined as the mean value of the free oscillation test in still water. However, in reality the actual natural frequency changes in time due to the changing wetted length of the cylinder as the wave train passes, as well as due to the nonlinearities at the free surface.

Numerically both third-order free surface point loads, surface distortion term D in Rainey theory (Eq. 4.5, Section 4.1.2) and F^{ψ} in FNV theory (Eq. 4.8, Section 4.1.3), consider relative acceleration. The coefficient next to the body acceleration is caused to move to the left-hand side of the equation of motion (Eq. 4.9, Section 4.2.1), changing the inertia of the system and thus the natural frequency.

To illustrate this, the previously discussed experiments from Grue and Huseby (2002) are recreated with a slight modification. In the original experiment a fixed cylinder with radius $R = 0.03\ m$ was subjected to waves with steepness $kA = 0.32$, wave height $H = 0.077\ m$ and period $T = 0.703\ s$ in water depth $h = 0.6\ m$. In the investigated case the cylinder is bottom-hinged, allowing one degree of freedom.

In order to set this scaled offshore structure in the range of the excitations by third harmonic, the design frequency was prescribed as three times the frequency of regular incident waves: $f_n = 3/T = 4.267\ Hz$. Just as in, for example, Chaplin et al. (1997) experiments, the rotational stiffness of the cylinder κ, which represents the soil-structure interaction, was set to match the prescribed design frequency in still water ($f_n = 4.267\ Hz$) and equals to $\kappa = 355.77\ rad/m$ in this case.

Then, in order to investigate how different wave frequencies affect different hydrodynamic loading models, this specific 1DOF structure was subjected to a range of incoming waves with periods ranging from 0.69 s to 0.73 s instead of just the predetermined $T = 0.703\ s$, keeping the wave height fixed as $H = 0.077\ m$.

The first and second harmonics remained relatively constant across the range of incoming waves with values of $F^{1\omega} \approx 2.3\ N$ and $F^{2\omega} \approx 0.5\ N$. Therefore Figure 6.3 shows the mean value of the third harmonic from the FFT analysis of the horizontal force ($F^{3\omega}$) with all four hydrodynamic loading models (Morison inertia term (Mor; Eq. 4.2), MAI (Eqs. 4.2-4.4), MAID (Eqs. 4.2-4.5), and FNV (Eq. 4.6)) with Rienecker-Fenton kinematics (R-F; Section 3.1.3). Value for each simulation of different incoming wave settings is shown as a marker, connected for each hydrodynamic loading model for ease of reading. The blue ver-

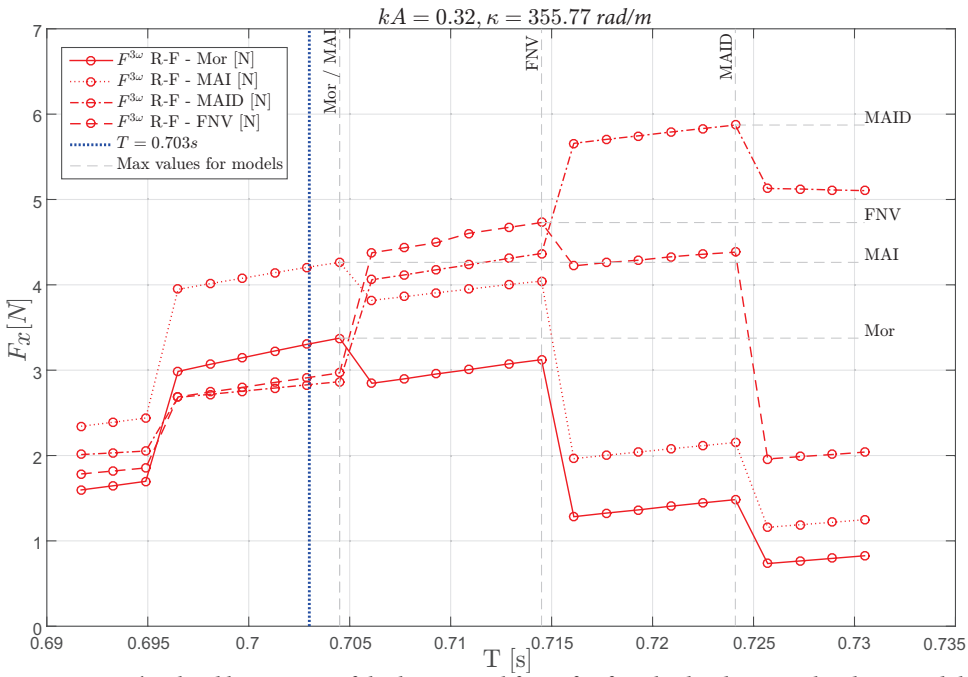

Figure 6.3: The third harmonic of the horizontal force for four hydrodynamic loading models with Rienecker-Fenton kinematics over a range of incident wave periods. Blue vertical line marks the predetermined wave period, while grey markers denote the maximum values for each hydrodynamic loading model.

tical marker coincides with the wave period $T = 0.703\ s$, to which the system was adjusted, whereas the grey lines mark the maximum values for each hydrodynamic loading model.

Looking at just the vertical cut at the wave period $T = 0.703\ s$ for which the system was adjusted (blue line) it can be seen that the most amplified responses are modelled with MAI ($F^{3\omega} = 4.20\ N$), followed by Morison equation ($F^{3\omega} = 3.28\ N$). The more nonlinear hydrodynamic loading models, FNV and MAID, which would be expected to predict the highest loading, are instead both lower with $F^{3\omega} < 3\ N$. For this reason it is critical to look at a range of wave periods: the actual maxima for FNV and MAID models in the third harmonic is at lower wave frequencies – higher wave periods. This can be explained by the additional added mass stemming from the nonlinear free surface terms in both MAID and FNV.

As discussed in Section 4.1.3, these third-order terms D (Eq. 4.5) and F^{ψ} (Eq. 4.8) are similar, but have three key differences: Rainey's D term is applied at the instantaneous free surface with a coefficient of 3.5, and the F^{ψ} from FNV is applied at the mean water surface with a coefficient of 4, and different formulations for relative velocity. These differences are amplified in steep waves, when the distance between the mean and instantaneous free surface is exaggerated, and especially when nonlinear kinematics are used due to the sharper peaks (as was illustrated in Figure 3.2a). The discussed differences lead to FNV model peaking with $F^{3\omega} = 4.73\ N$ at $T = 0.715\ s$ and MAID model peaking with a significant $F^{3\omega} = 5.87\ N$ at $T = 0.724\ s$. The difference between this actual highest value for MAID ($F^{3\omega} = 5.87\ N$) and the one seen at the design frequency ($F^{3\omega} < 3\ N$) is double, illustrating the importance of considering the nonlinear fluid-structure interaction in the design, and implementing it appropriately.

Comparing the MAI and Morison inertia (Mor) models it can be seen that they both peak triggered by the same wave period $T = 0.705\ s$, which is the closest to the wave period $T = 0.703\ s$, but not exact due to the time-dependent wetted surface as the wave crests and troughs pass the cylinder. Peaking at the same wave frequency is due to the fact that neither the integrated axial divergence term A (Eq. 4.3), nor the surface intersection point load I (Eq. 4.4) contain relative acceleration which would influence the added mass, therefore the inertia of the system is determined by only the Morison inertia term (Eq. 4.2). Nonetheless, the two nonlinear terms A and I do influence the amplitude of the response: $F^{3\omega} = 4.263\ N$ for MAI and $F^{3\omega} = 3.375\ N$ for Morison inertia.

To summarise, this section shows the importance of nonlinear fluid-structure interaction and the necessity to remember that the natural frequency of the structure changes depending on it. Therefore a range of wave settings and natural frequencies should be investigated in order to avoid omitting resonant excitations, and hydrodynamic loading models which consider nonlinear fluid-structure interaction (FNV or MAID) would help to assess the loading more realistically.

6.2 Non-operational offshore wind turbine subjected to regular wave loading

Even though an actual offshore wind turbine would not be subjected to regular waves, it is useful to investigate the response in regular waves first as they provide more predictable environment. The NREL 5-MW baseline offshore wind turbine, described in section 4.2.2.4, is analysed in this study. The offshore wind turbine is modelled in parked condition since there have been numerous studies showing that the largest danger of resonant amplifications appears when the turbine is not operating due to reduced aerodynamic damping, e.g. Marino et al. (2013b), Schløer et al. (2016), and Marino et al. (2017).

Waves with period $T = 11.8\ s$ in water depth of $h = 20\ m$ are simulated with increasing wave height ranging from $H = 1\ m$ to $H = 9\ m$. This corresponds to wave steepness $kA \approx [0.02 - 0.19]$. With the $kR \approx 0.12$ this places the values on the (kA, kR)-graph (Figure 5.1) across the diffraction and inertia regimes. With the $d/gT^2 = 0.0146$ and $H/gT^2 = [0.000732 - 0.0066]$ these wave conditions fall in the intermediate water depth, across the Stokes 5^{th} order and higher stream function theories on the wave limits graph (Figure 5.2). Both of these conditions coincide with the conditions where the Kristiansen and Faltinsen (2017) results on fixed cylinder are investigated in Chapter 5, therefore if the assumption that the parked monopile-supported offshore wind turbine behaves as a truncated cylinder, similar results may be expected. Final 50 of the 60 simulated wave periods are analysed to avoid any initialisation interference.

6.2.1 General trends of response

Figure 6.4 shows the normalised response amplitudes of the tower base shear force (denoted as TwrBsFxt) of the first three harmonics (left to right) over increasing wave height H. Note should be taken that having learned from the findings of the Section 6.1.2, rather than taking the value at the exact frequency of the harmonic, the maximum value of a narrow range around that frequency was selected instead to avoid omitting the nonlinear excitations. Normalisation is chosen over the wave height H to the power of the harmonic, $\rho g R^2$ in order to eliminate the factor of cylinder dimension since all models are inertia based, and water depth h to the power of the harmonic minus one to ensure nondimensionlessness.

Some general trends are observed. Firstly, the numerical loading models grow rather monotonically with the increasing wave steepness (bear in mind that the y-axis spans over a very small range for the first harmonic). Secondly, the nonlinearities in hydrodynamic loading models increase the wave loading response for all wave kinematics and all harmonics. Lastly, the loading predictions are grouped more by the wave kinematics rather than the hydrodynamic loading models. All of these trends, and the ones in each harmonic separately, described in the paragraph below, show striking similarity to the trends observed on a fixed cylinder in regular waves in intermediate water depth (Figure 5.7 and Section 5.6), validating the extension of the main trends across from the fixed cylinder onto the offshore wind turbine.

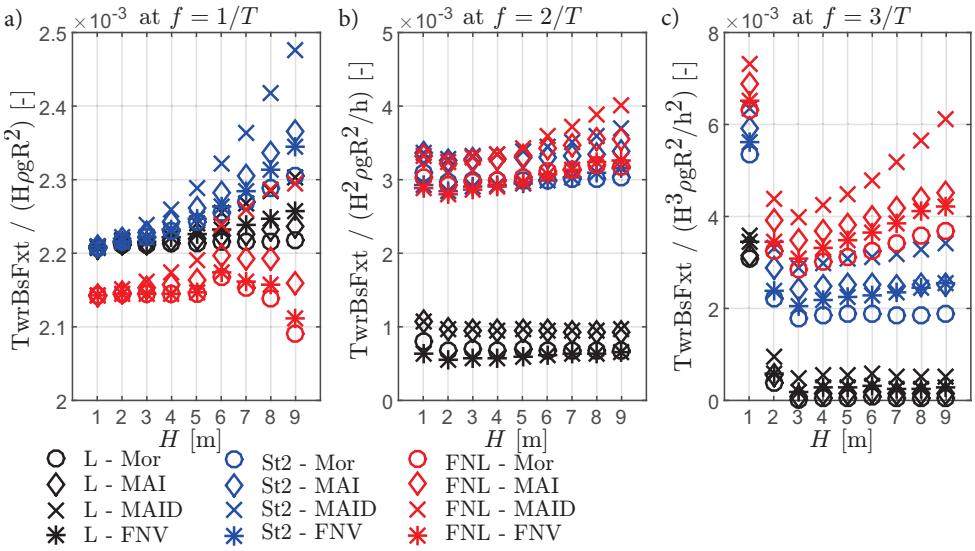

Figure 6.4: First three harmonics (left to right) of normalised horizontal force over increasing steepness on a parked offshore wind turbine in regular waves.

To discuss each harmonic separately in greater detail:

1. In the first harmonic (Fig. 6.4a) linear wave kinematics increase linearly with the increasing wave height. Second order wave kinematics tend towards faster growth of the loading predictions as the steepness increases, while fully nonlinear wave kinematics – towards slower growth as more energy is passed to the higher harmonics.
2. In the second harmonic (Fig. 6.4b) all wave loading models grow quadratically – monotonically with the increasing wave steepness. Linear wave kinematics, regardless of the hydrodynamic loading model, grow at a smaller rate than the other loading models – a previously observed phenomenon in the intermediate water depth on a fixed cylinder in Section 5.6. Second order wave kinematics model nearly identical response to wave loading as fully nonlinear wave kinematics up to higher wave steepnesses, where second order wave kinematics start underpredicting.
3. In the third harmonic (Fig. 6.4c) once more linear wave kinematics show significantly lower predictions than the higher order wave kinematics. Moreover, on the contrary to the second harmonic, the second order wave kinematics underpredict the third harmonic loading across all steepnesses.

6.2.2 Response amplitudes over increasing steepness

To discuss the response of a parked offshore wind turbine in more detail, Figure 6.5 shows the response amplitudes over the first three harmonics (left to right) for the mudline shear force (TwrBsFxt, Fig. 6.5a-c), mudline bending moment (TwrBsMyt, Fig. 6.5d-f) and tower top displacement (TTDspFA, Fig. 6.5g-i) over the wave height increasing from $H = 1\ m$ to $H = 9\ m$ in $1\ m$ increments.

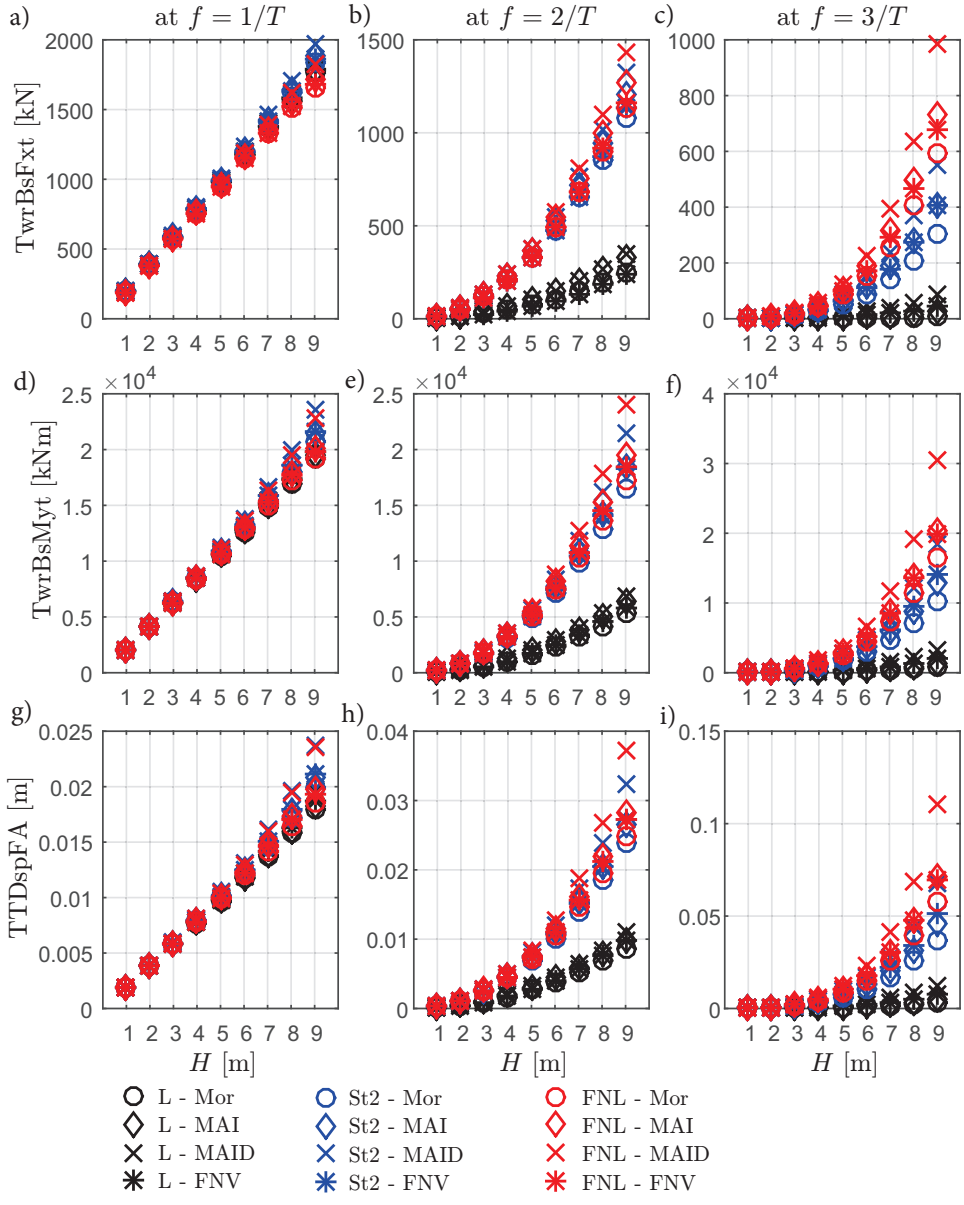

Figure 6.5: a-c) tower base shear force, d-f) tower base bending moment, and g-i) tower top displacement response amplitudes of the first three harmonics (left to right) for an offshore wind turbine in regular waves over increasing wave height H.

The key observations are that as the wave steepness increases the higher harmonics become increasingly important, however to different extent for each turbine response. In the tower base shear force response the first harmonic (Fig. 6.5a) still dominates even at the highest steepness, with the third harmonic (Fig. 6.5c) accounting for half or less of the first harmonic. In the meantime, in the tower base bending moment response all the harmonics become of similar magnitude (Fig. 6.5d-f), while for the tower top displacement the third harmonic (Fig. 6.5i) dominates significantly, accounting for as much as four times the magnitude of the first harmonic (Fig. 6.5g). The difference between the shear force (Fig. 6.5a-c) and base bending moment (Fig. 6.5d-f) responses may be explained by the large arm of the moment at the crest of the wave (water depth $h = 20\ m$ plus the highest wave height of $9\ m$).

Finally, the discussion from Section 5.5 on the suitability of the surface distortion correction D (Eq. 4.5) for predicting loading on a fixed cylinder in steep regular waves is extended here for the complex offshore wind turbine in regular waves. As can be seen from Figure 6.5, the separation between MAID model (crosses) from all the other models is increased in the higher harmonics, in more resonant-prone responses (tower base bending moment (Fig. 6.5e-f) and tower top displacement (Fig. 6.5h-i) rather than tower base shear force (Fig. 6.5b-c)), and as more nonlinear wave kinematics are used. Therefore, however, just as the other trends in behaviour can be transferred from a cylinder to a parked offshore wind turbine (Section 6.2.1), so is the poor appropriateness of the surface distortion term in increasing wave steepness, especially in combination with nonlinear wave kinematics.

6.3 Response of an offshore wind turbine in irregular seas

The environment in which offshore wind turbines are placed is harsh, complex and unpredictable. Regular waves, so far discussed in this thesis, do not reflect the real sea conditions. However, they are much closer described by irregular waves. The three main analytic and numerical methods to model irregular wave kinematics which have been described in Sections 3.2 and 3.3.5. As discussed in those sections, each of these irregular sea models have limitations and do not capture the real-life sea conditions fully. Thus, this section, after a parameter study in Section 6.3.1, investigates multiple aspects and limitations of modelling offshore wind turbines in irregular waves.

First of all, Section 6.3.2 investigates the influence of wind-wave misalignment and aerodynamic damping on the sensitivity of parked and operational wind turbines to the nonlinearities in wave kinematics, in order to assess whether co-directional parked case is the most critical one or operational wind turbine in misaligned wind and waves scenario is as sensitive to resonant amplifications. Then, Section 6.3.3 investigates the behaviour of the wave loading models over increasing wave steepness, to determine the limits of suitability of the numerical wave loading models. Finally, encompassing all the prior findings, Section 6.3.4 describes a one-hour-long case study of an offshore wind turbine in rough sea conditions, its structural response to wave and wind loading, and the impact of the nonlinear resonant amplifications on the turbine.

6.3.1 Parameter independence and numerical modelling limitations

Analytical and numerical studies encounter not only fundamental limitations imposed by the theories on which the methods are based, which were discussed in depth in Sections 3.2 and 3.3.5, but also additional limitations in implementation and dependence on various parameters. Therefore in this section two main limitations related to the implementation of irregular waves are discussed: the time step independence for the frequency domain implementation of the second order waves, as well as the spacial discretisation for fully nonlinear waves in BEM solver.

6.3.1.1 Time step independence for second order waves

As introduced in Section 3.2.2, for computational efficiency Sharma-Dean second order wave kinematics were computed in frequency domain and then converted to time domain by the use of Inverse Fast Fourier Transform (IFFT). Therefore the time step is determined by the number N in Equations 3.12 and 3.13. However, the larger the number N is, the larger the matrices for frequency analysis are, leading to longer simulations and even computational limitations, making smaller number N more desirable. Nonetheless, if the time step becomes too large, the quality of the results might suffer. Thus especially for longer simulations it becomes essential to determine the most optimal time step. For this purpose a number of

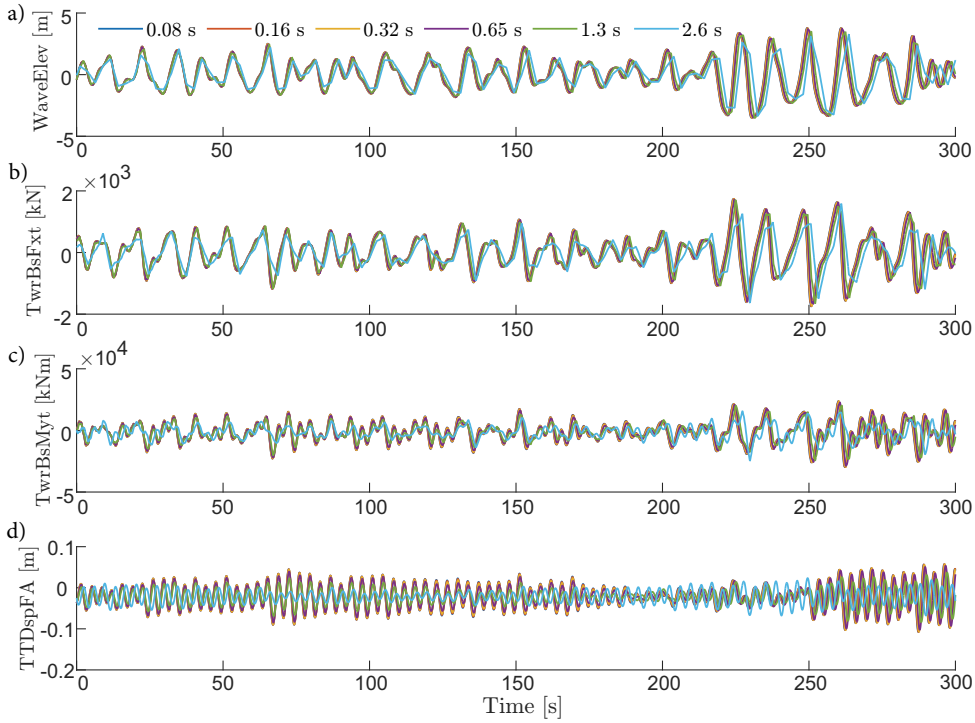

Figure 6.6: a) wave elevation (WaveElev), b) monopile base shear force (TwrBsFxt), c) monopile base bending moment (TwrBsMyt) and d) tower top displacement (TTDspFA) time series for second order wave time step independence study.

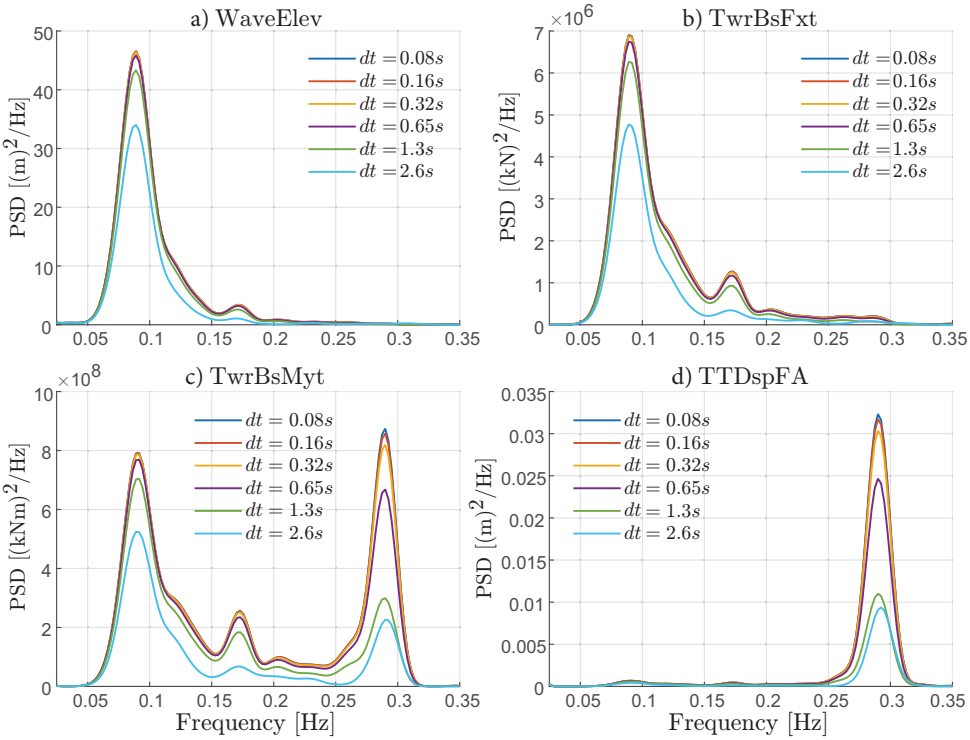

Figure 6.7: Power spectral density of: a) wave elevation, b) tower base shear force, c) tower base bending moment, d) tower top displacement for the second order wave time step independence study.

simulations were carried out with Sharma-Dean second order waves (Eqs. 3.12 and 3.13) and Morison equation (Eq. 4.2) as hydrodynamic loading model. Simulations with 330 s of wave kinematics were conducted and the first 30 s were omitted from the analysis to avoid initial transient effects, leading to 5 *min* time series.

Figures 6.6 and 6.7 show the time series and the corresponding power spectral density analysis with time steps ranging from $dt = 2.6\ s$ ($N = 2^7$) to $dt = 0.08\ s$ ($N = 2^{11}$). Wave elevation (WaveElev), tower base shear force (TwrBsFxt), tower base bending moment (TwrBsMyt) and the fore-aft tower top displacement (TTDspFA) are investigated.

Already from the time series (Figure 6.6) it is evident that the largest time step $dt = 2.6\ s$ is completely unsuitable. All the other solutions, nonetheless, are similar with only the amplitudes of the response differentiating. A deeper insight is given by the power spectral density (PSD) in Figure 6.7. From the wave elevation (WaveElev, Fig. 6.7a) and tower base shear force (TwrBsFxt, Fig. 6.7b) the coarse time step of $dt = 1.3\ s$ can be eliminated, since it notably underpredicts the amplitudes of both the elevation and the response.

The tower base bending moment (TwrBsMyt, Fig. 6.7c) and tower top displacement (TTDspFA, Fig. 6.7d) are both more susceptible to the amplifications at the natural frequency ($f \approx 0.28\ Hz$), and this is where the largest difference between discretisation appears. While

the medium time step $dt = 0.65\ s$ predicts the response at the wave frequency ($f \approx 0.09\ Hz$) relatively well, it becomes evidently insufficient at predicting the amplifications at the structural frequency ($f \approx 0.28\ Hz$). Finally, even though the time step of $dt = 0.32\ s$ seems to be predicting the loading well, compared to the fine time steps of $dt = 0.16\ s$ and $dt = 0.08\ s$ it does still lead to a slight underprediction at natural frequency. Therefore time step from $dt \approx 0.32\ s$ is expected to be representative, however ideally it would be kept closer to $dt \approx 0.16\ s$.

6.3.1.2 *Grid independence for fully nonlinear wave modelling*

Since linear and second order waves are analytical models and can be solved solely for the location of the turbine, the grid independence study does not apply. The fully nonlinear waves, however, are computed using the boundary element bounded domain, therefore the grid resolution on the boundary is very important.

Increasing the resolution normally tends to give better accuracy of results at the expense of computational effort. However, as discussed in Sections 3.3.3.1 and 3.3.3.3, very steep waves tend to overturn, and the re-entry of a breaking wave is a fundamental limitation of potential flow on which the BEM model is based. Therefore a compromise had to be made between the accuracy in terms of grid discretisation, and the amount of smoothing (Section 3.3.3.3) applied in order to avoid overturning waves.

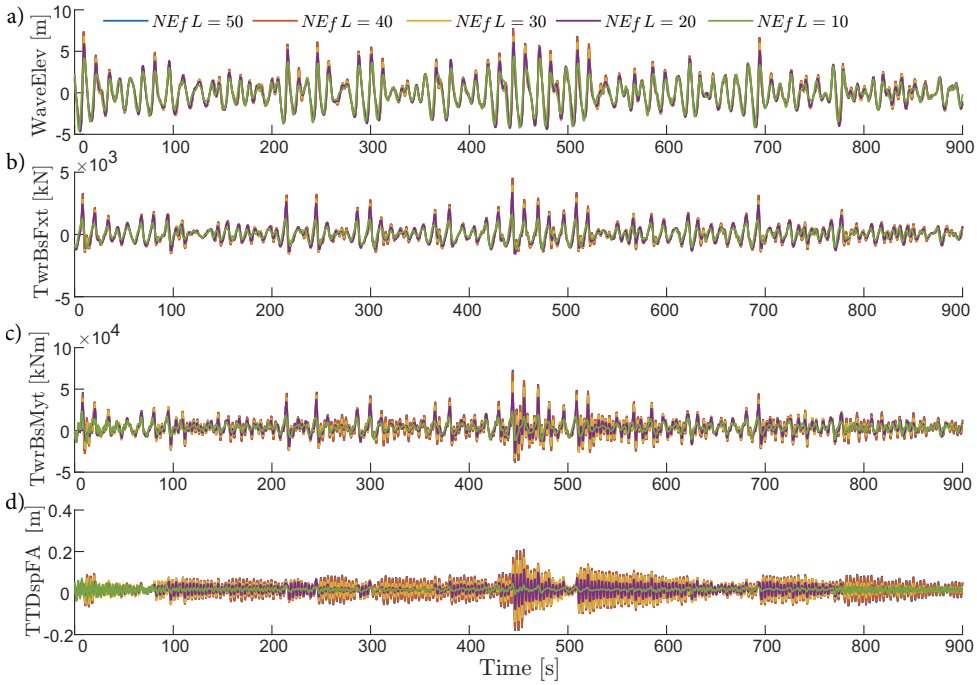

Figure 6.8: a) wave elevation (WaveElev), b) monopile base shear force (TwrBsFxt), c) monopile base bending moment (TwrBsMyt), and d) tower top displacement (TTDspFA) time series for the fully nonlinear wave time step independence study.

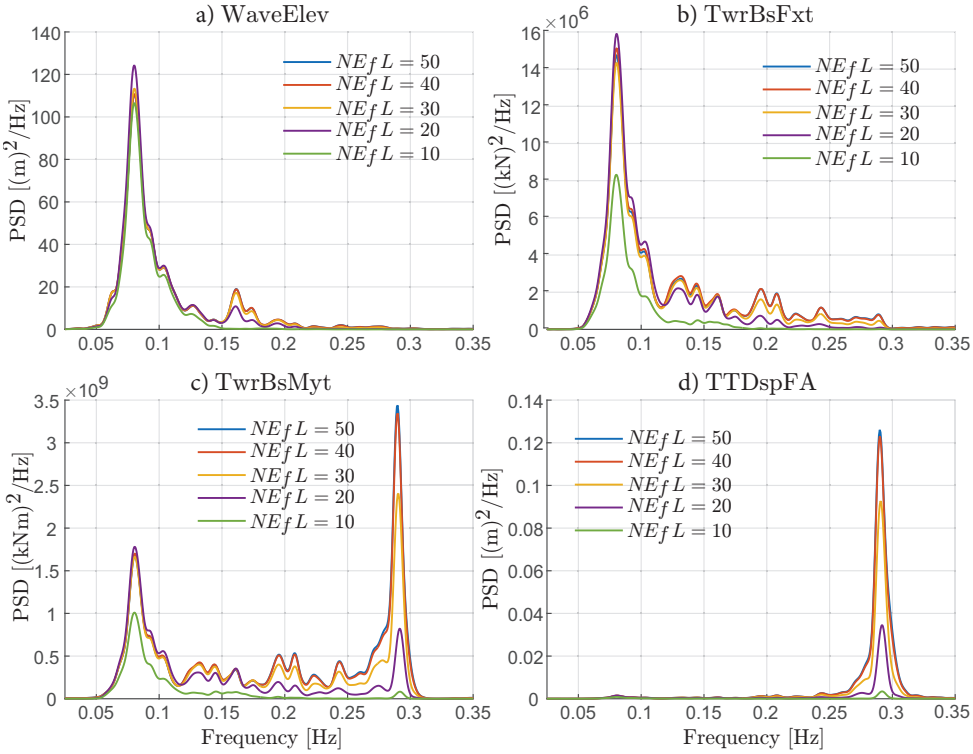

Figure 6.9: Power spectral density of: a) wave elevation, b) tower base shear force, c) tower base bending moment, d) tower top displacement for the fully nonlinear wave grid independence study.

Grid convergence study was conducted with a rough sea state of significant wave height $H_s = 7\ m$ and peak wave period $T_p = 12.5\ s$, simulated for total simulation time $T_{sim} = 15\ min$ with number of elements per wavelength on the free surface (NE_fL) ranging from $NE_fL = 12$ to $NE_fL = 50$. In the simulation with $NE_fL = 60$ the wave profile was detailed enough to overturn regardless of the amount of smoothing applied. Figures 6.8 and 6.9 show the results in time series and the Power Spectral Density (PSD) consequently for wave elevation and three response variables: tower base shear force, tower base bending moment, and tower top displacement.

From the time series (Figure 6.8) it can be seen that the wave elevation (WaveElev, Fig. 6.8a) is captured relatively well by all discretisations, with the lowest discretisation settings ($NE_fL = 10$ and $NE_fL = 20$) only slightly underestimating the peak amplitudes. Power Spectral Density (Figure 6.9a) confirms that the peak frequency of waves ($f = 1/T_p \approx 0.08\ Hz$) is captured well with all discretisations, just $NE_fL = 10$ underpredicting and $NE_fL = 20$ overpredicting slightly, when compared to the more highly discretised models. However, the significant difference appears at the second harmonic ($f = 2/T_p \approx 0.16\ Hz$), where the lowest discretisation of $NE_fL = 10$ omits the amplification completely, while $NE_fL = 20$ strongly

underestimates. The higher discretisations from $NE_fL = 30$ and higher have very similarly in terms of the wave elevation.

The unsuitability of coarser grid to capture the amplifications in the higher harmonics is evident in the turbine response as well. For both the tower base shear force (Fig. 6.8b, Fig. 6.9b) and the tower base bending moment (Fig. 6.8c, Fig. 6.9c) $NE_fL = 10$ falls out of context completely even for the first harmonic, but the $NE_fL = 20$ nearly omits the amplifications at the natural frequency $f \approx 0.28\ Hz$. What is more, the power spectral density of the tower base bending moment response (Fig. 6.9c) reveals the limitation of the medium discretisation with $NE_fL = 30$, where the amplifications at the natural frequency ($f \approx 0.28\ Hz$) are still underestimated compared to the fine meshes ($NE_fL = 40$ and $NE_fL = 50$). From the time domain (Fig. 6.8c) it appears that the underestimation stems not from the omission of the resonant response but rather from lower amplitudes throughout. Finally, the tower top displacement response from such nonlinear waves is concentrated nearly solely at the natural frequency of the turbine (see Figures 6.8d and 6.9d). Here once again the simulations with low spacial discretisation are completely unsuited, and the medium discretisation $NE_fL = 30$ leads to a lower response stemming from the underestimation of the amplitudes.

In summary, to successfully capture the response of the turbine from irregular fully nonlinear waves a fine spacial discretisation of the HOBEM domain is required. From the convergence study no less than 40 elements per wavelength on the free surface are recommended, and for the rest of the studies within this chapter $NE_fL = 50$ is used in order to ensure all nonlinear amplifications are fully captured.

6.3.2 Sensitivity of operational wind turbine to wave nonlinearities in the case of wind-wave misalignment

As discussed in the literature review (Chapter 2, Section 2.5), operating offshore wind turbines are not as susceptible to the resonant amplifications as parked turbines, due to the aerodynamic damping in the direction of the waves. The only exception which has not been investigated in depth for the potential sensitivity of operational turbines to resonant amplifications is under wind-wave misalignment conditions, where the aerodynamic damping in the direction of incoming waves is reduced. Therefore it has been investigated within the framework of this thesis (Mockute et al., 2016; Mockute et al., 2017a) in order to determine whether a study on a parked turbine is sufficient, or an operational turbine should be modelled as well.

Since the focus of this study is to observe the difference between parked and operational (Power Production, PP) at a number of misalignment angles rather than to investigate the differences between the wave loading models, only fully nonlinear (FNL) and linear (L) waves with full Morison equation (Eq. 4.1) were modelled. A case with no waves (NW) was also simulated as a base case. A rough sea state was investigated with significant wave height $H_s = 5.6\ m$, spectral period $T_p = 10.82\ s$, and close to rated mean wind speed of $12\ m/s$ with turbulence class A as defined in the IEC standard 61400-1, ed.3 (International Electrotechnical Commission, 2005).

Seven misalignment angles were investigated in equal increments of 15° from 0° to 90°, as illustrated in Figure 6.10. The wave direction was kept constant at 0°, since the varying an-

gle is not enabled for kinematics that are read-in from external files, functionality necessary for fully nonlinear kinematics (see Section 4.2.2.2). The wind direction was varied instead, and to ensure that the nacelle was facing the wind, the yaw angle was adjusted accordingly. Therefore the bending moment around the y-axis (TwrBsMyt) represents the constantly maximum wave loading with decreasing influence of aerodynamic loading and damping as the misalignment angle increases.

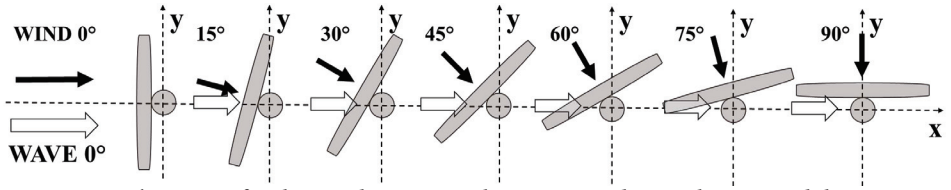

Figure 6.10: The set-up for the wind-wave misalignment study simulations and the associated coordinate systems.

The influence of wind-wave misalignment on the sensitivity to wave nonlinearities was assessed by a percentage difference between fully nonlinear and linear damage equivalent loads $\Delta DEL_{FNL/L}$, Equation 6.1. DEL uses rainflow-counting algorithm to estimate the same amount of damage as the variable-amplitude stress time series over a fixed number of cycles, 1000 for this study. This results in a normalised constant amplitude stress range, allowing easier comparison due to a single numerical value. In particular, the percentage difference between fully nonlinear (FNL) and linear (L) damage-equivalent loads ($\Delta DEL_{FNL/L}$) emphasises the influence of wave nonlinearities on the turbine response.

$$\Delta DEL_{FNL/L} = \frac{DEL_{FNL} - DEL_L}{DEL_L} \times 100 \tag{6.1}$$

Figure 6.11 shows the total value of the Damage-Equivalent Loads (left column) and the DEL percentage differences calculated by Equation 6.1 (right column) over increasing wind-wave misalignment angles, for the fore-aft base bending moment TwrBsMyt (top row), and the side-side bending moment TwrBsMxt (bottom row).

First of all, the fore-aft bending moment (TwrBsMyt, Fig. 6.11a) shows the full wave loading regardless of the misalignment angle, and decreasing wind loading and aerodynamic damping as the misalignment increases. By comparing the trends of the operating (circular markers) and parked (cross markers) turbine responses, it can seen that the operating case is dominated by the aerodynamic loads (the observed loading strongly decreases as the influence of wind decreases), while the parked turbine is dominated by the wave loading (staying relatively constant regardless of the wind direction). The reference cases of no waves (dotted lines) for operational case is close to the cases with waves (dashed and solid lines) showing wind load dominance. Meanwhile for the parked case the difference from cases with waves is drastic (7 *MNm* for no waves, 22 *MNm* for linear waves, and 26 *MNm* for fully nonlinear waves at co-aligned wind and waves).

The main trends for the differences between the linear (L, solid lines) and fully nonlinear (FNL, dashed lines) cases already can be noted from Fig. 6.11a, but they are amplified

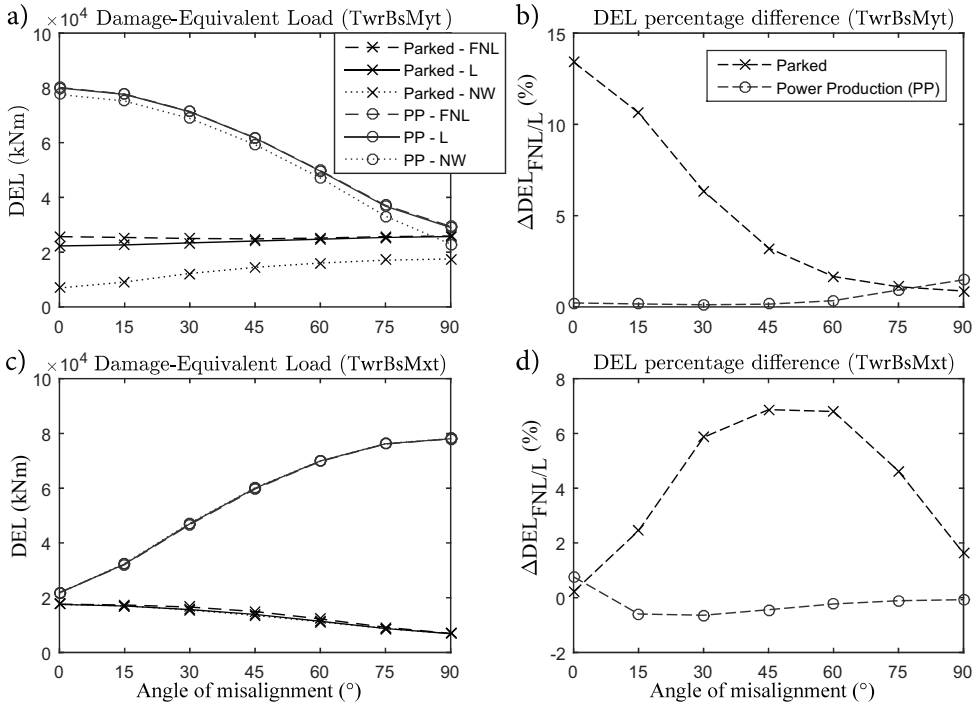

Figure 6.11: Damage-Equivalent Loads over increasing angle of misalignment for: a) the fore-aft bending moment (TwrBsMyt); c) the side-side bending moment (TwrBsMxt); and their DEL percentage differences between fully nonlinear and linear waves (b and d correspondingly).

in Fig. 6.11b, showing the percentage difference $\Delta DEL_{FNL/L}$. It is evident that for an operating wind turbine (circular markers) the sensitivity to wave nonlinearities increases with increasing angle of misalignment, due to decreasing influence of aerodynamic damping – from negligible 0.2% at 0° to 1.5% at 90°. Nonetheless, the most critical case for the influence of wave nonlinearities is in fact the co-aligned (wind and waves in the same direction) case on a parked turbine (cross marker at 0°), accounting for 13.4% higher damage when modelled with fully nonlinear waves rather than linear.

For illustration in time domain, Figure 6.12 shows the nonlinear events of both the operational case with 90° misalignment in Fig. 6.12a, and co-aligned parked case in Fig. 6.12b with linear (blue) and fully nonlinear (red) wave kinematics. It can be observed in Fig. 6.12b that due to the lack of aerodynamic damping due to pitched blades the amplifications observed with fully nonlinear wave kinematics proceed (omitted by linear wave kinematics). Meanwhile for the operational case even reduced aerodynamic damping dampens the amplifications much faster.

Fig. 6.11c, in contrast to Fig. 6.11a, shows the side-side base bending moment (TwrBsMxt), which illustrates the cases with increasing wind loading as the misalignment angle increases. This also corresponds to minimal wave loading (waves are coming in at 90° for all misalign-

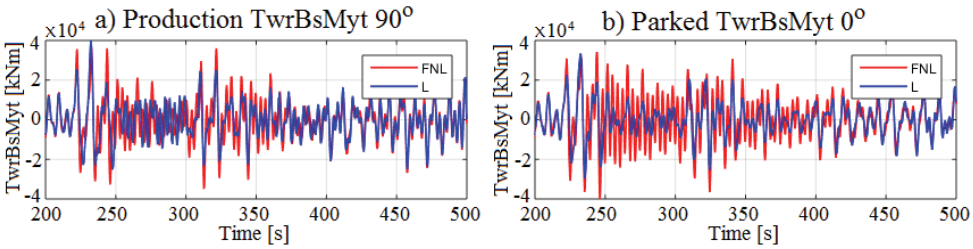

Figure 6.12: Time series of the fore-aft tower base bending moment in a) operational case at 90° misalignment; b) co-aligned parked case.

ment angles), leading to no tangible difference between the no wave cases (dotted lines) and cases with waves (dashed and solid lines). The differences between parked and operational cases can be seen comparing the lines with cross and circular markers consequently over increasing angles of misalignment. The operating case is dominated by wind loading, therefore the increasing influence of wind loading leads to increasing overall damage-equivalent load. Whereas for a parked turbine, when the blades are pitched to 90°, the wind loading has no effect but the aerodynamic damping still softens the wave loading, leading to the decreasing overall damage.

Finally, the DEL percentage differences $\Delta DEL_{FNL/L}$ for the side-side base bending moment TwrBsMxt, shown in Figure 6.11d, indicate that when the wave loading is minimal for an operating wind turbine (circular markers) the influence of wave nonlinearities is negligible, while for the parked turbine (cross markers) the influence of wave nonlinearities interestingly peaks at intermediate misalignment angles ($\theta \approx [30°\text{-}60°]$).

To conclude, even though the wind-wave misalignment does increase the sensitivity of the operating offshore wind turbine to the nonlinear resonant amplifications, but the co-aligned parked case still remains the most critical. Therefore the parked co-aligned case is used for the rest of the studies within this thesis.

6.3.3 Suitability of wave loading models over increasing wave steepness

Studying the numerical predictions over increasing wave steepness allows to discuss the limitations of each model as the roughness of the sea increases. In this case, to conduct an equivalent study to the study in regular waves (Section 6.2) and to allow an easier analysis with only one variable changing, the peak wave period T_p was fixed to the value of 11.8 s whilst the significant wave height H_s was varied from $H_s = 1\ m$ to $H_s = 9\ m$. It should be noted, however, that such conditions are not realistic, since the wave heights corresponding to the spectral period of $T_p = 11.8\ s$ are in the range $H_s \approx [5 - 6]\ m$ (Faltinsen, 1990), and anything above such wave heights would involve an unrealistically harsh sea with constantly overturning waves. Therefore this study is considered purely parametric to investigate the limitations of the numerical models.

Wave steepness is discussed in Tayfun steepness for intermediate water $\mu_m = kH_s/4$, where k is the wave number in intermediate water depth and H_s is significant wave height. Detailed description of the Tayfun steepness is available in Appendix A, Section A.1.

Wave loading at the wave frequency ($f = 1/T_p$) was predicted very similarly by all the loading models, while the predictions at the natural frequency f_n, which include the resonant oscillations, differed significantly. Therefore Figure 6.13 shows the maximum Power Spectral Density value of the tower base bending moment (TwrBsMyt) at the natural frequency of the turbine (taken as a range rather than a single value as per findings of Section 6.1.2) for each simulation over the increasing wave height.

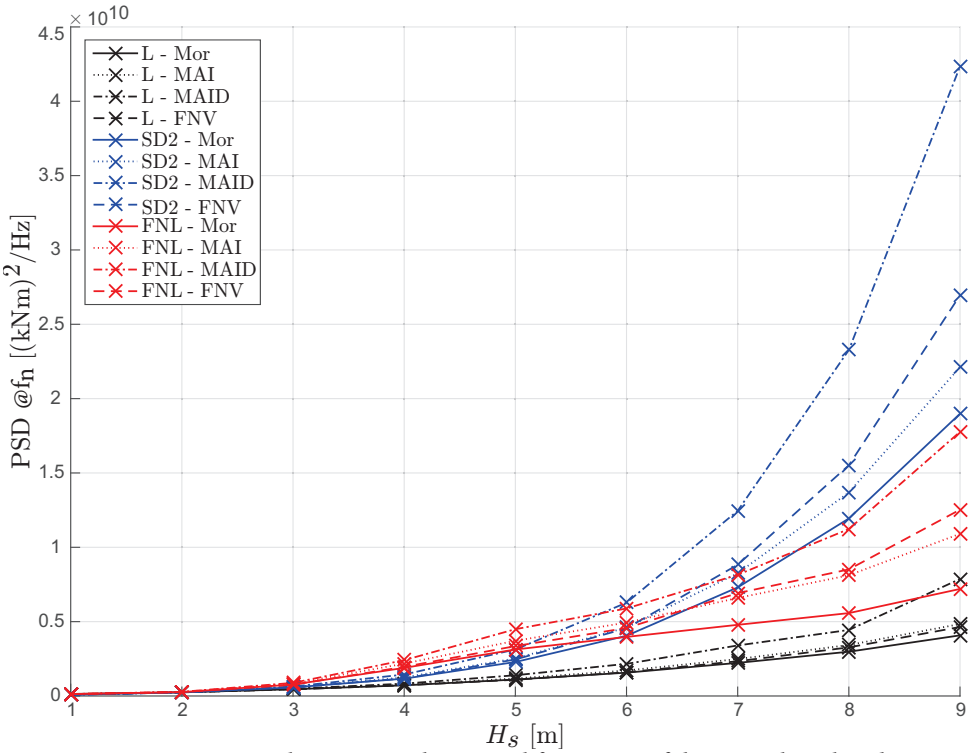

Figure 6.13: Power Spectral Density at the natural frequency of the tower base bending moment over increasing wave height.

First of all, on the lower end of the wave steepness spectrum, such as $H_s = 1\ m$, all the loading models behave very similarly. Then, as the wave height increases the numerical loading models grow monotonically with increasing wave steepness, as was seen on a fixed cylinder in Section 5.6, and start differentiating. Linear wave kinematics (black lines) predict the lowest loading, and already at $H_s = 4\ m$ can be seen to underpredict notably, therefore its limitation can be assigned to Tayfun steepness $\mu_m \approx 0.03$. Second order wave kinematics (blue lines) result in higher loading than linear wave kinematics throughout the increasing steepness, while fully nonlinear wave kinematics (red lines) predict the highest loading regardless of the hydrodynamic loading model up to wave height $H_s = 6\ m$ ($\mu_m \approx 0.08$).

As seen in Figure 6.13, at wave height $H_s = 6\ m$ the loading modelled with second order wave kinematics and with fully nonlinear wave kinematics start changing places. This can be explained by the limitations of both of these irregular wave solvers. First of all, fully non-

linear wave kinematics at such high wave steepness would encounter numerical instabilities and overturning waves, both of which are prevented by the use of smoothing techniques (see Section 3.3.3.3). However, the use of smoothing softens the extreme kinematics associated with breaking and near-breaking waves. Even though minimum possible amount of smoothing was applied for each wave steepness, smoothing still does have an increasing reduction effect in loading as wave steepness grows. The effect of smoothing becomes so dominant for $H_s = 9\ m$ that FNL Morison wave loading combination predicts lower loading than linear wave kinematics with MAID. The break of the increasing trend of the fully nonlinear wave loading (red lines) is especially evident from $H_s = 6\ m$.

Another reason for second order waves predicting much higher amplifications at the natural frequency at the highest steepnesses is that the Sharma-Dean second order wave theory is said to be valid only up to wave steepness ≈ 0.08 (Hu and Zhao, 1993; Agarwal and Manuel, 2011). In Agarwal and Manuel (2011), from which the second order irregular wave solver was implemented, steepness is defined as $s = H_s/\lambda_z = 0.08$, where H_s is significant wave height and λ_z is the wavelength derived from the mean zero-crossing period with linear dispersion relation. However, due to the intermediate water depth for this study the Tayfun steepness μ_m for intermediate water was deemed more suitable. In fact, in these conditions (water depth $h = 20\ m$, peak wave period $T_p = 11.8\ s$) the Tayfun steepness $\mu_m = 0.08$ is approached at wave height $H_s = 6\ m$.

Therefore above the values of Tayfun steepness $\mu_m = 0.08$ (or $H_s = 6\ m$) in this case, the second order theory is expected to lead to overprediction of the wave loading, while the smoothing in the FNL study will tend the FNL loading towards underprediction. Nonetheless, if the trends from a truncated cylinder may be extended to a parked turbine (see Section 6.2), the experimental values over increasing steepness were seen to increase much less than the numerical models predict (Section 5.6), which would follow the trend of FNL waves much more than those of second order. Nonetheless, an experimental campaign dedicated to confirming such findings would be greatly beneficial.

The hydrodynamic loading models tend to follow the same order on predictions: Morison inertia term (Eq. 4.2) predicting the lowest loading, followed by MAI (Eqs. 4.2-4.4), FNV (Eq. 4.6) and MAID (Eqs. 4.2-4.5) in the increasing order due to more nonlinearities considered in the fluid-structure interaction. The values that increase at a much higher and unproportional rate are the ones modelled with the MAID hydrodynamic loading model (dash-dot lines). Even with linear wave kinematics (black dash-dot line) the increase in the final increment between $H_s = 8\ m$ and $H_s = 9\ m$ is unproportionally high. This builds up on the discussion on the suitability of the surface distortion term D (Eq. 4.5), and once again its suitability as the wave steepness increases, especially in combination with nonlinear wave kinematics, is lacking confidence. The strong increase can already be seen at $H_s = 5\ m$, therefore the limitation of MAID could be considered at Tayfun steepness $\mu_m \approx 0.06$.

All in all, this study over increasing steepness in irregular waves has determined the upper limit for linear wave kinematics at intermediate water depth as Tayfun steepness $\mu_m \approx 0.03$, for the second order wave kinematics at Tayfun steepness $\mu_m \approx 0.08$, and for the surface distortion term D around Tayfun steepness $\mu_m \approx 0.06$. It should be noted that these limita-

tions are identified for the specific case of a slender monopile in inertia-dominated regime in intermediate water depth and their applicability in wider context should be studied further.

6.3.4 Case study under rough sea conditions

To analyse the suitability of the wave loading models under rough sea conditions, where resonant amplifications are expected and the wave loading models are still valid (see Section 6.3.3), a sea state of $H_s = 5.5\ m$ and $T_p = 11.5\ s$ was investigated. With water depth of 20 m the resulting Tayfun steepness $\mu_m = 0.0735$. Wind speed was kept constant with the magnitude of 21.5 m/s, corresponding to the current sea state in the North Sea (Table 2.3 in Faltinsen, 1990).

Such sea state leads to nondimensional water depth of $d/(gT_p^2) = 0.0154$ implying intermediate water depth, while the nondimensional wave height $H/(dT^2)$ equivalent in irregular waves $\sigma/(dT_p^2) = H_s/4/(dT_p^2) = 0.0011$ in reference to the wave theory limits (Figure 3.1) would point to 5^{th} order Stokes theory or 3^{rd} order Stream Function, reinforcing the importance of wave nonlinearities. With the wave number k for intermediate water depth coming to the value of $k = 0.0534$, the kA wave steepness equivalent in irregular waves, the Tayfun steepness $\mu_m = 0.0735$, so just under the upper limit of the second order theory, discussed in Section 6.3.3. The nondimensional wave number $kR = 0.1604$ places this case on the equivalent of (kA, kR)-graph (Figure 5.1) in the range of diffraction regime, in the vicinity of inertia regime, but far away from drag regime, justifying neglection of the drag term in the Morison equation.

As was discussed in Section 6.2, the behaviour trends from a fixed cylinder in regular waves can be extended to the more complex offshore wind turbine structure. Therefore it is worth mentioning that comparing to the cases discussed in Chapter 5, these wave conditions fall to the range of the lower end of the Kristiansen and Faltinsen (2017) cases. The main associated observations are: i) much stronger influence of nonlinearities in wave kinematics rather than in hydrodynamic loading models (Section 5.6); ii) increasing differences between the hydrodynamic loading models as the kR decreased (Section 5.7); iii) non-monotonic growth of experimental loading over increasing steepness (Section 5.6); and iv) the best-fitting predictions were seen by nonlinear wave kinematics in combination with diffraction based loading model FNV or second order kinematics with most nonlinear hydrodynamic loading models, as evident in Figure 5.11. For more detailed discussion see Section 5.8.

A representative one-hour-long sea state was simulated with linear (L, black lines), second order Sharma-Dean (SD2, blue lines), and fully nonlinear BEM (FNL, red lines) wave kinematics. The second order wave kinematics were discretised in time with the time step of $dt = 0.22\ s$, ensuring time step independence (see Section 6.3.1.1). Moreover, based on the discussions on the suitability of the surface distortion term D (Eq. 4.5) in Section 5.5 for fixed cylinders in regular waves, Section 6.2.2 for an offshore wind turbine in regular waves, and Section 6.3.3 for an offshore wind turbine in irregular waves, the MAID loading model was omitted from this case study, leaving only the Morison inertia term (Eq. 4.2), MAI (Eqs. 4.2-4.4) and FNV (Eq. 4.6) hydrodynamic loading models in comparison. The first 30 seconds of the simulations were omitted from the analysis to avoid any initial transient effects.

The turbine is modelled in parked configuration with blades pitched at 90° representing minimum frontal surface area. Wind and waves are co-aligned, because this was found to be the critical case in terms of sensitivity to wave nonlinearities (see Section 6.3.2). The wind speed of 21.5 m/s falls in the operational range of this turbine since the cut-out speed is at 25 m/s (Jonkman et al., 2009), therefore such situation is representative of a faulty turbine in extreme yet still productive sea conditions. Nonetheless, due to the pitched blades the influence of the wind speed is minimised, therefore the main trends behind the results are applicable to a range of wind speeds.

The responses are analysed in terms of Power Spectral Density of the whole 1-hour simulation (Section 6.3.4.1), time series of nonlinear events (Section 6.3.4.2), and the accumulated fatigue damage (Section 6.3.4.4).

6.3.4.1 *Power Spectral Density*

Figure 6.14 shows the Power Spectral Density (PSD) of the whole one hour simulation for the wave elevation (Fig. 6.14a), tower base shear force (Fig. 6.14b), tower base bending moment (Fig. 6.14c), and the tower top displacement (Fig. 6.14d). Figures 6.14c,d also include close-ups at the natural frequency to allow a clearer distinction between the investigated wave loading combinations.

The first differences are evident at the PSD of wave elevation (Fig. 6.14a). Fully nonlinear waves have a significantly smaller peak at the wave frequency ($f = 1/T_p = 0.087\ Hz$) and the highest second order peak ($f = 2/T_p = 0.174\ Hz$) than other wave kinematics. Meanwhile the second order wave theory has the same amplitude as linear wave theory at the wave frequency ($f = 1/T_p = 0.087\ Hz$), but a clear second order peak ($f = 2/T_p = 0.174\ Hz$), which linear wave theory omits completely. The fact that second order wave theory predicts lower second order peak than fully nonlinear waves may be the consequence of long-crested waves (mean wavelength $\bar{\lambda} \approx 111\ m$), since otherwise the second order wave theory predicts the second harmonic well. Third order peak is negligible with all wave kinematics. Bearing in mind the high peaks at the natural frequency that the response shows in Figures 6.14b-d, it would be expected that at least with fully nonlinear waves the third harmonic would be notable in order to trigger such resonant responses. Such apparent inconsistency can be explained either by the assumption that the amplifications are triggered by the nonlinearities in the hydrodynamic loading model, or by the elastic response of the structure, or by local wave excitation during nonlinear events. This is investigated in Section 6.3.4.3, where a selection of nonlinear events are analysed.

The tower base shear force at the mudline (Fig. 6.14b) shows evident three peaks: at wave frequency ($f = 0.087\ Hz$), at twice the wave frequency ($f = 0.174\ Hz$), and at the natural frequency of the turbine ($f_n \approx 0.28\ Hz$). All of the peaks are strongly dominated by the fully nonlinear wave kinematics, regardless of the hydrodynamic loading model. The second order wave kinematics lead to the smallest first order peak at $f = 0.087\ Hz$, but reasonable second order and resonant peaks whereas linear kinematics omit them nearly completely. The second order peak at $f = 0.174$ with second order wave kinematics (SD2) is half of the one with fully nonlinear wave kinematics ($2.5 \times 10^6\ (kN)^2/Hz$ for SD2 and $4.7 \times 10^6\ (kN)^2/Hz$ for FNL), whereas the linear wave kinematics are half of second order still at $1.3 \times 10^6\ (kN)^2/Hz$.

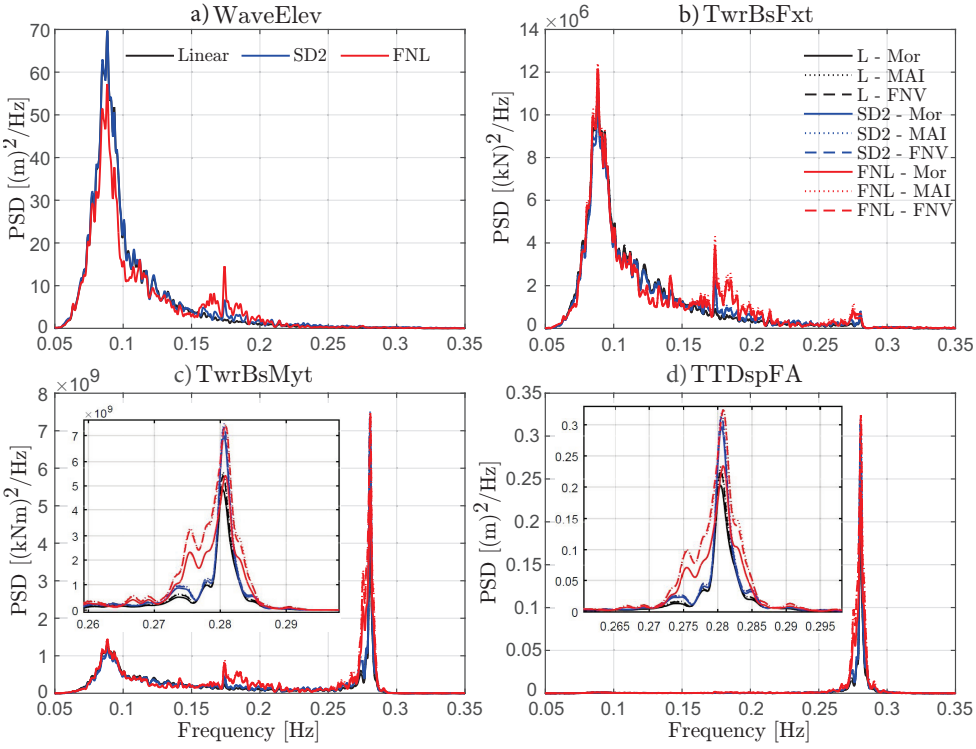

Figure 6.14: Power Spectral Density of the a) wave elevation; b) tower base shear force; c) tower base bending moment; d) tower top fore-aft displacement; for the one-hour-long rough sea study.

Similar behaviour is seen in the resonant peak around the natural frequency of the turbine $f_n = 0.28\ Hz$, where the predictions still follow the same trends dictated by the wave kinematics rather than hydrodynamic loading models: the predictions with linear wave kinematics are the lowest, with second order wave kinematics – higher, and with fully nonlinear wave kinematics – the highest.

The tower base bending moment at the mudline (Fig. 6.14c), similarly to the shear force (Fig. 6.14b), also exhibits the three peaks, but in this case it is strongly dominated by the resonant amplifications. This is a key difference compared to the case of an OWT subjected to regular waves (Section 6.2.2), where the amplifications at the third harmonic were to similar extent as the first harmonic. All loading models predict the peak at the wave frequency $f = 0.087\ Hz$ relatively similarly, while at the second order peak ($f = 0.174\ Hz$) fully nonlinear wave kinematics dominate, as seen in the shear force response (Fig. 6.14b).

The peak at the natural frequency, however, reveals interesting behaviour: while the linear and second order wave kinematics lead to more concentrated loading at exactly the given natural frequency $f_n = 0.28\ Hz$, the fully nonlinear wave kinematics lead to a much wider peak, ranging from $f \approx 0.272\ Hz$ to $f \approx 0.285\ Hz$, still with the highest peak at the resonant

frequency $f_n = 0.28\ Hz$. Such behaviour extends throughout the structural response: in the tower top displacement (Figure 6.14d) and the tower base shear force (Figure 6.14b) as well.

The influence of the hydrodynamic loading models throughout all responses (Fig. 6.14b-d) is visible as an increase in the amplitude in all harmonics. This corresponds to the behaviour seen in all previous cases, from fixed cylinder (Section 5.4) to offshore wind turbine in regular waves (Section 6.2.2). Nonetheless, the behaviour of the wave loading combinations still depends more strongly on the choice of wave kinematics, therefore it can be said that the nonlinearities in hydrodynamic loading models do not substitute the nonlinearities in wave kinematics. Both the MAI inertia-based hydrodynamic loading model and the diffraction based FNV are predicting similar overall results for each group of wave kinematics. From the overall PSD response slight differences can be observed that MAI predicts slightly higher tower base shear force (Fig. 6.14b), while FNV predicts higher tower top displacement (Fig. 6.14d). It can be justified by remembering that MAI is a second order hydrodynamic loading model whilst FNV – third (refer to Sections 4.1.2-4.1.3), and bearing in mind that tower top displacement is more third order dominated while in the tower base shear force smaller harmonics dominate.

For the tower top displacement (Fig. 6.14d) the response is concentrated nearly entirely on the resonant frequency, with the first and second order peaks barely visible. This once more illustrates how susceptible a parked offshore wind turbine is to the resonant phenomena, and the discomfort and potential danger to the maintenance workers if the sea state roughens up while fixing the nacelle in case of a turbine shut-down.

6.3.4.2 Time series of OWT response

Figure 6.15 shows the overview of the whole one-hour-long time series of this case study under rough sea conditions, where wave elevation (Fig. 6.15a), tower base shear force (Fig. 6.15b), tower base bending moment (Fig. 6.15c), and the tower top displacement (Fig. 6.15d) are shown.

First all, from the wave elevation (Fig. 6.15a) it can be seen that the waves are indeed highly nonlinear – the crests are much higher in magnitude than the troughs. The sharpest peaks can be seen the largest with fully nonlinear wave kinematics, while the lowest troughs, as expected, are predicted by the linear wave theory. The second order wave theory, in terms of the modelled wave elevation, is closer to the linear wave theory rather than fully nonlinear, especially in terms of the very low troughs.

Moreover, from the overall view of the time series of the turbine response (Figs. 6.15b-d) the discussion of the Power Spectral Density in Section 6.3.4.1 can be extended. The tower base shear force at the mudline has been seen to be dominated by the fully nonlinear wave kinematics, predicting the highest loading in most of the frequencies (see Fig. 6.14b). The time series of the same tower base shear force (Fig. 6.15b) reveal that in fact throughout the time domain the linear, second order and fully nonlinear wave kinematics predict the loading similarly, but with increasing amplitudes as the nonlinearities in wave kinematics and hydrodynamic loading models increase.

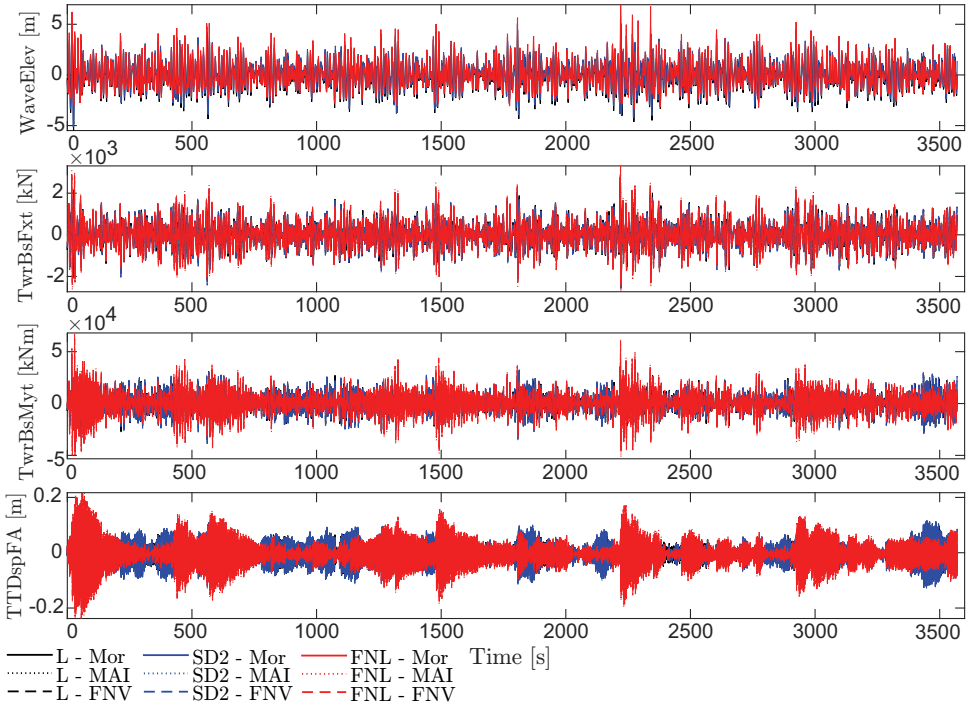

Figure 6.15: One-hour-long time series of the a) wave elevation; b) tower base shear force; c) tower base bending moment; d) tower top fore-aft displacement.

On the contrary, for the tower base bending moment and the tower top displacement, which are seen to be completely dominated by the fully nonlinear wave kinematics across the spectrum in PSD (Figs. 6.14c,d), in the time domain it is evident that the amplifications occur interchangeably in either linear/second order or in fully nonlinear waves, rather than at the same time events just of different magnitudes (see Figures 6.15c,d). This indicates that different nonlinear events were triggered by linear/second order wave kinematics, and by fully nonlinear wave kinematics. More detailed discussion in time domain is easier taking shorter time periods rather than the whole one hour, therefore the most nonlinear events are analysed separately in Section 6.3.4.3.

6.3.4.3 Nonlinear events

Wave elevation exceeds the significant wave height $H_s = 5.5\ m$ in three different events (Fig. 6.15a), therefore these three expected events of high nonlinearity are selected to be discussed in more detail, and are summarised in Table 6.1. Naturally, there are more events where the nonlinearities matter in this one hour simulation of extreme sea, but the underlying principles repeat, therefore these are considered sufficient for more detailed discussion. For easy comparison of the magnitude of each event, the y-axes of figures corresponding to time series of the events (Figs. 6.16, 6.18 and 6.21) are all fixed to the maxima and minima of every variable across the whole one-hour-long time series. The y-axes of the figures corresponding

to the Fast Fourier Transfer (FFT) analysis (Figures 6.17, 6.19 and 6.22), however, are not kept constant due to the significantly higher maximum values in Event 1.

Event no.	η_{max} [m]	Time period [s]	Figure no.	Figure of FFT
1	6.22	[0-170]	6.16	6.17
2	5.64	[1790-1940]	6.18	6.19
3	6.93	[2200-2400]	6.21	6.22

Table 6.1: Summary of most nonlinear events in the one-hour-long time series of rough sea.

Event 1 (Figs. 6.16-6.17) involves the passage of a wave train consisting of four strongly nonlinear waves, as clearly seen from the difference between the fully nonlinear wave kinematics from others in the wave elevation (see Fig. 6.16a). The fully nonlinear waves in this event, as seen from the FFT analysis in Figure 6.17a, contain a notable concentration at the third harmonic, which then triggers the resonant amplifications at the natural frequency. This is the key difference from the PSD of the full one hour series (Figure 6.14a), where the peak at the third harmonic was not visible and explains how the amplified response at the natural frequency could be triggered – by local concentration of wave nonlinearities.

In the response (Figs. 6.16b-d) small amplifications can already be seen from the impact of the first, smallest, of the waves at $t = 7.7\ s$. The impact of the second wave at $t = 18.8\ s$, the

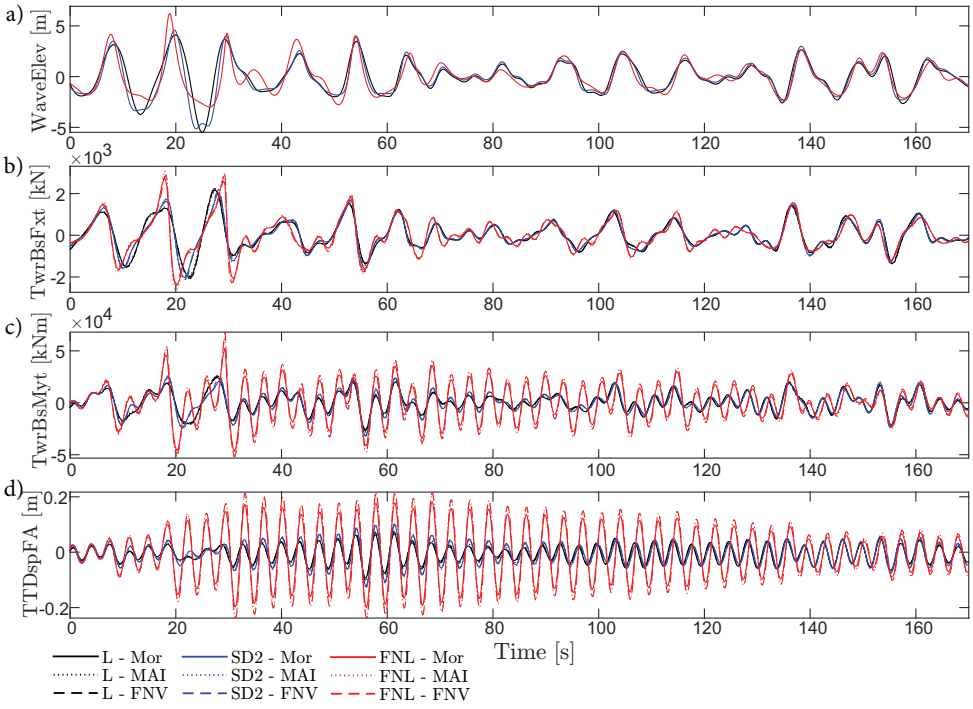

Figure 6.16: a) Wave elevation; b) tower base shear force; c) tower base bending moment; d) tower top fore-aft displacement for Event 1 of high nonlinearity.

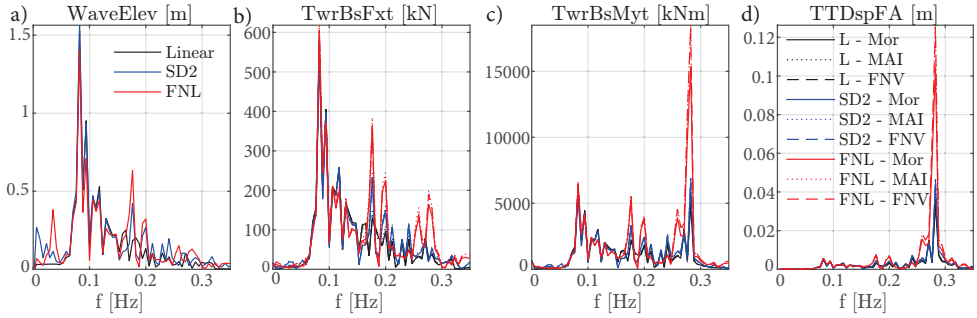

Figure 6.17: a) Wave elevation; b) tower base shear force; c) tower base bending moment; d) tower top fore-aft displacement FFT analysis for Event 1.

highest from this wave train and the second highest of the whole one-hour-long time series (refer to Table 6.1), can be seen as a strong amplification of the shear force (Fig. 6.16b), and the amplification with resulting strong oscillations in both tower base bending (Fig. 6.16c) and tower top displacement (Fig. 6.16d). However, the largest resulting impact and the highest following oscillations are observed after the third wave at $t = 29.7\ s$. In fact, the resulting tower top displacements (Fig. 6.16d) are the highest throughout the one-hour-long time series. It seems that in this case the incoming waves were phased exactly to complement each other in enhancing the response and point to the effect of wave grouping. This effect is repeated by another steeper wave at $t \approx 56\ s$, most evident in the tower top displacement (Fig. 6.16d), where the already slightly diminished response is amplified again.

In terms of the second order wave kinematics, despite the clearly more nonlinear profile of the troughs than linear waves (e.g. $t \approx 25\ s$, Fig. 6.16a), the wave profile followed linear more closely than the fully nonlinear wave profile, and the response (Figs. 6.16b-d) differed from linear with just an incremental increase in the magnitude, not nearly as excited as from the fully nonlinear wave kinematics. This is reflected well in the FFT analysis of this Event in Figure 6.17, where the difference at the natural frequency ($f = 0.28\ Hz$) of the response is more than double (Figs. 6.17b-d). Events such as this strongly contribute to the differences in the accumulated fatigue, discussed in Section 6.3.4.4.

It is also interesting to observe the phase shift between the response from fully nonlinear and other wave kinematics, most clearly visible in the tower top response (Fig. 6.16d). The strongest amplifications start in-phase at the impact of the third wave around $t = 29.7\ s$, but then, as the amplifications are left to diminish, the response from the fully nonlinear wave kinematics start lagging behind (evident around $t \approx [80 - 140]\ s$). It can be explained by the nonlinear wave celerity – as explained in Sections 3.1.2 and A.2 for Stokes regular waves, the wave celerity becomes nonlinear from the third order in wave kinematics, while linear and second order waves consider linear wave celerity.

In Event 2 (Figures 6.18-6.19) an interesting phenomenon may be observed. At the beginning of event at $t \approx 1810\ s$ all three wave kinematics are excited to the same extent and the amplifications continue. However, around $t = 1850\ s$ another steeper wave occurs. It is

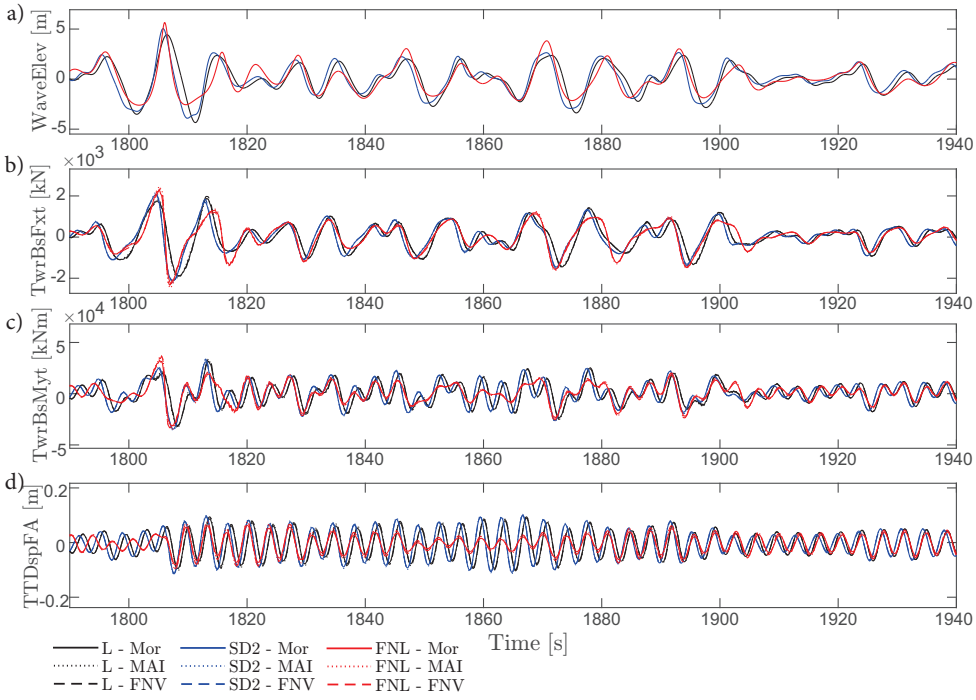

Figure 6.18: a) Wave elevation; b) tower base shear force; c) tower base bending moment; d) tower top fore-aft displacement for Event 2 of high nonlinearity.

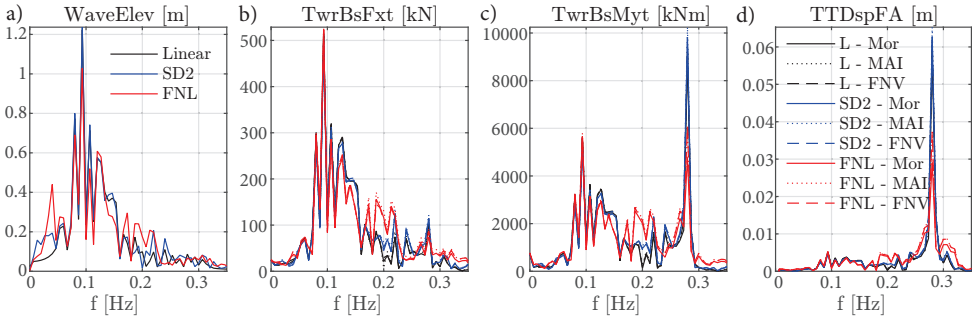

Figure 6.19: a) Wave elevation; b) tower base shear force; c) tower base bending moment; d) tower top fore-aft displacement FFT analysis for Event 2.

modelled with highest elevation by the fully nonlinear wave solver (Fig. 6.18a), and it interferes with the response, dampening the amplifications from fully nonlinear wave kinematics in the response, while the linear and second order wave-triggered amplifications proceed (Fig. 6.18b-d). In frequency domain (Figure 6.19) this leads to up to 1.7 times lower response at the natural frequency from fully nonlinear waves when compared to second order. Cases like this are not uncommon as seen in the full time series (Figure 6.15) and lead to

the fact that the PSD (Figure 6.14b-d) of the responses from fully nonlinear waves were not dramatically higher than from second order waves at the natural frequency. This shows that full consideration of the nonlinearities in wave kinematics not only models the resonant amplifications more accurately, but also does not overestimate the amplifications where they are damped out by the interference of the nonlinear waves themselves.

Another noteworthy observation in the Event 2 is that the response from linear and second order waves, regardless of the hydrodynamic loading models, is very similar: highly amplified at the natural frequency of the structure. It prompts the question of how linear wave kinematics could trigger third order oscillations, especially with linear Morison inertia term as hydrodynamic loading model. Therefore an even smaller time window was investigated in Figure 6.20, for only the wave elevation and the tower base bending moment. It can be seen from the FFT analysis of the wave elevation of this wave group (Figure 6.20a) that in fact, such wave group has energy in the third harmonic, apparently sufficient to trigger oscillations at the natural frequency. To place this event in some context, it should be noted that that these oscillations are about to the half of the extent of the oscillations triggered by the fully nonlinear waves in Event 1 in terms of tower top displacement (compare the peaks at the natural frequency in Figs. 6.19c,d with Figs. 6.17c,d).

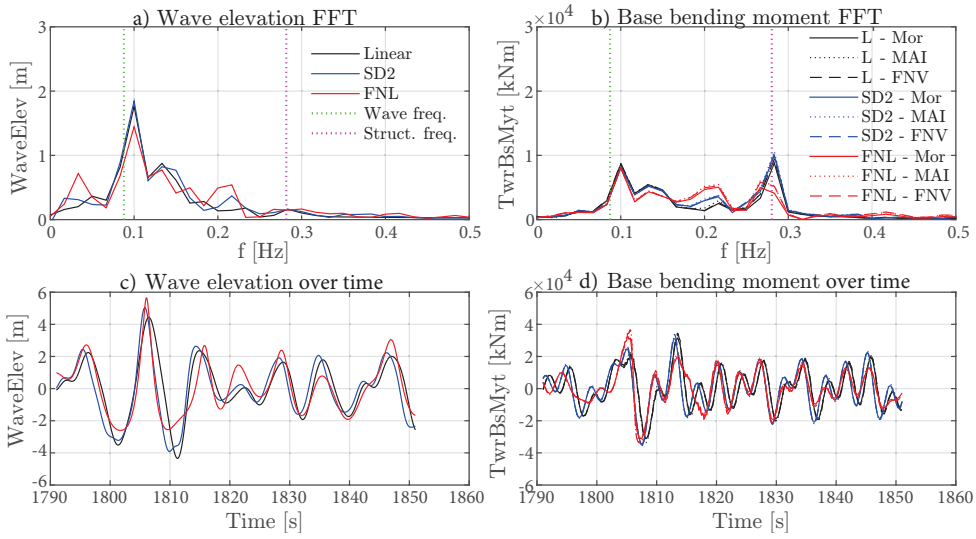

Figure 6.20: FFT analysis of a short time window for wave grouping. In frequency domain: a) wave elevation; b) tower base bending moment; and in time domain: c) wave elevation; d) tower base bending moment.

Moreover, the close up of the nonlinear wave train in Figure 6.20c reveals another effect of wave grouping. The second wave of the wave train, at $t \approx 1815\ s$, for both linear and second order wave kinematics causes an even larger base bending moment response (Fig. 6.20d) than the first, much higher wave at $t = 1806\ s$. For the fully nonlinear wave kinematics, however, the peak of the second wave comes in slightly later than that of the linear and second order (see $t \approx 1815\ s$ in Fig. 6.20c), therefore the impact from this wave does not coincide with

the amplification from the previous wave as it did for the linear and second order response, but rather comes in as a smaller peak during the decline of the loading (see $t \approx 1815\ s$ in Fig. 6.20d), resulting in smaller amplifications seen in the FFT of the base bending moment (Fig. 6.20b). Lastly, all of these observations hold true regardless of the hydrodynamic loading model, the nonlinearities in which only slightly increase the amplitude of the response, but do not influence the behaviour to an extent as the choice of wave kinematics does.

Event 3 (Figures 6.21-6.22) contains the highest wave of the whole one-hour-long wave train reaching elevation of nearly $7\ m$ (see Table 6.1). The impact from such a steep and high wave results in the highest tower base shear force of the whole time series. The tower base bending moment and tower top displacement, however, do not exceed their maximum reached during Event 1 (Fig. 6.16), where the wave train accumulated higher amplitudes of the response. The wave profile of the steepest wave ($t = 2220\ s$) is very different for each considered kinematics, with second order having a sharper crest than linear, and fully nonlinear wave even sharper still (Fig. 6.21a). This led to different responses (Figures 6.21b-d): second order is amplified visibly higher than linear, but still not as strongly as the response from fully nonlinear waves.

The FFT analysis of Event 3 (Figure 6.22) shows that the difference between fully nonlinear wave input and the other wave kinematics is the most significant – up to four times in terms of

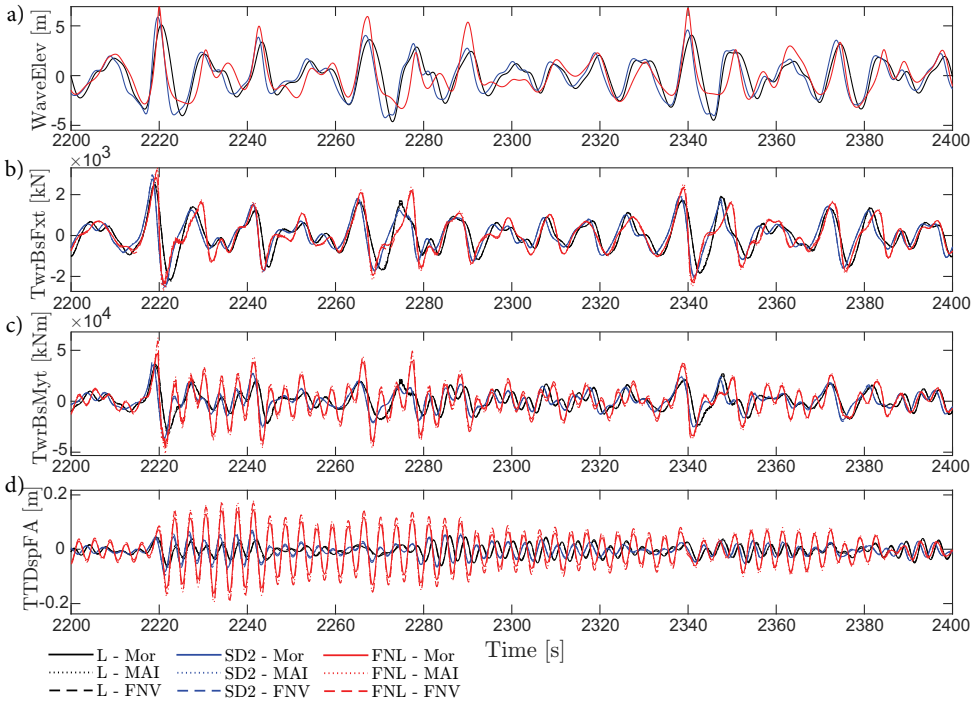

Figure 6.21: a) Wave elevation; b) tower base shear force; c) tower base bending moment; d) tower top fore-aft displacement for Event 3.

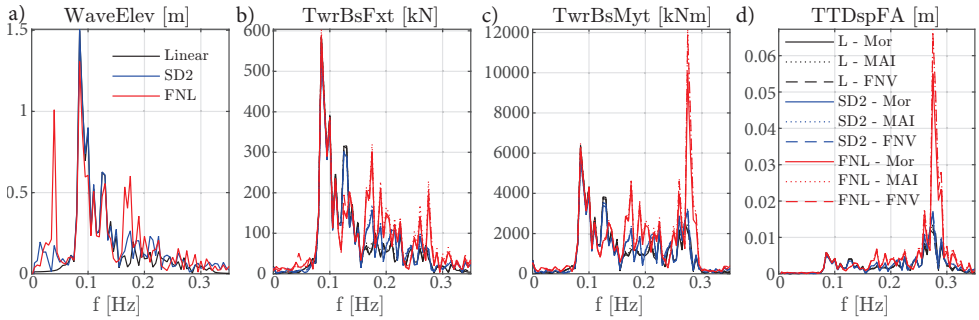

Figure 6.22: a) Wave elevation; b) tower base shear force; c) tower base bending moment; d) tower top fore-aft displacement FFT analysis for Event 3.

tower base bending moment (Fig. 6.22c) and tower top displacement (Fig. 6.22d). In these responses the nonlinearities in the hydrodynamic loading loading models, especially with fully nonlinear wave kinematics, become also significant: MAI and FNV loading models lead to 1.2 times higher response at the natural frequency of the turbine $f_n = 0.28\ Hz$ than with Morison inertia hydrodynamic loading model.

Finally, Event 3 (Fig. 6.21) shows a combination of the effects, previously discussed in Events 1 and 2. Firstly, the amplifications triggered by the steepest wave at $t = 2220\ s$ experience constructive interference from a much smaller wave at $t = 2230\ s$, and then a destructive interference of a steeper wave at $t = 2243\ s$. The latter is much more significant for linear and second order waves rather than fully nonlinear. It is followed by strongly destructive interference for another steep wave at $t = 2290\ s$, and a complete reduction of oscillations for fully nonlinear wave kinematics from one of the steepest waves ($\eta = 6.78\ m$) at $t = 2340\ s$, and another prompt of oscillations from a significantly smaller wave at $t = 2350\ s$. The noteworthy difference in the response from two of the steepest waves: wave with peak elevation $\eta = 6.9\ m$ at $t = 2220\ s$ triggers the strong oscillations, while the wave with peak at $\eta = 6.78\ m$ at $t = 2340\ s$ dampens all the remaining oscillations. It shows that the triggered response depends not solely on the size of the impacting wave, but also on its position on the wave train.

This difference is investigated in the sliding FFT analysis for the wave elevation and tower base bending moment, similarly to Fig. 6.20. In Fig. 6.23a the wave group including the highest wave at $t = 2220\ s$ is shown, while Fig. 6.23b shows the wave group around the second highest wave at $t = 2340\ s$. It can be seen that the first wave group in Fig. 6.23a has a third order peak in the wave elevation at the structural frequency, and triggers resonant response precisely at the structural frequency as well. However, for the second wave group shown in Figure 6.23b, the third order peak occurs at slightly lower than the structural frequency, and the response is amplified at the frequency lower than the structural as well. It seems that such wave groups are responsible for the wider peak around the natural frequency in the PSD of the whole one hour time series in Figures 6.14b-d.

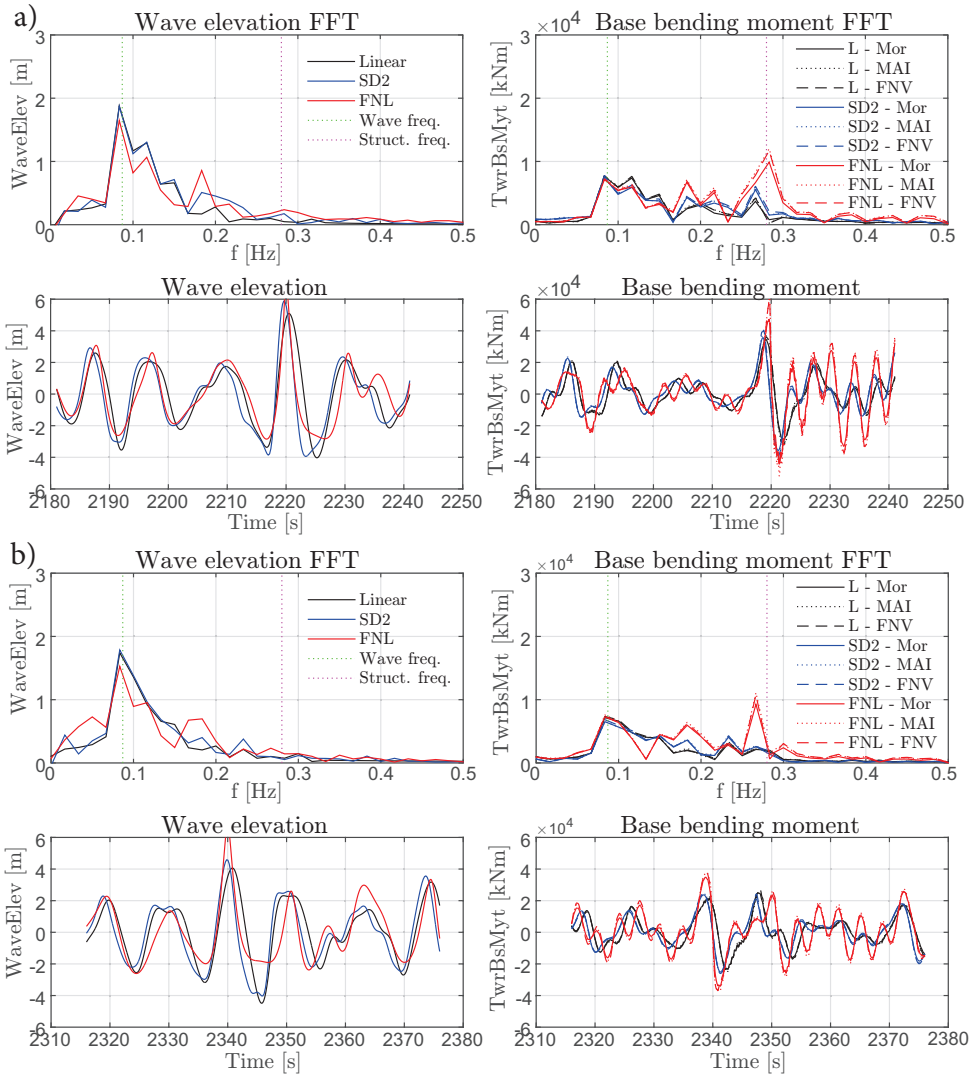

Figure 6.23: Captures of the sliding FFT analysis: a) with the peak wave of Event 3 at $t = 2220\ s$; b) with the second highest wave of Event 3 at $t = 2340\ s$.

6.3.4.4 *Accumulated fatigue damage*

As discussed in Section 6.3.4.1, even though this sea state is extremely rough, it has around 14% probability of occurrence in the North Sea (Table 2.3 in Faltinsen (1990)). In case of a non-operational wind turbine, presumably due to breakdown, the maintenance workers would not be able to access it until the sea is calmer because the wave height limit for the mobilisation window (the time that the maintenance crew transfer vessel is in the sea) is 1.5 *m* (Catterson et al., 2016). Therefore the assumption that the turbine would be subjected to one hour of rough sea state in parked condition is reasonable.

Equivalent Fatigue Loads To assess the fatigue damage to the turbine of this realistic case of one hour of shutdown time during a rough sea state, the equivalent fatigue loads (*EFL*) of the tower base bending moment (TwrBsMyt) are used. They are calculated with the standard rainflow cycle counting algorithm with the fatigue exponent parameter $m = 3$.

Moreover, a comparison between the discussed loading models and the most traditionally used wave loading model were conducted. The reference loading model was taken as linear wave kinematics (described in Section 3.2.1), used as input to the full Morison equation with both linear inertia ($C_m = 2$) and quadratic drag ($C_d = 1$), as described in Equation 4.1. The comparison is conducted by the use of percentage difference in *EFL*, named ΔEFL and calculated with Equation 6.2. The results of both *EFL* and ΔEFL are given in Table 6.2.

$$\Delta EFL = \frac{EFL_{InvestigatedModel} - EFL_{LinearMorison}}{EFL_{LinearMorison}} \times 100, \tag{6.2}$$

where $EFL_{InvestigatedModel}$ is the *EFL* of the investigated model, while the $EFL_{LinearMorison}$ is the *EFL* of the commonly used combination of the linear wave kinematics and full Morison formulation (Eq. 4.1).

	EFL [MNm]			ΔEFL [%]		
	Mor	MAI	FNV	Mor	MAI	FNV
L	18.6	19.4	19.2	0.1	4.7	3.7
SD2	24.9	25.6	25.1	34.2	38.3	35.3
FNL	24.2	28.1	28.0	30.6	51.4	50.9

Table 6.2: Summary of the Equivalent Fatigue Loads *EFL* and their percentage differences ΔEFL of the tower base bending moment for one hour of rough sea.

First of all, it can be seen that both the nonlinearities in wave kinematics (SD2 and FNL compared to L) and in hydrodynamic loading models (MAI and FNV compared to Mor) increase the final fatigue load. Nonetheless, the importance of nonlinearities in wave kinematics in this rough sea state in intermediate water depth is more significant than those from hydrodynamic loading models (difference in the final accumulated fatigue loads during the one hour study is of up to 5% with nonlinear hydrodynamic loading models on linear wave kinematics, while the difference by using other wave kinematics can be up to 35%).

The combined nonlinearities lead to the highest overall loading – up to 50% higher loading accumulated with fully nonlinear wave kinematics and nonlinear hydrodynamic loading models compared to the full Morison formulation with linear wave kinematics as input. Moreover, the neglection of drag in the Morison equation in fact led to 0.1% higher equivalent fatigue loads with the same linear wave kinematics. "Mor" loading model used in this study is Morison inertia term only (Eq. 4.2), while the comparison is conducted with the full Morison formulation including drag as per Equation 4.1, showing the damping effect of the drag term in this rough sea state.

Lastly, the fact that the second order wave kinematics over this one hour long study predicted the accumulated fatigue closer to fully nonlinear waves rather than linear waves, shows the significant improvement by stepping up from linear wave kinematics to even weakly nonlinear wave solvers.

Damage Equivalent Loads To compare the loading models in a more neutral way – over the same amount of cycles rather than the same amount of time – Damage-Equivalent Load (*DEL*) is used, already introduced in the study on wind-wave misalignment (Section 6.3.2). It is related to the equivalent fatigue loads (*EFL*) by the normalisation over chosen number of cycles $N^* = 1000$ with the fatigue exponent parameter $m = 3$, same as for the *EFL* (Marino et al., 2017). The relation is defined by equation: $DEL = EFL \times (N/N^*)^{(1/m)}$. The percentage difference to assess the impact of nonlinearities, similarly to *EFL*, is calculated by Equation 6.3. The results for both *DEL* and ΔDEL are summarised in Table 6.3.

$$\Delta DEL = \frac{DEL_{InvestigatedModel} - DEL_{LinearMorison}}{DEL_{LinearMorison}} \times 100, \tag{6.3}$$

where $DEL_{LinearMorison}$ is the damage-equivalent load computed with Morison equation (both inertia and drag as per Eq. 4.1) with linear wave kinematics (Section 3.2.1) as input, while $DEL_{InvestigatedModel}$ is the damage-equivalent load accumulated with any of the investigated wave loading models, where Mor stands for Morison linear inertia term only (Eq. 4.2).

	DEL [MNm]			ΔDEL [%]		
	Mor	MAI	FNV	Mor	MAI	FNV
L	22.7	23.6	23.4	-0.8	3.0	2.2
SD2	24.7	25.4	25.5	7.8	11.1	11.3
FNL	29.2	33.2	32.8	27.7	45.1	43.4

Table 6.3: Summary of the Damage Equivalent Loads *DEL* and their percentage differences ΔDEL of the tower base bending moment for 1000 cycles.

The overall trends of loading increasing with consideration of both nonlinearities in wave kinematics and in hydrodynamic loading models are similar to the findings for the Equivalent Fatigue Loads. Nonetheless, there are some key differences. Firstly, contrary to the loading over the same amount of time, the Morison equation without drag term results in reduction of loading because the drag term adds the loading from viscous forces, leading to higher overall loading in the same amount of cycles (0.8% higher loading with the drag term over 1000 cycles compared to 0.1% higher loading without the drag term over one hour of sea state, see Tables 6.2-6.3). Moreover, the loading from second order waves over the same amount of cycles results in closer loading to linear waves rather than fully nonlinear – with difference from Morison equation with linear wave kinematics between 8-11%, while fully nonlinear wave kinematics cause a 28-45% difference. The difference from fully nonlinear wave kinematics overall is slightly lower for 1000 cycles rather than for this specific one hour of sea, around 28-45% rather than 31-51% (see Table 6.2).

6.4 Conclusions of the Chapter

This chapter discussed the dynamic structural response to wave loading in increasingly complex conditions: simplified one-degree-of-freedom cylinder subjected to regular waves, full scale offshore wind turbine in regular waves, and the full scale offshore wind turbine in irregular seas. The following conclusions have been drawn:

- One-degree-of-freedom cylinder in regular waves:
  - In comparison with past experimental data the importance of structural damping on the structural motion rather than loading, and the importance of choosing appropriate coefficients for the semi-empirical loading models was stressed.
  - The numerical study in very steep waves revealed the sensitivity of the natural frequency of offshore structures to the nonlinear fluid-structure interaction which is considered only by FNV and MAID hydrodynamic loading models. Its influence on the magnitude of the resonant response was found to the extent of nearly double the loading predictions.
- Non-operational offshore wind turbine subjected to regular wave loading:
  - Despite the more complex geometry and multiple degrees of freedom of the offshore wind turbine, the results show the same trends as wave loading models on a fixed cylinder, allowing to extend the findings on behavioural trends to the more complex study.
  - The importance of wave kinematics over hydrodynamic loading models was observed to prevail even when the structural motion was accounted for, and the limitations of linear wave theory in intermediate water depth were enforced.
  - It was predicted that the tower base shear force is least affected by the resonant phenomenon, tower base bending moment gets amplified on all three of the first harmonics, and that the tower top displacement is most affected with up to four times higher displacements in the third harmonic compared to the first.
  - Due to the significantly higher loading and response predictions caused by the surface distortion term D in increasingly steep waves, its suitability, especially in combination with nonlinear wave kinematics, is doubted also on an offshore wind turbine.
- Full scale offshore wind turbine in irregular waves:
  - An identified gap in knowledge was closed by finding that an operating offshore wind turbine in the case of wind-wave misalignment does become more sensitive to wave nonlinearities due to the reduced aerodynamic damping. However, the increase in damage is minor compared to the critical case of a non-operational wind turbine subjected to aligned wind and wave loading, therefore this case was modelled in the rest of the studies.
  - Limitations of the wave loading models for the monopile-supported offshore wind turbine in intermediate water depth were noted in a study over increasing wave steepness as: Tayfun steepness $\mu_m \approx 0.03$ for linear wave kinematics, $\mu_m \approx 0.08$ for the second order wave kinematics, and $\mu_m \approx 0.06$ for the surface distortion term D.
  - A case study under rough sea conditions confirmed that the nonlinearities in wave kinematics are predominant in intermediate water depth, thus the nonlinearities in the hydrodynamic loading models do not compensate for the nonlinearities in wave kinematics. Therefore another open scientific question was answered: ringing on monopile-supported OWTs is omitted with second order wave kinematics regardless of the hydrodynamic loading model, requiring the use of fully nonlinear wave kinematics in order to capture the highly nonlinear phenomena.

Chapter 7

Conclusions

7.1 Achievements

This thesis discussed the wave loading on slender bottom-fixed surface-piercing monopiles with the application to offshore wind turbines. It was aimed at discovering the most efficient combination of wave kinematics and hydrodynamic loading models for the specific wave and monopile conditions, especially at the steeper waves where the wave theories and loading models tend to lose validity and the structure is prone to dangerous nonlinear effects.

Literature review (Chapters 1-2) revealed more gaps in knowledge which were investigated in addition to the main scientific question stated in the first paragraph:

1. whether an operational wind turbine could be as sensitive to wave nonlinearities as a parked one due to the reduced aerodynamic damping in the case of wind-wave misalignment;
2. whether second order irregular wave kinematics in combination with a more sophisticated hydrodynamic loading model could capture ringing which has only been hitherto captured by significantly more computationally intensive fully nonlinear wave kinematics;
3. whether the newly developed finite-depth FNV hydrodynamic loading model would capture the secondary load cycle in a two-dimensional study.

Wave kinematics			Hydrodynamic loading models	& Structure	
Regular	Linear	Linear Airy	Morison MAI MAID FNV	Fixed	Fixed cylinder
	Weakly nonlinear	Stokes 2nd order		Moving	1DOF cylinder
		Stokes 3rd order			
		Stokes 5th order			
	Fully nonlinear	Rienecker-Fenton		Moving (FAST)	Parked 5-MW OWT
		Fully nonlinear periodic BEM			
Irregular	Linear	Linear superimposition	Morison MAI MAID FNV	Moving (FAST)	5-MW offshore wind turbine
	Weakly nonlinear	Second order Sharma-Dean			
	Fully nonlinear	Fully nonlinear BEM with ramp			

Table 7.1: Summary of wave loading model combinations and the structures they are tested on. BEM – Boundary Element Method model; FAST – hydro-aero-servo-elastic solver used in this thesis; 1DOF – one-degree-of-freedom; OWT – offshore wind turbine.

The study grid in Table 7.1 summarises the increasing levels of nonlinearity in wave kinematics (Chapter 3), hydrodynamic loading models and offshore structures (Chapter 4) which were implemented in this thesis. Notable due to their novelty are:

- fully nonlinear BEM kinematics, for which in regular waves periodic boundary conditions were implemented overcoming a compatibility issue between them and the potential continuity in corners;
- implementation and discussion of the finite-depth FNV hydrodynamic loading model since it was only derived for fixed cylinders by Kristiansen and Faltinsen (2017), whereas the derivation for a moving body was acquired via private communication with prof. Faltinsen, who extended it in August 2018 (Faltinsen, 2018);
- incorporation of the more nonlinear hydrodynamic loading models, MAID and finite-depth FNV, in the aero-hydro-servo-elastic solver FAST to model the 5-MW monopile-supported offshore wind turbine.

The main findings of the thesis are summarised separately for each key phase of the study.

Chapter 5 – Regular wave loads on a fixed cylinder:

- Distinct influences of nonlinearities were determined as:
  - Nonlinearities in wave kinematics cause a reduction in the first harmonic and an increase in the higher harmonics;
  - Nonlinearities in hydrodynamic loading models increase all harmonics;
  - Combined nonlinearities lead to the highest loading in the higher harmonics.
- Nonlinearities in wave kinematics are more significant in intermediate water depth while nonlinearities in hydrodynamic loading models – in deep water.
- Numerical wave loading predictions were seen to increase monotonically with increasing wave steepness in all harmonics whilst experimental behaviour in higher harmonics is reported to increase with a slower trend. This leads to an increasing overestimation of loading from steeper waves.
- The surface distortion term leads to strong overprediction in the steepest waves. It was deemed unsuitable from wave steepness $kA \approx 0.3$ but was seen to deviate already from $kA \approx 0.2$, where other hydrodynamic loading models capture the experimental loading better.
- The secondary load cycle has been confirmed to be omitted in the two-dimensional domain by all of the compared numerical loading models, including the newly derived finite-depth FNV theory which considers wave diffraction.

Chapter 6, Sections 6.1-6.2 – Moving structures in regular waves:

- Importance of structural damping was found to be more significant on the resultant cylinder motion rather than the loading on the cylinder.
- Natural frequency of offshore structures was found to be affected by the nonlinear fluid-structure interaction, therefore considering free surface nonlinearities with regards to the design frequency is critical to avoid underestimation of the resonant amplifications to the extent of half the loading predictions in extreme waves.

- The behaviour of wave loading models on offshore wind turbine in parked configuration follows the same trends as on a cylinder, allowing to extend the findings from the fundamental phases of the thesis to the application on an offshore wind turbine in irregular seas.
- Most sensitive to the resonant amplifications at the third harmonic were the tower base bending moment (to similar values as the first harmonic) and the tower top displacement (up to four times of the first harmonic), both of which are key to structural integrity and safety of on-site workers.

Chapter 6, Section 6.3 – Offshore wind turbine in irregular seas:

- Sensitivity of an operating wind turbine to wave nonlinearities increases with increasing wind-wave misalignment angles due to reduced aerodynamic damping. However, non-operational co-aligned case remains the most critical configuration in terms of sensitivity to wave nonlinearities.
- The suitability of wave loading models over increasing wave steepness can be summarised as:
  - Linear wave kinematics resulted in significant underestimation of wave loading already from Tayfun steepness $\mu_m \approx 0.03$;
  - Second order wave kinematics were limited to Tayfun steepness $\mu_m = 0.08$ above which they tended towards overprediction;
  - The loading from fully nonlinear waves was reduced by the use of smoothing, therefore was increasing slower than wave steepness;
  - Hydrodynamic loading model MAID strongly overpredicted the wave loading from $\mu_m \approx 0.06$, therefore was excluded from case study in rough sea.
- Case study of a non-operational offshore wind turbine in rough sea and intermediate water depth resulted in the following findings:
  - The nonlinearities in irregular wave kinematics were more significant than the nonlinearities in wave loading models. The nonlinearities in hydrodynamic loading models do not substitute the nonlinearities in wave kinematics in intermediate water depth.
  - Linear wave kinematics, as expected, lost validity and underperformed. Second order wave kinematics provided a significant improvement compared to linear wave kinematics. Nonetheless, to fully capture the nonlinear phenomena in the wave loading fully nonlinear wave kinematics are required.
  - Nonlinear hydrodynamic loading models resulted in notable increase in the accumulated fatigue loads compared to the commonly implemented Morison equation, especially in combination with nonlinear wave kinematics. Both MAI and FNV loading models predicted similar increase.
  - Effect of wave grouping was noted: a group of steep linear and second order waves was seen to gather enough energy to trigger oscillations at third harmonic with linear hydrodynamic loading models, while in fully nonlinear modelling wave grouping was seen to both amplify and diminish the resonant oscillations.

7.2 Implication of the results

The impact of the results on the design recommendations for monopile-supported offshore wind turbines can be summarised as follows.

The findings of this thesis stress that for intermediate water depth, where monopile supported offshore wind turbines are normally installed, nonlinearities in wave kinematics are predominant. Therefore as the wave steepness increases, or as more extreme sea states are considered, increasingly nonlinear wave kinematics are required.

The limitations of linear wave theory were stressed, and while the consideration of more nonlinear hydrodynamic loading models increased the predicted loading, their influence is not sufficient to compensate for the lack of nonlinearities in wave kinematics. Therefore to model the wave loading in rough seas more accurately and to avoid omitting nonlinear phenomena, fully nonlinear wave kinematics are critical. In the cases where modelling fully nonlinear wave kinematics is unavailable or unfeasible, more computationally efficient second order irregular waves have been shown to lead to significant improvement from linear wave kinematics, regardless of the hydrodynamic loading model. However, it should be noted that the second order irregular wave solver tends towards overestimation of the loading in very steep waves.

In terms of the hydrodynamic loading models, the difference in the final loading was not found to be as influential as the choice in wave nonlinearities in intermediate water depth. Nonetheless, throughout the fundamental studies the finite-depth FNV theory has stood out as the one which accounts for the most of physical phenomena. It is the only slender-body theory to include diffraction, which may become relevant as the monopiles for offshore wind turbines increase in size. Moreover, it was one of the two hydrodynamic loading models to consider nonlinear fluid-structure interaction in terms of the effect on the natural frequency of the offshore system. Furthermore, it was seen to perform well in most of wave and cylinder conditions, whereas MAID model was limited in the highest steepness. Therefore the finite-depth FNV would be the recommended hydrodynamic loading model to account for the highly nonlinear fluid-structure interaction to which offshore structures are subjected in rough seas.

7.3 Future work recommendations

Experimental campaign

The findings of the thesis could be greatly complemented by an experimental campaign dedicated to study the influences of nonlinearities in wave kinematics and in hydrodynamic loading models. A systematic experimental study to consistently fill the (kA, kR)-grid in the same cylinder and water depth conditions would provide more concrete recommendations. This rings especially true in the case of moving cylinder in regular waves, where only one experimental study suitable for comparison has been found, and only in relatively low steepness while higher steepness settings are where resonant effects would be expected. Lastly, experiments on a monopile-supported offshore wind turbine in a range of wave conditions would give a more solid basis for the discussion on the suitability of the wave loading models.

CFD study

Computational Fluid Dynamics (CFD) studies could also provide a much deeper insight in the physical and three-dimensional phenomena occuring around the cylinder, especially such as vortex shedding. Nonetheless, a well-conducted CFD study requires not only a significant amount of time, but also experimental results for validation, therefore could only be conducted in parallel with an experimental campaign.

Flexible cylinder

The most straightforward improvement would be the implementation of a flexible cylinder in the current solver. As discussed in Section 4.2.1, the one-degree-of-freedom moving cylinder model with a rigid cylinder on a spring recreates only the first mode of structural deflection, while a bottom-fixed flexible cylinder would capture the higher modes as well, recreating the structural behaviour of an actual offshore wind turbine better. Moreover, it would allow for a more direct comparison with numerous experiments on a flexible cylinder, especially in irregular waves.

Sloping bottom

The majority of monopile-supported offshore wind turbines are placed in shallow to intermediate waters, where the seabed slopes and the waves become increasingly nonlinear. A sloping bottom feature in the numerical BEM solver would allow for the shoaling effect to develop and for the waves to become naturally more nonlinear when transitioning from deep water towards shallow. Moreover, addition of sloping bottom would open additional resources of past experimental data on ringing-related experiments in wave tanks.

Real-life data on full-size turbine response

Despite the growing number of monopile-supported offshore wind farms, the only real-life data freely accessible for the scientific community are the environmental statistics from the FINO site (FINO, 2018). Measurements are being taken on the offshore wind turbines as well, but during the duration of this thesis no successful contacts have been made to acquire this often confidential data. Moreover, it is worth noting that for a meaningful comparison the geometry of the wind turbines on site would need to be obtained as well, in order to be implemented in FAST or another hydro-aero-servo elastic solver, making it a difficult task without a collaboration with industry. However, acquiring the observed data on a real-size monopile-supported offshore wind turbine could give a significantly more solid validation of numerical loading models and provide actual statistics of the occurrence of nonlinear resonant effects.

Investigation of the non-monotonic growth of loading with increasing steepness

As discussed in Section 5.6, the experimental loading was not seen to grow proportionally with the increasing wave steepness as the numerical loading models do, therefore leading to an increasing overestimation of loading as the wave steepness grows. Understanding these nonlinearities and accounting for them could help to avoid overdesigning.

Truncation of the FNV method

FNV method is a third-order perturbation theory, therefore to ensure that the finite-depth FNV method is working according to its derivation, only the forcing components to third order should be kept. As discussed in Kristiansen and Faltinsen (2017), the scattering potential is correct to only third order only, and all the higher nonlinearities are stemming only from the indicent wave potential. Even though the theory is applicable to regular and irregular waves as well as numerical wave tanks (Kristiansen and Faltinsen, 2017), an analytical truncation of the theory at the loading components up to third order, when both the nonlinearities in the wave kinematics and in the FNV theory are considered, could provide the best behaviour of this method.

Fully nonlinear loading models

Cai & Melum (1996) and Ferrant (1998) proposed fully nonlinear loading models in comparison to the weakly nonlinear perturbation theories as FNV and M&M. According to Huseby and Grue (2000), Ferrant's "results could not be obtained for wave slopes larger than $Ak = 0.145$", which is not as steep as the wave conditions in which ringing and secondary load cycle occur. However, these models are not implemented and widely discussed in literature, therefore remain an area which could be explored further.

Soil-structure interaction

The interaction between the soil and the support structure is a crucial factor in the restoring forces from all the environmental loads on the offshore structure, but since it was not the focus of this doctoral work, it was simplified to the one-degree-of-freedom spring with stiffness in the moving cylinder (Section 6.1), and was left as the default apparent fixity model in the FAST solver for the full offshore wid turbine (Sections 6.2-6.3). However, more nonlinear soil-structure interaction models lead to fewer discrepancies, and it has been shown that especially the peak displacements are affected – they were up to 50% higher when nonlinear soil properties were considered, regardless of the nonlinearities in the wave kinematics (Schafhirt et al., 2016). Implementation of a more nonlinear soil-structure interaction model, such as coupled or distributed springs, would lead to more reliable findings.

Appendix A

Useful equations and coefficients for analytic wave portrayal

This appendix provides more details on the analytical description of waves, including main useful equations and coefficients for weakly nonlinear waves.

A.1 Main equations

There are some useful universal equations in wave kinematics which are valid regardless of the order of nonlinearity:

- $k = 2\pi/\lambda$, where k is the wave number and λ is the wavelength.
- $\omega = 2\pi/T$, where ω is the angular frequency and T is the wave period.
- $c = \lambda/T = \omega/k$, where c is the phase velocity.

Other useful equation for regular waves is the linear dispersion relation for intermediate water depth connecting the wave number k and angular wave velocity ω:

- $\omega^2 = gk \tanh(kh)$.

For irregular waves the steepness kA cannot be directly applied, therefore Tayfun steepness μ_m is used. It is defined as:

- $\mu_m = k\sigma$, where:
  - $k = \omega_m^2/g$ for deep water, but for intermediate water depth it is derived from the linear dispersion $\omega_m^2 = gk \tanh(kh)$;
    - ω_m is the mean wave frequency defined as $\omega_m = m_1/m_0$, where
    - $m_j = \int S(\omega)\omega^j d\omega$ are the spectral moments.
  - $\sigma = \sqrt{\overline{\eta}^2} = H_s/4$;
    - $\overline{\eta}^2$ is the square of the mean wave elevation; and
    - H_s is the significant wave height.

A.2 Stokes wave theory

The main equations for wave elevation and potential for Stokes weakly nonlinear regular waves (Stokes, 1847; Stokes, 1880), previously listed in Section 3.1.2, are the following:

$$\eta_{Stokes^N}(x,t) = \frac{1}{k}\sum_{n=1}^{N}\varepsilon^n \sum_{m=1}^{N} B_{(n,m)} \cos(m\Theta),$$

and

$$\varphi_{Stokes^N}(x,z,t) = \frac{c}{k}\sum_{n=1}^{N}\varepsilon^n \sum_{m=1}^{N} A_{(n,m)} \cosh(mk(z+h)) \sin(m\Theta),$$

where:

- N is the order of truncation, $N = [2, 3, 5]$ in this study;
- h is the water depth;
- k is the wave number, determined from the linear dispersion relation for intermediate water depth for this study;
- $\Theta = kx - \omega t$, where $\omega = 2\pi/T$ with T being the wave period;
- $\varepsilon = kA$, where A is the wave amplitude.
- c is the nonlinear celerity found from the equation $c^2 = c_0^2(1 + \varepsilon^2 C_1 + \varepsilon^4 C_2)$, where:
  - $c_0^2 = (g/k)\tanh kh$ is the celerity from the linear wave theory with g standing for the gravitational constant,
  - C_1 and C_2 are non-dimensional coefficients listed in Subsection A.2.1.
- $A_{(n,m)}$ and $B_{(n,m)}$ are non-dimensional coefficients listed in the Subsection A.2.1, with the ones not listed being equal to zero.

A.2.1 Stokes coefficients

The following coefficients are reported from the fifth order Stokes theory described by Skjelbreia and Hendrickson (1961), although they are widely available in other sources too, such as textbook by Chakrabarti (1987). Nonetheless, as pointed out by Kristiansen and Faltinsen (2017), among others, the expression for C_2 contains a wrong sign in front of number 2592. Here the coefficients are given with the signs corrected to the best of the author's knowledge.

The coefficients are dependent on wave number k and water depth h in terms of $S = \sinh kh$ and $C = \cosh kh$.

$$A_{11} = 1/S$$

$$A_{13} = \frac{-C^2(5C^2+1)}{8S^5}$$

$$A_{15} = \frac{-(1184C^{10} - 1440C^8 - 1992C^6 + 2641C^4 - 249C^2 + 18)}{1536S^{11}}$$

$$A_{22} = \frac{3}{8S^4}$$

$$A_{24} = \frac{(192C^8 - 424C^6 - 312C^4 + 480C^2 - 17)}{768S^{10}}$$

$$A_{33} = \frac{(13 - 4C^2)}{64S^7}$$

$$A_{35} = \frac{(512C^{12} - 4224C^{10} - 6800C^8 - 12,808C^6 + 16,704C^4 - 3154C^2 + 107)}{4096S^{13}(6C^2 - 1)}$$

$$A_{44} = \frac{(80C^6 - 816C^4 + 1338C^2 - 197)}{1536S^{10}(6C^2 - 1)}$$

$$A_{55} = \frac{-(2880C^{10} - 72,480C^8 + 324,000C^6 - 432,000C^4)}{61,440S^{11}(6C^2 - 1)(8C^4 - 11C^2 + 3)} +$$
$$+ \frac{-(163,470C^2 - 16,245)}{61,440S^{11}(6C^2 - 1)(8C^4 - 11C^2 + 3)}$$

$$B_{11} = 1$$

$$B_{22} = C\frac{(2C^2+1)}{4S^3}$$

$$B_{24} = \frac{C(272C^8 - 504C^6 - 192C^4 + 322C^2 + 21)}{384S^9}$$

$$B_{33} = \frac{3(8C^6+1)}{64S^6}$$

$$B_{35} = \frac{(88,128C^{14} - 208,224C^{12} + 70,848C^{10})}{12,288S^12(6C^2-1)} +$$
$$+ \frac{(54,000C^8 - 21,816C^6 + 6264C^4 - 54C^2 - 81)}{12,288S^{12}(6C^2-1)}$$

$$B_{44} = \frac{C(768C^{10} - 448C^8 - 48C^6 + 48C^4 + 106C^2 - 21)}{384S^9(6C^2-1)}$$

$$B_{55} = \frac{(192,000C^{16} - 262,720C^{14} + 83,680C^{12})}{12,228S^{11}(6C^2-1)(8C^4-11C^2+3)} +$$
$$+ \frac{(20,160C^{10} - 7280C^8 + 7160C^6 - 1800C^4 - 1050C^2 + 225)}{12,228S^{11}(6C^2-1)(8C^4-11C^2+3)}$$

$$C_1 = \frac{(8C^4 - 8C^2 + 9)}{8S^4}$$

$$C_2 = \frac{(3840C^{12} - 4096C^{10} - 2592C^8 - 1008C^6 + 5944C^4 - 1830C^2 + 147)}{512S^{10}(6C^2-1)}$$

A.3 Transfer functions for the second order Sharma-Dean waves

These transfer functions have been derived by Sharma and Dean (1981), in order to model second order nonlinear irregular waves. Bearing in mind that $R_m = k_m \tanh k_m h$, and $k^{\pm}_{mn} = |k_m \pm k_n|$, the transfer functions used in Equations 3.12 and 3.13 are:

$$D^+_{mn} = \frac{\left(\sqrt{R_m}+\sqrt{R_n}\right)\left\{\sqrt{R_n}\left(k_m^2 - R_m^2\right) + \sqrt{R_m}\left(k_n^2 - R_n^2\right)\right\}}{\left(\sqrt{R_m}+\sqrt{R_n}\right)^2 - k^+_{mn}\tanh(k^+_{mn}h)} +$$
$$+ \frac{2\left(\sqrt{R_m}+\sqrt{R_n}\right)^2\left(k_m k_n - R_m R_n\right)}{\left(\sqrt{R_m}+\sqrt{R_n}\right)^2 - k^+_{mn}\tanh\left(k^+_{mn}h\right)}$$

$$D^-_{mn} = \frac{\left(\sqrt{R_m}-\sqrt{R_n}\right)\left\{\sqrt{R_n}\left(k_m^2 - R_m^2\right) - \sqrt{R_m}\left(k_n^2 - R_n^2\right)\right\}}{\left(\sqrt{R_m}-\sqrt{R_n}\right)^2 - k^-_{mn}\tanh(k^-_{mn}h)} +$$
$$+ \frac{2\left(\sqrt{R_m}-\sqrt{R_n}\right)^2\left(k_m k_n - R_m R_n\right)}{\left(\sqrt{R_m}-\sqrt{R_n}\right)^2 - k^-_{mn}\tanh\left(k^-_{mn}h\right)}$$

$$B^+_{mn} = \frac{1}{4}\left[\frac{D^+_{mn} - (k_m k_n - R_m R_n)}{\sqrt{R_m R_n}} + (R_m + R_n)\right]$$

$$B^-_{mn} = \frac{1}{4}\left[\frac{D^-_{mn} - (k_m k_n + R_m R_n)}{\sqrt{R_m R_n}} + (R_m + R_n)\right]$$

Appendix B

Implementing periodic waves in HOBEM

This appendix is related to the BEM code for the fully nonlinear wave kinematics, in particular the regular periodic wave implementation presented in Section 3.3.4. Here the compatibility issue between corner continuity and periodic boundary conditions is discussed and the implemented periodicity is presented.

B.1 Corner problem

Corners in the BEM domain cause an additional issue, therefore need special treatment. The issue is that at every corner node there is only one unique boundary integral equation stemming from identical coordinates, equally as there is a single potential value, but due to two different normal vectors there are two separate fluxes. It has been shown that even a small numerical instability at the corners quickly expands throughout the domain (Grilli and Svendsen, 1990), therefore various ways to deal with this problem have been developed, such discontinuous elements (Brebbia and Dominguez, 1998) and multiple flux method (Hague and Swan, 2009) to mention a few. The most common technique, which is implemented in this model too, are double nodes (Grilli et al., 1989). At every corner, instead of treating it as a single node, two nodes are assigned, both with identical coordinates. To ensure continuity, identical value for potential must be imposed on both nodes representing the same corner. This is done easily on the already reordered A matrix, overwriting one of the two identical rows. Changes also must be made to the F vector of the known values, yet the method is described in detail by Grilli and Svendsen (1990).

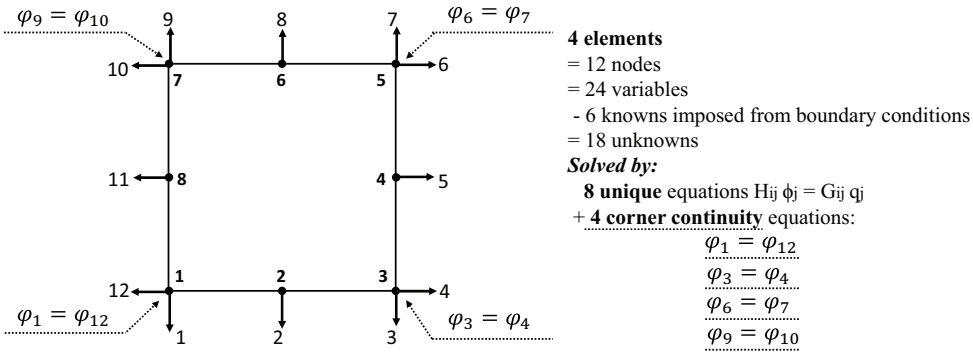

Figure B.1: Example of corner potential continuity condition applied on a rectangular domain with 1 quadratic element per side.

For the example illustrated in Figure B.1, on a square domain with 1 quadratic element per side and double corner nodes, there are 12 nodes for the 12 flux values. However, the four

pairs of nodes with identical coordinates lead to four sets of duplicate equations, because there are, as in this example, only 8 nodes with distinctive coordinates which provide unique equation $H_{ij}\varphi_j = G_{ij}q_j$. Moreover, both of the double corner nodes have a single potential value, and this condition needs to be imposed for correct solution. Consequently, the method substitutes the spare equations with potential continuity condition, which imposes that the potentials on both corner nodes have to be identical, as illustrated in Figure B.1.

Corner-associated issues and their treatment have been a topic of great interest, and to this day numerous guidelines and considerations are provided in the literature. Nonetheless, periodicity is excluded from the discussion, only briefly mentioning that in the case of periodicity corners do not impose an issue (Grilli and Svendsen, 1990).

B.2 Periodic BEM

BEM is a common choice for periodic gravity wave problems; however, the methodology of imposing periodicity on a rectangular BEM domain is not widely described in detail. Literature was found on simulating periodic waves on a transformed coordinate system, i.e. conformal mapping as first introduced by Longuet-Higgins and Cokelet (1976). However, such method is limited to solely periodic waves and is therefore unsuited for this research project. Studies on physical plane with imposed periodicity were found in literature, e.g. Vinje and Brevig (1981), Grilli et al. (1989), and Ortiz and Douglass (1993), but the methodology was not provided in sufficient detail to be implemented.

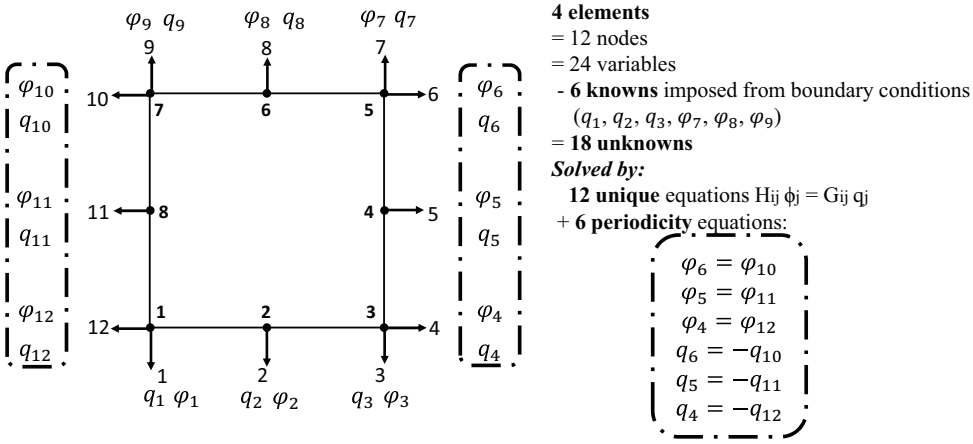

Figure B.2: Example of imposed periodicity condition on rectangular domain with 1 quadratic element per side.

Nonetheless, Ang (2009) has provided an algorithm for implying a 2D periodicity in a BEM model. This method treats the horizontal boundaries (the bottom and free surface) as usual with Neumann and Dirichlet conditions, but considering all variables on vertical walls as unknowns, and assigning no conditions at all. This leads to additional unknowns, equating to the number of nodes on both inflow and outflow walls ($NN_{in} + NN_{out}$). Therefore

the square HH and GG matrices are expanded by this number, six in the case illustrated in Figure B.2. To avoid underdefined system, additional periodicity equations are also provided, where inflow potential is forced to be equal to outflow potential ($\varphi_{in} = \varphi_{out}$), and inflow flux is the exact opposite (due to the opposite direction of the outward normal) of the outflow flux ($q_{in} = -q_{out}$), as illustrated in Figure B.2.

However, in the case of quadratic elements only the periodicity condition is not sufficient, since corner continuity condition needs to be solved as well, as explained in Section B.1. Unfortunately, the methodology of periodic BEM solver with corner condition on quadratic elements was not found in literature and proved to be incompatible if applied directly together.

B.3 Compatibility issue

The problem arises when combining the periodic condition with potential continuity in corners, especially on quadratic elements. Initially all items were accounted for as they were originally intended – using the quadratic elements, imposing the periodicity condition on all variables belonging to the lateral walls, and using the potential continuity on four corners, as illustrated in the Figure B.3. The imposed conditions were working as expected: the potentials on the corners and on the lateral walls were equal, the fluxes on the vertical walls were equal in magnitude but opposite in sign. However, the magnitudes of the values were misbehaving, causing numerical instabilities, and after multiple checks it was acknowledged that the system has become over-imposed.

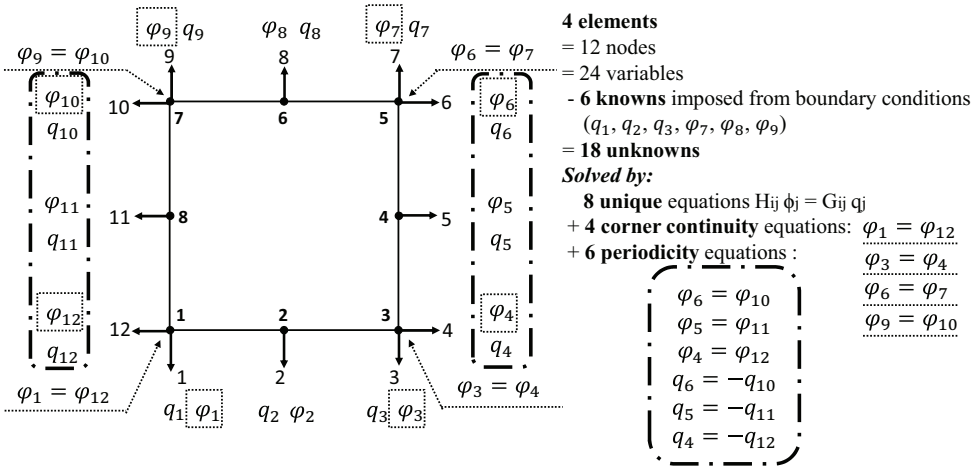

Figure B.3: Example of domain with 1 quadratic element per side, where both periodic and corner treatment conditions are imposed.

Numerous unsuccessful trials were attempted to rearrange the system to appropriately define it and avoid over-imposing. They included multiple flux method even though it is not suited for Dirichlet-Dirichlet corners; modelling with no vertical walls at all; other changes

in the influence coefficient matrices; imposing Neumann condition on both vertical walls with flux values from analytic solutions even though the values are actually unknown. In the end, a solution which fits the physics behind the model and is properly working was found.

B.4 Implementation

The solution to prove successfully functioning was the one which incorporates the continuity condition and periodicity, but not precisely as each of the methods would be implemented separately.

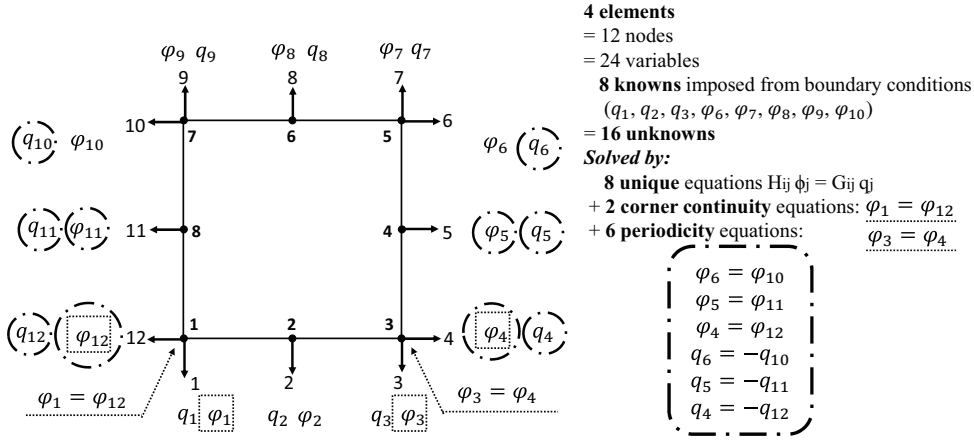

Figure B.4: Example of periodic quadratic BEM domain with 1 element per side and appropriate corner treatment.

The main modification is that the potentials at the top corners on lateral walls (e.g. φ_6 and φ_{10} in Fig. B.4) are treated as known values. Due to the potential continuity on corners they are equal to the end values at the free surface (φ_7 and φ_9 in Fig. B.4), which are in turn imposed from the boundary conditions (BC). This removes two unknowns, but also three equations associated with them: two continuity and one periodicity (for comparison refer to Fig. B.3). This created a need for an extra equation. After multiple trials of rearranging the system to either remove another unknown or impose another equation, a properly functioning solution was identified: to impose the fluxes at the end of the free surface (q_7 and q_9 in Fig. B.4) as equal due to periodicity. No such amendment was needed for the bottom corners because there both potentials are unknown as a result of the imposed Neumann boundary condition.

After the rest of the steady solver was adapted to these changes in the core solver, this solution for periodic waves on a rectangular domain proved to be well defined, quickly converging and successfully working, therefore it was used in the further development of the BEM model for fully nonlinear gravity waves.

Appendix C

UserTwrLoad subroutines

This appendix provides the `UserTwrLoad` subroutines for implementing the MAI, MAID and finite-depth FNV models in FAST solver.

C.1 MAI

```
SUBROUTINE UserTwrLd ( JNode, TwrDiam, TwrCA, TwrCD, NNodes, X, XD, ZTime,
    TwrAM, TwrFt )

  USE Precision
  USE Waves

  IMPLICIT NONE

    ! Passed Variables:
  REAL(ReKi), INTENT(OUT) :: TwrAM (6,6) ! Added mass matrix per unit length
       of current tower element (kg/m, kg-m/m, kg-m^2/m)
  REAL(ReKi), INTENT(OUT) :: TwrFt (6) ! The portion of the current tower
      element load per unit length associated with everything but the added
      mass effects; positive forces in the direction of motion (N/m, N-m/m)
  REAL(ReKi), INTENT(IN) :: TwrCA ! Normalized hydrodynamic added mass
      coefficient of current tower element (-)
  REAL(ReKi), INTENT(IN) :: TwrCD ! Normalized hydrodynamic viscous drag
      coefficient of current tower element (-)
  REAL(ReKi), INTENT(IN) :: TwrDiam ! Diameter of current tower element (m)
  REAL(ReKi), INTENT(IN) :: X (6) ! 3 components of translational (m) and
      rotational (rad) displacement of current tower element relative to MSL
  REAL(ReKi), INTENT(IN) :: XD (6) ! 3 components of translational (m/s) and
       rotational (rad/s) velocity of current tower element relative to MSL
  REAL(ReKi), INTENT(IN) :: XDD (6) ! 3 components of translational (m/s^2)
      and rotational (rad/s^2) acceleration of current tower element
      relative to MSL
  REAL(ReKi), INTENT(IN) :: ZTime ! Current simulation time (sec)
  INTEGER(4), INTENT(IN) :: JNode ! The number of the current tower node (-)
       [1 to TwrNodes]

    ! Local Variables:
  REAL(ReKi) :: DZFract ! The fraction of current tower element that is
      below the free surface of the incident wave and above the seabed (0.0
      <= DZFract <= 1.0): 0.0 = the element is entirely above free surface,
      1.0 = element is entirely below the free surface and above seabed (-)
```

```
REAL(ReKi) :: DZFractS ! The fraction of current tower element that is
    above the seabed (0.0 <= DZFractS <= 1.0): 0.0 = the element is
    entirely below seabed, 1.0 = element is entirely above seabed (-)
REAL(ReKi) :: DZFractW ! The fraction of current tower element that is
    below the free surface of the incident wave (0.0 <= DZFractW <= 1.0):
    0.0 = the element is entirely above free surface, 1.0 = element is
    entirely below free surface (-)
REAL(ReKi) :: InertiaForce (2) ! Wave inertia force in xi- (1) and yi- (2)
     directions, on current tower element at current time (N)
REAL(ReKi) :: MagVRel ! The magnitude of the horizontal incident wave
    velocity relative to the current tower node at the current time (m/s)
REAL(ReKi) :: MomArm ! Moment arm in the vertical direction from the
    current tower node to the center of pressure of the wave load on the
    current tower element (m)
REAL(ReKi) :: TowerAM ! Force-translation component of TwrAM (kg/m)
REAL(ReKi) :: TowerAMM ! Force-rotation and moment-translation component
    of TwrAM (kg-m/m)
REAL(ReKi) :: TowerAMM2 ! Moment-rotation component of TwrAM (kg-m^2/m)
REAL(ReKi) :: TwrArea ! Cross-sectional area of current tower element (m
    ^2)
REAL(ReKi) :: TwrVelocity (2) ! Velocity of the center of pressure of the
    wave load on the current tower element in the xi- (1) and yi- (2)
    directions, respectively, at the current time (m/s)
REAL(ReKi) :: ViscousForce (2) ! Viscous drag force in xi- (1) and yi- (2)
     directions, on current tower element at current time (N)
REAL(ReKi) :: WaveAcceleration0(2) ! Incident wave acceleration in xi- (1)
     and yi- (2) directions, at current tower node and time (m/s^2)
REAL(ReKi) :: WaveElevation0 ! Elevation of incident waves at the platform
     reference point and current time (meters)
REAL(ReKi) :: WaveVelocity0 (2) ! Incident wave velocity in xi- (1) and yi
    - (2) directions, at current tower node and time (m/s)
REAL(ReKi) :: AxialDivForce (2) ! Integrated Axial Divergence force (N)
REAL(ReKi) :: SurfIntersForce (2) ! Surface Intersection point load (N)
REAL(ReKi) :: WaveVelSurfT ! Wave velocity at instantaneous free surface
    at current time (m/s)
REAL(ReKi) :: WaveAccSurfT ! Wave acceleration at instantaneous free
    surface at current time (m/s^2)
REAL(ReKi) :: WaveSlopeT ! Wave slope detadx at current time (-)
REAL(ReKi) :: dvzdzT ! Derivative of vertical velocity over depth at
    current time (-/s)
INTEGER(4) :: K ! Generic index for the loop over x- and y- directions

  ! Initialize TwrAM and TwrFt to zero:
  DO K = 1,6 ! Loop through all six directions
    TwrAM(K,:) = (/ 0.0, 0.0, 0.0, 0.0, 0.0, 0.0 /)
    TwrFt(K) = 0.0
  ENDDO ! K - All 6 directions

  ! Find the fraction of the current tower element that is below the free
       surface of the incident wave and above the seabed:
```

```
IF ( WaveStMod == 0 ) THEN ! .TRUE. if we have no stretching; therefore,
     integrate up to the MSL, regardless of the instantaneous free surface
     elevation.
   IF ((WaveKinzi0(JNode) - 0.5*DZNodes(JNode)) >= 0.0) THEN ! .TRUE. if
       the current tower element lies entirely above the MSL.
      DZFractW = 0.0
   ELSEIF ((WaveKinzi0(JNode) + 0.5*DZNodes(JNode)) <= 0.0) THEN ! .TRUE.
       if the current tower element lies entirely below the MSL.
      DZFractW = 1.0
   ELSE ! The free surface of the incident wave must fall somewhere along
       the current tower element; thus, interpolate.
      DZFractW = ((0.0 - (WaveKinzi0(JNode) - 0.5*DZNodes(JNode)))/DZNodes(
          JNode))
   ENDIF
ELSE ! We must have some sort of stretching.
   WaveElevation0 = WaveElevation ( 1, ZTime )
   IF ((WaveKinzi0(JNode) - 0.5*DZNodes(JNode)) >= WaveElevation0) THEN !
       .TRUE. if the current tower element lies entirely above the free
       surface of the incident wave.
      DZFractW = 0.0
   ELSEIF ((WaveKinzi0(JNode) + 0.5*DZNodes(JNode)) <= WaveElevation0)
       THEN ! .TRUE. if the current tower element lies entirely below the
       free surface of the incident wave.
      DZFractW = 1.0
   ELSE ! The free surface of the incident wave must fall somewhere along
       the current tower element; thus, interpolate.
      DZFractW = ((WaveElevation0 - (WaveKinzi0(JNode) - 0.5*DZNodes(JNode)
          ))/DZNodes(JNode))
   ENDIF
ENDIF

IF ((WaveKinzi0(JNode) - 0.5*DZNodes(JNode)) >= -WtrDpth) THEN ! .TRUE. if
     the current tower element lies entirely above the seabed.
      DZFractS = 1.0
ELSEIF ((WaveKinzi0(JNode) + 0.5*DZNodes(JNode)) <= -WtrDpth) THEN ! .TRUE
     . if the current tower element lies entirely below the seabed.
      DZFractS = 0.0
ELSE ! The seabed must fall somewhere along the current tower element;
    thus, interpolate.
      DZFractS = (((WaveKinzi0(JNode) + 0.5*DZNodes(JNode)) - (-WtrDpth))/
          DZNodes(JNode))
ENDIF

DZFract = DZFractW*DZFractS

   ! Compute the hydrodynamic loads using MAI equation for the portion of
       the current tower element that lies below the free surface of the
       incident wave and above the seabed:
IF ( DZFract > 0.0 ) THEN ! .TRUE. if a portion of the current tower
     element lies below the free surface of the incident wave.
```

```
! Compute the moment arm in the vertical direction between the current
    tower node and the center of pressure of the wave load on the
    current tower element:
MomArm = 0.5*DZNodes(JNode)*( DZFractW - DZFractS ) ! NOTE: MomArm =
    0.0 when the entire element is submerged in the fluid; consequently
    , the roll and pitch components of the load are zero when the
    entire element is submerged in the fluid

! Compute velocity and acceleration of incident waves in xi- (1) and yi
    - (2) directions, at current tower node and time:
DO K = 1,2 ! Loop through the xi- (1) and yi- (2) directions
   WaveVelocity0(K) = WaveVelocity ( JNode, K, ZTime )
   WaveAcceleration0(K) = WaveAcceleration ( JNode, K, ZTime )
ENDDO ! K - The xi- (1) and yi- (2) directions

! Interpolate the needed kinematics at current node and time instant:
WaveVelSurfT = WaveVelSurf(ZTime)
WaveAccSurfT = WaveAccSurf(ZTime)
WaveSlopeT = WaveSlope(ZTime)
dvzdzT = dvzdz ( JNode, ZTime )

! Compute wave velocity and acceleration at current tower element in xi
    - (1) and yi- (2) directions at current time:
TwrVelocity(1) = XD(JNode,1) + XD(JNode,5)*MomArm
TwrVelocity(2) = XD(JNode,2) - XD(JNode,4)*MomArm
TwrAcceleration(1) = XDD(JNode,1) + XDD(JNode,5)*MomArm
TwrAcceleration(2) = XDD(JNode,2) - XDD(JNode,4)*MomArm

! Compute the magnitude of the horizontal incident wave velocity at the
     center of current tower element at current time:
MagVRel = SQRT( ( WaveVelocity0(1) - TwrVelocity(1) )**2 + (
    WaveVelocity0(2) - TwrVelocity(2) )**2 )

! Compute the cross-sectional area of the current tower element:
TwrArea = PiOvr4*TwrDiam*TwrDiam

! Compute added mass matrix per unit length of current tower element:
TowerAM = TwrCA*WtrDens*TwrArea*DZFract ! force-translation component
TowerAMM = TowerAM *MomArm ! force-rotation and moment-translation
    component
TowerAMM2 = TowerAMM*MomArm ! moment-rotation component

TwrAM(1,1) = TwrAM(1,1) + TowerAM ! surge-surge component
TwrAM(2,2) = TwrAM(2,2) + TowerAM ! sway -sway component
TwrAM(4,4) = TwrAM(4,4) + TowerAMM2 ! roll -roll component
TwrAM(5,5) = TwrAM(5,5) + TowerAMM2 ! pitch-pitch component
TwrAM(2,4) = TwrAM(2,4) - TowerAMM ! sway -roll component
TwrAM(4,2) = TwrAM(4,2) - TowerAMM ! roll -sway component
TwrAM(1,5) = TwrAM(1,5) + TowerAMM ! surge-pitch component
TwrAM(5,1) = TwrAM(5,1) + TowerAMM ! pitch-surge component
```

```
      ! Compute the portions of the current tower element load per unit
          length associated with inertia and viscous drag forces:
      DO K = 1,2 ! Loop through the xi- (1) and yi- (2) directions
         InertiaForce(K) = ( 1.0 + TwrCA )*WtrDens*TwrArea*WaveAcceleration0(K
             )*DZFract - TwrCA*WtrDens*TwrArea*TwrAcceleration(K)*DZFract
         ViscousForce(K) = 0.5*TwrCD*WtrDens*TwrDiam*( WaveVelocity0(K) -
             TwrVelocity(K) )*MagVRel*DZFract
      ENDDO ! K - The xi- (1) and yi- (2) directions

      ! Computing the MAI components in one direction only:
      ! Compute the distributed load components:
      AxialDivForce(1) = WtrDens * TwrArea * (WaveVelocity0(1) - TwrVelocity
          (1)) * dvzdzT * DZFract
      AxialDivForce(2) = 0.0

      ! Calculate the point loads at surface intersections:
      IF ( DZFractW < 1.0 .AND. DZFractW > 0.0 ) THEN ! only for the nodes at
           free surface intersection
         SurfIntersForce(1) = -0.5 * WtrDens * TwrArea * (WaveVelSurfT -
             TwrVelocity(1)) * (WaveVelSurfT - TwrVelocity(1)) * WaveSlopeT /
             DZNodes(JNode)
         SurfIntersForce(2) = 0.0
      ELSE
         SurfIntersForce(1) = 0.0
         SurfIntersForce(2) = 0.0
      ENDIF

      ! Final tower loading from MAI:
      TwrFt(1 ) = TwrFt(1 ) + InertiaForce(1) + AxialDivForce(1) +
          ViscousForce(1) + SurfIntersForce(1) ! surge component
      TwrFt(2 ) = TwrFt(2 ) + InertiaForce(2) + AxialDivForce(2) +
          ViscousForce(2) + SurfIntersForce(2) ! sway component
      TwrFt(4 ) = TwrFt(4 ) - ( InertiaForce(2) + AxialDivForce(2) +
          ViscousForce(2) )*MomArm - 0.5*SurfIntersForce(2)*(WaveElevation0 -
           WaveKinzi0(JNode)) ! roll component
      TwrFt(5 ) = TwrFt(5 ) + ( InertiaForce(1) + AxialDivForce(1) +
          ViscousForce(1) )*MomArm + 0.5*SurfIntersForce(1)*(WaveElevation0 -
           WaveKinzi0(JNode)) ! pitch component
   ENDIF
RETURN
END SUBROUTINE UserTwrLd
```

C.2 MAID

Compared to MAI subroutine listed in Section C.1, only a few additional lines are required.

```
SUBROUTINE UserTwrLd ( JNode, TwrDiam, TwrCA, TwrCD, NNodes, X, XD, ZTime,
    TwrAM, TwrFt )
```

```
   ! Local Variables:
REAL(ReKi) :: SurfDistForce (2) ! Point load of the Surface Distortion
    force (N)

IF ( DZFract > 0.0 ) THEN ! .TRUE. if a portion of the current tower
    element lies below the free surface of the incident wave.

   ! Compute the added mass matrix per unit length of the current tower
       element and the additional added mass relating to the point load (
       only on the free surface node):
   TowerAM = TwrCA*WtrDens*TwrArea*DZFract ! force -translation component
   IF ( DZFractW < 1.0 .AND. DZFractW > 0.0 ) THEN ! only for the nodes at
        free surface intersection
     TowerAM = TowerAM + 3.5 / 9.81 * WtrDens * TwrArea * (WaveVelSurfT -
         TwrVelocity(1)) * (WaveVelSurfT - TwrVelocity(1)) / DZNodes(JNode
         ) ! Surface distortion contribution to the added mass (the part
         multiplied by tower acceleration)
   ENDIF
   TowerAMM = TowerAM *MomArm ! force-rotation and moment-translation
       component
   TowerAMM2 = TowerAMM*MomArm ! moment-rotation component

   ! Computing the MAID components in one direction only:
   ! Calculate the point loads at surface intersections:
   IF ( DZFractW < 1.0 .AND. DZFractW > 0.0 ) THEN ! only for the nodes at
        free surface intersection
      SurfDistForce(1) = 3.5 / 9.81 * WtrDens * TwrArea * (WaveVelSurfT -
          TwrVelocity(1)) * (WaveVelSurfT - TwrVelocity(1)) * (WaveAccSurfT
           - TwrAcceleration(1)) / DZNodes(JNode)
      SurfDistForce(2) = 0.0
   ELSE
      SurfDistForce(1) = 0.0
      SurfDistForce(2) = 0.0
   ENDIF

   ! Final tower loading from MAID:
   TwrFt(1 ) = TwrFt(1 ) + InertiaForce(1) + AxialDivForce(1) +
       ViscousForce(1) + SurfIntersForce(1) + SurfDistForce(1) ! surge
       component
   TwrFt(2 ) = TwrFt(2 ) + InertiaForce(2) + AxialDivForce(2) +
       ViscousForce(2) + SurfIntersForce(2) + SurfDistForce(2) ! sway
       component
   TwrFt(4 ) = TwrFt(4 ) - ( InertiaForce(2) + AxialDivForce(2) +
       ViscousForce(2) )*MomArm - 0.5*(SurfIntersForce(2)+SurfDistForce(2)
       )*(WaveElevation0 - WaveKinzi0(JNode)) ! roll component
   TwrFt(5 ) = TwrFt(5 ) + ( InertiaForce(1) + AxialDivForce(1) +
       ViscousForce(1) )*MomArm + 0.5*(SurfIntersForce(1)+SurfDistForce(1)
       )*(WaveElevation0 - WaveKinzi0(JNode)) ! pitch component
ENDIF
RETURN
END SUBROUTINE UserTwrLd
```

C.3 FNV

Compared to MAI and MAID, FNV has the most different script from Morison equation. Nonetheless, the passed variables, the initalisation of `TwrAM` and `TwrFt`, and the definition of `DZFract`, `MomArm`, `WaveVelocity0`, `WaveAcceleration0`, `TwrArea` and `ViscousForce` are the same, therefore these are omitted in this script for brevity.

```
SUBROUTINE UserTwrLd ( JNode, TwrDiam, TwrCA, TwrCD, NNodes, X, XD, XDD,
    ZTime, TwrAM, TwrFt )

  ! Local Variables:
REAL(ReKi) :: DZFract
REAL(ReKi) :: DZFractS
REAL(ReKi) :: DZFractW
REAL(ReKi) :: MagVRel
REAL(ReKi) :: MomArm
REAL(ReKi) :: TowerAM
REAL(ReKi) :: TowerAMM
REAL(ReKi) :: TowerAMM2
REAL(ReKi) :: TwrArea
REAL(ReKi) :: TwrDispl (NNodes,2) ! Displacement of each tower element in
    the xi- (1) and yi- (2) directions at current time (m)
REAL(ReKi) :: TwrVelocity (NNodes,2) ! Velocity of each tower element in
    the xi- (1) and yi- (2) directions at current time (m/s)
REAL(ReKi) :: TwrAcceleration (NNodes,2) ! Acceleration of the center of
    each tower element in xi- (1) and yi- (2) directions at current time (
    m/s^2)
REAL(ReKi) :: dDispldz ! Derivative of tower displacement over depth for
    the current tower element at the current time (-)
REAL(ReKi) :: dDispldzM1 ! Derivative of tower displacement over depth for
     the current tower element at the current time (-)
REAL(ReKi) :: dDispldzP1 ! Derivative of tower displacement over depth for
     the current tower element at the current time (-)
REAL(ReKi) :: ddDisplddz ! Second order derivative of tower displacement
    over depth for the current tower element at the current time (-/m)
REAL(ReKi) :: dVeldz ! Derivative of tower velocity over depth for the
    current tower element at the current time (-/s)
REAL(ReKi) :: dAccdz ! Derivative of tower acceleration over depth for the
     current tower element at the current time (-/s^2)
REAL(ReKi) :: ViscousForce (2) ! Viscous drag force in the xi- (1) and yi-
     (2) directions on the current tower element at the current time (N)
REAL(ReKi) :: WaveAcceleration0(2) ! Acceleration of incident waves in xi-
     (1) and yi- (2) directions at current tower node and time (m/s^2)
REAL(ReKi) :: WaveElevation0 ! Elevation of incident waves at the platform
     reference point and current time (m)
REAL(ReKi) :: WaveVelocity0 (2) ! Velocity of incident waves in the xi-
    (1) and yi- (2) directions at the current tower node and time (m/s)
REAL(ReKi) :: WaveVelMeanT ! Wave velocity at the mean water surface at
    current time (m/s)
```

```
REAL(ReKi) :: WaveAccMeanT ! Wave acceleration at the mean water surface
    at current time (m/s^2)
REAL(ReKi) :: dvxdxT ! Derivative of horizontal velocity over x at current
     time (-/s)
REAL(ReKi) :: dvxdzT ! Derivative of horizontal velocity over depth at
    current time (-/s)
REAL(ReKi) :: dvzdzT ! Derivative of vertical velocity over depth at
    current time (-/s)
REAL(ReKi) :: FNV_i1 (2) ! First part of the integrated FNV force (N)
REAL(ReKi) :: FNV_i2 (2) ! Second part of the integrated FNV force (N)
REAL(ReKi) :: FNV_i (2) ! Total integrated part of the FNV force (N)
REAL(ReKi) :: FNV_psi(2) ! Point load of the FNV force (N)
REAL(ReKi) :: FNV (2) ! Total FNV force in x- and y-direction at current
    time (N)
INTEGER(4) :: J ! Generic index for looping over tower nodes (NNodes)
INTEGER(4) :: K ! Generic index for looping over x- and y- directions

   ! Compute the hydrodynamic loads using FNV equation for the portion of
       the current tower element that lies below the free surface of the
       incident wave and above the seabed:
IF ( DZFract > 0.0 ) THEN ! .TRUE. if a portion of the current tower
    element lies below the free surface of the incident wave.

   ! Interpolate the needed kinematics at current time instant:
   WaveVelMeanT = WaveVelMean(ZTime)
   WaveAccMeanT = WaveAccMean(ZTime)
   dvxdxT = dvxdx ( JNode, ZTime )
   dvxdzT = dvxdz ( JNode, ZTime )
   dvzdzT = dvzdz ( JNode, ZTime )

   ! Compute the wave velocity and acceleration at the center each tower
       element in the xi- (1) and yi- (2) directions at the current time:
   DO J = 1,NNodes
      TwrDispl(J,1) = X(J,1) + X(J,5)*MomArm
      TwrDispl(J,2) = X(J,2) - X(J,4)*MomArm
      TwrVelocity(J,1) = XD(J,1) + XD(J,5)*MomArm
      TwrVelocity(J,2) = XD(J,2) - XD(J,4)*MomArm
      TwrAcceleration(J,1) = XDD(J,1) + XDD(J,5)*MomArm
      TwrAcceleration(J,2) = XDD(J,2) - XDD(J,4)*MomArm
   ENDDO

   ! Computing the derivatives over depth for tower displacement, velocity
        and acceleration:
   IF (JNode > 1) THEN
      IF (JNode < NNodes) THEN ! Central differences scheme
         dDispldz = (TwrDispl(JNode+1,1)-TwrDispl(JNode-1,1)) / (2*DZNodes(
             JNode))
         dVeldz = (TwrVelocity(JNode+1,1)-TwrVelocity(JNode-1,1)) / (2*
             DZNodes(JNode))
         dAccdz = (TwrAcceleration(JNode+1,1)-TwrAcceleration(JNode-1,1)) /
              (2*DZNodes(JNode))
```

```
   ELSE ! Backward differences scheme
      dDispldz = (TwrDispl(JNode,1)-TwrDispl(JNode-1,1)) / DZNodes(JNode
          )
      dVeldz = (TwrVelocity(JNode,1)-TwrVelocity(JNode-1,1)) / DZNodes(
          JNode)
      dAccdz = (TwrAcceleration(JNode,1)-TwrAcceleration(JNode-1,1)) /
          DZNodes(JNode)
   ENDIF
ELSE ! Forward differences scheme
   dDispldz = (TwrDispl(JNode+1,1)-TwrDispl(JNode,1)) / DZNodes(JNode)
   dVeldz = (TwrVelocity(JNode+1,1)-TwrVelocity(JNode,1)) / DZNodes(
       JNode)
   dAccdz = (TwrAcceleration(JNode+1,1)-TwrAcceleration(JNode,1)) /
       DZNodes(JNode)
ENDIF

! Computing second order derivatives over depth for tower displacement:
IF (JNode > 2) THEN
   IF (JNode < NNodes-1) THEN ! Central differences scheme
      dDispldzM1 = (TwrDispl(JNode ,1)-TwrDispl(JNode-2,1)) / (2*DZNodes
          (JNode))
      dDispldzP1 = (TwrDispl(JNode+2,1)-TwrDispl(JNode ,1)) / (2*DZNodes
          (JNode))
      ddDisplddz = (dDispldzP1 - dDispldzM1) / (2*DZNodes(JNode))
   ELSE ! Backward differences scheme
      dDispldzM1 = (TwrDispl(JNode,1)-TwrDispl(JNode-2,1)) / (2*DZNodes(
          JNode))
      ddDisplddz = (dDispldz - dDispldzM1) / DZNodes(JNode)
   ENDIF
ELSE ! Forward differences scheme
   dDispldzP1 = (TwrDispl(JNode+2,1)-TwrDispl(JNode,1)) / (2*DZNodes(
       JNode))
   ddDisplddz = (dDispldzP1 - dDispldz) / DZNodes(JNode)
ENDIF

! Compute the added mass matrix per unit length of the current tower
    element and the additional added mass relating to the point load (
    only on the mean water surface node):
TowerAM = WtrDens*TwrArea*DZFract ! force -translation component
IF ( ( WaveKinzi0(JNode) - 0.5*DZNodes(JNode) ) >= 0.0 ) THEN ! .TRUE.
    if the current tower element lies entirely above the MSL.
ELSEIF ( ( WaveKinzi0(JNode) + 0.5*DZNodes(JNode) ) <= 0.0 ) THEN ! .
    TRUE. if the current tower element lies entirely below the MSL.
ELSE ! The free surface of the incident wave must fall somewhere along
    the current tower element.
  TowerAM = TowerAM + 4 / 9.81 * WtrDens * TwrArea * (WaveVelMeanT -
      TwrVelocity(1,JNode) - WaveVelocity0(3)*dDispldz) * (WaveVelMeanT
       - TwrVelocity(1,JNode) - WaveVelocity0(3)*dDispldz) / DZNodes(
      JNode) ! F_psi contribution to the added mass (the part
      multiplied by tower acceleration)
ENDIF
```

```
   TowerAMM = TowerAM *MomArm ! force-rotation and moment-translation
       component
   TowerAMM2 = TowerAMM*MomArm ! moment-rotation component

   ! Computing the FNV components in one direction only:
   ! Compute the distributed FNV load components:
   FNV_i1(1) = WtrDens * TwrArea * ( 2 * WaveAcceleration0(1) -
       TwrAcceleration(JNode,1) - WaveVelocity0(3) * dVeldz - dDispldz *
       WaveAcceleration0(3) ) * DZFract
   FNV_i2(1) = WtrDens * TwrArea * ( (WaveVelocity0(1) - 0.5 * (
       TwrVelocity(JNode,1) + WaveVelocity0(3) * dDispldz)) * dvxdxT +
       WaveVelocity0(3) * ( 2*dvxdzT - dVeldz - dDispldz*dvzdzT -
       WaveVelocity0(3)*ddDisplddz) ) * DZFract
   FNV_i(1) = FNV_i1(1) + FNV_i2(1)
   FNV_i(2) = 0.0

   ! Compute the FNV point loads at mean surface:
   IF ( ( WaveKinzi0(JNode) - 0.5*DZNodes(JNode) ) >= 0.0 ) THEN ! .TRUE.
       if the current tower element lies entirely above the MSL.
     FNV_psi(1) = 0.0
     FNV_psi(2) = 0.0
   ELSEIF ( ( WaveKinzi0(JNode) + 0.5*DZNodes(JNode) ) <= 0.0 ) THEN ! .
       TRUE. if the current tower element lies entirely below the MSL.
     FNV_psi(1) = 0.0
     FNV_psi(2) = 0.0
   ELSE ! The mean surface of the incident wave must fall somewhere along
       the current tower element.
     FNV_psi(1) = 4 / 9.81 * WtrDens * TwrArea * (WaveVelMeanT -
         TwrVelocity(1,JNode) - WaveVelocity0(3)*dDispldz) * (WaveVelMeanT
          - TwrVelocity(1,JNode) - WaveVelocity0(3)*dDispldz) * (
         WaveAccMeanT - TwrAcceleration(1,JNode) - WaveVelocity0(3)*dVeldz
          - dDispldz*WaveAcceleration0(3)) / DZNodes(JNode)
     FNV_psi(2) = 0.0
   ENDIF

   ! Final tower loading from FNV:
   TwrFt(1 ) = TwrFt(1 ) + FNV_i(1) + FNV_psi(1) + ViscousForce(1) ! surge
        component
   TwrFt(2 ) = TwrFt(2 ) + FNV_i(2) + FNV_psi(2) + ViscousForce(2) ! sway
       component
   TwrFt(4 ) = TwrFt(4 ) - ( FNV_i(2) + ViscousForce(2) )*MomArm - 0.5*(
       FNV_psi(2))*(0 - WaveKinzi0(JNode)) ! roll component (the point
       load is applied at z=0, not z=eta)
   TwrFt(5 ) = TwrFt(5 ) + ( FNV_i(1) + ViscousForce(1) )*MomArm + 0.5*(
       FNV_psi(1))*(0 - WaveKinzi0(JNode)) ! pitch component (the point
       load is applied at z=0, not z=eta)
ENDIF
RETURN
END SUBROUTINE UserTwrLd
```

References

4C Offshore (2018a). *Kaorehamn Offshore Wind Farm*. URL: https://www.4coffshore.com/windfarms/k{\aa}rehamn-sweden-se08.html.

4C Offshore (2018b). *Lillgrund Offshore Wind Farm*. URL: https://www.4coffshore.com/windfarms/lillgrund-sweden-se05.html.

Agarwal, P. and L. Manuel (2011). Incorporating irregular nonlinear waves in coupled simulation and reliability studies of offshore wind turbines. *Applied Ocean Research* 33.3, pp. 215–227. DOI:10.1016/J.APOR.2011.02.001. URL: http://dx.doi.org/10.1016/j.apor.2011.02.001.

Airy, G. B. (1845). Tides and waves. *Encyclopedia Metropolitana* article 19, pp. 241–396.

Ang, W. T. (2009). *2D Potential Problems with Periodic Boundary Conditions*. URL: http://www.ntu.edu.sg/home/mwtang/periodic.pdf.

Bachynski, E. E., M. Thys, and V. Delhaye (2019). Dynamic response of a monopile wind turbine in waves : Experimental uncertainty analysis for validation of numerical tools. *Applied Ocean Research* 89.April, pp. 96–114. DOI:10.1016/J.APOR.2019.05.002. URL: https://doi.org/10.1016/j.apor.2019.05.002.

Brebbia, C. and J. Dominguez (1998). *Boundary Elements An Introductory Course*. Southampton, UK: WIT Press/Computational Mechanics Publications, p. 318.

Bredmose, H., J. Mariegaard, B. T. Paulsen, B. Jensen, S. Schløer, T. Larsen, T. Kim, and A. M. Hansen (2013). *The Wave Loads project*. Tech. rep. DTU Wind Energy, p. 119.

Catterson, V. M., D Mcmillan, I Dinwoodie, M Revie, J Dowell, and J Quigley (2016). An economic impact metric for evaluating wave height. *Wind Energy* 19, pp. 199–212. DOI:10.1002/WE.

Chakrabarti, S. K. (1987). *Hydrodynamics of offshore structures. 1. Offshore structures - Hydrodynamics I*. P. 435.

Chaplin, J. R., R. C. Rainey, and R. Yemm (1997). Ringing of a vertical cylinder in waves. *Journal of Fluid Mechanics* 350, pp. 119–147. DOI:10.1017/S002211209700699X.

De Ridder, E.-J., P. Aalberts, J. van den Berg, B. Buchner, and J. Peeringa (2011). The dynamic response of an offshore wind turbine with realistic flexibility to breaking wave impact. In: *Proceedings of the ASME 2011 30th International Conference on Ocean, Offshore and Arctic Engineering, June 19-24, 2011, Rotterdam, The Netherlands*, pp. 1–10.

Dean, R. G. (1965). Stream function representation of non-linear ocean waves. *Journal of Geophysical Research* 70, pp. 4561–4572.

Dean, R. G. and R. Dalrymple (1984). *Water Wave Mechanics for Engineers and Scientists*. on Ocean E. World Scientific.

Dold, J. W. (1992). An Efficient Surface-Integral Algorithm Applied to Unsteady Gravity Waves. 96115, pp. 90–115.

Dommermuth, D. (2000). The initialization of nonlinear waves using an adjustment scheme. *Wave Motion* 32, pp. 307–317. DOI:10.1016/S0165-2125(00)00047-0.

European Commission (2014). *2030 climate & energy framework*. URL: https://ec.europa.eu/clima/policies/strategies/2030{_}en.

European Commission (2018). *2050 low-carbon economy*. URL: https://ec.europa.eu/clima/policies/strategies/2050{_}en.

Eurostat (2017). *ENERGY FROM RENEWABLE SOURCES*. URL: https://ec.europa.eu/eurostat/web/energy/data/shares.

Faltinsen, O. M. (1990). *Sea loads on ships and offshore structures*. Cambridge, UK: Cambridge University Press, p. 328.

Faltinsen, O. M. (1999). Ringing loads on a slender vertical cylinder of general cross-section. *Journal of Engineering Mathematics* 35, pp. 199–217. DOI:10.1023/A:1004362827262.

Faltinsen, O. M. (2018). Generalized FNV with flexible body motions. *Private communication*.

Faltinsen, O. M., J. N. Newman, and T Vinje (1995). Nonlinear wave loads on a slender vertical cylinder. *Journal of Fluid Mechanics* 289, pp. 179–198.

Fenton, J. D. (1979). A high order cnoidal wave theory. *Journal of Fluid Mechanics* 94.1, pp. 129–161. DOI:10.1017/S0022112079000975.

FINO (2018). *Forschungsplattformen in Nord- und Ostsee Nr. 1,2,3*. URL: http://www.fino-offshore.de/.

GE Renewable Energy (2017). *4.8MW - WHY BIGGER IS BETTER*. URL: https://www.ge.com/renewableenergy/stories/48-158-why-bigger-is-better.

Gottlieb, M. H. and G. Milepael (2018). *Danmark sætter ny rekord i vind (Denmark sets new record in the wind)*. URL: https://www.danskenergi.dk/nyheder/danmark-saetter-ny-rekord-vind.

Grilli, S. T., J. Skourup, and I. Svendsen (1989). An efficient boundary element method for nonlinear water waves. *Engineering Analysis with Boundary Elements* 6.2, pp. 97–107.

Grilli, S. T. and R. Subramanya (1996). Numerical modeling of wave breaking induced by fixed or moving boundaries. *Computational Mechanics* 17, pp. 374–391.

Grilli, S. T. and I. Svendsen (1990). Corner problems and global accuracy in the boundary element solution of nonlinear wave flows. *Engineering Analysis with Boundary Elements* 7.4, pp. 178–195. DOI:HTTPS://DOI.ORG/10.1016/0955-7997(90)90004-S.

Grue, J. (2002). On four highly nonlinear phenomena in wave theory and marine hydrodynamics. *Applied Ocean Research* 24.5, pp. 261–274. DOI:10.1016/S0141-1187(03)00006-3.

Grue, J., G. Bjorshol, and Ø. Strand (1993). Higher harmonic wave exciting forces on a vertical cylinder. *Institute of Mathematics, University of Oslo Preprint* No. 2.2, p. 28.

Grue, J., G. Bjorshol, and Ø. Strand (1994). Nonlinear wave loads which may generate 'ringing' responses of offshore structures. In: *9th International Workshop on Water Waves and Floating Bodies*, pp. 77–81.

Grue, J. and M. Huseby (2002). Higher harmonic wave forces and ringing of vertical cylinders. *Applied Ocean Research* 24.4, pp. 203–214. DOI:10.1016/S0141-1187(02)00048-2.

Guyenne, P., S. T. Grilli, and F. Dias (2000). Numerical modelling of fully nonlinear 3D overturning waves over arbitrary bottom. *Coastal Engineering*, pp. 417–428.

GWEC (2017a). *Global Wind Report 2016*. Tech. rep., p. 76.

GWEC (2017b). *Wind in Numbers*. URL: https://gwec.net/global-figures/wind-in-numbers/.

GWEC (2018a). *Global Wind Report 2017*. Tech. rep., p. 72.

GWEC (2018b). *Key Findings of Global Wind Market Report 2017. Webinar.*

Hague, C. and C. Swan (2009). A multiple flux boundary element method applied to the description of surface water waves. *Journal of Computational Physics* 228.14, pp. 5111–5128. DOI:10.1016/J.JCP.2009.04.012.

Hu, S. J. and D. Zhao (1993). Non-Gaussian Properties of Second-Order Random Waves. *Journal of Engineering Mechanics* 119.2, pp. 344–364. DOI:10.1061/(ASCE)0733-9399(1993)119:2(344).

Huseby, M. and J. Grue (2000). An experimental investigation of higher-harmonic wave forces on a vertical cylinder. *Journal of Fluid Mechanics* 414, pp. 75–103. DOI:10.1017/S0022112000008533.

Hyers, R. W., J. G. Mcgowan, K. L. Sullivan, J. F. Manwell, and B. C. Syrett (2006). Condition monitoring and prognosis of utility scale wind turbines. *Energy Materials* 1.3, pp. 187–203. DOI:10.1179/174892406X163397.

IEA (2017). *World Energy Outlook 2017: China*. URL: https://www.iea.org/weo/china/.

International Electrotechnical Commission (2005). *INTERNATIONAL STANDARD IEC 61400-1 ed.3 Design requirements for onshore wind turbine*. Tech. rep., p. 92.

International Electrotechnical Commission (2009). *INTERNATIONAL STANDARD IEC 61400-3. Wind turbines – Part 3: Design requirements for offshore wind turbines*.

Jonkman, B. (2012). *Instructions for Compiling FAST using IVF for Windows ®*. Tech. rep., pp. 1–10.

Jonkman, J. M. (2007). Dynamics modeling and loads analysis of an offshore floating wind turbine. *National Renewable Energy Laboratory NREL/TP-500-41958* 68.November. URL: http://www.nrel.gov/docs/fy08osti/41958.pdf.

Jonkman, J. M. (2018). *FAST*. URL: https://nwtc.nrel.gov/FAST.

Jonkman, J. M. and M. L. Buhl Jr. (2005). *FAST User's Guide*. Tech. rep. DOI:10.2172/15020796. URL: http://www.ncbi.nlm.nih.gov/pubmed/21564034.

Jonkman, J. M., S Butterfield, W. Musial, and G Scott (2009). Definition of a 5-MW reference wind turbine for offshore system development. *Contract* February, pp. 1–75. DOI:10.1002/AJMG.10175. URL: http://tethys-development.pnnl.gov/sites/default/files/publications/Jonkman{_}et{_}al{_}2009.pdf.

Jonkman, J. M. and W. Musial (2010). Offshore Code Comparison Collaboration (OC3) for IEA Task 23 Offshore Wind Technology and Deployment. December.

Jonkman, J. M., A. N. Robertson, and G. J. Hayman (2014). *HydroDyn User ' s Guide and Theory Manual HydroDyn User ' s Guide and Theory Manual*. Tech. rep.

Jonkman, J. M. et al. (2012). Offshore Code Comparison Collaboration Continuation (OC4), Phase I - Results of Coupled Simulations of an Offshore Wind Turbine with Jacket Support Structure. March.

Kim, C. (2008). *Nonlinear Waves and Offshore Structures*. on Ocean E. World Scientific.

Korteweg, D. J. and G. de Vries (1895). On the Change of Form of Long Waves Advancing in a Rectangular Canal, and on a New Type of Long Stationary Waves. *Philosophical Magazine* 39.240, pp. 422–443. DOI:10.1080/14786449508620739.

Kristiansen, T. and O. M. Faltinsen (2017). Ringing loads on a vertical cylinder in finite water depth. In: *The International Workshop on Water Waves and Floating Bodies 2017*, pp. 1–4.

Krokstad, J. R. and F. Solaas (2000). Study of Nonlinear Local Flow. In: *Tenth (2000) International Offshore and Polar Engineering Conference*. Vol. 4, pp. 449–454.

Langen, I., O. Skjastad, and S. Haver (1998). Measured and predicted dynamic behaviour of an offshore gravity platform. *Applied Ocean Research* 20, pp. 15–26.

Liu, S., J. Jose, M. C. Ong, and O. T. Gudmestad (2019). Characteristics of higher-harmonic breaking wave forces and secondary load cycles on a single vertical circular cylinder at different Froude numbers. *Marine Structures* 64.October 2018, pp. 54–77. DOI:10.1016/J.MARSTRUC.2018.10.007. URL: https://linkinghub.elsevier.com/retrieve/pii/S0951833918301758.

Longuet-Higgins, M. and E. Cokelet (1976). The Deformation of Steep Surface Waves on Water. I. A Numerical Method of Computation. *Proceedings of the Royal Society A* 350, pp. 1–26. DOI:10.1098/RSPA.1976.0092.

Ma, Y., G. Dong, M. Perlin, S. Liu, J. Zang, and Y. Sun (2009). Higher-harmonic focused-wave forces on a vertical cylinder. *Ocean Engineering* 36, pp. 595–604. DOI:10.1016/J.OCEANENG.2009.02.009.

Malenica, Š. and B. Molin (1995). Third-harmonic wave diffraction by a vertical cylinder. *Journal of Fluid Mechanics* 302, pp. 203–229.

Marino, E. (2010). An integrated nonlinear wind-waves model for offshore wind turbines. PhD thesis. Firenze, Italy, p. 201.

Marino, E., C. Borri, and C. Lugni (2011a). Influence of wind-waves energy transfer on the impulsive hydrodynamic loads acting on offshore wind turbines. *Journal of Wind Engineering and Industrial Aerodynamics* 99, pp. 767–775. DOI:10.1016/J.JWEIA.2011.03.008.

Marino, E., C. Borri, and U. Peil (2011b). A fully nonlinear wave model to account for breaking wave impact loads on offshore wind turbines. *Journal of Wind Engineering and Industrial Aerodynamics* 99, pp. 483–490. DOI:10.1016/J.JWEIA.2010.12.015.

Marino, E., A. Giusti, and L. Manuel (2017). Offshore wind turbine fatigue loads: The influence of alternative wave modeling for different turbulent and mean winds. *Renewable Energy* 102, pp. 157–169.

Marino, E., C. Lugni, and C. Borri (2013a). A novel numerical strategy for the simulation of irregular nonlinear waves and their effects on the dynamic response of offshore wind turbines. *Computer Methods in Applied Mechanics and Engineering* 255, pp. 275–288. DOI:10.1016/J.CMA.2012.12.005.

Marino, E., C. Lugni, and C. Borri (2013b). The role of the nonlinear wave kinematics on the global responses of an OWT in parked and operating conditions. *Journal of Wind Engineering and Industrial Aerodynamics* 123, pp. 363–376. DOI:10.1016/J.JWEIA.2013.09.003.

Marino, E., C. Lugni, L. Manuel, H. Nguyen, and C. Borri (2014a). Simulation of Nonlinear Waves on Offshore Wind Turbines. In: *Proceedings of the ASME 2014 33rd International Conference on Ocean, Offshore and Arctic Engineering*, pp. 1–9.

Marino, E., C. Lugni, G. Stabile, and C. Borri (2014b). Coupled dynamic simulations of offshore wind turbines using linear , weakly and fully nonlinear wave models : the limitations of the second-order wave theory. In: *9th International Conference on Structural Dynamics EURODYN*. July, pp. 3603–3610.

Marino, E., H. Nguyen, C. Lugni, L. Manuel, and C. Borri (2015). Irregular Nonlinear Wave Simulation and Associated Loads on Offshore Wind Turbines. *Journal of Offshore Mechanics and Arctic Engineering* 137.2, p. 021901. DOI:10.1115/1.4029212.

MHI Vestas Offshore Wind (2017). *World's most powerful wind turbine once again smashes 24 hour power generation record as 9 MW wind turbine is launched*. URL: http://www.mhivestasoffshore.com/new-24-hour-record/.

MHI Vestas Offshore Wind (2018). *MHI Vestas Launches the First 10 MW Wind Turbine in History*. URL: http://www.mhivestasoffshore.com/mhi-vestas-launches-the-first-10-mw-wind-turbine-in-history/.

Midthaug, A. H. (2014). Nonlinear Wave Loads on Offshore Wind Turbines in Storm Condition. PhD thesis, p. 89.

Mockute, A., E. Marino, and C. Borri (2017a). Effects of wind-wave misalignment on the dynamic response of an offshore wind turbine in highly nonlinear waves. In: *7th European and African Conference on Wind Engineering*.

Mockute, A., E. Marino, A. Giusti, and C. Borri (2016). Effects of wind-wave misalignment in the case of nonlinear hydrodynamic loading of offshore wind turbines. In: *Proceedings of IN-VENTO 2016 - XIV Conference of the Italian Association for Wind Engineering*. 25-28 September 2016, Terni, Italy, pp. 207–214. URL: http://www.strutture.unipg.it/invento2016/docs/invento2016{_}proceedings.pdf.

Mockute, A., E. Marino, C. Lugni, and C. Borri (2017b). Comparison of hydrodynamic loading models for vertical cylinders in nonlinear waves. *Procedia Engineering* 199, pp. 3224–3229. DOI:10.1016/J.PROENG.2017.09.329.

Morison, J., M. O'Brien, J. Johnson, and S. Schaaf (1950). The Force Exerted by Surface Waves on Piles. *Petroleum Transactions, AIME* 189, pp. 149–154.

Newman, J. N. (1977). *Marine Hydrodynamics*. Cambridge, UK: MIT Press, p. 402.

Newman, J. N. (1996). Nonlinear Scattering of Long Waves by a Vertical Cylinder. In: *Waves and Nonlinear Processes in Hydrodynamics*. Ed. by J. Grue, B. Gjevik, and J. E. Weber. Dordrecht: Springer Netherlands, pp. 91–102. DOI:10.1007/978-94-009-0253-4_8.

Norwegian Petroleum Directorate (1992). *NPD Annual Report 1992*. Tech. rep., pp. 1–162.

Ortiz, J. C. and S. L. Douglass (1993). Overhauser boundary elements solution for periodic water waves in the physical plane. *Engineering Analysis with Boundary Elements* 11, pp. 47–54. DOI:HTTP://DX.DOI.ORG/10.1016/0955-7997(93)90078-Y.

Paulsen, B. T., H. Bredmose, H. B. Bingham, and N. G. Jacobsen (2014). Forcing of a bottom-mounted circular cylinder by steep regular water waves at finite depth. *Journal of Fluid Mechanics* 755, pp. 1–34. DOI:10.1017/JFM.2014.386.

Plate, E. (1971). *Aerodynamic Characteristics of Atmospheric Boundary Layers. AEC Crit. Rev. Ser. TID15465*. Tech. rep. Technical Information Center, US Department of Energy.

Rainey, R. C. (1989). A new equation for calculating wave loads on offshore structures. *Journal of Fluid Mechanics* 204, pp. 295–324. DOI:10.1017/S002211208900176X.

Rainey, R. C. (1995). Slender-body expressions for the wave load on offshore structures. *Proceedings: Mathematical and Physical Sciences* 450.1939, pp. 391–416.

Rainey, R. C. (2007). Weak or strong nonlinearity : the vital issue. *Journal of Engineering Mathematics* Newman Hon, pp. 1–27.

Rezaei, R., P. Fromme, and P. Duffour (2018). Fatigue life sensitivity of monopile-supported offshore wind turbines to damping. *Renewable Energy* 123, pp. 450–459. DOI:10.1016/J.RENENE.2018.02.086. URL: https://doi.org/10.1016/j.renene.2018.02.086.

Rienecker, M. M. and J. D. Fenton (1981). A Fourier approximation method for steady water waves. *Journal of Fluid Mechanics* 104, pp. 119–137.

Riise, B. H., J. Grue, and A. Jensen (2018a). A note on the secondary load cycle for a monopile in irregular deep water waves. *Journal of Fluid Mechanics* 849.R1, R1–12. DOI:10.1017/JFM.2018.450.

Riise, B. H., J. Grue, A. Jensen, and T. B. Johannessen (2018b). High frequency resonant response of a monopile in irregular deep water waves. *Journal of Fluid Mechanics* 853, pp. 564–586. DOI:10.1017/JFM.2018.499.

Robertson, A. N. et al. (2016). OC5 Project Phase Ib : Validation of Hydrodynamic Loading on a Fixed , Flexible Cylinder for Offshore Wind Applications. *Energy Procedia* 94.January, pp. 82–101. DOI:10.1016/J.EGYPRO.2016.09.201. URL: http://dx.doi.org/10.1016/j.egypro.2016.09.201.

Robertson, A. N. et al. (2017). *OC5 Project Phase II : Validation of Global Loads of the DeepCwind Floating Semisubmersible Wind Turbine*.

Sarpkaya, T. and M. Isaacson (1981). *Mechanics of Wave Forces on Offshore Structures*. Van Nostrand Reinhold Company.

Schafhirt, S., A. Page, G. R. Eiksund, and M. Muskulus (2016). Influence of Soil Parameters on the Fatigue Lifetime of Offshore Wind Turbines with Monopile Support Structure. *Energy Procedia* 94.January, pp. 347–356. DOI:10.1016/J.EGYPRO.2016.09.194.

Schløer, S., H. Bredmose, and H. B. Bingham (2016). The influence of fully nonlinear wave forces on aero-hydro-elastic calculations of monopile wind turbines. *Marine Structures* 50, pp. 162–188. DOI:10.1016/J.MARSTRUC.2016.06.004.

Sharma, J. N. and R. G. Dean (1981). Second-Order Directional Seas and Associated Wave Forces.. *Society of Petroleum Engineers journal* 21.1, pp. 129–140. DOI:10.2118/8584-PA.

Skjelbreia, L. and J. Hendrickson (1961). FIFTH ORDER GRAVITY WAVE THEORY. In: pp. 184–196.

Stansberg, C. (1997). *Comparing ringing loads from experiments with cylinder of different diameters - an experimental study*.

Stansberg, C., H. Huse, J. R. Krokstad, and E. Lehen (1995). Experimental Study of Non-Linear Loads on Vertical Cylinders in Steep Random Waves. In: *Fifth International Offshore and Polar Engineering Conference*, pp. 75–82.

Stehly, T., D. Heimiller, G. Scott, T. Stehly, D. Heimiller, and G. Scott (2017). *2016 Cost of Wind Energy Review 2016 Cost of Wind Energy Review*. Tech. rep., p. 38.

Stokes, G. G. (1847). *On the Theory of Osciallatory Waves*.

Stokes, G. G. (1880). Supplement to a paper on the theory of Oscillatory waves. *Mathematical and Physical Papers, Cambridge University Press* I, pp. 314–326.

Suja-Thauvin, L., J. R. Krokstad, and E. E. Bachynski (2018). Critical assessment of non-linear hydrodynamic load models for a fully flexible monopile offshore wind turbine. *Ocean Engineering* 164.December 2017, pp. 87–104. DOI:10.1016/J.OCEANENG.2018.06.027.

Suja-Thauvin, L., J. R. Krokstad, E. E. Bachynski, and E.-J. de Ridder (2017). Experimental results of a multimode monopile offshore wind turbine support structure subjected to steep and breaking irregular waves. *Ocean Engineering* 146.November 2016, pp. 339–351. DOI:10.1016/J.OCEANENG.2017.09.024.

Swan, C., T Bashir, and O. Gudmestad (2002). Nonlinear inertial loading. Part I : accelerations in steep 2-D water waves. *Journal of Fluids and Structures* 16.3, pp. 391–416. DOI:10.1006/J.

United Nations (2019). *Paris Agreement*. URL: https://unfccc.int/process-and-meetings/the-paris-agreement/the-paris-agreement.

Van Der Meulen, M. B., T Ashuri, G. J. W. V. Bussel, and D. P. Molenaar (2012). Influence of Nonlinear Irregular Waves on the Fatigue Loads of an Offshore Wind Turbine. In: *The Science of Making Torque From Wind*, p. 10.

Vinje, T and P Brevig (1981). Numerical simulation of breaking waves. *Advances in Water Resources* 4.2, pp. 77–82. DOI:HTTP://DX.DOI.ORG/10.1016/0309-1708(81)90027-0.

Vorpahl, F. (2011). IEA Wind Annex 30 - OC4 Project The Offshore Code Comparison Collaboration Continuation OC4 project background and overview Phase I : Turbine on jacket substructure Phase II : Turbine on floating semisubmersible.

Wang, C. and G. Wu (2010). Interactions between fully nonlinear water waves and cylinder arrays in a wave tank. *Ocean Engineering* 37.4, pp. 400–417. DOI:10.1016/J.OCEANENG.2009.12.006. URL: http://linkinghub.elsevier.com/retrieve/pii/S0029801809002856.

Wienke, J. and H. Oumeraci (2005). Breaking wave impact force on a vertical and inclined slender pile - theoretical and large-scale model investigations. *Coastal Engineering* 52.5, pp. 435–462. DOI:10.1016/J.COASTALENG.2004.12.008.

Wind Power Monthly (2018). *TEN OF THE BIGGEST TURBINES*. URL: https://www.windpowermonthly.com/10-biggest-turbines.

World Energy Council (2017). *World Energy TRILEMMA | 2017 Changing Dynamics - Using Distributed Energy Resources to Meet the Trilemma Challenge*. Tech. rep., p. 85.